Airway Macrophage Metabolic Reprogramming During Interstitial Lung Disease

A thesis submitted to Imperial College London for the degree of Doctor of Philosophy

Pia Patricia Ogger, MRes

Inflammation, Repair & Development Section

National Heart & Lung Institute

Faculty of Medicine

Imperial College London

SW7 2AZ

2020

Declaration of Originality

I hereby certify that all the work outlined in this thesis was conducted by myself, apart from the following exceptions. Simone Walker operated the Flexivent system. Lorraine Lawrence (IRD Histology Service) embedded, sectioned and stained all the lung sections with Sirius red stain. Mass spectrometry measurements for glycolysis and TCA cycle metabolites were performed at King's College London, Centre of Excellence for Mass Spectrometry by Professor John Halket and Robert Gray. The FACS sorting of cells was performed in the Imperial College London Flow Cytometry Facility with the help of Dr. Jessica Rowley, Jane Srivastava and Radhika Patel. Professor Toby Maher, Dr. Richard Hewitt, Dr. Phil Molyneaux and Dr. Richard Toshner performed bronchoscopies of ILD patients and healthy controls, including obtaining consent, at the Royal Brompton Hospital. Poonam Ghai coordinated the initial processing of BAL samples obtained from the Royal Brompton Hospital.

Copyright Declaration

Acknowledgements

Firstly, I would like to thank my supervisors Dr. Adam Byrne, Professor Clare Lloyd and Professor Toby Maher for giving me the opportunity to carry out this PhD project under their guidance. In particular, I would like to thank my primary supervisor Dr. Adam Byrne for all the support, encouragement and mentorship over the last four years. Specifically, thank you for all your feedback on my many scholarship applications, always having my back at talks and conferences and for your infectious optimism! In addition, I would like to thank Professor Clare Lloyd for the career advice meetings and for being my role model as a strong female scientist! Furthermore, I would like to thank Professor Toby Maher for integrating me into his clinical research team and feedback on my writing.

I would like to thank the National Heart and Lung Institute for funding this studentship and for providing such a stimulating environment. Furthermore, my gratitude extends to the German Academic Scholarship Foundation, which has enabled my studies abroad, broadened my horizon with a variety of workshops and has funded the final year of this PhD.

Special thanks go to my Byrne Lab companion Gesa Albers – thank you for all the banter, laughter, and support on long experiment days! Furthermore, I would like to thank all the members of the Byrne lab for lending hands during long experiments and creating such a positive atmosphere at work. I would also like to thank Simone Walker for brightening up early morning experiments. I am particularly grateful for all my fellow PhD students and colleagues in the IRD section – thank you for the exchange of ideas, gossip, tea and cake!

Finally, I would like to thank all my friends and in particular my old housemates Leon, Leanne and Ralf for being my support network and for always listening. My gratitude extends further to my parents and my siblings, who have always believed in me and supported me throughout my studies and research! Lastly, I would like to thank my boyfriend Nick for the endless encouragement and especially for sticking out three months in lockdown with me during the Covid-19 Crisis!

Abstract

Airway macrophages (AM) play a key role during the pathogenesis of pulmonary fibrosis. The underlying metabolic alterations driving this phenotype however are little understood. The aim of this thesis was to investigate the metabolic phenotype of AMs during pulmonary fibrosis (PF), to identify factors, which influence the pathogenesis of PF and to investigate the role of the immune modulatory metabolite itaconate during PF.

In chapter 3, AM metabolic phenotype was analysed in patients with idiopathic pulmonary fibrosis (IPF) or chronic hypersensitivity pneumonitis (CHP) compared to healthy controls. In IPF AMs increased gene expression of first half TCA cycle genes was detected, as well as a dependency on glycolysis to sustain a pro-fibrotic phenotype, while AMs from CHP patients highly increased glycolysis and OXPHOS utilisation and a more pro-inflammatory macrophages phenotype was observed. These results highlight the influence of the environment and identify distinct AM phenotypes in clinically similar IPF and CHP. Recent paradigm shifting studies have shown that two types of AMs exist in the lung and during the pathogenesis of PF. In chapter 4, the underlying metabolic phenotype of tissue-resident (Tr-AM) and monocyte-recruited AMs (Mo-AM) was investigated using the bleomycin mouse model, which showed an increased utilisation of OXPHOS in Tr-AM but not Mo-AM during peak fibrosis. In chapter 5, the role of immune modulatory metabolite itaconate was investigated during PF. Itaconate has been shown to regulate AM metabolic activity and is anti-inflammatory and anti-microbial, however its role in the context of fibrosis is unknown. Analysis of the metabolic phenotype of AMs from IPF patients indicated that there was decreased expression of *ACOD1*, a gene which controls the synthesis of itaconate. Furthermore, Acod1$^{-/-}$ mice had more severe fibrosis compared to WT mice in bleomycin models, suggesting an anti-fibrotic role for itaconate. Ultimately, fibrosis was ameliorated by treatment with inhaled itaconate or adoptive transfer of itaconate-expressing Mo-AMs.

Collectively, these findings reveal underlying metabolic programmes driving AM phenotype during pulmonary fibrosis and identify new therapeutic targets.

Table of contents

List of Figures

List of Tables

List of abbreviations

Abbreviation	Full term
2-DG	2-deoxy glucose
5-HETE	5-hydroxyicosatetranoic acid
αKG	α-ketoglutarate
A2BR	Adenosine receptor
ACOD1	Cis-aconitate decarboxylase 1 (gene)
AEC	Alveolar epithelial cell
AHR	Airway hyperresponsiveness
AKT	Protein kinase B
AM	Airway macrophages
AMPK	AMP activated kinase
Arg1	Arginase 1
ATP	Adenosine triphosphate
BAL	Bronchoalveolar lavage
BMDM	Bone marrow derived macrophage
CAD	Cis-aconitate decarboxylase
CCL2	Chemokine ligand 2
CHP	Chronic HP
CIC	Mitochondrial citrate carrier
CLD	Chronic lung disease
Col1α1	Collagen 1 alpha 1
Col3α1	Collagen 3 alpha 1
Col4α1	Collagen 4 alpha 1
COPD	Chronic obstructive pulmonary disease
CPT1	carnitine palmitoyl transferase
CREB	cAMP response element binding protein
CSF1R	Colony stimulating factor 1 receptor
CX3CR1	CX3-chemokine receptor 1
d3-MMA	d_3-labelled methylmalonic acid
DC	Dendritic cells
D_{LCO}	Diffusing capacity of lung carbon monoxide
DMM	Dimethyl malonate
DON	Glutamine antagonist
ECAR	Extracellular acidification rate
ECM	Extracellular matrix
EDTA	Ethylenediaminetetraacetic acid
ERK	Extracellular signal regulated kinase
ETC	Electron transport chain
FACS	Fluorescence activated cell sorting
$FADH_2$	Flavin adenine dinucleotide
FAO	Fatty acid oxidation
FBS	Foetal bovine serum
FCCP	Carbonyl cyanide-4-(trifluoromethoxy)phenylhydrazone
FEV1	Forced expiratory volume
Fn1	Fibronectin 1
FVC	Forced vital capacity
GLUT	Glucose transporter
GM-CSF	Granulocyte macrophage colony-stimulating factor
GPR91	Succinate receptor
GSSG	Oxidised glutathione
GTP	Guanosine triphosphate
H&E	Haematoxylin & eosin
HBE	Human bronchial epithelial cells
HEPES	4-(2-hydroxyethyl)-1-piperazineethanesulfonic acid
Hif1α	Hypoxia inducible factor 1 alpha
HLF	Human lung fibroblasts
HO-1	Heme oxygenase 1
HP	Hypersensitivity pneumonitis
HRCT	High resolution computer tomography
IDH	Isocitrate dehydrogenase
IFN-γ	Interferon-gamma

Abbreviation	Full term
IL	interleukin
ILD	Interstitial lung disease
ILK	Integrin linked kinase
iNOS	Inducible nitric oxide synthase
IPF	Idiopathic pulmonary fibrosis
IRF5	Interferon regulatory factor 5
IRG1	Immune responsive gene 1
KEAP1	Kelch-like ECH-associated protein 1
LPS	Lipopolysaccharide
LTB_4	Leukotriene B_4
LTE_4	Leukotriene E_4
MACS	Magnetic activated cell sorting
M-CSF	Macrophage colony-stimulating factor
MDM	Monocyte derived macrophage
MMP	Matrix metalloproteinase
Mo-AM	Monocyte recruited AM
Mtb	Mycobacterium Tuberculosis
mTOR	Mammalian target of rapamycin
mtROS	Mitochondrial ROS
NADH	Nicotinamide dinucleotide hydrogen
NADPH	Nicotinamide dinucleotide phosphate
NK	Natural killer cells
NO	Nitric oxide
NOS	Nitric oxide synthase
NOS2	Nitric oxide synthase 2
NOX	NADPH oxidase
NRF2	nuclear factor erythroid 2-related factor 2
OCR	Oxygen consumption rate
$ONOO^-$	Peroxynitrite
OXPHOS	Oxidative phosphorylation
PAI-1	Plasminogen activator inhibitor 1
PAP	Pulmonary alveolar proteinosis
PBMC	Peripheral blood mononuclear cells
PGC-1α	Peroxisome proliferator activated receptor gamma coactivator 1α
PGE_2	Prostaglandin 2
PI3K	Phosphoinositol-3 kinase
PPARγ	peroxisome proliferator-activated receptor gamma
PPP	Pentose phosphate pathway
PRR	Pattern recognition receptor
ROS	Reactive oxygen species
SDH	Succinate dehydrogenase
siRNA	Small interfering RNA
SPA - D	Surfactant protein S - D
SR-A	Scavenger receptor alpha
SRC	Spare respiratory capacity
TCA	Tricarboxylic acid
TGF-β	Transforming growth factor beta
TLR	Toll-like receptor
TNF-α	Tumour necrosis factor alpha
Tr-AM	Tissue resident AM
UK5099	Inhibitor of mitochondrial pyruvate transporter

1. Introduction

1.1 Interstitial lung disease

1.1.1 Idiopathic pulmonary fibrosis

Interstitial lung disease (ILD) is a heterogeneous group of disorders characterized by deposition of excess extracellular matrix (ECM) and the destruction of lung architecture, leading to compromised gas exchange. Idiopathic pulmonary fibrosis (IPF) is the most common form of ILD with more than 5,000 new cases diagnosed each year, where age is the most strongly associated risk factor for IPF with the average age at diagnosis being 65 years[1]. IPF has a median prognosis of 3 - 5 years after diagnosis, which is worse than many types of cancer[2]. Although the disease is idiopathic, the current model for IPF involves exposure to heavy smoking, oxidative stress, environmental pollutants and dusts as factors contributing to disease development[3]. Repetitive alveolar injury as a result of exposure to these factors in genetically susceptible individuals causes activation of mesenchymal cells[2], recruitment of fibroblasts and differentiation into myofibroblasts to replace damaged alveolar epithelial cells (AEC) and provide a matrix for wound healing and tissue repair[4]. In IPF, the wound healing process is dysregulated, leading to fibrotic plaque formation and excessive build-up of extracellular matrix (ECM), constituted of collagens, leading to stiffness of the lung and impaired gas exchange.

1.1.2 Treatment options for IPF

Historically, the first line of treatment for IPF was anti-inflammatory corticosteroid therapy in combination with antioxidants[5], however new clinical trials have rendered this approach ineffective and in combination even harmful[6,7]. The last decade has brought two new anti-fibrotic drugs into the clinic: Nintedanib and Pirfenidone. Nintedanib is a tyrosine kinase inhibitor targeting the platelet-derived growth factor receptor (PDGFR), fibroblast growth factor receptor (FGFR) and vascular-endothelial growth factor receptor (VEGFR)[8], overall leading to decreased fibroblast proliferation, migration and differentiation[9] and showing significant improvement of forced vital capacity (FVC) decline in clinical trials[10,11]. Pirfenidone has anti-fibrotic, anti-inflammatory and antioxidant activity[12,13], resulting in

decreased collagen synthesis and has anti-fibrotic activity in lung, liver, kidney and heart, however its direct targets remain unknown[14,15]. Combination treatment of Pirfenidone and antioxidant N-Acetylcysteine did not result in improved FVC or 6-minute walk test[16]. While Nintedanib and Pirfenidone increase life expectancy and quality of life after diagnosis with IPF, they cannot reverse fibrosis and only slow disease progression. It is therefore still necessary to continue the search for treatment options and to better understand disease mechanism.

1.1.3 Chronic hypersensitivity pneumonitis

Hypersensitivity pneumonitis (HP) is a diffuse interstitial lung disease caused by an aberrant immunological response to inhaled antigens, such as microbes, animal and plant proteins as well as organic and inorganic chemicals. While the most common antigen is exposure to hay dust resulting in the so termed “Farmer’s lung”[17], other more specific antigens are avian dust, mould, mushrooms, cork dust, plastic residue and wheat moulds[18]. HP is categorised into acute, sub-acute and chronic subtypes, depending on the intensity and duration of exposure and type of antigen. Symptoms of HP are dyspnoea and cough and patients can present with variable amounts of interstitial fibrosis, which makes diagnosis challenging as these symptoms overlap with other ILDs[19]. The American Thoracic Society Guidelines listed a bronchoalveolar lavage (BAL) lymphocyte count > 50%, especially when neutrophils > 3% and mast cells > 1%[20] as indicative for a HP diagnosis. However, Salisbury *et al*. proposed recently either typical high resolution computer tomography (HRCT) features and BAL lymphocyte differential count > 20% or typical HRCT plus plausible and temporal antigen exposure as minimum criteria for HP diagnosis[21]. Thus, no established international guidelines for the diagnosis of HP exist and overlap between diagnosis of different multidisciplinary teams varies widely[22], while recently the aim of identifying diagnostic criteria for HP has been set again[23]. As many cases are either misdiagnosed or not recognised, it is difficult to determine incidence and prevalence of HP. In Europe, prevalence is estimated at 4 – 15%[24], while in the US at 2% of ILD cases, whose yearly incidence was about 30 per 100,000[25]. HP affects the lung parenchyma, alveoli, terminal

bronchioles and alveolar interstitium and pathogenesis involves mononuclear cell infiltration upon prolonged antigen exposure and sensitisation. Although advanced HP can be indistinguishable from IPF, its prognosis is much better with a 5-year survival rate of 93 %[26] and a selection of treatment options available. In this thesis, the focus will be on the chronic subtype of HP (CHP), of which fibrotic pathology is often not distinguishable from IPF.

1.1.4 Treatment options for CHP

The most promising treatment option for CHP is the avoidance of antigen, although this is not always possible, as it can be challenging to identify the underlying antigen[27]. Furthermore, corticosteroids and immunosuppressants are used widely for the treatment of HP[28], which work best for resolution of the acute subtype and have been shown not to have a long term effect[29]. With the advent of Nintedanib and Pirfenidone for the treatment of IPF, it has become more important than ever to differentiate the diagnoses of IPF and CHP. As corticosteroids and azathioprine have been shown to be deleterious for IPF patients, IPF patients misdiagnosed as CHP might be treated with potentially harmful immunosuppressants, while a CHP patient misdiagnosed as IPF might be denied effective therapy[30]. It remains unclear however, whether treatment with corticosteroids might be harmful for CHP patients with established fibrosis. A recent study has shown that Nintedanib slows pulmonary fibrosis of any cause, making it suitable for treatment of CHP patients with established fibrosis and potentially bridging the gap between IPF and CHP[10].

1.2 Airway macrophages: from inflammation to wound healing

Airway macrophages (AMs) are positioned in the airways and alveoli near the epithelium, at the interface of gas exchange[31]. To maintain pulmonary homeostasis and ensure gas exchange is not interrupted, a complex regulatory system is in place, of which AMs are a core component. AMs are the most numerous immune cell type present in healthy lungs and are critical sentinels of barrier immunity. AMs form the first line of defence against inhaled particles, pathogens and antigens[32]. Although inherently suppressive, AMs exhibit significant functional and phenotypical specialisation, allowing efficient responses to environmental signals and rapid alterations in phenotype. Increasing evidence suggests that metabolic alterations provide an additional layer of functional plasticity to AM populations. This strategic location allows for immediate innate immune response to pathogens in the inhaled air[33]. Furthermore, AMs are involved in tissue homeostasis[34], clearing apoptotic cells and surfactant from the alveolar space by phagocytosis[35], antigen presentation and initiating the inflammatory response[36,37]. AMs express TGF-βR, interleukin-(IL)-10R, CD200R and Sirp-α, key components mediating AM:AEC crosstalk and in turn, regulating AM activation. For example, AM-AEC contact decreases AM phagocytosis and cytokine production in a TGF-β-dependent manner[38]. Conversely, loss of the integrin αvβ6 such as through loss of contact of AMs with AEC upon toll-like receptor (TLR) activation leads to initiation of the AM pro-inflammatory phenotype and inflammatory response[39]. Human AMs express the lectin-binding transmembrane glycoprotein CD68, the adhesion molecule CD169 (SIGLEC1), mediating cell-cell interactions via sialic acid binding and highly express the integrin alpha X chain protein CD11c (ITGAX) and the mannose receptor CD206, which mediates the endocytosis of glycoproteins[40] (Figure 1.1). During homeostasis, human AMs express low levels of the adhesion mediating integrin alpha M chain protein CD11b compared to interstitial macrophages, although expression of CD11b on AMs can increase substantially upon activation. Expression of CD68, CD206, $CD11c^{hi}$ and $CD11b^{lo}$ is conserved in murine AMs[41–43], additionally these express the Mer tyrosine kinase (MerTK), sialic acid dependent adhesion molecule SiglecF, EGF-like module-

containing mucin-like hormone receptor-like 1 (F4/80), Fc receptor CD64 and the type I membrane glycoprotein CD200 receptor[44] (Figure 1.1).

Models of macrophage polarisation are widely utilised *in vitro* and the nomenclature has changed over the years. While initially the terms M1 and M2 macrophages were used to describe inflammatory (M1) or alternatively activated (M2) macrophages *in vitro*, there is no clear consensus on differentiation protocols to produce the phenotypes, which has made results difficult to reproduce. It is now common practise to indicate the source of activation e.g. M(IL-4) or M(IFN-γ) when describing *in vitro* macrophage populations. This concept has been well described by Murray *et al*[45]. To induce an inflammatory or alternatively activated macrophage phenotype in vitro, a range of stimuli can be used. Of these, IFN-γ and LPS are commonly used to induce a pro-inflammatory macrophage phenotype marked by expression of pSTAT1, IRF5, CCL-18, TNF, IL-6 and Nos2 as well as production of ROS and NO for microbial killing[46]. Culture with IL-4 on the other hand is most often used to induce an alternatively activated M(IL-4) macrophage phenotype, characterised by expression of pSTAT6, CCL-22, CCL-24, CD163 and Arg1[45], while other stimuli include IL-13, IL-10 and TGF-β[47–49]. Alternative activation produces a phenotype associated with parasitic defence and tissue remodelling[50]. While inflammatory and alternatively activated macrophages *in vitro* are a useful tool to investigate basic macrophage responses, AMs *in vivo* are more plastic and polarise in response to environmental stimuli[51]. These phenotypes are sustained by specific metabolic requirements, which dictate macrophage survival and function.

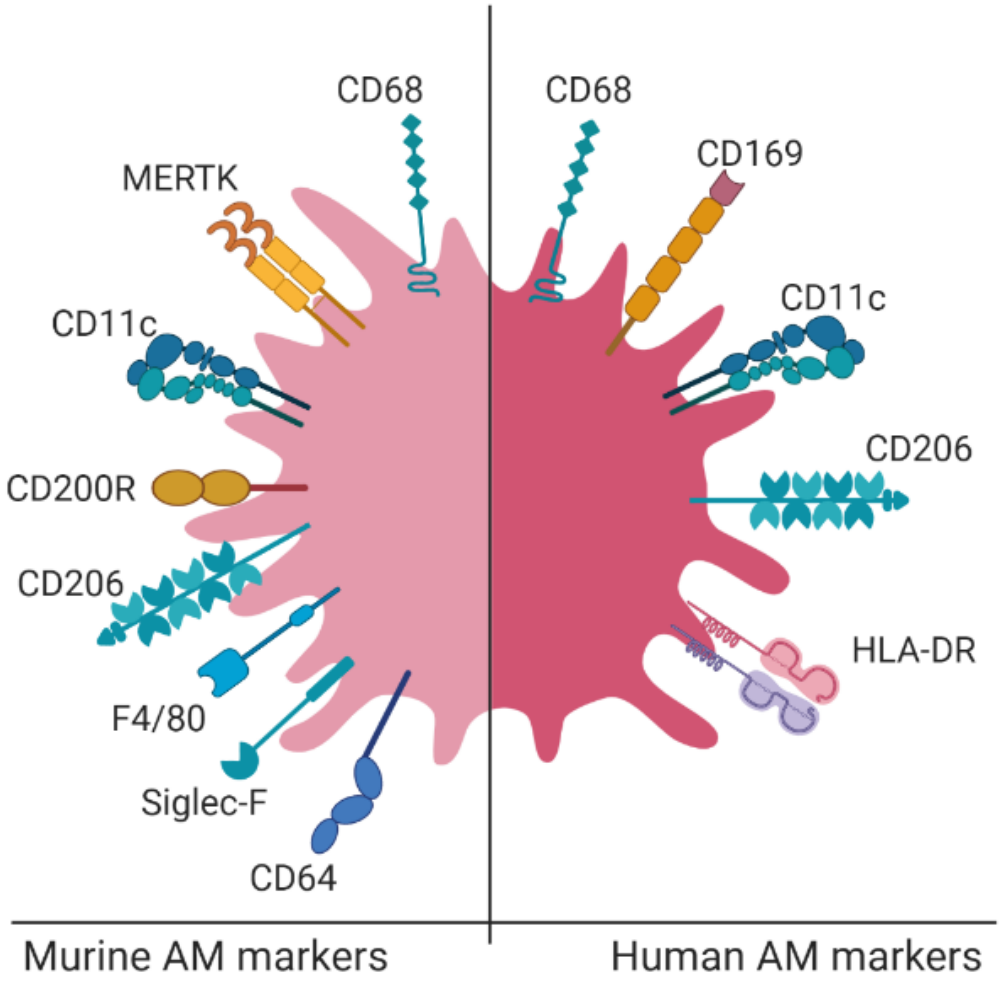

Figure 1.1. Human and murine airway macrophage surface receptors. Murine AMs express the lectin-binding transmembrane glycoprotein CD68, the Mer tyrosine kinase (MERTK), the integrin alpha X chain protein CD11c, the type I membrane glycoprotein CD200 receptor, the mannose receptor CD206, the EGF-like module-containing mucin-like hormone receptor-like 1 (F4/80), the sialic acid binding lectin SiglecF and the Fc receptor CD64. Human AMs express CD68, the adhesion molecule CD169, CD11c, CD206 as well as MHC class II receptor HLA-DR.

1.2.1 Airway macrophage ontogeny

Recent work in mice indicates that many tissue resident macrophages, including those found in the lung, are foetally derived and self-maintain locally with minimal contribution from circulating monocytes, during steady state conditions[52–56]. During prenatal development in mice, fetal liver or yolk sac macrophages are the major contributing pool to AM populations[57] and AM colonization of the lung occurs in sequential waves in the first week of life[58]. Furthermore, post birth and during maturation, circulating monocytes do not significantly contribute to lung macrophage populations at homeostasis[54]. During pulmonary inflammatory responses in mice, it has been shown that monocytes are recruited to the lung via chemokines such as chemokine ligand 2 (CCL2)[59] and CX3-chemokine receptor 1 (CX3CR1)[60,61]. Subsequently, in response to local cues such as macrophage colony-stimulating factor (M-CSF) or granulocyte-MCSF (GM-CSF), recruited monocytes develop into AM-like cells[54,62]. Thus, post-injury murine airways contain at least two ontologically distinct AM populations, prenatally derived tissue resident AMs (Tr-AMs) and monocyte-derived AMs (Mo-AMs). Several groups have studied samples from lung transplant patients to investigate the origins of AMs in the human lung[63–67]. Utilizing BAL from sex-mismatched lung transplant patients our group recently demonstrated that the majority of AMs in human lung post-transplant are derived from peripheral classical monocytes[68]. Consistent with a peripheral origin of AMs in the ageing human lung, proportions of classical monocytes (the circulating precursors of AMs) found in blood and BAL peak in adulthood and decline in older adults[68]. Interestingly, previous studies have reported monocyte subsets are significantly impacted during health with aging[69–71]. Thus, the unique airway niche combined with distinct ontological origins, age and environmental exposures results in remarkable AM plasticity and adaptability.

1.2.2 Airway macrophage function during ILD

AMs have been identified as key contributors to the dysregulated wound healing process in IPF, by contributing large amounts of ROS and TGF-β[72]. AM populations during pulmonary fibrosis are indeed diverse and display pro-inflammatory as well as pro-wound healing markers and functions (Figure 1.2). During pulmonary fibrosis, AMs secrete chemokines to attract monocytes and T-lymphocytes, including CCL-2, CCL-17, CCL-18 and CCL-22[73–76]. Furthermore, they regulate fibroblast recruitment, myofibroblast differentiation and ECM deposition by secreting fibronectin and MMPs[77]. As AMs are significant contributors to the pro-fibrotic environment during pulmonary fibrosis, recruiting immune cells and fibroblasts as well as interacting with the ECM, it is essential to understand the metabolic pathways underlying their phenotype and to identify alterations, which drive this pro-fibrotic phenotype.

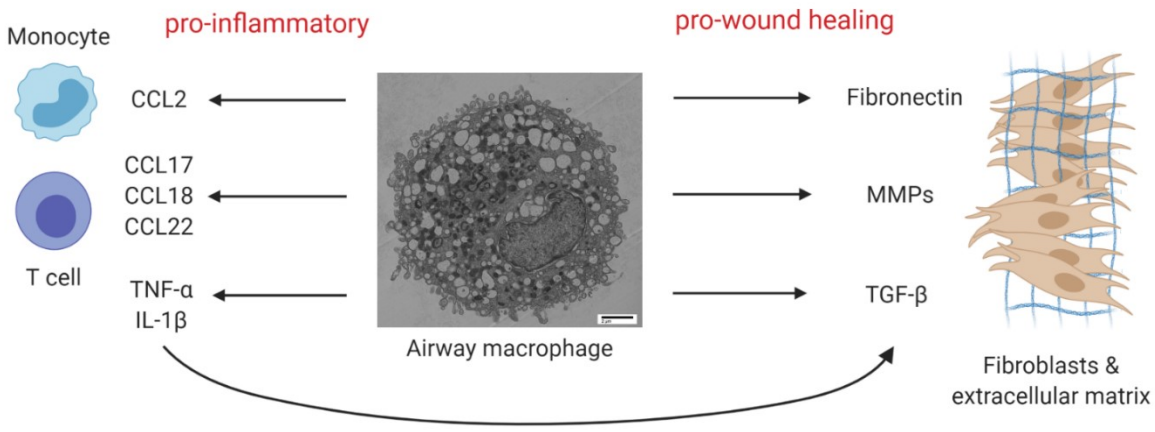

Figure 1.2. Airway macrophage functions during pulmonary fibrosis. AMs assume both pro-inflammatory as well as wound healing roles during pulmonary fibrosis. By secreting chemokine ligands-2, -17, -18 and -22 they recruit monocytes and lymphocytes to the site of injury, while the release of TNF-α and IL-1β induces production of TGF-β, which in turn supports the recruitment of fibroblasts and differentiation into myofibroblasts. Furthermore, AMs produce fibronectin and collagens, which contribute to the extracellular matrix (ECM) around injured sites, but also matrix metalloproteases, which can break the ECM down.

1.3 Cell metabolism – classics revisited

Activation of macrophages *in vitro* with a range of inflammatory stimuli, induces profound metabolic adaptations, such as the switch from oxidative phosphorylation (OXPHOS) to glycolysis in oxygen-sufficient conditions, similar to the 'Warburg effect' seen in some cancers[78]. It is now clear that how macrophages utilise energy dictates immune responses, and that manipulating cellular metabolism can alter many inflammatory pathways[78]. *In vivo*, the unique oxygen rich environment of the airways coupled with specific local nutrient availabilities, shapes AM phenotype and function. This highlights the necessity to study the metabolic programmes underlying AM phenotype during ILD to better understand AM dysfunction and to identify new therapeutic targets.

1.3.1 Glycolysis

During glycolysis, glucose is converted into pyruvate in ten enzyme-catalysed reactions, yielding 2 adenosine triphosphate (ATP) molecules and 2 nicotinamide adenine dinucleotide hydrogen (NADH; Figure 1.3 A)[79]. In addition, galactose, glycogen, mannose, and fructose can enter glycolysis. The first five reaction of glycolysis consume 2 molecules of ATP (investment phase), and the second five reactions generate 4 ATP molecules leading to a net gain of 2 ATP molecules[80]. Firstly, glucose is transformed into glucose-6-phosphate by hexokinase (1). This reduces extracellular glucose levels and traps glucose-6-phosphate inside the cell as there are no transporters for extracellular transport of glucose-6-phosphate[81]. Glucose-6-phosphate is then converted into fructose-6-phosphate by glucose-6-phosphate isomerase (2), or it can enter the pentose phosphate pathway. Fructose-6-phosphate is then converted into fructose-1,6-biphosphate by phosphofructokinase (3) and subsequently split by fructose biphosphate aldolase into glyceraldehyde 3-phosphate and dihydroxyacetone phosphate (4). Dihydroxyacetone phosphate can be interconverted to glyceraldehyde 3-phosphate by triosephosphate isomerase (5)[82]. Glyceraldehyde 3-phosphate is oxidised by glyceraldehyde phosphate dehydrogenase yielding 1,3-biphosphoglycerate (6), which is subsequently converted to 3-phosphoglycerate by phosphoglycerate kinase (7). 3-phosphoglycerate is then isomerised

to 2-phosphoglycerate by phosphoglycerate mutase (8), followed by conversion to phosphoenolpyruvate by enolase (9). Finally, phosphoenolpyruvate is phosphorylated by pyruvate kinase to yield pyruvate (10). Apart from generating ATP and NADH, glycolysis provides glucose-6-phosphate to feed into the pentose phosphate pathway as a precursor for nucleotide synthesis, 3-phosphoglycerate for amino acid biosynthesis and pyruvate to fuel the TCA cycle and fatty acid synthesis[83]. Thus, glycolysis is the most essential metabolic pathway for fast proliferating cells and can furthermore function during hypoxia. Glycolysis has been shown to be especially important to support activation of macrophages[84], as well as dendritic cells (DCs)[85], natural killer (NK) cells[86] and T cells[87]. Furthermore, inhibition of glycolysis by hexokinase inhibitor 2-deoxy glucose (2-DG) attenuated phagocytic capacity in macrophages[88].

1.3.2 Pentose phosphate pathway

The pentose phosphate pathway branches off glycolysis in the cytosol and converts glucose-6-phosphate into pentose as well as ribose 5-phosphate (Figure 1.3 B). Ribose 5-phosphate is a precursor for nucleotide synthesis, while glyceraldehyde-3-phosphate and fructose-6-phosphate generated in the pentose phosphate pathway feed back into glycolysis[82]. The pentose phosphate pathway furthermore generates NADPH, which is utilised for superoxide production by NOX[89]. The pentose phosphate pathway is therefore supporting cell proliferation and survival as well as pathogen defence. It has been found to be increased in LPS-stimulated macrophages, although it remains to be investigated why as these cells do not proliferate much[90].

1.3.3 Tricarboxylic acid cycle

The tricarboxylic acid (TCA) cycle consists of a series of nine reactions oxidising acetyl CoA thereby releasing stored energy (Figure 1.3 C). It yields three NADH and one flavin adenine dinucleotide ($FADH_2$) molecules, which can transfer electrons to the electron transport chain (ETC)[91], as well as one guanosine triphosphate (GTP). While acetyl CoA derived from pyruvate or fatty acids is the primary energy source for the TCA cycle, it can also utilise glutamate through direct conversion into TCA cycle intermediate α-ketoglutarate[92]. The

reactions of the TCA cycle comprise the following: acetyl CoA is converted into citrate by citrate synthase in an aldol condensation reaction (1). Citrate is then converted into isocitrate via cis-aconitate by aconitase by reversible isomerisation (2/3). Isocitrate dehydrogenase catalyses the oxidative decarboxylation of isocitrate into α-ketoglutarate, generating one NADH (4). Alpha-ketoglutarate is then converted into succinyl CoA by α-ketoglutarate dehydrogenase, yielding another NADH (5). Succinyl CoA synthase catalyses the phosphorylation of succinyl CoA to form succinate, generating one GTP (6). Succinate is subsequently oxidised to fumarate by succinate dehydrogenase, additionally generating one $FADH_2$ (7). Fumarase then generates malate from fumarate by hydration (8), while malate dehydrogenase oxidises malate to yield oxaloacetate and one NADH (9). This is the last step of the cycle and oxaloacetate can then again be extended to citrate in conjunction with acetyl CoA. The TCA cycle takes places in the mitochondrial matrix and fuels mainly quiescent, non-proliferating cells[83]. Quiescent T cells and alternatively activated macrophages are particularly reliant on the TCA cycle[87], while it is broken in inflammatory macrophages[93] and in activated DCs[94], resulting in accumulation of citrate to fuel fatty acid synthesis as well as signalling molecules itaconate, succinate and fumarate[95]. Succinate has been shown to stabilise hypoxia inducible factor (Hif1α), thereby supporting the production of IL-1β[96].

1.3.4 Electron transport chain

The electron transport chain is located in the inner mitochondrial membrane and consists of four complexes, two electron carriers (cytochrome C and coenzyme Q) and the ATP synthase proton pump[95]. NADH, $FADH_2$ and succinate generated in the TCA cycle are oxidised, creating a proton gradient through redox reactions (Figure 1.3 D). The established proton motive force then drives the ATP synthase to generate ATP. Through oxidative phosphorylation of one molecule of glucose, 36 molecule of ATP are produced, making it much more efficient than glycolysis[97].

1.3.5 Fatty acid synthesis and oxidation

During fatty acid synthesis lipids are generated, which store energy and are necessary for cellular growth and proliferation. The signalling hub mammalian target of rapamycin (mTOR) promotes fatty acid synthesis by regulating expression of key enzymes[98]. For the synthesis of straight-chain fatty acids, citrate is exported to the cytosol and converted into acetyl CoA and oxaloacetate by acetyl CoA lyase[99]. Acetyl CoA is then carboxylated to malonyl CoA and elongated to palmitic acid. For branched-chain fatty acid synthesis, branched-chain amino acids such as valine or leucine are necessary as starting material. Fatty acids can furthermore be condensed with glycerol produced during glycolysis, to yield triacylglycerols and phospholipids. Overall, a variety of metabolic intermediates from glycolysis, the TCA cycle or the pentose phosphate pathway can be used to generate fatty acids as a way of storing energy and providing essential cellular building blocks (Figure 1.3 E). When cells need additional energy sources, fatty acids can be broken down to yield acetyl CoA, NADH and $FADH_2$ by beta oxidation in the mitochondria, which can then fuel the TCA cycle (Figure 1.3 E). While short-chain fatty acids can diffuse into the mitochondria after activation in the cytosol, medium- and long-chain fatty acids are bound to carnitine by carnitine palmitoyl transferase (CPT1) and shuttled into the mitochondria where carnitine is removed by CPT2[100]. Fatty acid oxidation (FAO) is the most efficient energy generating pathway, as oxidation of one palmitic acid molecule can yield around 100 ATP. Especially non-inflammatory cells and long-living immune cells such as M2-macrophages, T_{regs} and memory T cells rely on fatty acid metabolism[83]. In particular, lipolysis is necessary for alternative macrophage activation[101], while oxidative metabolism attenuates macrophage inflammatory phenotype[102]. Furthermore, LPS activation of macrophages induces fatty acid synthesis[103,104], while constitutive activation of CPT1 in inflammatory macrophages increased fatty acid oxidation and reduced the production of inflammatory cytokines[105]. Finally, fatty acid synthesis genes are increased during the differentiation of monocytes into macrophages[106]. These studies highlight the fact that inflammatory immune cells primarily utilise fatty acid synthesis to generate biosynthetic molecules and support cell growth and

cytokine production, whereas long lived tolerogenic immune cells rely on lipid oxidation for energy generation.

1.3.6 Amino acid metabolism

Additional to glucose and fatty acids, glutamine and other amino acids[107] can contribute to the cellular carbon and energy pool[108]. Entering the cell through sodium fuelled glutamine transporters, glutamine can then enter the mitochondria and be converted into glutamate[109]. Glutamate is then synthesised into α-ketoglutarate, which is directly used in the TCA cycle (Figure 1.3 F), thereby contributing to the production of NADH and $FADH_2$ to fuel OXPHOS and ATP synthesis as well as pyruvate and citrate, which in turn can sustain acetyl-CoA production[110], fatty acid synthesis and lipid production. Glutaminolysis can also increase the lactate pool via pyruvate synthesis, which in turn can sustain NADPH levels for nucleotide synthesis.

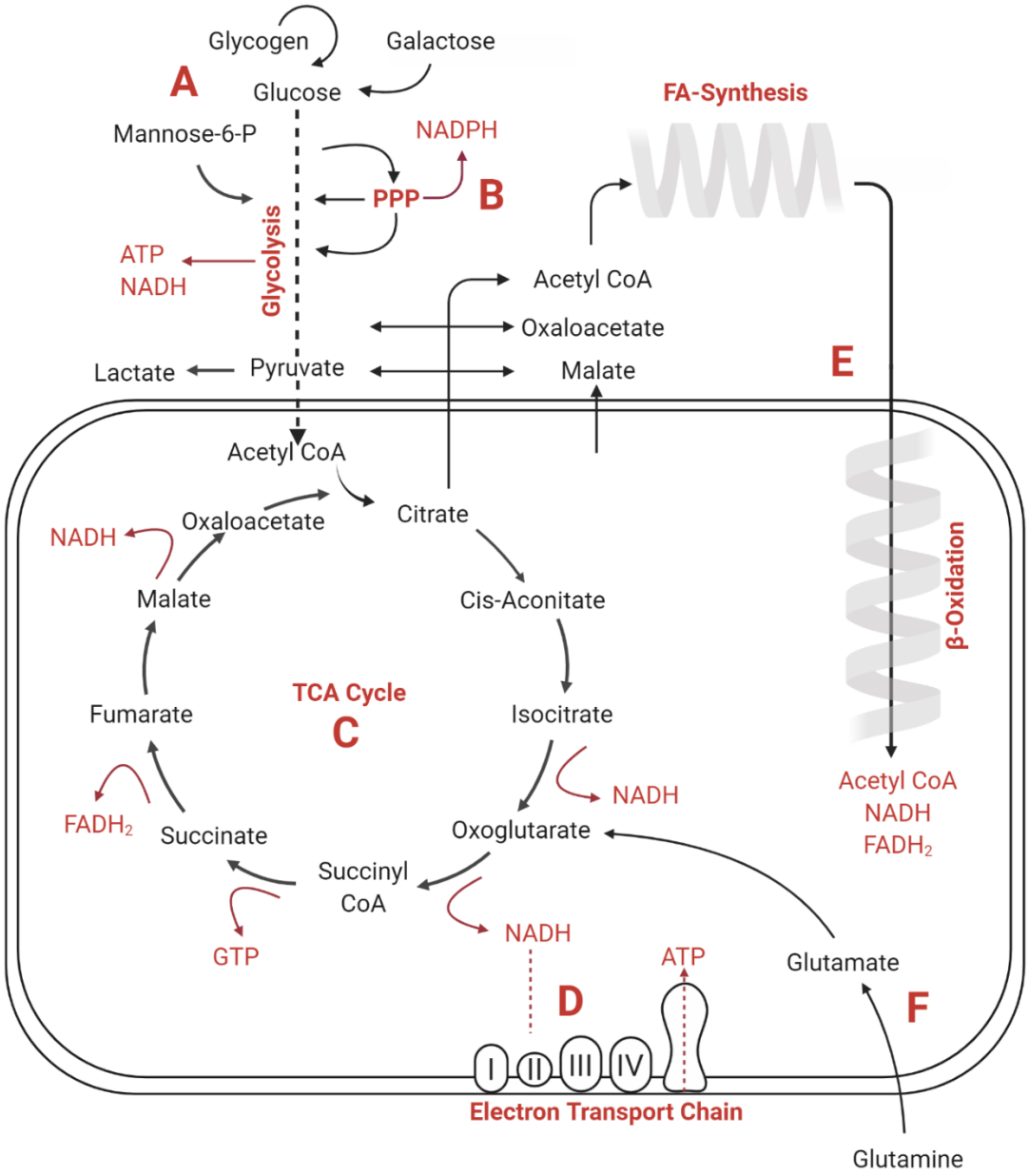

Figure 1.3. Central carbon metabolism. A) Glycolysis converts glucose into pyruvate, yielding ATP and NADH and can also be fuelled by glycogen, galactose or mannose. B) The pentose phosphate pathway branches off glycolysis and converts glucose-6-phosphate into pentose as well as ribose 5-phosphate, a precursor for nucleotide synthesis. It thereby generates glyceraldehyde-3-phosphate and fructose-6-phosphate, which can feed back into glycolysis and yields NADPH. C) Pyruvate is transported into the mitochondria and decarboxylated to produce acetyl CoA, fuelling the TCA cycle. Alternatively, it can be converted to lactate in the cytosol or feed back into glycolysis via gluconeogenesis (pyruvate – oxaloacetate – phosphoenolpyruvate). In the TCA cycle, acetyl CoA is oxidised in a series of reactions, yielding precursors of amino acids, NADH and $FADH_2$. D) These in turn are used in the electron transport chain to generate ATP. E) Citrate can leave the mitochondrion via the citrate carrier and be converted into acetyl CoA to act as a starting product for fatty acid synthesis. During beta-oxidation in the mitochondrion fatty acids can be broken down to yield acetyl CoA and function as energy source. F) Glutamine is converted into glutamate in the mitochondrion, which in turn yields 2-oxoglutarate and thereby replenishes TCA cycle intermediates.

1.4 Targeting metabolic pathways to treat IPF

Several drugs, which target metabolic pathways have been tested recently in IPF. Metformin is a potent metabolic remodelling drug often prescribed for type II diabetes; while on a systemic level, metformin lowers the amount of blood sugar in diabetic individuals, on a cellular level it activates AMP-activated protein kinase (AMPK) leading to inhibition of TGF-β induced activity of nicotinamide adenine dinucleotide phosphate (NADPH) oxidase-4 (NOX4)[111]. Sato *et al*., have shown that metformin inhibited TGF-β induced NOX4 activity *via* AMPK leading to inhibition of myofibroblast differentiation *in vitro* and reduced bleomycin induced collagen deposition *in vivo*[112]. This finding was strengthened by a study by Rangarajan *et al*. showing that metformin treatment reversed bleomycin induced pulmonary fibrosis via AMPK activation while IPF patients have decreased AMPK phosphorylation[113]. A *post hoc* analysis study of the effect of metformin in IPF patients however showed no change in clinical outcomes[114], once again highlighting the difficulty of translating *in vitro* and *in vivo* findings into the clinic. Another study investigating NOX4 and the imbalance of the NOX4 - nuclear factor erythroid 2-related factor 2 (NRF2) axis as a therapeutic target showed that *in vivo* knockdown of NOX4 and NOX1/4 inhibition restored the capacity of fibrosis resolution in aged mice using the bleomycin model[115]. It remains to be investigated however, whether this finding holds in clinical trials. While these treatment approaches target metabolic changes during pulmonary fibrosis, none is specific to airway macrophages. Targeting macrophage specific metabolic reprogramming, which sustains ROS production and TGF-β production and contributes to dysregulated wound healing in IPF would be a promising therapeutic option as it would be more targeted than systemic antioxidant or anti-metabolic therapy.

1.5 Immunometabolism – linking metabolic pathways with immune function

1.5.1 Macrophage metabolism *in vitro*

Metabolic programmes underlying function of M1 and M2 macrophages are well characterised *in vitro*. Seminal studies have demonstrated that M2 (IL-4 exposed) macrophages *in vitro* rely on fatty acid oxidation, an intact TCA cycle and OXPHOS and express high levels of arginase 1 (Arg1), which catalyses the production of ornithine from arginine as precursor for collagen to facilitate wound healing[78,96,116,117]. Conversely, M1-macrophages readily utilise glucose, rely on glycolysis and breaks in the TCA cycle lead to accumulation of metabolites such as citrate, succinate, fumarate and α-ketoglutarate[93,96,118]. However, although useful in defining the range of potential macrophage responses, *in vitro* derived cells do not recapitulate the core aspects of AM phenotypes which have been shaped by the local niche[40]. As AMs are highly adapted to the unique environment of the airway lumen, it is unsurprising that metabolic state of AMs is also distinctive. The glucose concentration of the alveolar lumen is less than 10% of blood glucose concentrations and AMs exhibit extremely low levels of glycolysis[119] and, in stark contrast to BMDMs, do not undergo glycolytic reprogramming in response to LPS[120]. Consequently, AMs readily engage OXPHOS, highly express the nuclear receptor peroxisome proliferator-activated receptor gamma (PPARγ), which is induced by GM-CSF[121] and have been shown to regulate lipid accumulation via scavenger receptors, such as CD36 and SR-A.

One of the most prominent differences between pro-and anti-inflammatory macrophage metabolism is their use of the amino acid arginine. Pro-inflammatory macrophages use arginine as a substrate for nitric oxide synthase (NOS), which upon stimulation by pro-inflammatory cytokines produces large amounts of the free radical NO, an important immune defence mechanism. Recently, Palmieri et al. have shown that NO induces citrate accumulation and suppression of the electron transport chain in murine macrophages, suggesting a link between NO levels and macrophage metabolic programme[122]. Anti-inflammatory macrophages on the other hand, use arginine to fuel arginase 1, which

catalyses the production of urea and ornithine, leading to proline, which fuel collagen synthesis and are necessary for wound healing. Other differences in the metabolic programme of pro- and anti-inflammatory macrophages lie in their use of glucose as a fuel, the activity of the TCA cycle and OXPHOS and their ability to sustain themselves in hypoxic conditions. Pro-inflammatory macrophages produce ROS as part of their defence programme[123]. This metabolic shift away from OXPHOS towards glycolysis is induced by stimulation of the TLR and pattern recognition receptors (PRRs), which recognise microbial compounds such as LPS and damaged tissue[118,124]. Reduced mitochondrial respiration and increased NADPH synthesis in the pentose phosphate pathway enables pro-inflammatory macrophages to produce large amounts of ROS and NO, which are key molecules for host defence[125]. NADPH can furthermore be reduced to glutathione to prevent auto-oxidative damage by ROS. This major metabolic reprogramming towards glycolysis further induces the expression of Hif-1α. Hif-1α is a main driver of glycolysis and regulates the conversion of pyruvate into lactate or acetyl-CoA, thereby effectively switching the TCA cycle on and off[126].

Another feature of LPS-stimulated, pro-inflammatory macrophages is their TCA cycle rewiring and accumulation of the metabolites citrate, succinate and fumarate, which each have effector functions, including immune cell recruitment, stabilisation of Hif1α and epigenetic remodelling[90,93,95,127]. The downregulation of isocitrate dehydrogenase (IDH) and succinate dehydrogenase (SDH) mRNA and enzyme activity upon LPS stimulation in macrophages suggests two breakpoints in the TCA cycle at these locations and explains citrate and succinate accumulation. Increased expression of the mitochondrial citrate carrier (CIC)[128] leads to increased cytosolic citrate, which has been suggested to be involved in the regulation of ROS and NO production[129] and increased levels of cytosolic acetyl CoA[130]. Acetyl CoA is a co-factor for acetyltransferases, catalysing post-translational protein modifications, such as the regulation of IL-6 and IL-10 expression in macrophages[131,132]. Citrate further sustains the production of itaconate via isocitrate and cis-aconitate. Itaconate is highly increased in activated macrophages *in vitro*[133] and has been shown to decrease ROS, NO, IL-1β and IL-6, whilst also being a weak inhibitor of SDH and triggering an anti-

inflammatory programme via the activation of kelch-like ECH-associated protein 1 (KEAP1) and NRF2[134]. The second breakpoint in the TCA cycle during macrophage activation, SDH, leads to an accumulation of succinate[90,93]. Succinate has been shown to signal through the succinate receptor GPR91, which drives inflammation[135] and inhibition of SDH by dimethyl malonate (DMM) blocks mitochondrial ROS (mtROS) production[136]. Furthermore, fumarate inhibits histone demethylase, which induces promoters for genes including TNF-α and IL-6 and boost the cytokine pool upon LPS stimulation, while α-ketoglutarate (αKG) drives histone demethylation[137–140]. Fumarate and αKG are prime examples for how metabolites can alter cellular function through epigenetic modulation[141].

Anti-inflammatory macrophages in turn are not driven by pro-inflammatory mediators, but rather by type 2 mediators IL-4 and IL-13. These induce OXPHOS, while utilizing glycolysis and glutaminolysis at the same time[102,142–145]. This enables M2-like M(IL-4) macrophages to glycosylate the mannose receptors for pathogen recognition[93] and supports a prolonged helminth response, which is one of the main triggers for M2 polarization[146]. While the pentose phosphate pathway has been found to be suppressed in M2-like macrophages[147], CPT1 utilisation is increased, suggesting augmented FAO[143]. Furthermore, CD36 mediated lipid uptake has been suggested to sustain OXPHOS and M2 macrophage expression[78]. Still, the role of FAO during M2 polarization is a topic of debate and more studies are necessary to unravel its function, as during inhibition of CPT1 (by Etomoxir) and CPT2 deletion, IL-4 stimulation still induced an M2 phenotype[148,149].

1.5.2 Human AM metabolism during homeostasis

In vivo, AMs play a major role in the catabolism of pulmonary surfactant, a monolayer composed mainly of phosphocholine-based lipids, phospholipids and cholesterol which line the alveoli, lowering surface tension and preventing alveolar collapse during expiration[150]. Mice which lack GM-CSF or PPARγ, and thus the AM compartment, develop pulmonary alveolar proteinosis (PAP) an inflammatory lung syndrome caused by the defective clearance of surfactant[151–153]. In humans, mutations in genes encoding for GM-CSF receptors, result in hereditary PAP as a result of progressive alveolar surfactant

accumulation[154–157]. AM phenotype and behaviour is influenced by surfactant exposure, which has major implications for AM-mediated immune responses in pulmonary tissue. There are four principle surfactant proteins (SPA-D) and SP-A and SP-D have been shown to directly influence AM functions such as cell migration, phagocytosis and activation phenotypes[150]. Both SP-A and SP-D bind carbohydrates, lipids, and nucleic acids and initiate phagocytosis of inhaled pathogens and apoptotic cells[158]. Furthermore, SP-A block the binding of TLR ligands to TLR2, TLR4 and TLR co-receptors and furthermore, inhibits complement activation[159,160].

In addition to low glucose and lipid rich environment, the airways also have a unique distribution of amino acids and central carbon metabolites. Surowiec *et al.* showed that whilst several glucogenic and ketogenic amino acids were present in the bronchial wash, only alanine was present in the BAL[161]. In addition, the central airways contained key glycolytic and OXPHOS metabolites such as fructose, glucose-6-phosphate, fumarate and malate as well as oxidised glutathione (GSSG, indicating oxidative stress); interestingly, these could not be detected in the periphery, suggesting either minimal secretion, high utilisation or a result of anatomical location (i.e. close proximity to nutrient rich pulmonary capillaries)[161]. Thus, at homeostasis AMs are exposed to a unique oxygen/lipid rich environment, with minimal glucose availability and a distinct distribution of nutrients, which depend on anatomical location (Figure 1.4.)

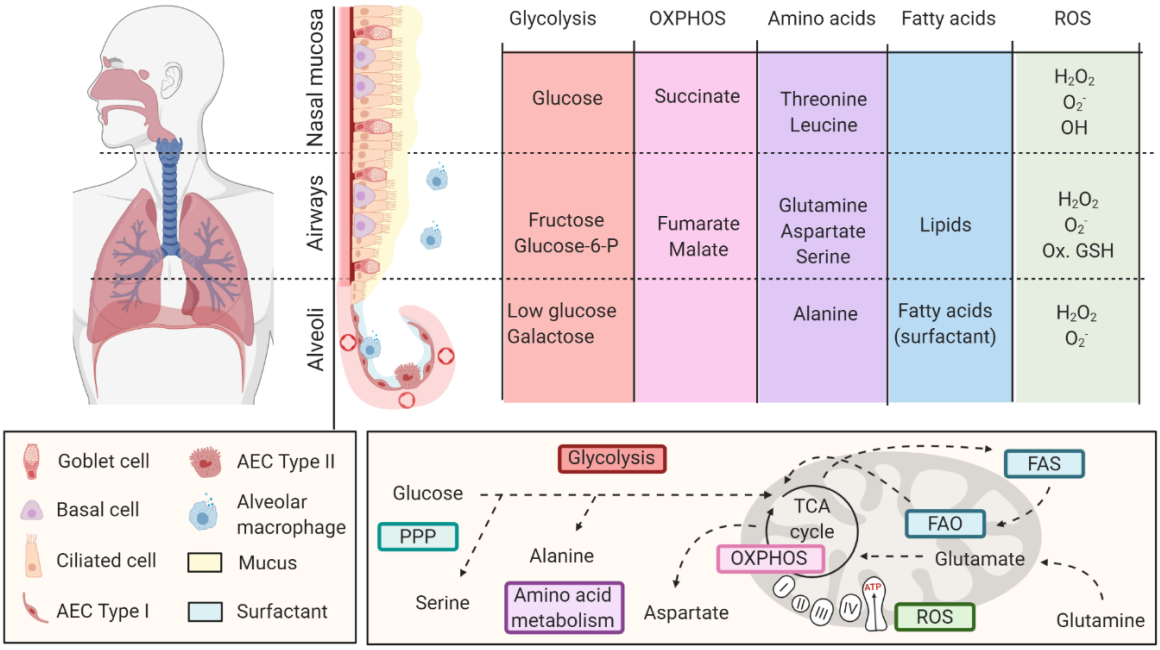

Figure 1.4. Nutrient environment at respiratory mucosal sites. The respiratory mucosa stretches from the nasal cavity to the alveoli and its pseudostratified epithelium in the upper respiratory tract consists of mucus producing goblet cells, ciliated cells and progenitor basal cells on top of a basement membrane, covered with a layer of mucus. The alveoli are lined with type I alveolar epithelial cells (AEC) interspersed with surfactant producing type II AEC. Distinct metabolites of the key metabolic pathways have been detected in nasal secretions, bronchial washes and bronchoalveolar lavage (BAL) at the different respiratory mucosal sites. These key metabolic pathways are schematically represented here. Varying reactive oxygen species (ROS) have been detected in the nasal cavity, conducting airway and parenchyma, contributing to the unique environment in each compartment.

1.5.3 AM metabolism during pulmonary fibrosis

To sustain change in effector function of AMs in IPF, specific parts of their metabolism are rewired. Specific changes outlined below are highlighted in Figure 1.5. ROS production is a key feature of AMs in IPF[162] and can occur via different mechanisms, such as during OXPHOS, in the electron transport chain, by the membrane bound NOX and by reaction of hydrogen peroxide with intracellular iron[163]. NOX is a transmembrane protein, transporting electrons across the cell membrane, thereby reducing NADPH to $NADP^+ + H^+$ and generating superoxide from O_2. NOX is activated either by binding of GTP-bound Rac1 (NOX_{1-4}) or by binding calcium (NOX_5)[164]. The small GTPase Rac1 is secreted from AMs in IPF and promotes the pro-fibrotic phenotype by activating NOX and superoxide production[165] as well as activating the mTOR signalling hub[166]. While Rac1 has been associated with translocation of the glucose transporter GLUT4 in skeletal muscle[167], this has not yet been investigated in airway macrophages. However, GLUT1 has been found to be increased in IPF AMs[168], enabling increased glucose uptake[169]. mTOR on the other hand is an activator of the serine/threonine kinase AKT, which is increased in IPF AMs[170] and also induces activation of other downstream effector molecules such as Hif-1α. Increased expression and activation of the kinases protein kinase B (AKT) and Rac1, major signalling molecules in the phosphoinositol-(PI)-3-kinase pathway, therefore has multiple downstream effector functions in IPF AMs, such as mTOR and NOX activation, superoxide production and glucose uptake. The increased glucose uptake via GLUT1 can furthermore sustain NADPH production in the pentose phosphate pathway and TCA cycle[171], which is a key substrate for superoxide production via the NADPH oxidase[89]. Superoxide produced by the NADPH oxidase can further react with NO to form peroxynitrite ($OONO^-$), another type of ROS. At the expense of NADPH, NO is produced by iNOS leading to increased levels of the cytotoxic $OONO^-$ in IPF AMs[172]. Similarly, increased levels of superoxide, NO and $OONO^-$ were detected in AMs in the bleomycin mouse model of pulmonary fibrosis[173]. Alternatively, arginase can convert L-arginine into ornithine, which is a proline precursor and therefore contributes to collagen production. As arginine is a substrate for both NO and ultimately ROS production as well as collagen synthesis, it is a key amino acid in IPF airway

macrophages and targeting arginine metabolism might be a way to rewire AM effector functions in IPF.

1.5.3.1 The ADORA2B regulatory pathway

Another pathway that is altered in airway macrophages in IPF is the adenosine-receptor and PPAR-γ pathway, with multiple downstream effector functions such as mTOR activation and antioxidant response via NRF2. The adenosine receptor ADORA2B catalyses the production of adenosine from ATP in the extracellular space, but also induced intracellular signalling via cAMP and the cAMP response element binding protein (CREB)[174]. While Zhou *et al.* show that adenosine signalling is altered in the lungs of IPF patients, resulting in increased adenosine production[175], knockout of the ADORA2B receptor in the bleomycin mouse model of pulmonary fibrosis resulted in reduced fibrotic phenotype suggesting a pro-fibrotic role[176]. Furthermore, Philip *et al*. show that inhibition of Hif-1α reduces ADORA2B expression in alternatively activated AMs in the bleomycin mouse model of pulmonary fibrosis, while ADORA2B deletion together with Hif-1α inhibition resulted in decreased IL-6 production in pro-fibrotic macrophages, suggesting that Hif-1α regulates ADORA2B expression on AMs and drives the progression of pulmonary fibrosis[177]. CREB in turn activates the peroxisome proliferator activated receptor gamma coactivator 1α (PGC-1α), a transcription factor inducing NRF1/2 and co-activating PPARγ. PPARγ can also activate PGC-1α upon binding of fatty acids or leukotrienes, thereby creating a feedback loop ultimately resulting in transcription of NRF1/NRF2[178]. While PPARγ expression has been found to be decreased in IPF lungs, it has not yet been investigated specifically in AMs[179].

1.5.3.2 NRF2 as an immunometabolic regulator

NRF2 is a basic leucine zipper protein, which regulates the expression of antioxidant proteins and protects against damage induced by oxidative stress. The PPARγ-NRF2 axis is therefore a key pathway regulating intracellular ROS production and accumulation and activation of this pathway could decrease AM ROS production in IPF and have anti-fibrotic potential. One such activator could be PPARγ agonists, which have been shown to be anti-

fibrotic[180,181]. In particular, Reddy *et al*. show that treatment with nitrated fatty acids, which act as PPARγ agonists, reversed pulmonary fibrosis in a mouse model by promoting collagen uptake by AMs and dedifferentiating myofibroblasts[179]. While NRF2 expression was decreased in whole lung tissue from aged mice during persistent fibrosis[115], preventing antioxidant response, this has not yet been investigated in IPF AMs in particular.

NRF2 furthermore regulates the expression of heme-oxygenase-1 (HO-1). While usually, HO-1 is induced by oxidative stress, its expression is decreased in IPF airway macrophages[182]. HO-1 is an oxidative stress response protein, responsible for the cleavage of heme groups into biliverdin, carbon dioxide and the release of ferrous iron[183]. Loss of HO-1 anti-inflammatory and antioxidant response function therefore results in decreased protection against oxidative damage. In line with decreased HO-1 activity in IPF AMs cleaving heme into ferrous iron, AMs in IPF patients have also been shown to be iron laden[184], which further induces oxidative stress and ROS production. Additionally, IPF AMs have a distinct signature expressing the scavenger receptor for the haemoglobin/haptoglobin complex (CD163)[185], which mediates the endocytosis of haemoglobin and haptoglobin by airway macrophages[186]. The proportion of transferrin receptor (CD71) expressing airway macrophages however, was decreased in IPF AMs, leading to an extracellular accumulation of transferrin[187]. Iron metabolism is therefore a key target in IPF airway macrophages and could be an option to decrease ROS production and oxidative stress.

Both Rac1 and PGC-1α can activate the key signalling hub mTOR and induce a downstream cascade leading to production of Hif1α and TGF-β. TGF-β is a key effector molecule of activated airway macrophages[188], as secreted it can recruit fibroblasts to the site of healing[189] and trigger fibroblast differentiation into myofibroblasts[190]. In IPF airway macrophages, Hif1α mediates TGF-β induced production of the plasminogen activator inhibitor-1 (PAI-1)[191], which inhibits the cleavage of plasminogen into plasmin, thereby preventing degradation of the extracellular matrix and contributing to excess matrix accumulation.

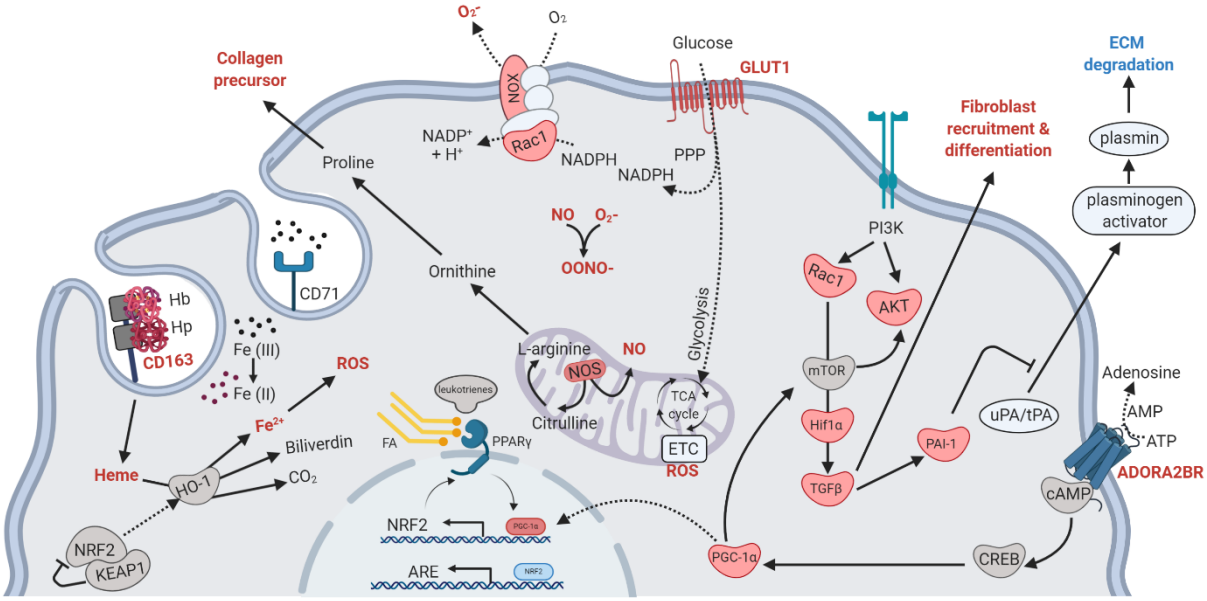

Figure 1.5. Metabolic alterations in IPF AMs. Increased expression of the scavenger receptor CD163 allows endocytosis of haemoglobin/haptoglobin. Heme is cleaved by heme-oxidase-1 (HO-1), which is regulated by NRF2 and induced by oxidative stress, into ferrous iron, yielding ROS. Expression of CD71 contributes to this pathway by importing transferrin bound iron. Superoxide (O_2^-) is a by-product of the NADPH oxidase cleaving NADPH, obtained from the pentose phosphate pathway (PPP), into $NADP^+$ and H^+. Combined with nitric oxide (NO), superoxide forms peroxinitrite ($OONO^-$). Glucose transporter GLUT-1 supports flux through the pentose phosphate pathway to generate superoxide and ROS in the electron transport chain (ETC). NO synthase (NOS) catalyses the production of NO from arginine. Alternatively, arginine can function as collagen precursor via ornithine and proline. The signalling G-protein Rac1 induces NOX activity and the mTOR signalling hub. mTOR has a variety of downstream effector proteins, such as signalling hub AKT and induction of Hif1α, which in turn induces expression of TGF-β. TGF-β activates plasminogen activator inhibitor-1 (PAI-1), which inhibits the degradation of extracellular matrix. Alternatively, mTOR is activated by PGC-1α, which can also induce expression of NRF2 via PPAR-γ. PPAR-γ can also activate PCA-1α upon binding of fatty acids or leukotrienes, thereby creating a positive feedback loop. The adenosine receptor ADORA2BR activates cAMP response element binding protein (CREB), which in turn activates PCG-1α, presenting another route of activating this key transcription factor.

Genes/proteins increased in pulmonary fibrosis are highlighted in red.

1.5.4 AM metabolism during chronic hypersensitivity pneumonitis

The impact of metabolic pathways during CHP remains largely unknown. Only one study recently investigated the microbiome in CHP BAL, which can release large amounts of short chain fatty acids and thereby alter the nutrient environment. In this study, Invernizzi *et al*. showed that the bacterial burden in the lower airways was higher in CHP samples compared to healthy controls, however it was lower than in IPF samples[192], highlighting the distinct nutrient environment in CHP and IPF. However, further studies are needed to better understand the metabolic pathways underlying CHP phenotype and especially that of AMs and T cells, the two most frequent largest immune cell populations during CHP. In contrast to IPF, CHP is driven by antigenic exposure, and therefore studies of other inflammatory chronic lung diseases may give important insights into metabolic phenotype of AMs and identify potential targets to study in the context of CHP.

For example, AMs are central to mediating type-2 inflammation against allergens and parasitic worms[193]. Numerous lines of evidence suggest that metabolic stress leading to the production of ROS play a role in asthma, a chronic inflammatory airways disease caused by a combination of allergens, air pollution and genetic factors. Increased ROS have been detected in AMs of asthmatic patients[194], and ROS contributes to lung injury[195] and tumour necrosis factor alpha (TNF-α) and IL-1β secretion by macrophages[196]. HO-1, which mediates ROS production, is increased in AMs in asthmatics[197]. In asthmatic patients, increased production of arachidonic acid metabolism intermediate 5-hydroxyicosatetranoic acid (5-HETE) and leukotrienes B_4 (LTB_4) and E_4 (LTE_4) have been detected in AMs cultured *ex vivo*[198]. These factors contribute to bronchial constriction and pro-inflammatory phenotype and failure to generate the anti-inflammatory 15-HETE and prostaglandin E_2 (PGE_2) was associated with reduced AM phagocytosis[199]. Furthermore, IL-13 induces Arg1 while reducing nitric oxide synthase 2 (NOS2), which may further contribute to asthma via metabolism of collagen precursors ornithine and proline[200,201].

Expression of genes related to glutathione metabolism, mitochondrial transport, pyruvate metabolism, TCA cycle and electron transport chain were altered in smokers and patients

with chronic obstructive pulmonary disease (COPD), another chronic inflammatory lung disease[202]. Due to long-term exposure to cigarette smoke, the oxidant environment in COPD is altered and ROS are released from AMs into the airways[195,203–205], whilst glutamyl cysteine ligase (important in GSH synthesis), is downregulated[206]. Cigarette smoking also alters iron homeostasis[207] and AMs in COPD show increased sequestering of iron[208]. Furthermore, Bewley *et al*. showed recently that mtROS-dependent bacterial clearance is deregulated in COPD AMs, resulting in impaired bacterial clearance[205]. However, while mtROS production is increased in AMs in COPD patients, the mitochondrial membrane potential is decreased[209]. This phenomenon has recently been linked to AM exposure to particulate matter[204] and may further explain the impaired phagocytic capacity of AMs in COPD, as decreased mitochondrial membrane potential results in energy failure in the cell, proton leakage and increased mtROS[210].

These studies of other inflammatory chronic lung diseases highlight that while short term AM metabolic rewiring supports the clearing of invading pathogens and the inflammatory response, long-term activation can have negative implications (Figure 1.6). In particular glycolysis supports inflammatory responses of AM, including cytokine production and ROS generation, while metabolites produced in the TCA cycle as well as iron can function as bacterial substrates and contribute to pathogen survival. While fatty acid synthesis and oxidation is useful for storing energy and as an alternative energy source during times of macrophage activation, fatty acid synthesis can also contribute to mucus production. Leukotrienes contribute to the AM pro-inflammatory phenotype but also cause bronchial constriction and contribute to airway remodelling in asthmatics by causing smooth muscle thickening. The amino acid arginine is a proliferator for collagen via ornithine and proline and can thereby contribute to extracellular matrix deposition.

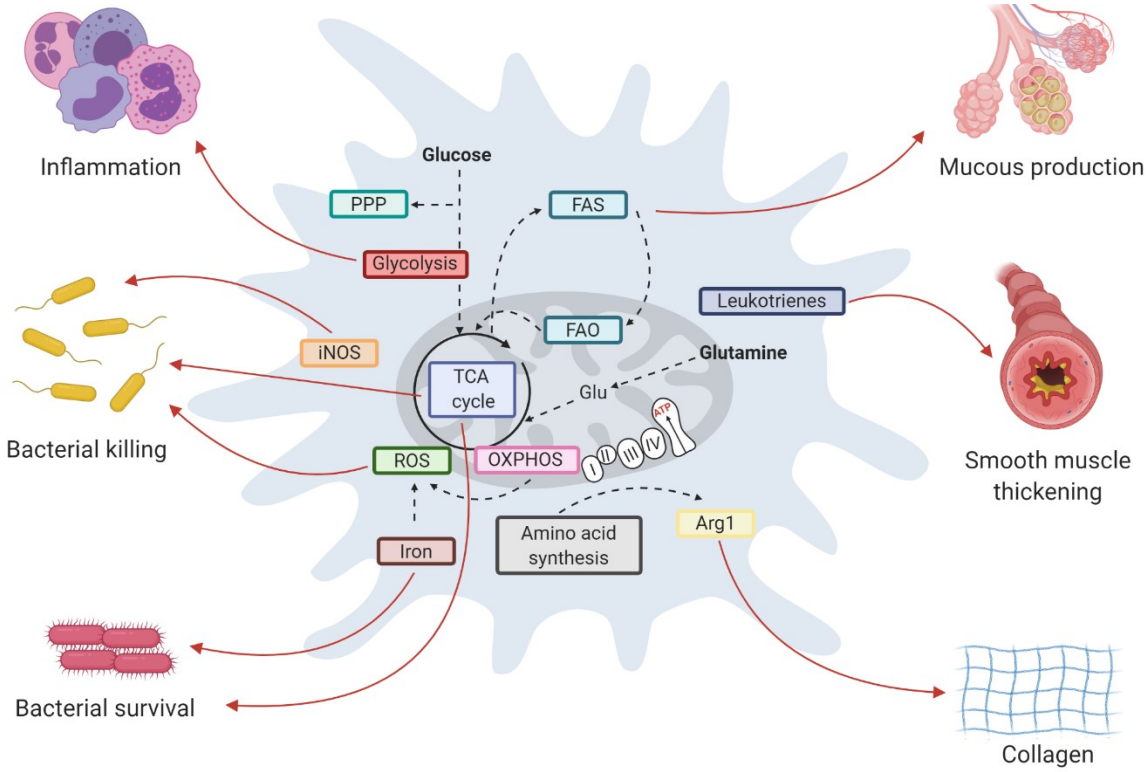

Figure 1.6. Altered metabolic pathways in AMs drive key features of chronic lung disease. Several metabolic pathways are rewired during chronic lung disease. While this response exists to clear invading pathogens and launch an inflammatory response, long-term activation of these pathways has negative implications. The glycolysis pathway supports inflammatory responses of AM, while iron and metabolites produced in the TCA cycle can function as bacterial substrates and contribute to pathogen survival. While fatty acid synthesis and oxidation is useful as a way of storing energy and alternative energy source during times of macrophage activation, fatty acid synthesis can also contribute to mucus production. Leukotrienes contribute to the AM pro-inflammatory phenotype but also cause bronchial constriction and contribute to airway remodelling in asthmatics by causing smooth muscle thickening. The amino acid arginine is a proliferator for collagen via ornithine and proline and can thereby contribute to extracellular matrix deposition.

1.6 Hypothesis and aims

Whilst many advances have been made recently at better understanding pulmonary fibrosis disease mechanisms and the role of airway macrophages, the metabolic underpinnings driving AM function during pulmonary fibrosis have not yet been studied in depth. The overall aim of this thesis was to better understand the metabolic phenotype of AMs during pulmonary fibrosis underlying their dysfunction and to identify factors which influence the pathogenesis of pulmonary fibrosis.

Overall hypothesis: Airway macrophage metabolic reprogramming underlies AM pro-fibrotic function and manipulation of AM metabolism represents a potential novel therapeutic strategy.

Overall aims:

1. To delineate AM metabolic profiles during fibrotic lung diseases such as IPF and CHP.
2. To investigate metabolic differences in tissue-resident and monocyte-recruited AMs during pulmonary fibrosis
3. To manipulate AM metabolism *ex vivo* and using mouse models of pulmonary fibrosis to restore function and prevent development of pulmonary fibrosis

2. Materials and methods

2.1 Human samples

All patients and control subjects provided written consent to participate in this study, which was approved by an external research ethics committee (10/HO720/12, 15/SC0101 and 15-LO-1399). In total, samples from 129 IPF patients, 68 CHP patients and 22 healthy donors were used for the research described in this thesis. Demographic and clinicopathological features are detailed in Table 2.1. Healthy volunteers had no self-reported history of lung disease, an absence of infection within the last 6 months and normal spirometry. Tables detailing the demographic and clinicopathological features of patient subgroups used for each experiment are presented in the results section.

Table 2.1: Subject demographics of all patients recruited for this thesis

Table showing sex, age, drug-treatment, forced expiratory volume (FEV1), FEV1 % predicted, forced vital capacity (FVC), % predicted FVC, diffusing capacity of lung carbon monoxide (D_{LCO}) and smoking status of healthy (n = 22), IPF (n = 129) and CHP (n = 68) samples of patients recruited for this thesis research. Data presented as mean ± S.D.

	IPF (n = 129) Mean ± S.D.	CHP (n = 68) Mean ± S.D.	Healthy (n = 22) Mean ± S.D.
Sex (M/F)	90 / 39	32 / 36	12 / 10
Age	70.4 ± 8.6	66.5 ± 8.5	48 ± 9.5
Anti-fibrotic treatment Of which: Nintedanib Pirfenidone	46 % 36 % 80 %	13 % 55 % 45 %	N/A
FEV1	2.2 ± 0.7	2.1 ± 0.6	3.0 ± 0.7
FEV1 (predicted)	85.5 ± 17.9	87.2 ± 20.5	100.4 ± 6.7
FVC	2.7 ± 0.9	2.6 ± 0.9	3.7 ± 0.9
FVC (predicted)	81.5 ± 17.5	87.9 ± 22.5	99.7 ± 8.0
D_{LCO} (single breath)	3.8 ± 1.4	3.9 ± 1.2	N/A
Ever smoked Ex-smoker Current smoker	60 % 5 % 95 %	53 % 100 %	N/A

2.2 Cell culture

2.2.1 Processing human bronchoalveolar lavage

Bronchoscopy of the right middle lobe was performed after informed consent as approved by an external Research Ethics Committee for ILD subjects (Ref. Nos. 10/H0720/12 and 15/SC0101) and healthy control subjects (Ref. No. 15-LO-1399) according to the Royal Brompton Hospital protocol (Royal Brompton & Harefield NHS Foundation Trust, 2016). Bronchoscopies were performed under a light sedation with midazolam in combination with local anesthesia with lidocaine. Four 60-ml aliquots of warmed sterile saline were instilled in the right middle lung lobe and aspirated by syringe and lavage aliquots collected after each instillation were pooled for each patient. Volume and BAL appearance were recorded for all samples.

2.2.2 Enrichment of $CD206^+$ macrophages

Up to $1x10^7$ BAL cells were stained with anti-CD206 (Biolegend) and Human TruStain FcX block (Biolegend) for 15 minutes at 4°C in 0.5% FBS/2mM EDTA in PBS prior to incubation with MACS anti-Cy7 microbeads (Miltenyi Biotec) for 15 minutes at 4°C. Cells were enriched in MACS magnetic separation column (Miltenyi Biotec) and purity was confirmed by flow cytometry. MACS enriched human AM were cultured in complete RPMI (10% FBS, 100U/ml penicillin/streptomycin) (Gibco, ThermoFisher) for 24 h for subsequent experiments.

2.2.3 Culture of CD206+ AMs

$CD206^+$ enriched AMs were cultured at a density of 100,000/well in a 48-well plate for 24 hours, during culture with metabolic inhibitors or controls. Cells were incubated with 500 µl of the following in complete RPMI medium (10% FBS, 1% P/S): 0.1 mM UK5099 containing 0.2 % DMSO, DMSO-control (0.2 %), 0.2 mM Etomoxir, 0.25 mM 6-diazo-5-oxo-L-norleucine (DON), 25 mM 2-deoxy glucose (2-DG), 10 mM dimethyl malonate (DMM), 10mM succinate, 10mM itaconate or medium only. After 24 hours, the supernatant was removed, 200µl cold RLT buffer (Qiagen) containing 1 % β-mercaptoethanol (Sigma

Aldrich) was added, and cells were scraped, lysed and stored at -80 °C for later RNA extraction.

2.2.4 Isolating fibroblasts from lung tissue

Primary human lung fibroblasts were isolated from lung resections of patients undergoing lung cancer surgery or lung transplantation performed after informed consent as approved by an external Research Ethics Committee (REC 15/SC0101) according to the Royal Brompton Hospital protocol (Royal Brompton & Harefield NHS Foundation Trust, 2016). Briefly, lung tissue was cut into 1 mm^3 cubes and cultured in 6-well plates with parallel scratches on the bottom to allow for outgrow of fibroblasts in complete Dulbecco's modified eagle medium (10% FBS, 100U/ml penicillin/streptomycin; Gibco, ThermoFisher). Media was changed every 3 days. After 10 days, cells were lysed with TrypleE, 6 wells combined (per donor) and transferred to a T75 flask (P1). Once confluent, cells were detached with Tryple and stored in liquid nitrogen in 1 x 10^6 aliquots (P2). Cells were expanded from liquid nitrogen for experiments and used until passage four.

2.3 Experimental animals

Mice were housed in specific-pathogen-free conditions and given food and water *ad libitum*. All procedures were approved by the United Kingdom Home Office and conducted in strict accordance with the Animals (Scientific Procedures) Act 1986. The Imperial College London Animal Welfare and Ethical Review Body (AWERB) approved this protocol. *Acod1*$^{-/-}$ (C57BL/6NJ-Acod1^(em1J)/J, JAX stock number 029340) mice and littermate controls were bred on a C57BL/6 background. Unless otherwise stated, all mice were between 8 and 12 weeks of age. Bleomycin or PBS control was administered as described in section 2.3.1 and mice were monitored daily for signs of ill health or weight loss. All surgery was performed under ketamine and sodium pentobarbital anesthesia and all efforts were made to minimize suffering.

2.3.1 Bleomycin model of pulmonary fibrosis in WT mice

Unless otherwise stated, all mice were male and between 8 and 12 weeks of age. Mice were administered either 0.05U (1U/ml solution dissolved in PBS) of bleomycin sulphate (Sigma Aldrich) or 50µl PBS via the oropharyngeal route and culled after 7, 21 or 42 days. For therapeutic experiments, mice were administered 0.25mg/kg (1mM solution dissolved in PBS, 50µl) itaconic acid (Sigma Aldrich) or PBS via the oropharyngeal route twice a week, beginning 10 days after of bleomycin administration. For AM targeted drug administration, 10µl liposomes encapsulating 9.8mM dimethyl malonate (DMM; Encapsula Nanosciences) or empty control liposomes (Encapsula Nanosciences) were diluted 1:4 in PBS and 40µl of these mixtures or PBS was administered via the oropharyngeal route at d0, d10 or every third day between d10 and d21. Mice were monitored for signs of ill health and weight loss daily.

2.3.2 Lung function assessment

Mice were administered 50mg/kg intraperitoneal (i.p.) pentobarbitol (Sigma Aldrich) and 100mg/kg intramuscular ketamine (Ketaset, Zoestis) to obtain surgical anaesthesia. Tracheas were cannulated allowing mechanical ventilation of mice, using the Flexivent^{TM} apparatus (Scireq) as described previously. Mice were ventilated with a tidal volume of 7 ml/kg body weight, a ventilation rate of 150 breaths per minute and a positive end-expiratory pressure of approximately 2 cm H_2O, which is similar to normal breathing. Two deep inflations were performed prior to starting measurement, to standardise lung volume history. A user-defined protocol was utilised to measure dynamic resistance, elastance and compliance at baseline, using the snapshot-150 perturbation, a single frequency sinusoidal waveform. Using the FlexiWare software (Scireq) data was fitted to a single compartment model and using multiple linear regression analysis, airway resistance and pulmonary elastance and compliance were calculated: pressure = (resistance x flow) + (elastance x volume) + fitting constant.

2.3.3 Bronchoalveolar lavage of mice

In order to obtain BAL, the airways of the mice were lavaged three times with 0.4 ml of PBS via a tracheal cannula. BAL fluid was centrifuged (700 X g, 5 min, 4°C); cells were resuspended in 0.5 ml complete media (RPMI + 10% fetal calf serum [FCS], 2 mM L-glutamine, 100 U/ml penicillin/ streptomycin). Cells were counted and pelleted onto glass slides by cyto-centrifugation (5 $\times 10^4$ cells/slide).

2.3.4 Adoptive transfer of Mo-AMs

Female WT or *Acod1*$^{-/-}$ mice were dosed with 0.05U bleomycin via the oropharyngeal route and lavaged at d7 post bleomycin to obtain Mo-AMs. Cells recovered from BAL were stained with live/dead stain and extracellular antibodies as described above and live, CD45$^+$, CD64$^+$, CD11c$^+$, SigF^{int} Mo-AMs were isolated by FACS sorting. Subsequently, 50,000 WT or *Acod1*$^{-/-}$ Mo-AMs were administered via the oropharyngeal route to male *Acod1*$^{-/-}$ mice, which had been dosed with bleomycin 7 days prior. Mice were sacrificed at d21 post initial bleomycin exposure.

2.3.5 Dissection and preparation of tissues

To disaggregate cells from lung tissue, one finely chopped left lobe of lung was incubated at 37°C for 1 h in digest reagent (0.15 mg/ml collagenase type D, 25 µg/ml DNase type I) in complete RPMI media. The recovered cells were filtered through a 70-µm nylon sieve, washed twice, resuspended in 1ml complete media, and counted in a hemocytometer prior to cyto-centrifugation; lung cell counts are quoted as total cell number/ml of this suspension.

2.3.6 Histology and fibrosis scoring in mice

Paraffin-embedded sections (4 µm) of lungs (apical lobe) were stained with hematoxylin/ eosin (H&E) and Sirius Red. For assessment of fibrosis, the semi-quantitative Ashcroft scoring system was used as previously described[211]

. All scoring and measurements were performed by 3-5 blinded independent observers.

2.4 Flow cytometry

2.4.1 Staining of extracellular antigens

250,000 cells were used per panel and stained in round-bottom 96-well plates. Cells were washed with PBS by centrifuging at 1800 rpm for 2 minutes, stained with near IR fixable live/dead (1:1,000; ThermoFisher) for 10 minutes in PBS and washed again, once in PBS and once in FACS buffer (1% FBS/2.5% HEPES/0.2% EDTA in PBS). Cells were subsequently stained with extracellular antigens for 20 minutes at 4°C (Biolegend, see Tables 2.2 and 2.3 for details of antibody clone, fluorophore and concentration used). Afterwards, cells were washed in FACS buffer three times and fixed overnight using the IC fix kit (eBioscience). The next day, cells were washed once in FACS buffer and resuspended in 100µl FACS buffer before data acquisition.

Table 2.2 Overview of extracellular antibodies (human)

Target species	Antibody	Fluorophore	Clone	Concentration
Human	CD177	FITC	MEM-166	1:100
Human	CD45	PercPCy5.5	HI30	1:100
Human	CD56	PEdazzle	HCD56	1:100
Human	Ckit	BV605	104D2	1:100
Human	Siglec8	PE	7C9	1:100
Human	CD19	BV421	HIB19	1:100
Human	FC-epsilon	AF700	AER-37	1:100
Human	CD3	PE Cy7	UCHT1	1:100
Human	CD14	BV711	M5E2	1:100
Human	CD206	APC	15-2	1:100
Human	CD206	APC Cy7	15-2	1:100
Human	CD163	BV605	GHI/61	1:100
Human	HLA-DR	BV421	L243	1:100
Human	CD11c	PE Cy7	3.9	1:100
Human	CD86	BV605	IT2.2	1:100
Human	CD71	PE	A015	1:100
Human	CD11b	AF700	M1/70	1:100
Human	CSF1R	APC	9-4D2-1E4	1:100

Table 2.3 Overview of extracellular antibodies (mouse)

Target species	Antibody	Fluorophore	Clone	Concentration
Mouse	CD64	BV421	X54-5/7.1	1:100
Mouse	Ly6G	BV510	1A8	1:200
Mouse	CD19	BV605	6D5	1:100
Mouse	CD90.2	BV605	53-2.1	1:200
Mouse	CD45	BV711	30-F11	1:200
Mouse	CD103	FITC	2E7	1:100
Mouse	MHC-II	PercPCy5.5	M5/114.15.2	1:100
Mouse	SiglecF	PE	E50-2440	1:100
Mouse	CD11c	PEdazzle	N418	1:100
Mouse	F4/80	PE Cy7	BM8	1:50
Mouse	CD11b	APC	M1/70	1:200
Mouse	Ly6C	AF700	HK1.4	1:200
Mouse	CD11c	BV605	N418	1:100
Mouse	CD4	BV421	RM4-5	1:200
Mouse	CD8	BV605	53-6.7	1:100
Mouse	CD3	PE Cy7	145-2C11	1:100

2.4.2 Staining with MitoSOX

For assessment of mitochondrial superoxide, cells were stained with 5 µM MitoSOX Red (ThermoFisher) in PBS for 10 minutes at 37°C after staining with fixable live/dead and extracellular antibodies as described in 2.4.1. Cells were then washed once in PBS and once in FACS buffer and fixed using IC fix kit (eBioscience) overnight before data acquisition.

2.4.3 Cell tracker staining for tissue resident AMs

PKH26 Red Fluorescent Cell Linker dye (Sigma Aldrich) was titrated and ultimately used at 0.5 µM to label phagocytic cells in BAL. It was administered oropharyngeal to mice one day before exposure to bleomycin to label tissue resident AMs. Staining efficiency was assessed by flow cytometry of BAL. This method was utilised to confirm SiglecF as a marker to differentiate between Tr-AM and Mo-AM[212] as suggested by Misharin *et al*.

2.4.4 Analysis of flow cytometry data

Data was acquired on a Fortessa II flow cytometer and cell sorting on an Aria III (BD Biosciences) and analysis was performed in Flowjo software, using fluorescence minus one (FMO) controls for each antibody. Gating strategies are shown for each experiment in results section.

2.4.5 FACS sorting of AMs from murine BAL

Murine BAL cells were pelleted by centrifugation at 3,000 rpm for 3 minutes at 4°C and supernatant was removed and stored for later analysis. Red blood cells were lysed in 1X red blood cell lysis buffer (Thermo Fisher) for 3 minutes at room temperature, followed by washing with PBS by centrifugation (3,000 rpm, 3 minutes, 4°C). Cells were then stained with near infrared fixable live/dead stain and extracellular antibodies as described in 2.4.1 and resuspended in 450 µl FACS buffer. Cells were sorted on an Aria III flow cytometer (BD) with a 100 µm nozzle, 20 psi using isoflow sheath fluid (Beckman Coulter). AMs were selected as live, $CD45^+$, $CD64^+$, $CD11c^+$ and $SigF^{high}$ (tissue resident AM) and $SigF^{int}$ (monocyte-recruited AMs) were sorted into non-stick polypropylene tubes in FACS buffer. Sorted AMs were either used right away for Seahorse analysis or lysed in RLT buffer + 1% β-mercaptoethanol and stored at -80 °C for later RNA extraction.

2.5 Gene expression analysis

2.5.1 Extraction and quality control of RNA

Total RNA from cultured cells, FACS sorted or MACS enriched cells stored in RLT plus buffer containing 1% β-mercaptoethanol was extracted using the QIAGEN RNeasy Micro Kit plus (QIAGEN) and concentration and RNA integrity were confirmed using the TapeStation analyser and RNA kit (Agilent) according to manufacturer's instructions. To extract RNA from the post-caval murine lung lobe, 350 µl RLT buffer containing 1% β-mercaptoethanol was added and samples were lysed using a tissue homogeniser and ceramic beads (2 x 1 minute), followed by centrifugation (3000 rpm for 3 minutes). The lung homogenate was then transferred onto gDNA columns from the QIAGEN RNeasy Mini Kit

plus (QIAGEN) and RNA was extracted following manufacturer's instructions. Concentration was measured on the NanoDrop.

2.5.2 Preparation of cDNA

Total RNA was reverse transcribed into cDNA using the High Capacity cDNA Reverse Transcription kit (Life Technologies), or GoScript reverse transcription system (Promega) for AMs, according to manufacturer's instructions in a 20 µl reaction, which was diluted 1:4 in ultrapure H_2O after reverse transcription.

2.5.3 Taqman assays

Real-time PCR was performed using fast-qPCR MasterMix (Life technologies) on a Viia-7 instrument (Applied Biosciences) with Taqman primers for murine *Acod1, Col-1α1, Col3α1, Col4α1, Fn-1* or human *ACOD1, CCL-2, CD163, FN-1, IL-1β, MMP-1, MMP-9* using *ACTB (*Life Technologies) as housekeeping gene.

Table 2.4. Overview of murine and human Taqman primers

Species	Gene	Primer ID	Description
Mouse	*Actb*	Mm01224532_m1	Beta Actin
Mouse	*Col1α1*	Mm00801666_g1	Collagen 1 subunit alpha 1
Mouse	*Col3α1*	Mm00802300_m1	Collagen 3 subunit alpha 1
Mouse	*Col4α1*	Mm01210125_m1	Collagen 4 subunit alpha 1
Mouse	*Fn-1*	Mm01256744_m1	Fibronectin 1
Mouse	*Irg1*	Mm01224532_m1	Aconitase decarboxylase 1
Human	*ACOD1*	Hs00985781_m1	Aconitase decarboxylase 1
Human	*ACTB*	Hs01060665_g1	Beta Actin
Human	*CCL-2*	Hs00234140_m1	C-C Motif chemokine ligand 2
Human	*CCL-18*	Hs00268113_m1	C-C Motif chemokine ligand 18
Human	*CCL-22*	Hs01574247_m1	C-C Motif chemokine ligand 22
Human	*CD71*	Hs00951083_m1	Cluster of differentiation 71 (Transferrin receptor)

Human	*CD86*	Hs01567026_m1	Cluster of differentiation 86
Human	*CD163*	Hs00174705_m1	Cluster of differentiation 163
Human	*FN-1*	Hs00287359_m1	Fibronectin 1
Human	*HIF1α*	Hs00153153_m1	Hypoxia inducible factor 1 alpha
Human	*IL-1β*		Interleukin 1 beta
Human	*IL-6*	Hs00174131_m1	Interleukin 6
Human	*IL-10*	Hs00961622_m1	Interleukin 10
Human	*IRF5*	Hs00158114_m1	Immune regulatory factor 5
Human	*MMP-1*	Hs00899658_m1	Matrix metallopeptidase 1
Human	*MMP-2*	Hs01548727_m1	Matrix metallopeptidase 2
Human	*MMP-7*	Hs01042796_m1	Matrix metallopeptidase 7
Human	*MMP-9*	Hs00957562_m1	Matrix metallopeptidase 9
Human	*MMP-12*	Hs00159178_m1	Matrix metallopeptidase 12

2.5.4 Qiagen 84x gene array

For analysis of glucose metabolism related genes in human CD206^{+} AMs total RNA (0.08 µg) of MACS sorted AMs was reverse transcribed into cDNA using the RT^{2} first-strand synthesis kit as per manufacturer's instructions (QIAGEN). Gene expression of 84 genes in glucose metabolism (details in Table 2.4) was assessed using fast-qPCR SYBR Green Master Mix (Qiagen, Germany) and Human Glucose Metabolism QIAGEN RT^{2} Profiler PCR Array (PAHS-006ZA) on a Viia-7 instrument. For analysis of murine AM fibrosis gene expression, total RNA (0.08 µg) of FACS sorted Mo-AMs or Tr-AMs was reverse transcribed into cDNA and gene expression of 84 genes in murine fibrosis (details in Table 2.5) was assessed using the mouse fibrosis 96-well gene array (120Z, QIAGEN). Gene expression was analyzed using the QIAGEN data analysis center and the ΔΔCT was calculated by subtracting the house-keeping control ACTB and the average of the control group. Results are shown as Log10(ΔΔCT) in a heatmap format or as single genes as $2^{-(\Delta\Delta CT)}$ to show relative gene expression.

Table 2.5. Human Glucose Metabolism QIAGEN RT^2 Profiler PCR Array (PAHS-006ZA)

UniGene	GenBank	Symbol	Description
Hs.387567	NM_001096	ACLY	ATP citrate lyase
Hs.567229	NM_002197	ACO1	Aconitase 1, soluble
Hs.643610	NM_001098	ACO2	Aconitase 2, mitochondrial
Hs.904	NM_000028	AGL	Amylo-alpha-1, 6-glucosidase, 4-alpha-glucanotransferase
Hs.513490	NM_000034	ALDOA	Aldolase A, fructose-bisphosphate
Hs.530274	NM_000035	ALDOB	Aldolase B, fructose-bisphosphate
Hs.155247	NM_005165	ALDOC	Aldolase C, fructose-bisphosphate
Hs.198365	NM_001724	BPGM	2,3-bisphosphoglycerate mutase
Hs.430606	NM_004077	CS	Citrate synthase
Hs.335551	NM_001931	DLAT	Dihydrolipoamide S-acetyltransferase
Hs.131711	NM_000108	DLD	Dihydrolipoamide dehydrogenase
Hs.525459	NM_001933	DLST	Dihydrolipoamide S-succinyltransferase (E2 component of 2-oxo-glutarate complex)
Hs.517145	NM_001428	ENO1	Enolase 1, (alpha)
Hs.511915	NM_001975	ENO2	Enolase 2 (gamma, neuronal)
Hs.224171	NM_001976	ENO3	Enolase 3 (beta, muscle)
Hs.494496	NM_000507	FBP1	Fructose-1,6-bisphosphatase 1
Hs.61255	NM_003837	FBP2	Fructose-1,6-bisphosphatase 2
Hs.592490	NM_000143	FH	Fumarate hydratase
Hs.212293	NM_000151	G6PC	Glucose-6-phosphatase, catalytic subunit
Hs.294005	NM_138387	G6PC3	Glucose 6 phosphatase, catalytic, 3
Hs.461047	NM_000402	G6PD	Glucose-6-phosphate dehydrogenase
Hs.435012	NM_138801	GALM	Galactose mutarotase (aldose 1-epimerase
Hs.436062	NM_000158	GBE1	Glucan (1,4-alpha-), branching enzyme 1
Hs.1270	NM_000162	GCK	Glucokinase (hexokinase 4)
Hs.466471	NM_000175	GPI	Glucose-6-phosphate isomerase
Hs.466828	NM_019884	GSK3A	Glycogen synthase kinase 3 alpha
Hs.445733	NM_002093	GSK3B	Glycogen synthase kinase 3 beta
Hs.386225	NM_002103	GYS1	Glycogen synthase 1 (muscle)

Hs.82614	NM_021957	GYS2	Glycogen synthase 2 (liver)
Hs.463511	NM_004285	H6PD	Hexose-6-phosphate dehydrogenase (glucose 1-dehydrogenase)
Hs.406266	NM_000189	HK2	Hexokinase 2
Hs.411695	NM_002115	HK3	Hexokinase 3 (white cell)
Hs.593422	NM_005896	IDH1	Isocitrate dehydrogenase 1 (NADP+), soluble
Hs.596461	NM_002168	IDH2	Isocitrate dehydrogenase 2 (NADP+), mitochondrial
Hs.591110	NM_005530	IDH3A	Isocitrate dehydrogenase 3 (NAD+) alpha
Hs.436405	NM_174856	IDH3B	Isocitrate dehydrogenase 3 (NAD+) beta
Hs.410197	NM_174869	IDH3G	Isocitrate dehydrogenase 3 (NAD+) gamma
Hs.526521	NM_005917	MDH1	Malate dehydrogenase 1, NAD (soluble)
Hs.147816	NM_001039845	MDH1B	Malate dehydrogenase 1B, NAD (soluble)
Hs.520967	NM_005918	MDH2	Malate dehydrogenase 2, NAD (mitochondrial)
Hs.488181	NM_002541	OGDH	Oxoglutarate (alpha-ketoglutarate) dehydrogenase (lipoamide)
Hs.89890	NM_000920	PC	Pyruvate carboxylase
Hs.1872	NM_002591	PCK1	Phosphoenolpyruvate carboxykinase 1 (soluble)
Hs.75812	NM_004563	PCK2	Phosphoenolpyruvate carboxykinase 2 (mitochondrial)
Hs.530331	NM_000284	PDHA1	Pyruvate dehydrogenase (lipoamide) alpha 1
Hs.161357	NM_000925	PDHB	Pyruvate dehydrogenase (lipoamide) beta
Hs.470633	NM_002610	PDK1	Pyruvate dehydrogenase kinase, isozyme 1
Hs.256667	NM_002611	PDK2	Pyruvate dehydrogenase kinase, isozyme 2
Hs.658190	NM_005391	PDK3	Pyruvate dehydrogenase kinase, isozyme 3
Hs.8364	NM_002612	PDK4	Pyruvate dehydrogenase kinase, isozyme 4
Hs.654693	NM_020786	PDP2	Pyruvate dehydrogenase phosphatase catalytic subunit 2
Hs.655245	NM_017990	PDPR	Pyruvate dehydrogenase phosphatase regulatory subunit
Hs.255093	NM_002626	PFKL	Phosphofructokinase, liver

Hs.632642	NM_000290	PGAM2	Phosphoglycerate mutase 2 (muscle)
Hs.78771	NM_000291	PGK1	Phosphoglycerate kinase 1
Hs.367727	NM_138733	PGK2	Phosphoglycerate kinase 2
Hs.466165	NM_012088	PGLS	6-phosphogluconolactonase
Hs.1869	NM_002633	PGM1	Phosphoglucomutase 1
Hs.23363	NM_018290	PGM2	Phosphoglucomutase 2
Hs.708038	NM_015599	PGM3	Phosphoglucomutase 3
Hs.201379	NM_002637	PHKA1	Phosphorylase kinase, alpha 1 (muscle)
Hs.78060	NM_000293	PHKB	Phosphorylase kinase, beta
Hs.715728	NM_006213	PHKG1	Phosphorylase kinase, gamma 1 (muscle)
Hs.196177	NM_000294	PHKG2	Phosphorylase kinase, gamma 2 (testis)
Hs.95990	NM_000298	PKLR	Pyruvate kinase, liver and RBC
Hs.56	NM_002764	PRPS1	Phosphoribosyl pyrophosphate synthetase 1
Hs.169284	NM_175886	PRPS1L1	Phosphoribosyl pyrophosphate synthetase 1-like 1
Hs.654581	NM_002765	PRPS2	Phosphoribosyl pyrophosphate synthetase 2
Hs.282417	NM_002863	PYGL	Phosphorylase, glycogen, liver
Hs.154084	NM_005609	PYGM	Phosphorylase, glycogen, muscle
Hs.11916	NM_022128	RBKS	Ribokinase
Hs.282260	NM_199229	RPE	Ribulose-5-phosphate-3-epimerase
Hs.469264	NM_144563	RPIA	Ribose 5-phosphate isomerase A
Hs.440475	NM_004168	SDHA	Succinate dehydrogenase complex, subunit A,
Hs.465924	NM_003000	SDHB	Succinate dehydrogenase complex, subunit B,
Hs.444472	NM_003001	SDHC	Succinate dehydrogenase complex, subunit C,
Hs.356270	NM_003002	SDHD	Succinate dehydrogenase complex, subunit D,
Hs.546323	NM_003850	SUCLA2	Succinate-CoA ligase, ADP-forming, beta subunit
Hs.270428	NM_003849	SUCLG1	Succinate-CoA ligase, alpha subunit

Hs.655250	NM_003848	SUCLG2	Succinate-CoA ligase, GDP-forming, beta subunit
Hs.438678	NM_006755	TALDO1	Transaldolase 1
Hs.89643	NM_001064	TKT	Transketolase
Hs.524219	NM_000365	TPI1	Triosephosphate isomerase 1
Hs.516217	NM_006759	UGP2	UDP-glucose pyrophosphorylase 2
Hs.520640	NM_001101	ACTB	Actin, beta
Hs.534255	NM_004048	B2M	Beta-2-microglobulin
Hs.592355	NM_002046	GAPDH	Glyceraldehyde-3-phosphate dehydrogenase
Hs.412707	NM_000194	HPRT1	Hypoxanthine phosphoribosyltransferase 1
Hs.546285	NM_001002	RPLP0	Ribosomal protein, large, P0

Table 2.6 Mouse Fibrosis QIAGEN RT^2 Profiler PCR Array (PAMM-120ZA)

UniGene	GenBank	Symbol	Description
Mm.213025	NM_007392	Acta2	Actin, alpha 2, smooth muscle, aorta
Mm.301626	NM_007428	Agt	Angiotensinogen (serpin peptidase inhibitor, clade A, member 8)
Mm.6645	NM_009652	Akt1	Thymoma viral proto-oncogene 1
Mm.257460	NM_009741	Bcl2	B-cell leukemia/lymphoma 2
Mm.595	NM_007557	Bmp7	Bone morphogenetic protein 7
Mm.28278	NM_007616	Cav1	Caveolin 1, caveolae protein
Mm.4686	NM_011330	Ccl11	Chemokine (C-C motif) ligand 11
Mm.867	NM_011331	Ccl12	Chemokine (C-C motif) ligand 12
Mm.1282	NM_011337	Ccl3	Chemokine (C-C motif) ligand 3
Mm.6272	NM_009915	Ccr2	Chemokine (C-C motif) receptor 2
Mm.439656	NM_009883	Cebpb	CCAAT/enhancer binding protein (C/EBP), beta
Mm.277792	NM_007743	Col1a2	Collagen, type I, alpha 2
Mm.249555	NM_009930	Col3a1	Collagen, type III, alpha 1
Mm.390287	NM_010217	Ctgf	Connective tissue growth factor
Mm.1401	NM_009911	Cxcr4	Chemokine (C-X-C motif) receptor 4
Mm.56769	NM_007833	Dcn	Decorin
Mm.14543	NM_010104	Edn1	Endothelin 1
Mm.252481	NM_010113	Egf	Epidermal growth factor
Mm.225297	NM_007932	Eng	Endoglin
Mm.3355	NM_010177	Fas	Fas ligand (TNF superfamily, member 6)
Mm.166318	NM_011824	Grem1	Gremlin 1
Mm.267078	NM_010427	Hgf	Hepatocyte growth factor
Mm.240327	NM_008337	Ifng	Interferon gamma
Mm.874	NM_010548	Il10	Interleukin 10
Mm.1284	NM_008355	Il13	Interleukin 13
Mm.368330	NM_008356	Il13ra2	Interleukin 13 receptor, alpha 2
Mm.15534	NM_010554	Il1a	Interleukin 1 alpha
Mm.222830	NM_008361	Il1b	Interleukin 1 beta

Mm.276360	NM_021283	Il4	Interleukin 4
Mm.4461	NM_010558	Il5	Interleukin 5
Mm.274846	NM_010562	Ilk	Integrin linked kinase
Mm.3510	NM_008382	Inhbe	Inhibin beta E
Mm.482186	NM_001033228	Itga1	Integrin alpha 1
Mm.5007	NM_008396	Itga2	Integrin alpha 2
Mm.57035	NM_013565	Itga3	Integrin alpha 3
Mm.227	NM_008402	Itgav	Integrin alpha V
Mm.263396	NM_010578	Itgb1	Integrin beta 1 (fibronectin receptor beta)
Mm.87150	NM_016780	Itgb3	Integrin beta 3
Mm.6424	NM_010580	Itgb5	Integrin beta 5
Mm.98193	NM_021359	Itgb6	Integrin beta 6
Mm.217000	NM_177290	Itgb8	Integrin beta 8
Mm.275071	NM_010591	Jun	Jun oncogene
Mm.172	NM_010728	Lox	Lysyl oxidase
Mm.269747	NM_019919	Ltbp1	Latent transforming growth factor beta binding protein 1
Mm.5022	NM_008607	Mmp13	Matrix metallopeptidase 13
Mm.280175	NM_008608	Mmp14	Matrix metallopeptidase 14 (membrane-inserted)
Mm.156952	NM_032006	Mmp1a	Matrix metallopeptidase 1a (interstitial collagenase)
Mm.29564	NM_008610	Mmp2	Matrix metallopeptidase 2
Mm.4993	NM_010809	Mmp3	Matrix metallopeptidase 3
Mm.16415	NM_008611	Mmp8	Matrix metallopeptidase 8
Mm.4406	NM_013599	Mmp9	Matrix metallopeptidase 9
Mm.2444	NM_010849	Myc	Myelocytomatosis oncogene
Mm.256765	NM_008689	Nfkb1	Nuclear factor of kappa light polypeptide gene enhancer in B-cells 1, p105
Mm.2675	NM_008808	Pdgfa	Platelet derived growth factor, alpha
Mm.144089	NM_011057	Pdgfb	Platelet derived growth factor, B polypeptide
Mm.154660	NM_008872	Plat	Plasminogen activator, tissue

Mm.4183	NM_008873	Plau	Plasminogen activator, urokinase
Mm.971	NM_008877	Plg	Plasminogen
Mm.439692	NM_009243	Serpina1a	Serine (or cysteine) peptidase inhibitor, clade A, member 1a
Mm.250422	NM_008871	Serpine1	Serine (or cysteine) peptidase inhibitor, clade E, member 1
Mm.22708	NM_009825	Serpinh1	Serine (or cysteine) peptidase inhibitor, clade H, member 1
Mm.391091	NM_010754	Smad2	MAD homolog 2 (Drosophila)
Mm.7320	NM_016769	Smad3	MAD homolog 3 (Drosophila)
Mm.100399	NM_008540	Smad4	MAD homolog 4 (Drosophila)
Mm.325757	NM_008542	Smad6	MAD homolog 6 (Drosophila)
Mm.34407	NM_001042660	Smad7	MAD homolog 7 (Drosophila)
Mm.2093	NM_011427	Snai1	Snail homolog 1 (Drosophila)
Mm.4618	NM_013672	Sp1	Trans-acting transcription factor 1
Mm.277406	NM_009283	Stat1	Signal transducer and activator of transcription 1
Mm.121721	NM_009284	Stat6	Signal transducer and activator of transcription 6
Mm.248380	NM_011577	Tgfb1	Transforming growth factor, beta 1
Mm.18213	NM_009367	Tgfb2	Transforming growth factor, beta 2
Mm.3992	NM_009368	Tgfb3	Transforming growth factor, beta 3
Mm.197552	NM_009370	Tgfbr1	Transforming growth factor, beta receptor I
Mm.172346	NM_009371	Tgfbr2	Transforming growth factor, beta receptor II
Mm.101034	NM_009372	Tgif1	TGFB-induced factor homeobox 1
Mm.4159	NM_011580	Thbs1	Thrombospondin 1
Mm.26688	NM_011581	Thbs2	Thrombospondin 2
Mm.8245	NM_011593	Timp1	Tissue inhibitor of metalloproteinase 1
Mm.206505	NM_011594	Timp2	Tissue inhibitor of metalloproteinase 2
Mm.4871	NM_011595	Timp3	Tissue inhibitor of metalloproteinase 3
Mm.255607	NM_080639	Timp4	Tissue inhibitor of metalloproteinase 4
Mm.1293	NM_013693	Tnf	Tumor necrosis factor

Mm.282184	NM_009505	Vegfa	Vascular endothelial growth factor A
Mm.328431	NM_007393	Actb	Actin, beta
Mm.163	NM_009735	B2m	Beta-2 microglobulin
Mm.343110	NM_008084	Gapdh	Glyceraldehyde-3-phosphate dehydrogenase
Mm.3317	NM_010368	Gusb	Glucuronidase, beta
Mm.2180	NM_008302	Hsp90ab1	Heat shock protein 90 alpha (cytosolic), class B member 1

2.6 Hydroxyproline assay

Hydroxyproline was measured using 10 mg of tissue from the inferior lobe of murine samples using a Hydroxyproline Assay Kit (Sigma Aldrich), as per manufacturer's instructions and fold change of bleomycin/PBS groups was calculated.

2.7 Seahorse XFp assay

The Seahorse mitochondrial stress test measures oxygen consumption rate (OCR) and extracellular acidification rate (ECAR) as surrogates for OXPHOS and glycolysis activity, respectively.

2.7.1 Cell Tak coating

Seahorse XFp 8-well plates were coated with 2.25 µg Cell Tak (BD Biosciences) per well, in 0.1 M Sodium Bicarbonate, pH 8.0, according to manufacturer's instructions. Plates were incubated with Cell Tak for 20 minutes at 37 °C and subsequently washed twice with sterile water. Plates were air-dried and stored for up to two weeks at 4 °C.

2.7.2 FCCP titration

FCCP titration was performed for human $CD206^{+}$ AMs (seeded at 150 000 per well) and murine FACS sorted Tr-AM or Mo-AM (seeded at 100 000 per well) using the XFp FCCP titration kit (Agilent) following the manufacturer's instructions. Briefly, cells were exposed to six different concentrations of FCCP ranging from 0 µM to 2.0 µM and oxygen consumption rate (OCR) was measured in response. The concentration inducing the highest maximal

respiration was selected, which was 0.5 µM FCCP for human AMs and 2.0 µM for murine AMs.

2.7.3 Agilent mitochondrial stress test

MACS sorted $CD206^+$ human AM (150 000 per well) or FACS sorted murine Tr-/Mo-AM (100,000 per well) were plated in a Cell Tak coated Seahorse plate and analyzed using the Seahorse Mito Stress Test kit (Agilent) after resting in complete (10% FBS, 1% P/S) RPMI at 37°C, 5% CO_2 overnight. OCR and ECAR were measured in XF medium (non-buffered RPMI containing 2mM glutamine, 1mM pyruvate and 10mM glucose, pH 7.4, Agilent) using the XFp extracellular flux analyzer (Agilent). OCR and ECAR were measured under basal conditions and after the sequential addition of 1.5 µM Oligomycin, 2.0 µM FCCP (murine AM) / 0.5 µM FCCP (human AM) and 0.5 µM Rotenone/Antimycin A (Agilent). As Oligomycin blocks the ATP synthase, it reduces OCR by the amount generated through ATP production and only shows oxygen consumed through proton leakage. FCCP is a potent uncoupler of OXPHOS and disrupts ATP synthesis by transporting protons across the mitochondrial inner membrane resulting in disturbed proton gradient. Addition of FCCP after Oligomycin results in maximal respiration through both glycolytic and OXPHOS pathways. Spare respiratory capacity (SRC) was calculated as subtraction of basal from maximal OCR. Non-mitochondrial oxygen consumption was defined as OCR after injection of rotenone/antimycin A, which inhibit complexes I and IIII, respectively, in the electron transport chain, thereby depleting all but non-mitochondrial respiration. Proton leak was defined as OCR after injection of Oligomycin after subtraction of non-mitochondrial oxygen consumption. ATP production was calculated by subtraction of proton leak from basal respiration.

2.7.4 Agilent glycolysis stress test

Glycolytic function was measured in MACS sorted $CD206^+$ human AMs using the Seahorse Glyco Stress Test (Agilent) following manufacturer's instructions. Cells were plated at a density of 150 000 cells per well on Cell Tak coated 8-well XFp Seahorse plates and analysed using the Seahorse XFp flux analyser after resting in complete (10% FBS, 1%

P/S) RPMI at 37°C, 5% CO_2 overnight. The next day, media was changed to XF medium without glucose or pyruvate (non-buffered RPMI containing 2mM glutamine, pH 7.4, Agilent) and cells were incubated for 1 hour at 37°C. ECAR was then measured at no-glucose basal conditions and after the addition of 10 mM glucose, 1 mM Oligomycin and 50 mM 2-DG. ECAR prior to glucose injection is referred to as non-glycolytic acidification. Glycolysis rate is calculated by subtracting non-glycolytic acidification from ECAR after injection of glucose. Maximal glycolytic capacity is calculated by subtracting non-glycolytic acidification from ECAR after injection of Oligomycin. The difference between glycolytic capacity and glycolysis rate defines glycolytic reserve.

2.8 JuLI Stage live cell imaging

Primary human lung fibroblasts were seeded in a 96-well plate for proliferation assay (5,000 per well) or 24-well plate for wound healing assay and serum-starved overnight prior to treatment with 10 mM itaconate in complete DMEM for 48 - 72 hrs. For wound healing assays, a standardized scratch was applied in each well using a p10 pipette tip. Images were taken on the JULI-Stage system (NanoEntek) at three to five positions per well every 30 minutes and proliferation rate or wound closure were calculated using JULI-Stage software (NanoEntek).

2.9 Targeted GC-MS strategy

Freeze dried BAL samples were spiked with d_3-labelled methylmalonic acid (d3-MMA, synthesized in house) and derivatized with 30µl methoxyamine hydrochloride (Sigma-Aldrich, 20mg/ml in pyridine, 40°C for 20min) to modify any carbonyls (multi-component method). After cooling, 70µl of N,O-bis(trimethylsilyl)trifluoroacetamide containing 1% trimethylchlorosilane (BSTFA Sigma-Aldrich) were added and the mixture incubated for 30 minutes at 60°C to effect trimethylsilylation of the hydroxy groups. Finally, supernatants from centrifuged reaction mixtures were transferred to injection vials. GC/MS analysis was performed on an Agilent 6890 gas chromatograph coupled to a 5973 MSD quadrupole mass spectrometer. Samples were injected in splitless mode with the inlet maintained at 280°C. Separation of the derivatives was performed on a DB-1701 capillary column 30m x 250µm

x 0.25µm (Agilent Technologies) using a three-stage temperature program to optimize the separation. Mass spectral data was acquired by selected ion monitoring (SIM) of m/z 259 (quantifier) and m/z 215 (qualifier) at approx. 6 min retention time. A five-level calibration plot was constructed over the concentration range 0-16 ng/ml. Quantitation was achieved by interpolation using the regression equation of the calibration curve. All data processing and concentration calculations were performed using Agilent MassHunter (v. B.07.01) software. Data is presented as fold change compared to the healthy control group. Therefore, the mean of the control group was calculated and all data points (control group, IPF and CHP patients) were divided by this value, to obtain the fold change of metabolite expression compared to control.

2.10 Quantification and statistical analysis

Differences between non-continuous groups were compared using an unpaired *t* test (parametric data sets), Mann-Whitney *U* test (nonparametric data sets), one-way analysis of variance (ANOVA) with Tukey's multiple comparison test (parametric data sets) or Kruskal-Wallis with Dunn's multiple comparison test (non-parametric data sets), or a one-sample *t* test where appropriate. For analysis of matched data, a Wilcoxon matched pairs signed rank test was used to compare between treated and control groups. Data are presented as mean ± standard error mean (SEM). For correlation studies, the Pearson test (parametric datasets) or Spearman-Rank test (nonparametric datasets) was used to correlate nonparametric data sets; The *r* values are presented in a heatmap format and significant *p* values are indicated. For the gene expression assays, gene expression was analyzed using the QIAGEN data analysis center and the ΔΔCT was calculated by subtracting the house-keeping control ACTB and the average of the control group. Results are shown as Log10(ΔΔCT) in a heatmap format or comparing single genes between disease groups as $2^{-(\Delta\Delta CT)}$ to show relative gene expression. Principal component analysis was performed on the gene expression data using the non-linear iterative partial least squares (NIPALS) method. Survival analysis of $ACLY^{high/low}$ and $PCK2^{high/low}$ expressing groups was performed using the Gehan-Breslow-Wilcoxon test. When comparing areas

under the curve (AUC), a *t* test (parametric data sets) or Mann Whitney *U* test (nonparametric datasets) was performed comparing the replicates per group. For all experiments, the number of patients or animals (*n*) per group is indicated. Analysis was performed using Prism software (GraphPad Software). Heatmaps were generated using the Morpheus Software tool (https://software.broadinstitute.org/morpheus/).

3. Distinct metabolic phenotype underlies AM phenotype in IPF and CHP

3.1 Introduction

Interstitial lung disease (ILD) comprises a diverse group of pathologies, characterised by excessive collagen deposition in the pulmonary interstitium leading to impaired gas exchange[213]. Idiopathic pulmonary fibrosis (IPF) is the most common of the ILDs and an age-associated disease, as incidence and prevalence increase significantly with age and the median age at diagnosis is 65 years[4]. IPF shows as a pattern of usual interstitial pneumonia without alternative aetiology, honeycombing of sub-pleura and dilation of bronchi as well symptoms of cough and dyspnoea. Until recently, IPF was considered an inflammatory disease; however, anti-inflammatory treatment with steroids has been shown to worsen symptoms and are no longer recommended for the treatment of IPF[214]. Recently studies have suggested that the pathology of IPF is initiated via repetitive micro injuries to the alveolar epithelium, resulting in fibroblast and immune cell recruitment and myo-fibroblast differentiation in susceptible individuals. Active myo-fibroblasts in IPF secrete excessive amounts of extracellular matrix and collagen, leading to permanent remodelling of lung architecture[215]. Patients can be grouped into slow- and fast-progressors and acute exacerbations of disease can result in a rapid deterioration of symptoms. While unknown aetiology is a requirement for diagnosis of IPF, genetic and environmental risk factors increase susceptibility. These include genetic predispositions for genes associated with surfactant production, telomere biology and epithelial barrier function, as well as smoking or chronic dust exposure[216]. Nintedanib and Pirfenidone are now the first line of treatment as both have demonstrated anti-fibrotic effects in clinical trials and reduced FVC decline[11,12].

Hypersensitivity pneumonitis (HP, previously known as extrinsic allergic alveolitis[18]), accounts for about 5 – 15% of ILD cases in Europe[24]. HP is characterised by parenchymal inflammation caused by inhalation of antigen, which if left unrecognised can result in interstitial fibrosis and honeycombing[217]. Over 200 antigens have been identified as causal agents for CHP, derived from fungi, bacteria, and animal protein or biochemical sources. Occupational groups that are most often affected by CHP include farmers, tobacco workers, woodworkers, millers, machinists and bird breeders[218]. Hypersensitivity pneumonitis is

grouped into three phases: acute, sub-acute and chronic. During acute hypersensitivity pneumonitis, AMs are activated upon inhalation of antigen and recruit neutrophils, T cells and monocytes. In the sub-acute phase, granulomas form, Th1 lymphocytes proliferate and B cells become activated, whereas in the chronic phase activated AMs secrete TGF-β, leading to collagen deposition by myofibroblasts, ECM deposition and permanent lung remodelling[219]. Of these subtypes, only chronic HP (CHP) is usually fibrotic and will be considered here in more detail. CHP has been considered as an orphan disease in the past, with an incidence rate of only 1 per 100,000 in the UK[28]. However, CHP is often unrecognised or misdiagnosed as IPF, contributing to the low incidence rate. While clinical, radiological and pathological features of CHP and IPF can be indistinguishable, it is essential to differentiate between these two ILD, as treatment routes and outcomes are very different[220]. CHP has a favourable prognosis in comparison to IPF if detected early and the causative agent is removed[219]. Furthermore, oral corticosteroid treatment is considered as primary treatment in CHP, although others such as cell cycle inhibitors and anti-inflammatories are tested in clinical trials[221]. Prominent differences between CHP and IPF include an increased proportion of lymphocytes in BAL[23] and specific IgG positivity in CHP. However, other studies have reported that in the chronic form of hypersensitivity pneumonitis many cases do not show a strong lymphocytosis anymore[222]. Only recently a Delphi survey was applied to an international panel of ILD experts to reach a consensus for the diagnosis of CHP, which yielded a new questionnaire to aid with the diagnosis of CHP[23,223].

AMs play an important role in the pathogenesis of both CHP and IPF. While *in vitro*, macrophage phenotype can be clearly linked to polarisation by LPS/IFN-γ or IL-4/IL-13, *in vivo* macrophage phenotypes are much more diverse, especially in a complex inflammatory environment. Whilst it is well established that AM numbers are increased during fibrotic lung disease, both pro-inflammatory and pro-wound healing macrophage subtypes have been reported. While the pro-inflammatory AMs produced CCL-3, CCL-4, CCL-20, CXCL-1, CXCL-5, CXCL-7, CXCL-8 and IL-8[76], others had a pro-wound healing phenotype by expressing CCL-2, CCL-13, CCL-27, CCL-18, CCL-22 and CCL-24[224].

In recent years, seminal studies have contributed to a better understanding of AM origin and sustainability in the lungs. AMs originate from embryonic precursors and foetal liver monocytes, seeding the lung during embryonic development and differentiating into macrophages in the early days of life. The current consensus is that later in life and during fibrotic lung disease, peripheral blood monocytes are recruited to the lungs and differentiate into AMs to replenish the resident population[34]. In the bleomycin model of pulmonary fibrosis, both monocyte-derived and tissue-resident AMs upregulate both pro-inflammatory and pro-wound healing genes, however this response is more pronounced in monocyte-derived macrophages[212]. AMs are actively involved in the pathogenesis, as they induce fibroblast recruitment, myofibroblast differentiation and collagen deposition via secretion of cytokines and chemokines. Furthermore, efferocytosis has been shown to be impaired in AMs during IPF[225] as well as iron sequestration[226].

Recently metabolic programmes and metabolic rewiring has gained interest as an influence on disease pathophysiology. During fibrotic lung disease higher metabolic activity in the lung has been shown[227] with increased uptake of glucose in fibrotic foci and honeycombing areas[168]. Mitochondrial dysfunction may be one of the reasons for impaired wound healing and cellular senescence and has been detected in key cell populations driving pulmonary fibrosis, alveolar epithelial cells and fibroblasts[228]. This can lead to excess ROS production, which has been shown in bleomycin induced pulmonary fibrosis[229]. Furthermore, glycolytic reprogramming has been demonstrated to be essential for myofibroblast differentiation[230]. Although Xie *et al*. showed that bleomycin lung AMs utilise increased glycolysis and upregulated fatty acid oxidation, rather than glutaminolysis[231], the specific role of metabolic programmes underlying macrophage function during pulmonary fibrosis is not yet fully understood. Thus, this chapter aims to investigate AM metabolic phenotype during IPF and CHP.

3.1.1 Hypothesis & Aims

Metabolic reprogramming underlies AM-wound healing phenotypes during fibrotic lung disease and AMs from IPF and CHP exhibit distinct metabolic phenotypes.

Aims:

1. To characterise cellular and metabolic profile of IPF and CHP BAL and AMs
2. To assess how AM metabolic phenotype relates to disease pathology
3. To determine whether inhibition of AM metabolic pathways can alter pro-fibrotic phenotypes

3.2 Methods

3.2.1 Bronchoalveolar lavage processing and analysis

Bronchoscopy of the right middle lobe was performed after informed consent of ILD patients or healthy controls according to the Royal Brompton Hospital protocol. BAL was transported to the lab on ice and processed within three hours of collection. It was filtered through a 70 µm cell strainer, lysed for red blood cells and white blood cells were counted using crystal violet. An aliquot of 1 ml BAL supernatant was then snap-frozen and freeze-dried and later sent for targeted GC-MS analysis for central carbon metabolites.

5 – 10 x 10^6 BAL cells were used for enrichment for CD206+ AMs by magnetic activated cell sorting (MACS). Purity of sorted AMs was analysed by flow cytometry. Gene expression analysis of enriched CD206+ AM was performed using a QIAGEN gene array targeting 84 central carbon metabolism genes or Taqman qPCR for specific genes, while the overall metabolic profile was determined by Seahorse mitochondrial stress test. The remaining BAL cells were stained with extracellular and intracellular antibodies for multi-colour flow cytometry. An overview of human BAL processing and subsequent analysis is shown in Figure 3.1.

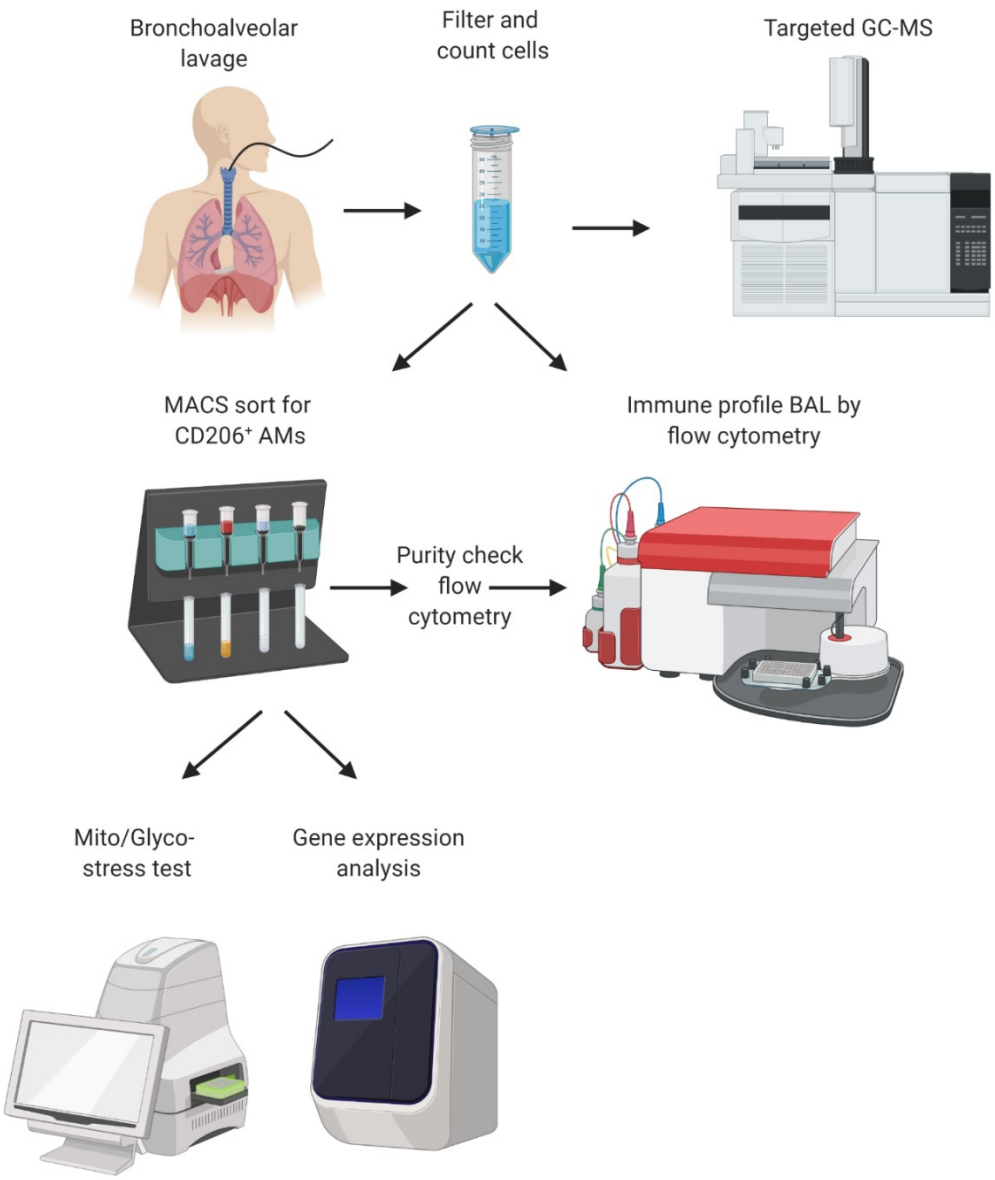

Figure 3.1. Flow chart of human bronchoalveolar lavage processing and analysis. BAL was passed through 70µm filter and cells are counted. A 1 ml sample of BAL supernatant is snap frozen and sent for targeted GC-MS analysis for central carbon metabolites. 5 – 10 x 10^6 BAL cells are enriched for $CD206^+$ AMs by MACS sorting and purity is checked by flow cytometry. The remaining BAL is stained with antibodies for multi-colour flow cytometry. Enriched $CD206^+$ AMs are further analysed using the Mito – or Glyco-Stress Test (Seahorse assay) or by qPCR for gene expression.

3.3 Results

3.3.1 Flow cytometric analysis of ILD BAL

To determine the immune cell profile in the BAL of recruited IPF and CHP patients and healthy controls, multi-colour flow cytometry was performed. After exclusion of debris and identifying single cells, live cells were identified using a near-ultra red fixable viability dye. Of all CD45+ immune cells, the following populations were enumerated (Figure 3.2): $CD206^+$ airway macrophages, $CD206^-/CD14^+$ monocytes, $CD3^+$ T cells, $CD3^+/CD56^+$ NK T cells, $CD56^+/CD3^-$ NK cells, $CD19^+/CD3^-$ B cells, $Siglec8^+$ eosinophils, FC-epsilon$^+$ basophils and $CD177^+$ neutrophils. This gating strategy was applied to 107 BAL samples from IPF patients, 59 CHP patients and 15 healthy controls. Table 3.1 shows the demographic distribution and lung function of this cohort. BAL was obtained for diagnosis at first presentation with symptoms. BAL from IPF patients contained an increased proportion of AMs (Figure 3.3 A), monocytes and eosinophils (Figure 3.3 H), compared to CHP BAL. Furthermore, proportions of B cells (Figure 3.3 E), eosinophils (Figure 3.3 H), and neutrophils (Figure 3.3 I) were increased in IPF BAL compared to healthy control samples. Similarly, BAL from CHP patients showed decreased proportions of AMs and monocytes along with increased proportions of T cells (Figure 3.3 D), NK T cells (Figure 3.3 F), eosinophils (Figure 3.3 H) and neutrophils (Figure 3.3 I).

Analysis of total numbers of each immune cell population revealed that there was significantly increased number of AMs (Figure 3.4 A) and monocytes (Figure 3.4 B), as well as NK T cells (Figure 3.4 F), NK cells (Figure 3.4 G), eosinophils (Figure 3.4 H) and neutrophils (Figure 3.4 I) in IPF. BAL from CHP patients had increased total numbers of T cells (Figure 3.4 D), NK T cells (Figure 3.4 F), NK cells (Figure 3.4 G), eosinophils (Figure 3.4 H) and neutrophils (Figure 3.4 I).

Table 3.1: Subject demographics of samples used for FACS analysis (Figure 3.2 – 3.4)

Table showing sex, age, drug-treatment, FEV1, FEV1 % predicted, forced vital capacity (FVC), % predicted FVC, DLCO and smoking status of healthy (n = 15), IPF (n = 104) and CHP (n = 57) samples used for FACS analysis of BAL (Figures 3.2 – 3.4). Data presented as mean ± S.D.

	IPF (n = 104) Mean ± S.D.	CHP (n = 57) Mean ± S.D.	Healthy (n = 15) Mean ± S.D.
Sex (M/F)	76/28	23/34	7/8
Age	70.3 ± 8.5	66.8 ± 8.6	49.8 ± 11.4
Anti-fibrotic treatment Of which: Nintedanib Pirfenidone	43% 42% 75%	10% 67% 33%	N/A
FEV1	2.2 ± 0.7	2.0 ± 0.6	2.8 ± 0.7
FEV1 (predicted)	87.2 ± 17.5	87.8 ± 19.8	101.3 ± 6.5
FVC	2.7 ± 0.9	2.6 ± 0.8	3.6 ± 0.9
FVC (predicted)	83.1 ± 17.3	88.8 ± 20.7	100.4 ± 8.2
DLCO (single breath)	3.9 ± 1.5	3.8 ± 1.1	N/A
Ever smoked Of which: Ex-smoker Current smoker	62.5% 94% 6%	65% 100% 0%	20% 33% 67%

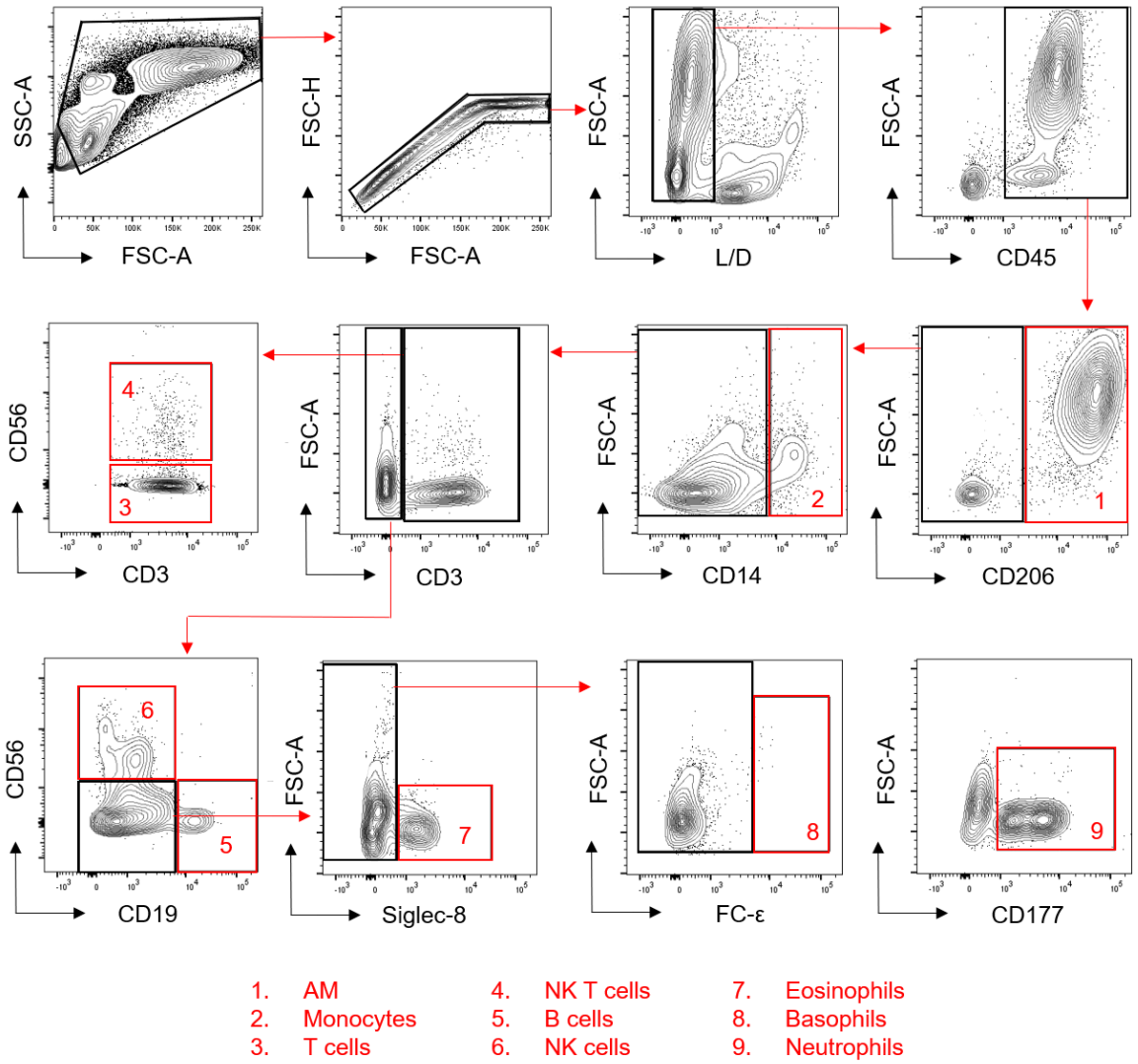

Figure 3.2. Gating strategy for human BAL flow cytometry panel. After gating out debris and doublets, live, CD45^{+} cells were selected. Of the CD45+ cells, airway macrophages (CD206^{+}), monocytes (CD14^{+}, CD206^{-}), T cells (CD3^{+}), NK T cells (CD3^{+}, CD56^{+}), NK cells (CD3^{-}, CD56^{+}), B cells (CD3^{-}, CD19^{+}), eosinophils (Siglec-8+), basophils (FC-epsilon+) and neutrophils (siglec-8^{-}, CD177^{+}) were gated as shown. Representative human flow cytometry plots for analysis of BAL.

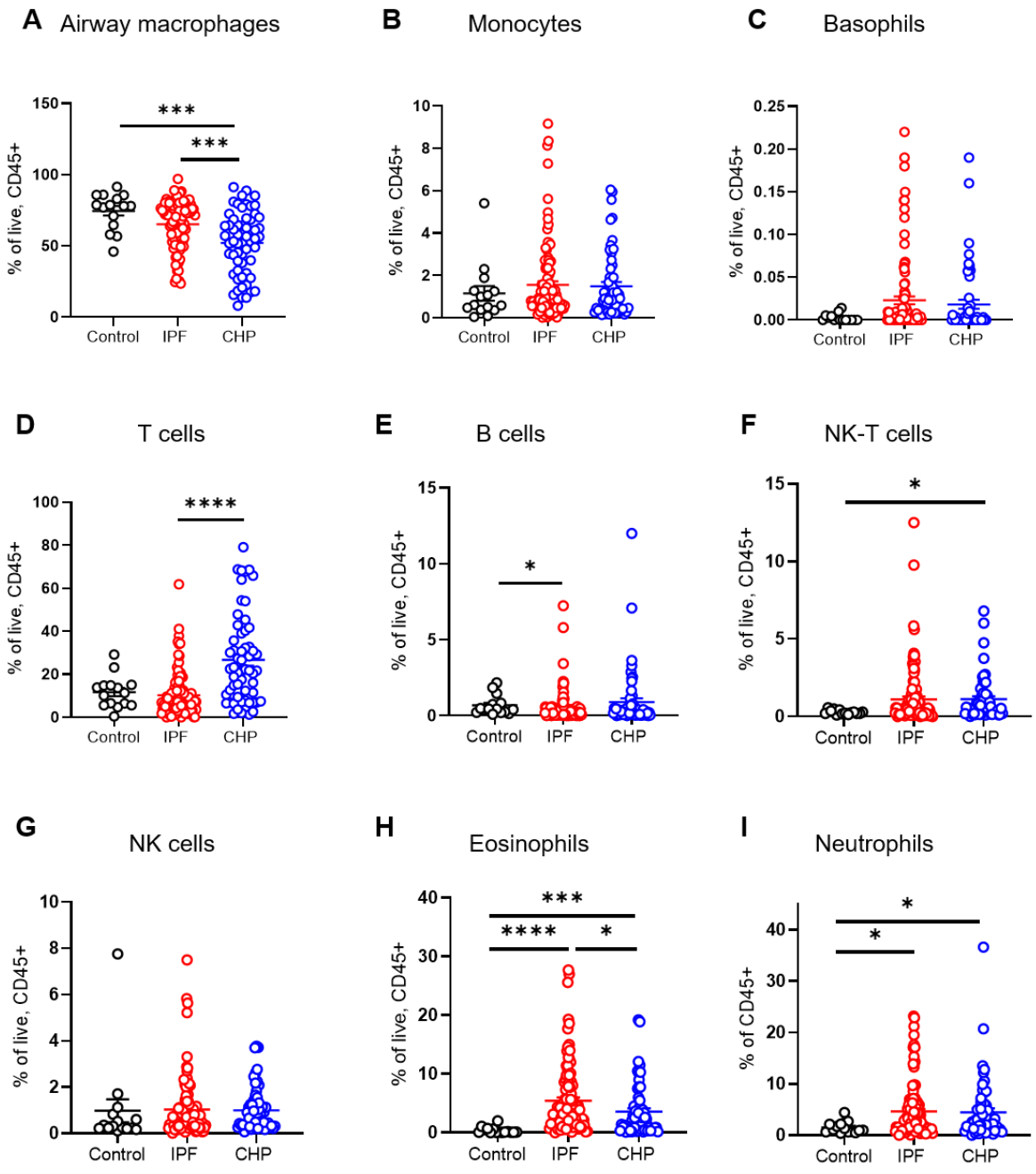

Figure 3.3. Proportions of immune cell populations in ILD and control BAL. Data shown as percentage of live, CD45⁺ BAL cells. A) Airway macrophages B) Monocytes C) Basophils D) T cells E) B cells F) NK-T cells G) NK cells H) Eosinophils I) Neutrophils. Populations gated based on Figure 3.2. Control n = 15, IPF n = 107, CHP n = 59. Data presented as mean ± S.E.M. Statistical significance tested by One-Way ANOVA with Kruskal Wallis multiple comparison test, * $P < 0.05$, ** $P < 0.01$, *** $P < 0.005$, **** $P < 0.001$.

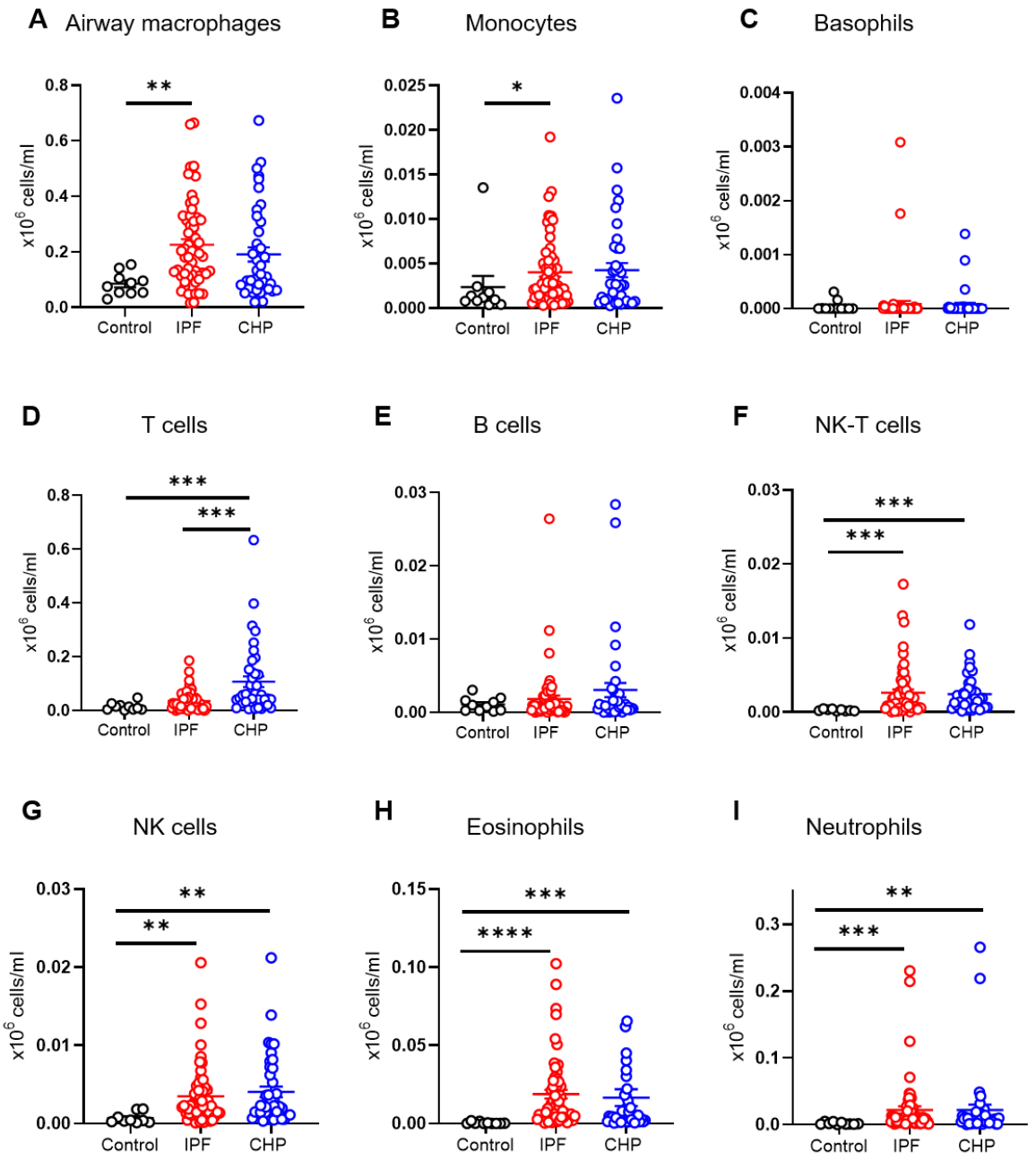

Figure 3.4. Total numbers of immune cell populations in ILD and control BAL Data shown as cells/ml BAL based on proportions shown in Figure 3.3. A) Airway macrophages B) Monocytes C) Basophils D) T cells E) B cells F) NK-T cells G) NK cells H) Eosinophils I) Neutrophils. Populations gated based on Figure 3.2. Control n = 10, IPF n = 59, CHP n = 41. Data presented as mean ± S.E.M. Statistical significance tested by One-Way ANOVA with Kruskal Wallis multiple comparison test, * P < 0.05, ** P < 0.01, *** P < 0.005, **** P < 0.001.

3.3.2 Targeted GC-MS analysis of BAL

To investigate how the metabolic profile of the airways is impacted during IPF/CHP, we developed a targeted GC-MS method for analysis of BAL together with the King's College Mass Spectrometry facility. All interrogated metabolites are shown in the schematics in panels C of Figures 3.5 – 3.7. Analysis was performed on 11 healthy control BAL supernatant samples, 68 IPF BAL supernatant samples and 44 CHP BAL supernatant samples (see Table 3.2). For simplicity, results are shown in Figure 3.5 comparing IPF to healthy controls, Figure 3.6 comparing CHP to healthy controls and Figure 3.7 comparing CHP to IPF samples. This targeted GC-MS analysis of central carbon intermediates showed that in IPF BAL, lactate was significantly increased in IPF compared to healthy controls (Figure 3.5 A). Of the TCA cycle intermediates analysed, isocitrate and malate were significantly increased (Figure 3.5B) in IPF. In contrast, most of both glycolysis related (Figure 3.5A) and TCA-cycle related metabolites were significantly increased in CHP BAL supernatant compared to healthy controls (Figure 3.6C). These results suggest that CHP BAL contains more glycolytic and TCA related intermediates than IPF BAL, which is confirmed by direct comparison of the two ILDs. Here, pyruvate and lactate were significantly increased in CHP BAL (Figure 3.7 A) as well as isocitrate, fumarate and succinate of the TCA cycle related metabolites, compared to IPF (Figure 3.7 B).

Table 3.2: Subject demographics of samples used for GC-MS analysis (Figure 3.5 – 3.7)

Table showing sex, age, drug-treatment, FEV1, FEV1 % predicted, forced vital capacity (FVC), % predicted FVC, DLCO and smoking status of healthy (n = 11), IPF (n = 68) and CHP (n = 44) samples used for targeted GC-MS analysis of BAL (Figures 3.5 – 3.7). Data presented as mean ± S.D.

	IPF (n = 68) Mean ± S.D.	CHP (n = 44) Mean ± S.D.	Healthy (n = 11) Mean ± S.D.
Sex (M/F)	57/22	27/17	6/5
Age	66.4 ± 10.0	67.0 ± 10.6	50.7 ± 2.4
Anti-fibrotic treatment Of which: Nintedanib Pirfenidone	56% 34% 85%	14% 67% 33%	N/A
FEV1	2.1 ± 0.7	2.2 ± 0.8	2.9 ± 0.7
FEV1 (predicted)	82.7 ± 19.2	89.3 ± 21.7	97.0 ± 4.8
FVC	2.7 ± 0.8	2.9 ± 1.1	3.5 ± 1.0
FVC (predicted)	81.7 ± 17.8	90.4 ± 21.9	94.5 ± 3.2
DLCO (single breath)	4.0 ± 1.7	4.3 ± 1.7	N/A
Ever smoked Of which: Ex-smoker Current smoker	65% 90% 10%	45% 85% 15%	18% 100%

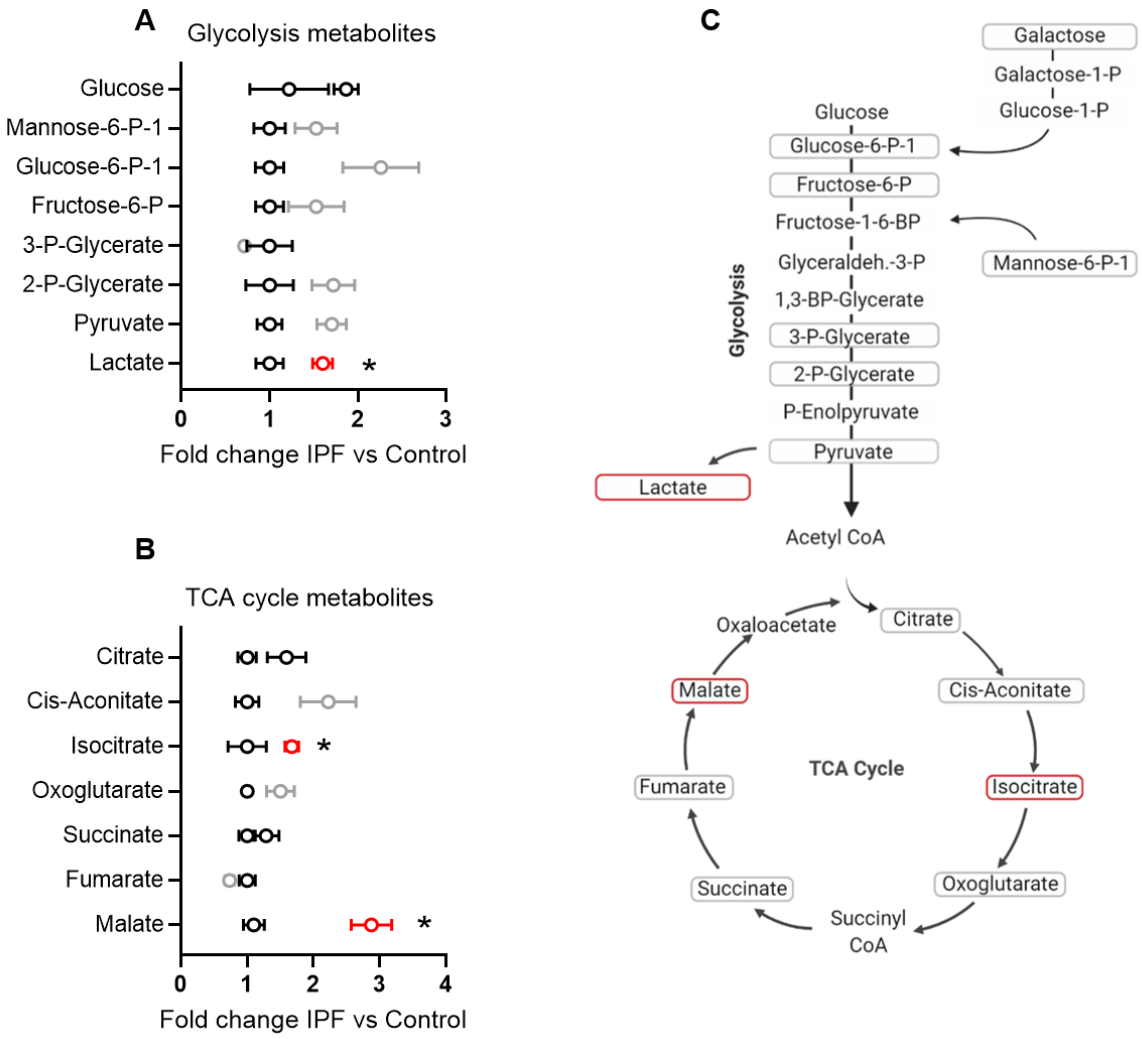

Figure 3.5. Lactate, isocitrate and malate are increased in IPF BAL supernatant compared to healthy. Targeted GC-MS analysis of freeze-dried BAL supernatant of n = 11 healthy controls and n = 68 IPF samples assessing glycolysis related (A) and TCA cycle related (B) metabolites shown as fold change against control group (in black). Significant increases in IPF are shown in red, unaltered IPF data is shown in grey. C) Schematic of analysed (grey) and increased (red) metabolites. Data presented as mean ± S.E.M. Statistical significance tested by Mann Whitney U test, * $P < 0.05$.

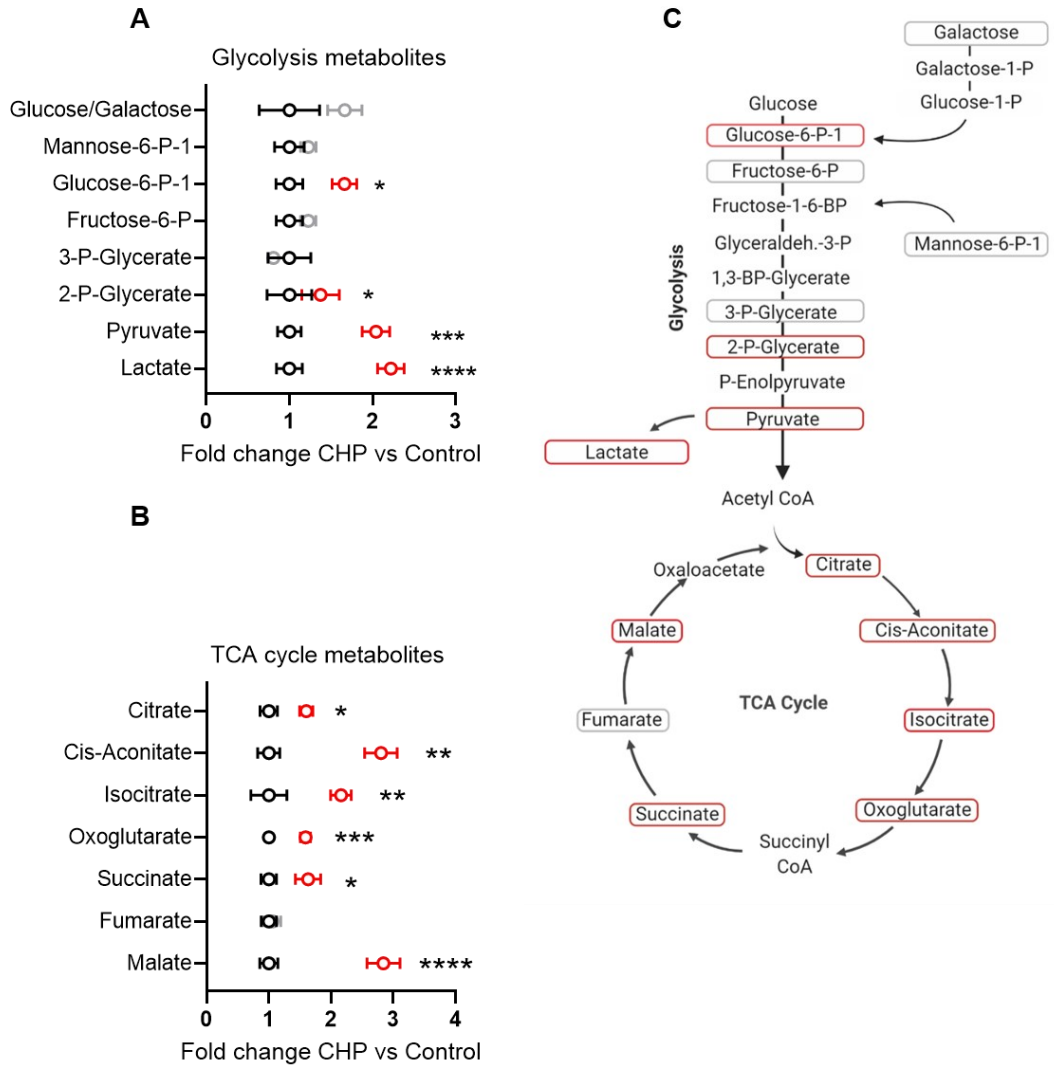

Figure 3.6. Increased glycolysis and TCA-cycle related metabolites in CHP BAL supernatant compared to healthy. Targeted GC-MS analysis of freeze-dried BAL supernatant of n = 11 healthy controls and n = 44 CHP samples assessing glycolysis related (A) and TCA cycle related (B) metabolites, shown as fold change against control group (in black). Significant increases in CHP are shown in red, unaltered CHP data is shown in grey. C) Schematic of analysed (grey) and increased (red) metabolites. Data presented as mean ± S.E.M. Statistical significance tested by Mann Whitney U test, * $P < 0.05$, ** $P < 0.01$, *** $P < 0.005$, **** $P < 0.001$.

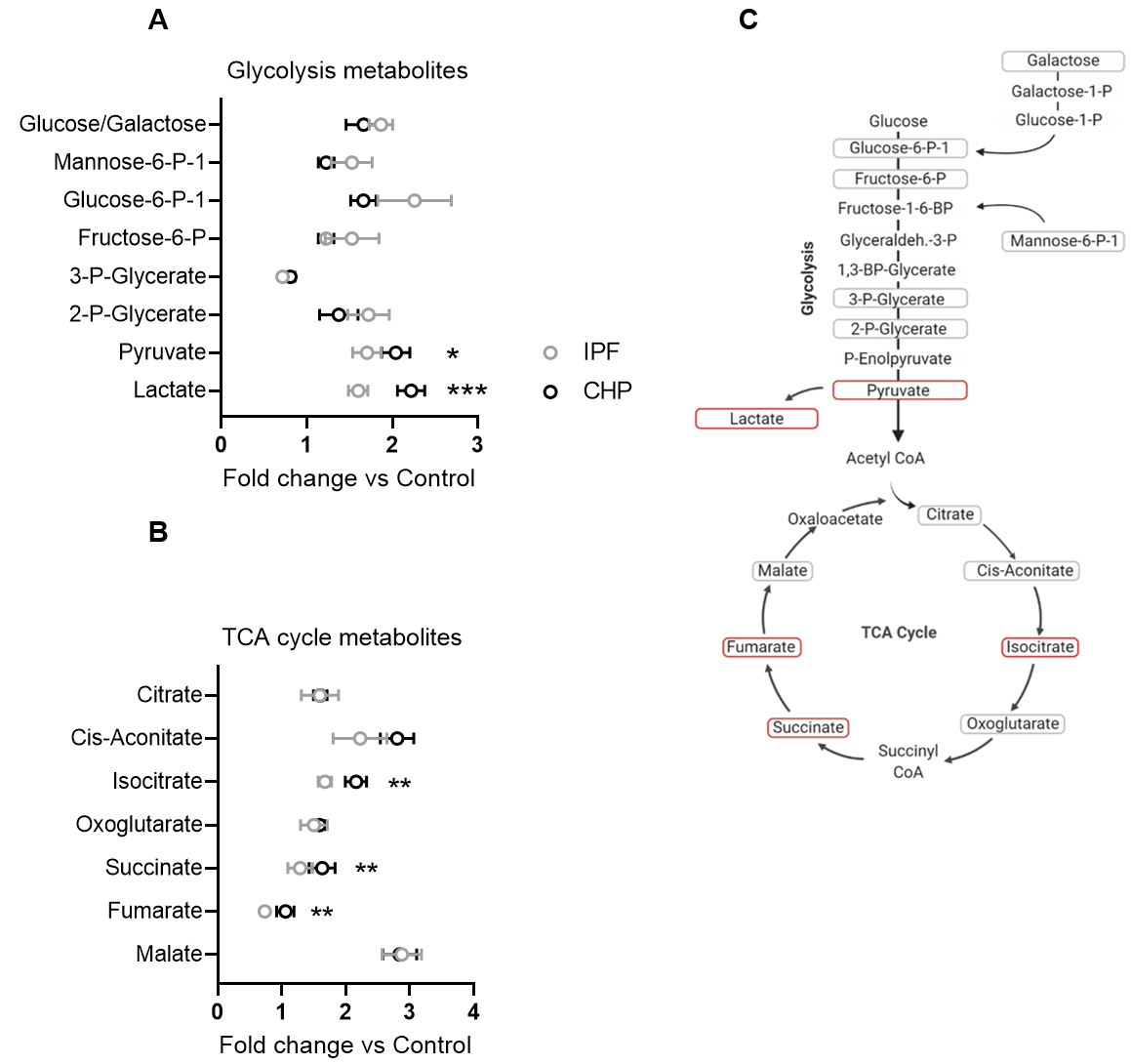

Figure 3.7. Distinct central carbon metabolites in CHP and IPF BAL supernatant. Targeted GC-MS analysis of freeze-dried BAL supernatant of IPF (n = 76) and CHP (n = 44) samples assessing glycolysis (A) and TCA cycle (B) fold change of metabolites. Shown are fold changes against control (Figure 3.5 – 3.6). C) Schematic of analysed (grey) and increased (red) metabolites. Data presented as mean ± S.E.M. Statistical significance tested by Mann Whitney U test, * $P < 0.05$, ** $P < 0.01$.

3.3.3 Correlation of BAL cells with BAL supernatant metabolites

To analyse the correlation between total BAL cell number of diverse populations and BAL supernatant metabolite concentration, a Spearman-Rank correlation text was performed on matched Control (n = 6), IPF (n = 26) and CHP (n = 15) samples. Results are shown on a scale from -1 (negative correlation, blue) to 1 (positive correlation, red), with 0 denoting no correlation (white). In IPF, numbers of neutrophils and eosinophils in BAL correlate positively with glycolysis and TCA cycle related metabolites, while AMs show a significant negative correlation with succinate (Figure 3.8 middle panel). Conversely, in the CHP samples, NK cells, NK T cells, T cells and monocytes correlated positively with glycolysis and TCA cycle related metabolites while AMs show a trend towards a negative correlation with these (Figure 3.8 right panel). These results suggest that cell types, which correlate positively with BAL supernatant metabolites (neutrophils/eosinophils in IPF and lymphocytes in CHP) may secrete these factor, while AMs, which correlate negatively with BAL supernatant metabolites do not secrete these or may even utilise these intermediates.

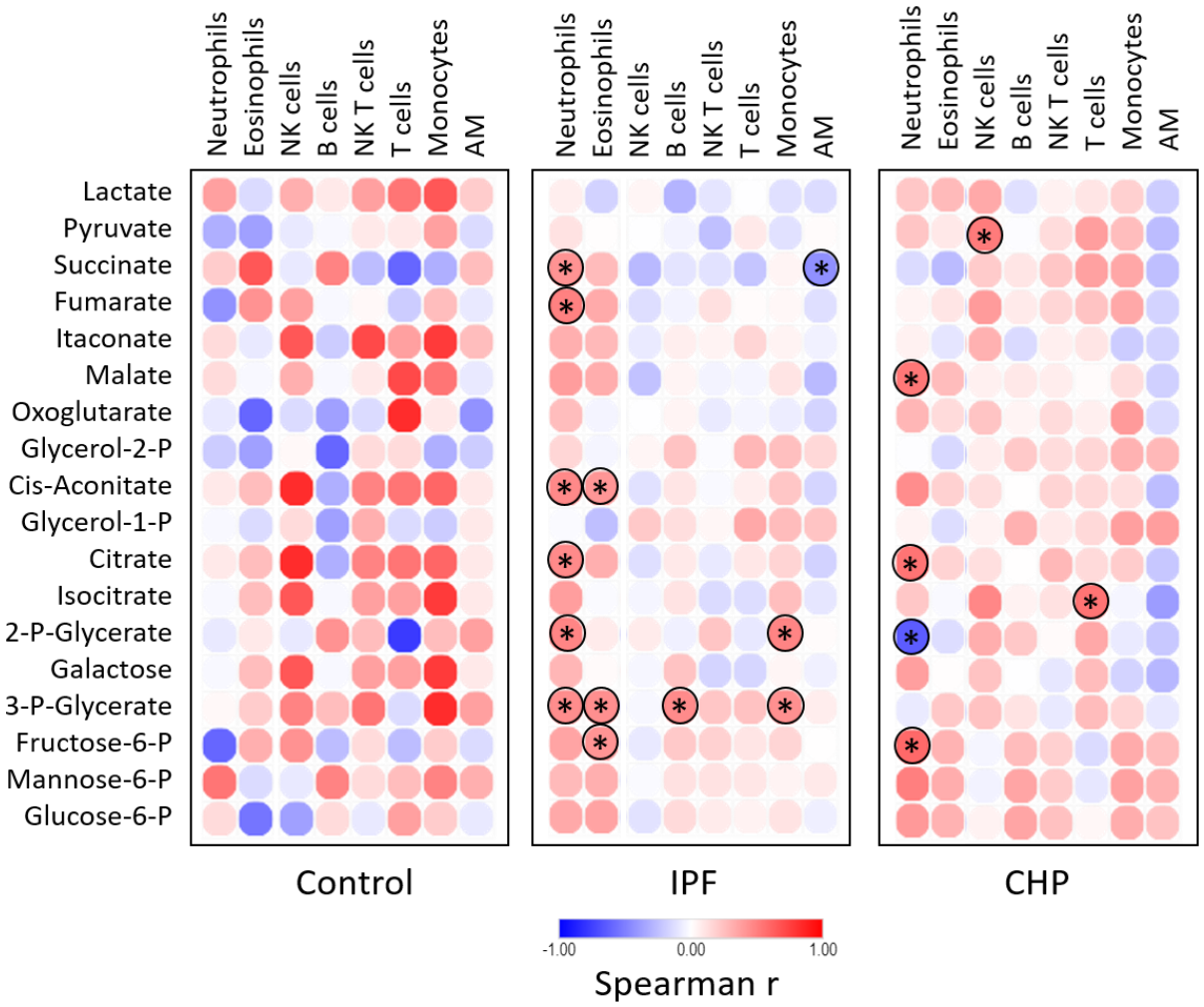

Figure 3.8. Spearman Rank correlation between BAL metabolites and immune cell populations. Spearman-Rank correlation between total BAL cells (x10^6) and BAL supernatant metabolite concentration (ng/ml). Control n = 6, IPF n = 26, CHP n = 15. Data shown as r-value of Spearman Rank correlation, positive correlation shown in red, negative correlation shown in blue, * $P < 0.05$.

3.3.4 Characterisation of macrophage phenotype

AMs make up the highest proportion of immune cells in BAL, numbers are increased even further during ILD and AMs have been suggested as key drivers of fibrotic lung disease. Human airway macrophages can be identified by auto fluorescence and expression of CD11c, HLA-DR and CD206[40]. Furthermore, CD11b is a marker for AM activation, while CD86 is primarily expressed on pro-inflammatory human macrophages[232,233] and colony-stimulating factor 1 receptor (CSF1R) is primarily expressed on pro-wound healing human macrophages[234]. To further characterise AMs in BAL of IPF and CHP patients (compared to healthy controls), single, live, $CD45^+$ cells were gated on $HLA\text{-}DR^+$, $CD11c^+$, $CD206^+$ expression to identify AMs. Of these, the geometric mean of staining intensity of CD11b and CD206 was analysed. Furthermore, proportions expressing CD86 and CSF1R were calculated and geometric mean of CD86 or CSF1R expression within $CD86^+$ or $CSF1R^+$ cells analysed (Figure 3.9).

Compared to healthy controls, both IPF and CHP BAL had decreased proportions of CD86+ AMs (Figure 3.10 A). Furthermore, proportions of total AMs expressing CSF1R were decreased in CHP both compared to healthy controls and compared to IPF AM (Figure 3.10 B). Within the $CD86^+$ and $CSF1R^+$ AM populations, intensity of marker expression however was unchanged (Figure 3. 10 C – D). Intensity of CD206 expression remained unchanged between control, IPF and CHP total AMs (Figure 3.10 E), while expression of CD11b was significantly increased on CHP total AMs (Figure 3.10 F), indicating increased activation status.

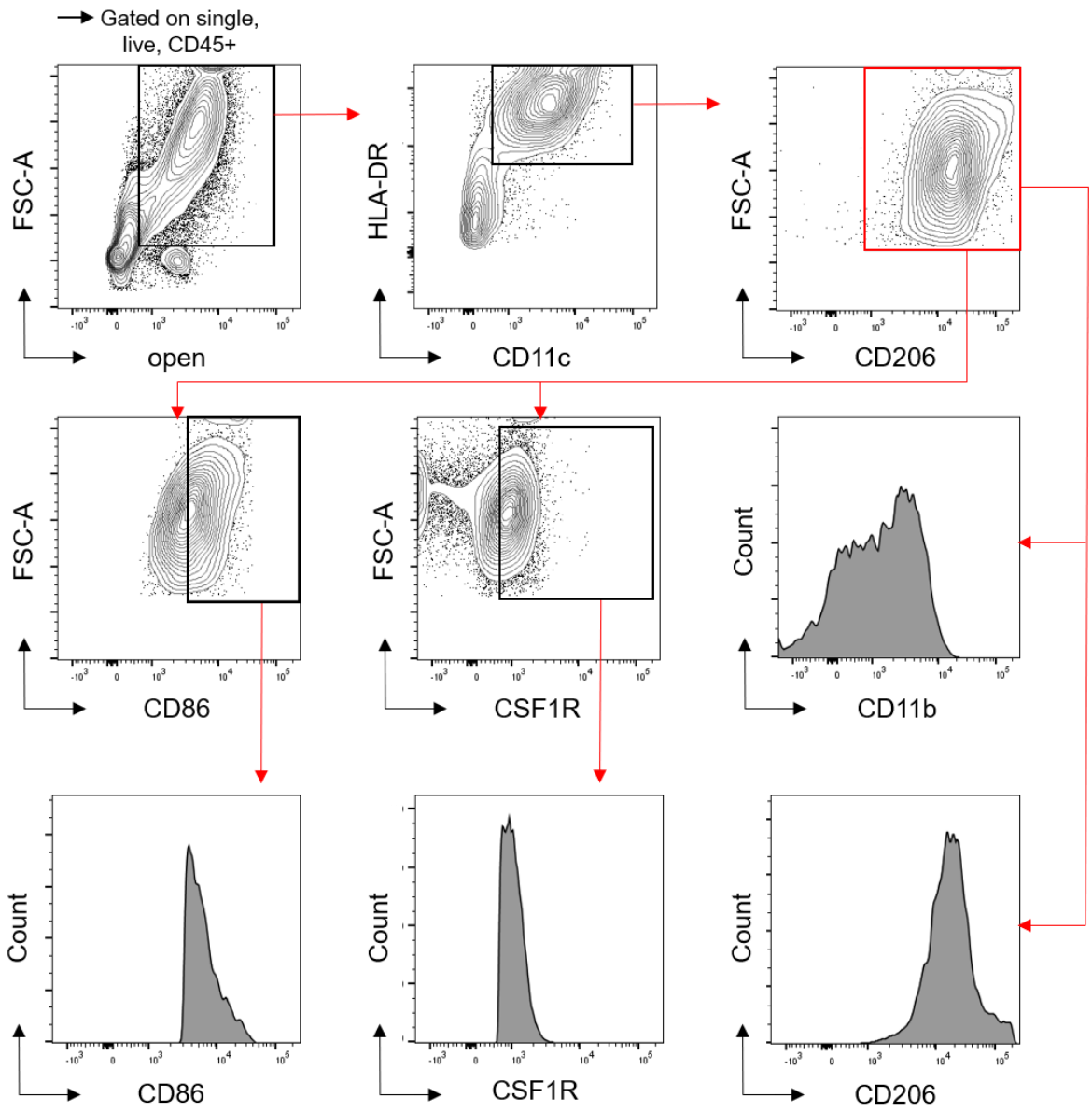

Figure 3.9. Gating strategy for human BAL macrophage characterisation. After gating out debris and doublets, live, CD45$^+$ cells were selected. AMs were identified by expression of CD11c, HLA-DR and CD206. Of these, geometric mean of CD11b and CD206 expression was analysed. Furthermore, proportions of CD86$^+$ and CSF1R$^+$ AM and their respective geometric mean of expression were calculated. Representative human flow cytometry plots for analysis of BAL.

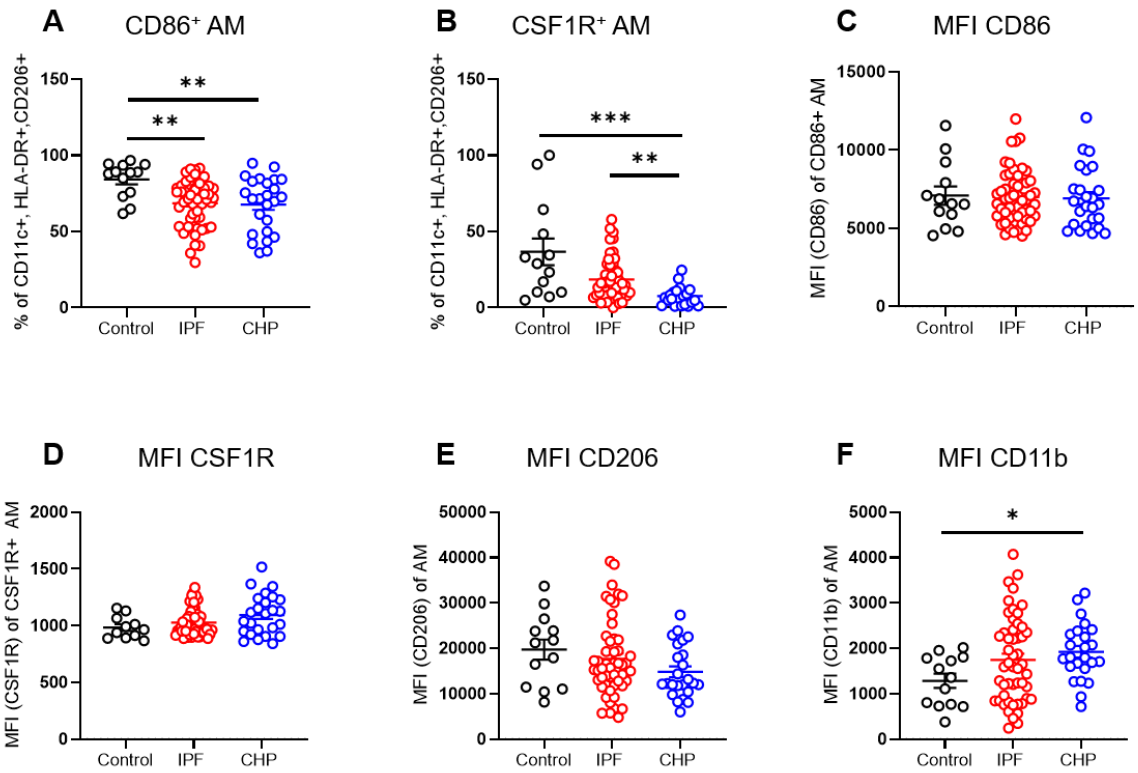

Figure 3.10. Characterisation of BAL AM by flow cytometry. A) Proportions of CD86⁺ AM of total AM as defined in Figure 3.7. B) Proportions of CSF1R⁺ AM of total AM. C) MFI of CD86 of CD86+ AM. D) MFI of CSF1R of CSF1R⁺ AM. E – F) MFI of CD206 and CD11b of total AM. MFI = Mean Fluorescent Intensity. Healthy control n = 13, IPF n = 52, CHP n = 25. Data presented as mean ± S.E.M. Statistical significance tested by One-Way ANOVA with Kruskal Wallis multiple comparison test, * $P < 0.05$, ** $P < 0.01$, *** $P < 0.005$, **** $P < 0.001$.

3.3.5 MACS sorting of CD206+ AM

To enable further analysis of AM specific metabolic and phenotypic changes during IPF and CHP, AMs were enriched using a magnetic-activated cell sorting (MACS) system. Enrichment of AMs was performed based on the expression of C-type lectin mannose receptor (CD206), which has been shown to be widely expressed on AMs during homeostasis and disease[235] and was not altered in IPF compared to healthy controls. The AM population in BAL was assessed before and after sorting by flow cytometry to analyse purity after MACS enrichment. Live, $CD45^+$ cells were gated on $CD206^+$ expression for purity analysis (Figure 3.11 A). Purity check by flow cytometry could not be performed on every sample due to low yields, but analysis of 49 samples (healthy, IPF and CHP) showed that MACS sorting enriched the AM population significantly, to an average purity of 94% (Figure 3.11 B).

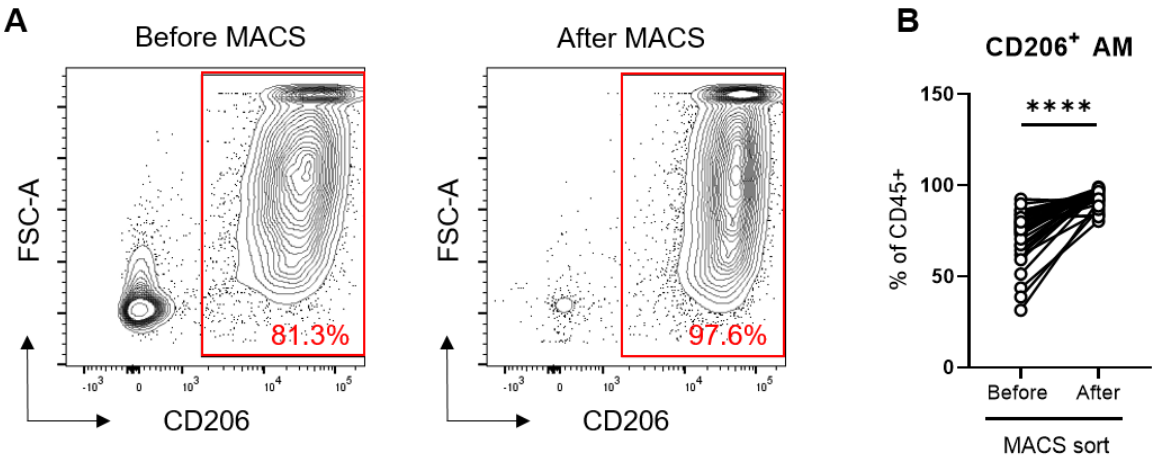

Figure 3.11. MACS enrichment of $CD206^+$ airway macrophages. A) Representative flow cytometry plots of $CD206^+$ cells before and after MACS sorting. Previously gated on single cells, live, $CD45^+$. B) Proportion of CD206+ AMs before and after MACS sort. N = 49 (healthy, IPF and CHP pooled). Data presented as mean, statistical significance tested by Mann Whitney U test, **** P < 0.001.

3.3.6 Metabolic gene expression in CD206$^+$ macrophages

To investigate the metabolic profile of CD206$^+$ AM in IPF and CHP BAL samples compared to healthy control, gene expression of 84 key metabolic enzymes was analysed using a QIAGEN metabolism targeted gene array for qPCR. The full list of genes investigated is shown in Table 2.5. Due to the small number of healthy control samples available, IPF and CHP samples were both compared to the same set of healthy control samples and are shown here separately (see Table 3.3). Heat maps were generated showing log10 of the ΔΔCT for IPF-AMs in comparison to control (Figure 3.12) or for CHP-/Control comparisons (Figure 3.14) as well as IPF compared to CHP (Figure 3.16); genes were clustered using Euclidian distance, supervised between disease groups. In IPF AMs, there was no change in gene expression of glycolysis related genes compared to healthy controls (Figure 3.13 A), while *phosphoenolpyruvate carboxykinase 2 (PCK2), oxoglutarate dehydrogenase (OGDH), isocitrate dehydrogenase 2 (IDH2), aconitase 2 (ACO2)* and *ATP citrate lyase (ACLY)* were significantly increased (Figure 3.13 B). These alterations are shown in Figure 3.13 C, which highlights that all increased gene expressions occured in the first half of the TCA cycle or in the loop feeding citrate back into glycolysis via oxaloacetate and phosphoenolpyruvate. Despite these specific alterations however, principal component analysis using the Nonlinear Iterative partial Least Squares (NIPALS) method did not result in separation of IPF and healthy control groups, when taking all 84 investigated genes into account (Figure 3.13 D).

When comparing CHP AM metabolic gene expression to healthy controls however, a different image emerged. Here, most of the investigated glycolysis or TCA cycle related genes were altered. Of the glycolysis related genes, *phosphoglycerate kinase 1 (PGK1)* was decreased in CHP AMs, while *phosphofructokinase (PFKL), hexokinase 3 (HK3), glucose-6-phosphate isomerase (GPI), galactose mutarotase (GALM), enolase 1 (ENO1), enolase 3 (ENO3)* and *fructose biphosphate aldolase (ALDOA)* were significantly increased (Figure 3.15 A). Of the TCA cycle related genes, *succinate CoA ligase 1* and *2 (SUCLG1 and SUCLG2) succinate dehydrogenase subunit C* and *D (SDHC and SDHD), malate*

dehydrogenase 1 and *subunit 1b (MDH1 and MDH1B)* and *aconitase 1 (ACO1)* were decreased, while *SDH subunit A (SDHA), PCK2, pyruvate carboxylase (PC), OGDH, IDH2, ACO2* and *ACLY* were significantly increased (Figure 3.15 B). The schematic in Figure 3.15 C highlights that most glycolysis related genes are increased as well as the first half TCA cycle genes and those feeding citrate back into glycolysis and pyruvate into oxaloacetate, while the second half TCA cycle genes are decreased. Furthermore, principal components analysis using the NIPALS method resulted in distinct clustering of CHP compared to healthy control samples when taking all 84 investigated genes into account (Figure 3.15 D).

Direct comparison of IPF and CHP AM samples showed that gene expression of glycolysis enzymes *GPI* and *ENO1* was significantly increased, while expression of *PGK* was decreased (Figure 3.17 A). Furthermore, although expression of *ACO2* was increased in IPF compared to healthy control, its expression in CHP samples was still significantly higher, as well as the succinate binding SDH subunit *SDHA*. Second-half TCA cycle gene expression however was decreased in CHP samples compared to IPF (Figure 3.17B), suggesting a break in the TCA cycle. These differences are highlighted in red in the schematic in Figure 3.17 C. Principal component analysis using the NIPALS method did not show a distinct clustering of CHP compared to IPF samples (Figure 3.17 D), which may be due heterogeneity within disease groups and the high chance of misdiagnosis of CHP.

These results suggest that increased gene expression of first half TCA cycle genes is preserved between IPF and CHP samples compared to healthy controls, while CHP AMs also show an upregulation of glycolysis gene expression together with a decrease in second half TCA cycle gene expression.

Table 3.3: Subject demographics of samples used for Gene array analysis (Figure 3.11 – 3.14)

Table showing sex, age, drug-treatment, FEV1, FEV1 % predicted, forced vital capacity (FVC), % predicted FVC, DLCO and smoking status of healthy (n = 5), IPF (n = 21) and CHP (n = 10) samples used for gene array analysis of AMs (Figures 3.11 – 3.14). Data presented as mean ± S.D.

	IPF (n = 21) Mean ± S.D.	CHP (n = 10) Mean ± S.D.	Healthy (n = 5) Mean ± S.D.
Sex (M/F)	16/5	7/3	4/1
Age	69.0 ± 9.5	62.9 ± 7.8	45.6 ± 13.7
Anti-fibrotic treatment Of which: Nintedanib Pirfenidone	43% 44% 77%	0%	N/A
FEV1	2.3 ± 0.7	2.2 ± 0.6	2.5 ± 1.1
FEV1 (predicted)	85.4 ± 19.6	78.7 ± 15.3	N/A
FVC	2.8 ± 1.0	2.7 ± 0.8	3.3 ± 1.4
FVC (predicted)	81.8 ± 19.6	77.3 ±16.7	N/A
DLCO (single breath)	4.1 ± 1.9	3.8 ± 1.1	N/A
Ever smoked Of which: Ex-smoker Current smoker	80% 100% 0%	60% 100% 0%	20% 100% 0%

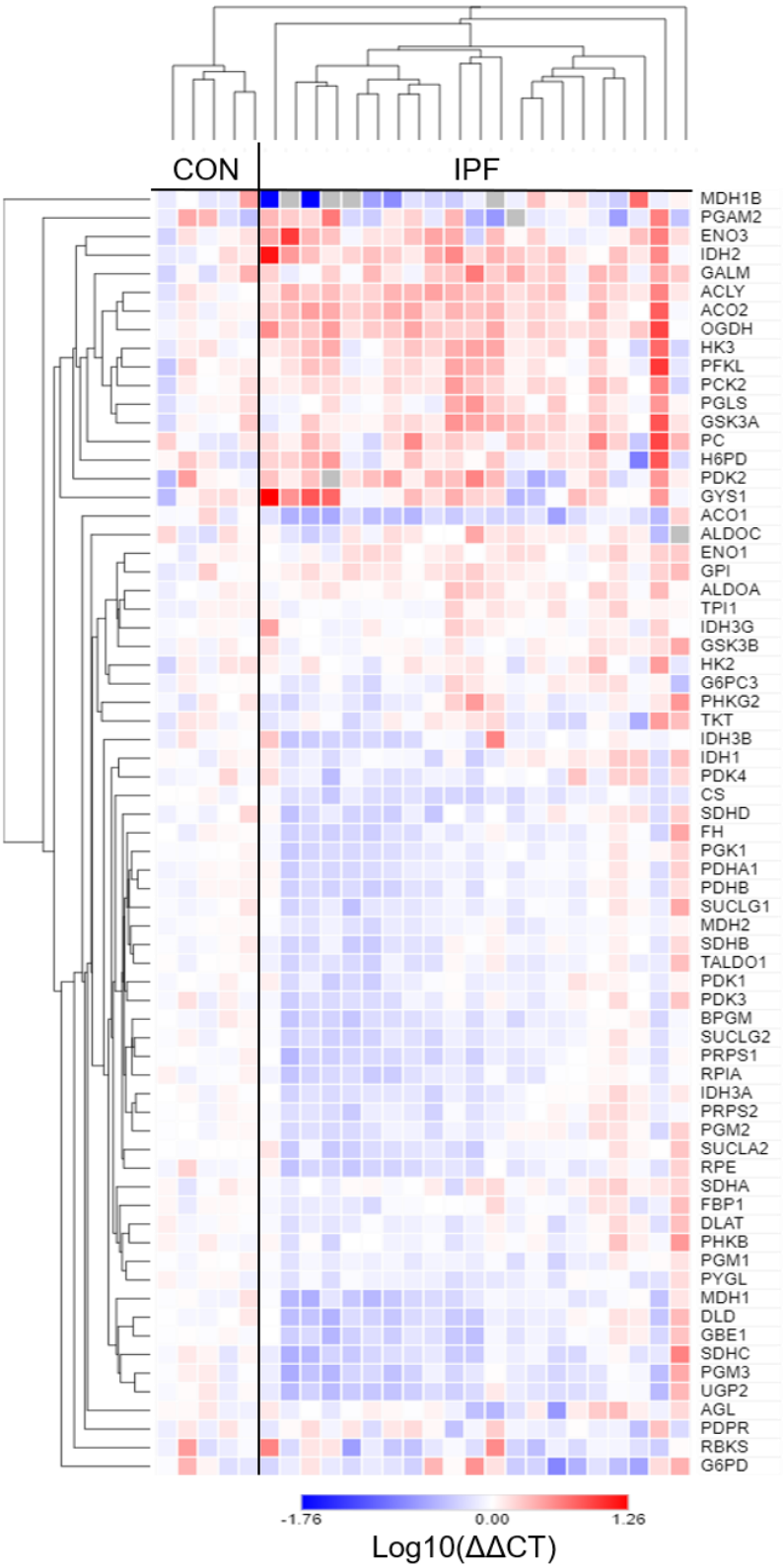

Figure 3.12. Heat map of key metabolic enzymes relative gene expression in IPF vs healthy control AM. Data shown as Log10(ΔΔCT), *ATCB* was used as housekeeping control gene. Supervised Euclidian distance clustering was performed between healthy control (n = 5) and IPF (n = 21) groups. Compared to the average of the control group, increased gene expression is shown in red, decreased gene expression is shown in blue.

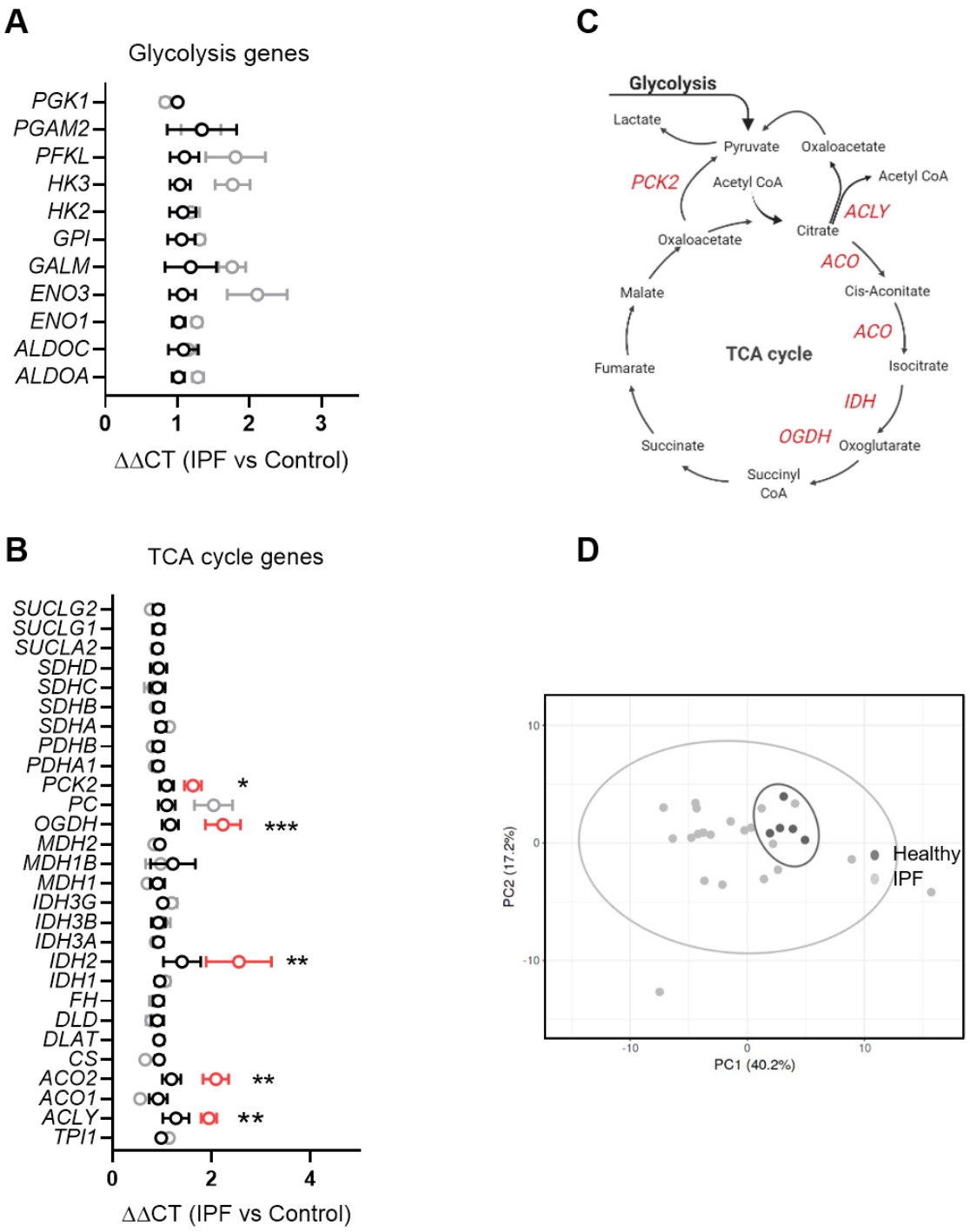

Figure 3.13. Increased gene expression of first-half TCA cycle enzymes in IPF AM. A – B) Gene expression analysis of glycolysis (A) and TCA cycle related (B) key enzymes, *ACTB* was used as housekeeping control. Data presented as mean ± S.E.M of $2^{-(\Delta\Delta CT)}$ to show relative gene expression of IPF (n = 21) compared to healthy control (n = 5). C) Schematic of significantly altered gene expression in IPF compared to healthy control AM based on analysis shown in A – B. Increased genes are shown in red. D) Principal component analysis using NIPALS method based on all 84 genes analysed (as shown in Figure 3.10). Statistical significance (A – B) tested by Mann Whitney U test, * $P < 0.05$, ** $P < 0.01$, *** $P < 0.005$.

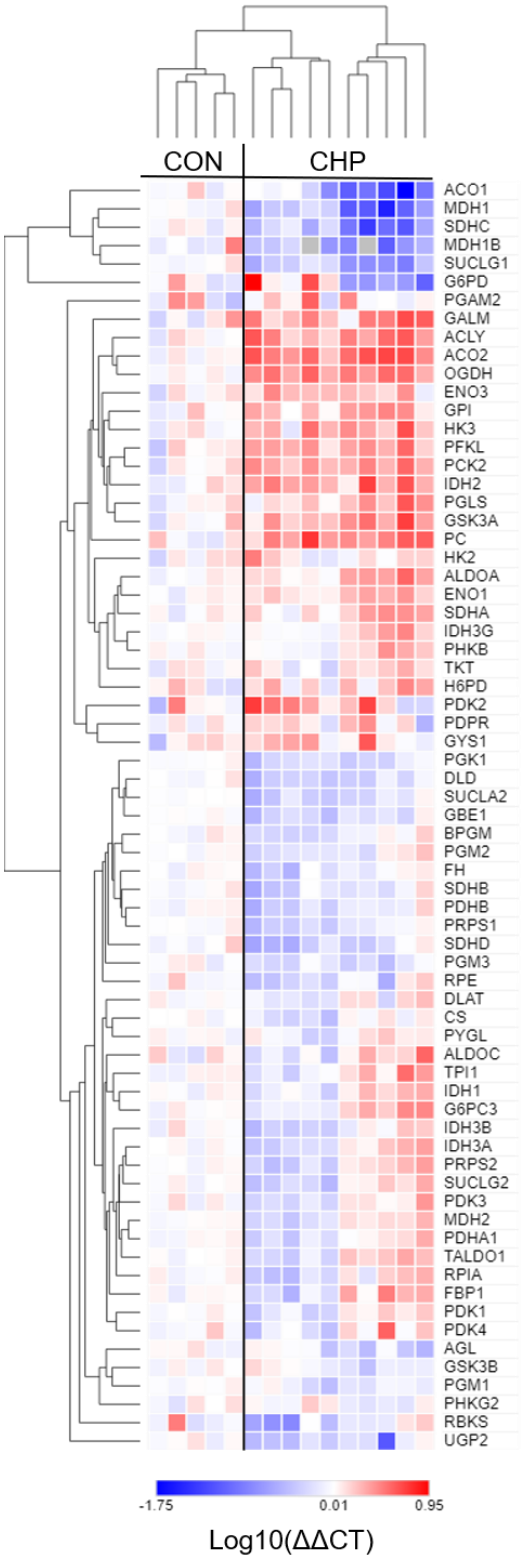

Figure 3.14. Heat map of key metabolic enzymes relative gene expression in CHP vs healthy control AM. Data shown as Log10(ΔΔCT), *ATCB* was used as housekeeping control gene. Supervised Euclidian distance clustering was performed between healthy control (n = 5) and CHP (n = 10) groups. Compared to the average of the control group, increased gene expression is shown in red, decreased gene expression is shown in blue.

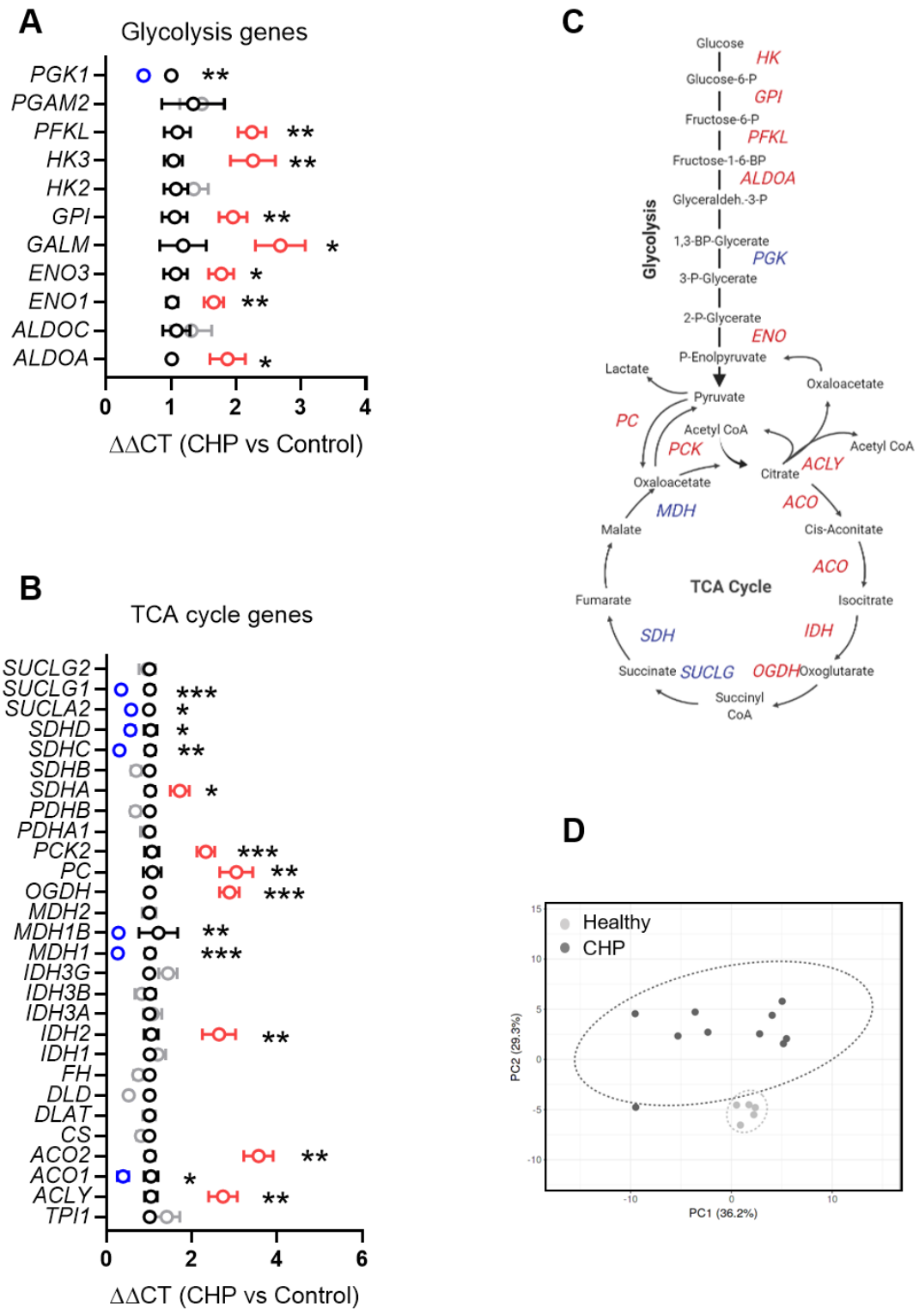

Figure 3.15. Increased gene expression of glycolysis and TCA cycle enzymes in CHP AM. A – B) Gene expression analysis of glycolysis (A) and TCA cycle related (B) key enzymes, *ACTB* was used as housekeeping control. Data presented as mean ± S.E.M of $2^{-(\Delta\Delta CT)}$ to show relative gene expression of CHP (n = 10) compared to healthy control (n = 5). C) Schematic of significantly altered gene expression in CHP compared to healthy control AM based on analysis shown in A – B. Increased genes are shown in red, decreased genes are shown in blue. D) Principal component analysis using NIPALS method based on all 84 genes analysed (as shown in Figure 3.13). Statistical significance (A – B) tested by Mann Whitney U test, * P < 0.05, ** P < 0.01, *** P < 0.005.

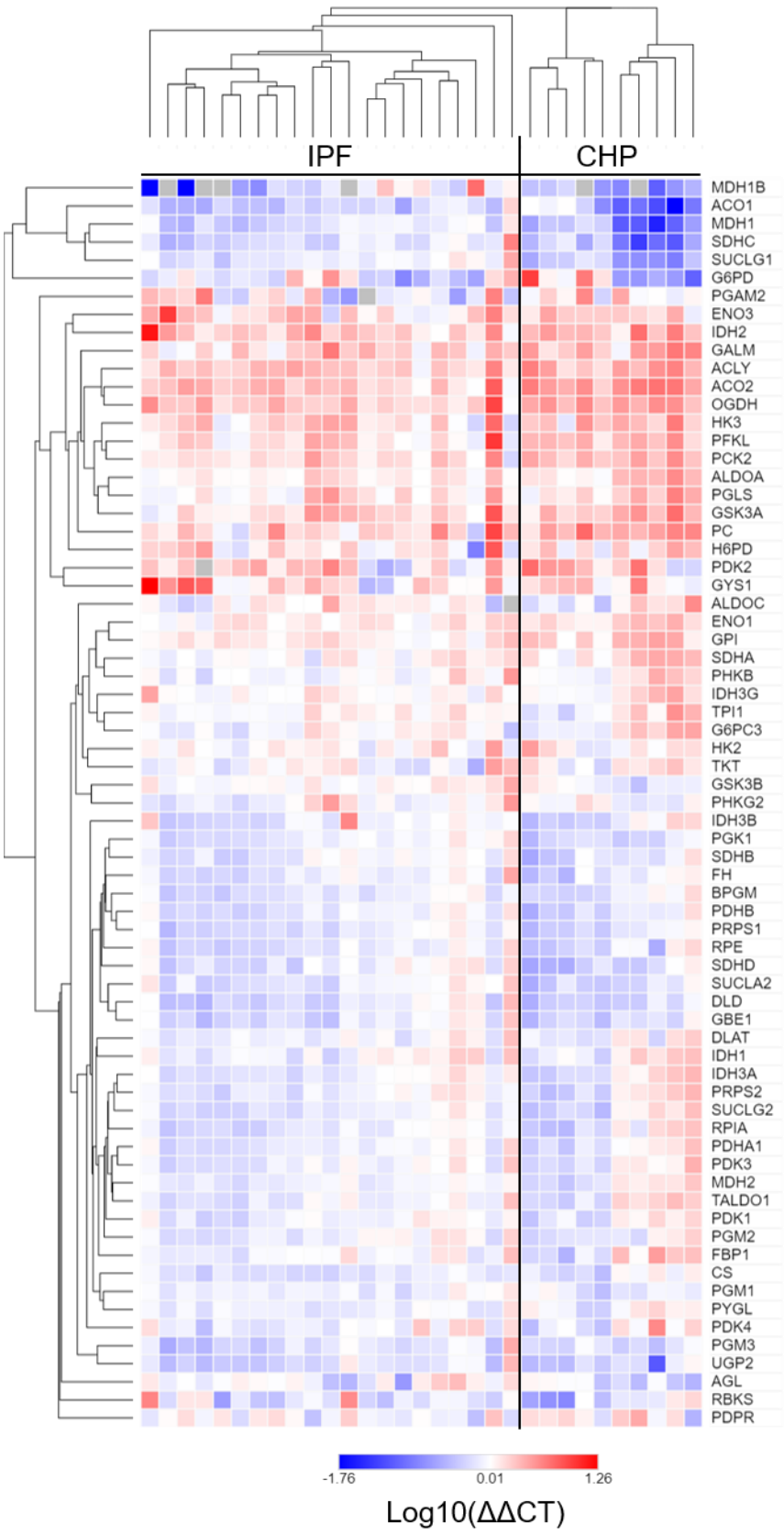

Figure 3.16. Heat map of key metabolic enzymes relative gene expression in CHP vs IPF AM. Data shown as Log10(ΔΔCT), *ATCB* was used as housekeeping control gene. Supervised Euclidian distance clustering was performed between IPF (n = 21) and CHP (n = 10) groups. Compared to the average of the control group, increased gene expression is shown in red, decreased gene expression is shown in blue.

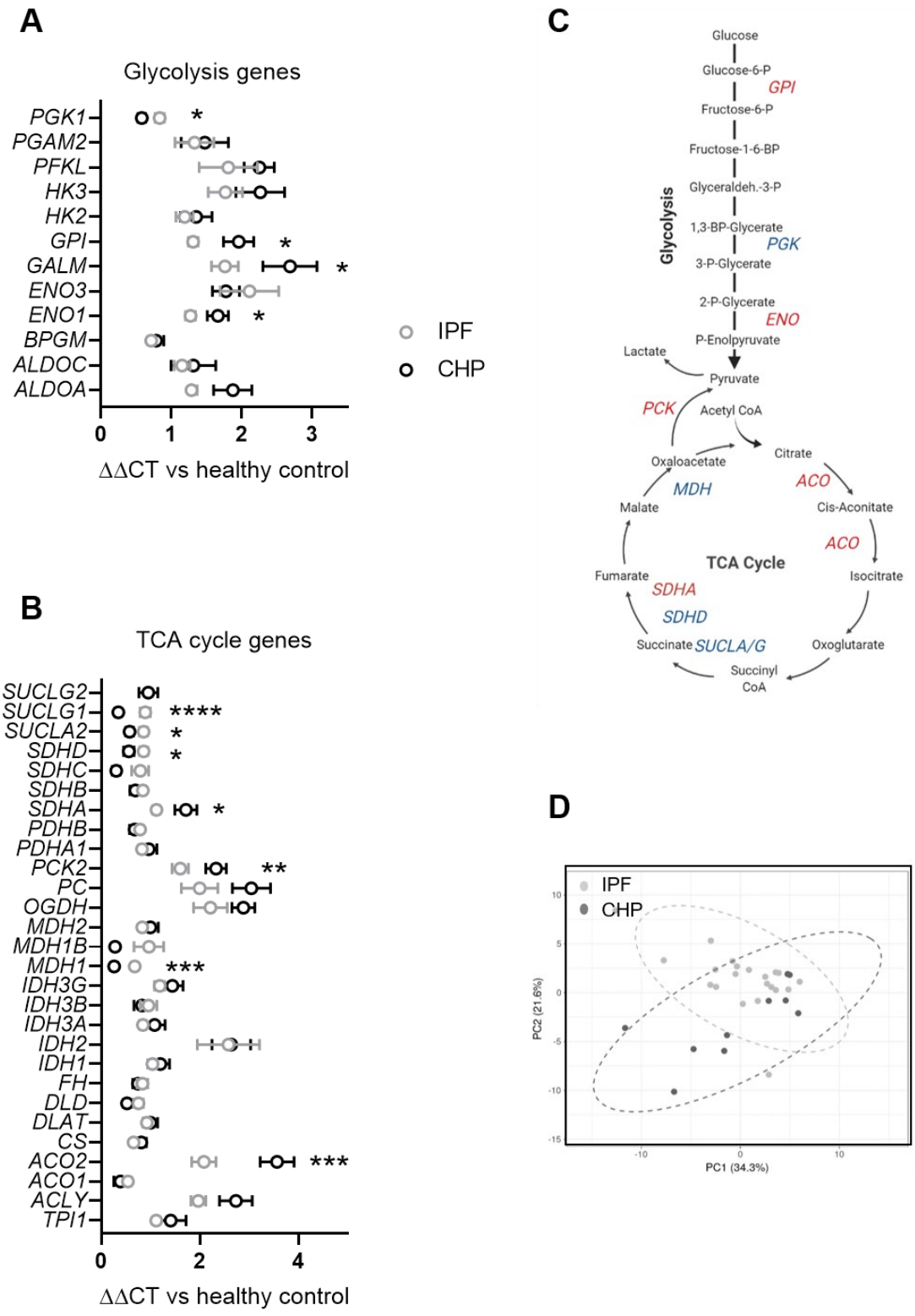

Figure 3.17. Distinct gene expression of glycolysis and TCA cycle enzymes in CHP and IPF AM. A – B) Gene expression analysis of glycolysis (A) and TCA cycle related (B) key enzymes, *ACTB* was used as housekeeping control. Data presented as mean ± S.E.M of $2^{-(\Delta\Delta CT)}$ to show relative gene expression of CHP (n = 10) and IPF (n = 20) compared to healthy controls (not shown, see Figure 3.12 and 3.14). C) Schematic of significantly altered gene expression in CHP compared to IPF AM based on analysis shown in A – B. Increased genes are shown in red, decreased genes are shown in blue. D) Principal component analysis using NIPALS method based on all 84 genes analysed (as shown in Figure 3.15). Statistical significance (A – B) tested by Mann Whitney U test, * P < 0.05, ** P < 0.01, *** P < 0.005, **** P < 0.001.

3.3.7 Glycolytic and OXPHOS capacity is altered in CHP CD206^{+} AM

Next, the metabolic phenotype of CD206^{+} AMs was investigated in IPF and CHP patients and compared to healthy controls (see Table 3.4) using Seahorse assays. Seahorse mitochondrial stress test was used to assess OXPHOS, while the Seahorse glycolytic stress test was used to analyse glycolytic function.

Using this assay on 8 healthy control and 12 IPF samples, no significant difference in baseline ECAR, OCR or derived parameters could be detected between IPF and healthy controls (Figure 3.18). As previous experiments showed an increase in gene expression of first-half TCA cycle enzymes in IPF, these might not be sufficient to translate into global metabolic reprogramming.

CD206+ AM from CHP patients did however show increased metabolic activity compared to healthy controls. Using the same controls as for the comparison with IPF (n = 8) and 3 CHP samples, the mitochondrial stress test showed that CHP AM have a significantly increased ECAR baseline (Figure 3.19 C) and maximal OXPHOS respiration capacity (Figure 3.19 D) compared to healthy controls. Furthermore, basal OXPHOS respiration, non-mitochondrial respiration and ATP production showed a trend towards an increase in CHP. However, the variation for these parameters was quite high. Taking the gene expression data shown in Figure 3.15 into account, these results suggest that when gene expression of glycolysis as well as first half TCA cycle enzyme genes is increased, this is also mirrored by increases in overall OXPHOS capacity, but this does not seem to be impacted by the decrease in second half TCA cycle gene expression.

Comparing IPF to CHP samples (Figure 3.20) showed increased maximal respiration capacity (Figure 3.20 D), basal OCR (Figure 3.20 F) and ATP production in CHP AMs (Figure 3.20 H), as well as increased proton leak (Figure 3.20 I), in comparison to IPF. These results confirm increased OXPHOS capacity of CHP AMs, compared to IPF samples.

Table 3.4: Subject demographics of samples used for Seahorse Mito Stress Test analysis (Figure 3.18 – 3.19)

Table showing sex, age, drug-treatment, FEV1, FEV1 % predicted, forced vital capacity (FVC), % predicted FVC, DLCO and smoking status of healthy (n = 8), IPF (n = 12) and CHP (n = 3) samples used for mitochondrial stress test analysis of AMs (Figures 3.18 – 3.19). Data presented as mean ± S.D.

	IPF (n = 12) Mean ± S.D.	CHP (n = 3) Mean ± S.D.	Healthy (n = 8) Mean ± S.D.
Sex (M/F)	5/7	0/3	5/3
Age	69.5 ± 7.5	59 ± 6.5	48.5 ± 13.7
Anti-fibrotic treatment Of which: Nintedanib Pirfenidone	25% 33% 67%	67% 0% 100%	N/A
FEV1	2.3 ± 0.7	1.6 ± 0.3	2.7 ± 0.7
FEV1 (predicted)	94.8 ± 14.4	86.4 ± 8.6	N/A
FVC	2.8 ± 1.0	2.0 ±0.4	3.4 ± 0.9
FVC (predicted)	89.3 ± 13.7	88.8 ± 9.8	N/A
DLCO (single breath)	4.2 ± 1.8	3.2 ± 0.6	N/A
Ever smoked Of which: Ex-smoker Current smoker	58% 100% 0%	33% 100% 0%	

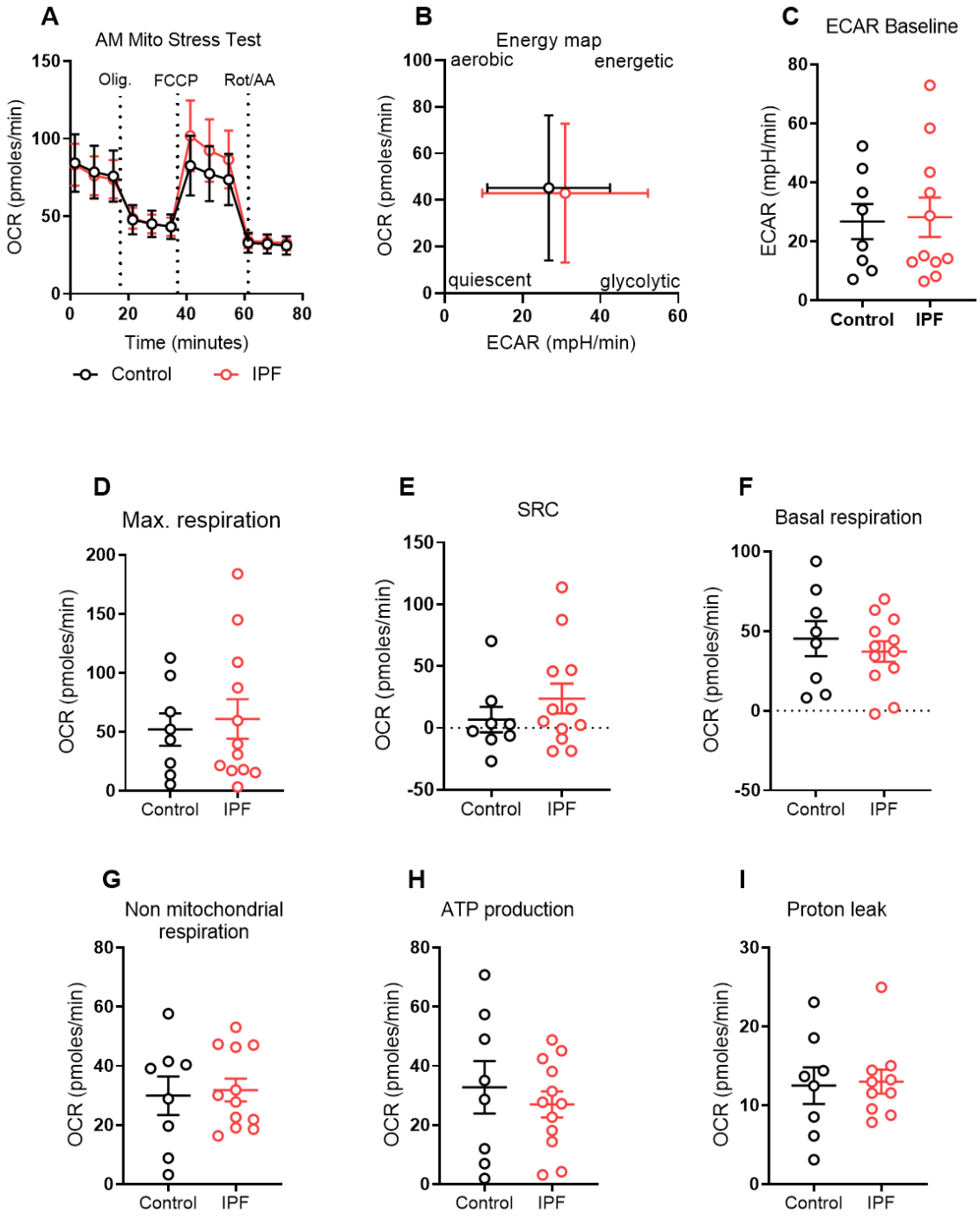

Figure 3.18. Respiratory capacity is unaltered in IPF AMs compared to healthy. Mitochondrial stress test of healthy (n = 8) and IPF (n = 12) BAL AM; assessed after injection of Oligomycin, FCCP and Rotenone/Antimycin A. 150 000 MACS-sorted CD206^{+} AM were plated on Cell-Tak coated plates. A) Analysis of oxygen consumption rate (OCR). B) Energy map of healthy and IPF AM showing four energy states: quiescent, energetic, aerobic, and glycolytic. C) Maximal respiration, defined as the maximal oxygen consumption rate after FCCP injection. D) Spare respiratory capacity (SRC), defined as subtraction of basal from maximal OCR. E) Basal respiration, defined as subtraction of non-mitochondrial oxygen consumption from basal respiration. F) Non-mitochondrial oxygen consumption, defined as oxygen consumption rate after injection of rotenone/antimycin A. G) ATP production, defined as subtraction of proton leak from basal respiration. H) Proton leak, defined as oxygen consumption rate after injection of oligomycin, after subtraction of non-mitochondrial oxygen consumption. Data presented as mean ± S.E.M. Significance tested by Mann Whitney U test.

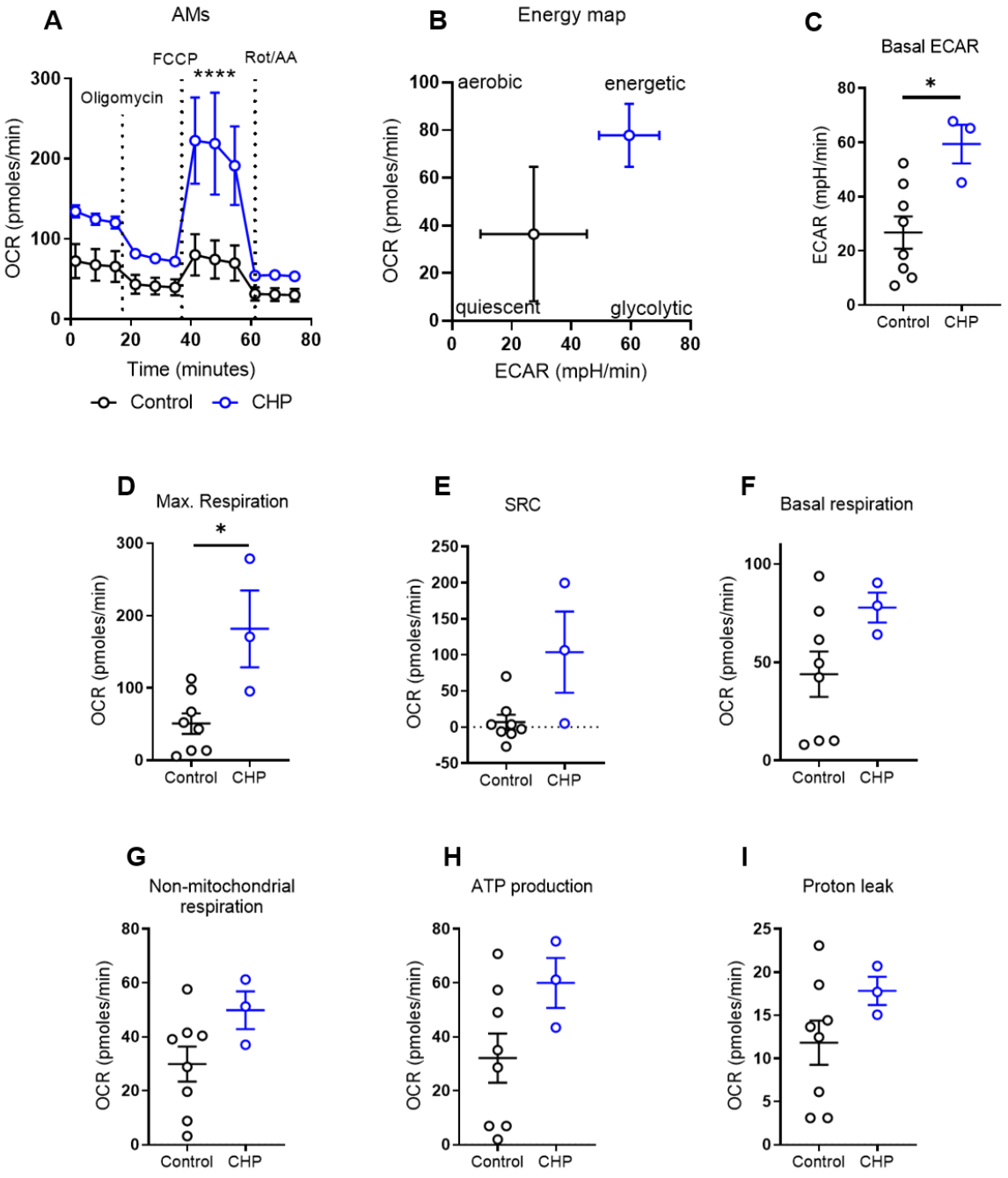

Figure 3.19. Respiratory capacity is increased in CHP AMs compared to healthy. Mitochondrial stress test of healthy (n = 8) and CHP (n = 3) BAL AM; assessed after injection of Oligomycin, FCCP and Rotenone/Antimycin A. 150 000 MACS-sorted CD206^{+} AM were plated on Cell-Tak coated plates. A) Analysis of OCR. B) Energy map of healthy and CHP AM C) Maximal respiration D) Spare respiratory capacity E) Basal respiration. F) Non-mitochondrial oxygen consumption G) ATP production H) Proton leak. Data presented as mean ± S.E.M. Significance tested by Mann Whitney U test, * $P < 0.05$.

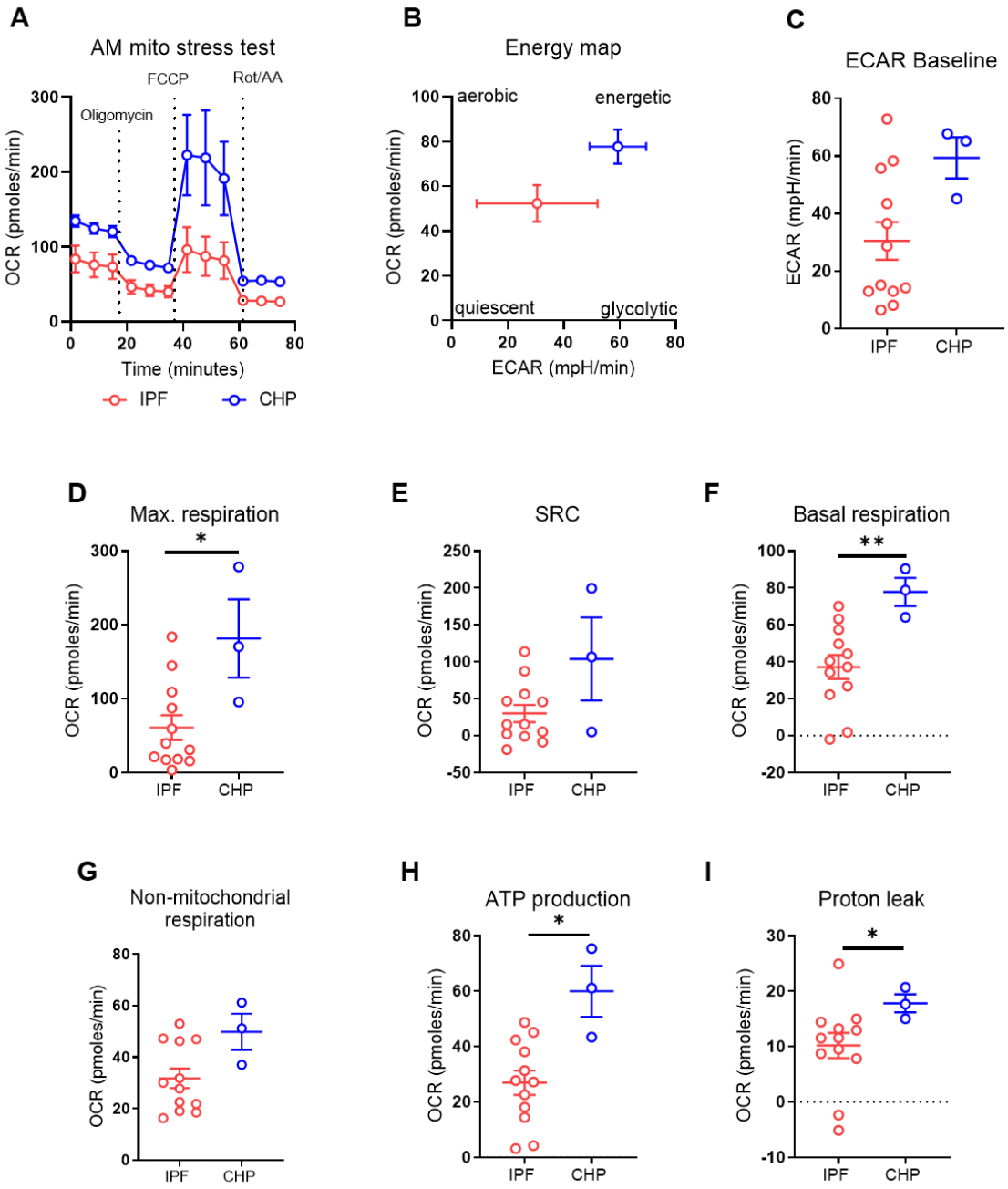

Figure 3.20. OXPHOS is increased in CHP AMs compared to IPF. Mitochondrial stress test of IPF (n = 12) and CHP (n = 3) BAL AM; assessed after injection of Oligomycin, FCCP and Rotenone/Antimycin A. 150 000 MACS-sorted CD206⁺ AM were plated on Cell-Tak coated plates. A) Analysis of OCR. B) Energy map of healthy and CHP AM C) Maximal respiration D) Spare respiratory capacity E) Basal respiration. F) Non-mitochondrial oxygen consumption G) ATP production H) Proton leak. Data presented as mean ± S.E.M. Significance tested by Mann Whitney U test, * $P < 0.05$, ** $P < 0.01$.

3.3.8 No change in glycolytic capacity in IPF CD206$^+$ AM

A glycolytic stress test was performed on 6 healthy control and 5 IPF CD206$^+$ AM samples, however, like the mitochondrial stress test no significant differences could detected in any of the measured parameters (Figure 3.21). Unfortunately, we could not recruit sufficient CHP patients for a powered analysis of CHP-AM metabolic phenotype by this assay.

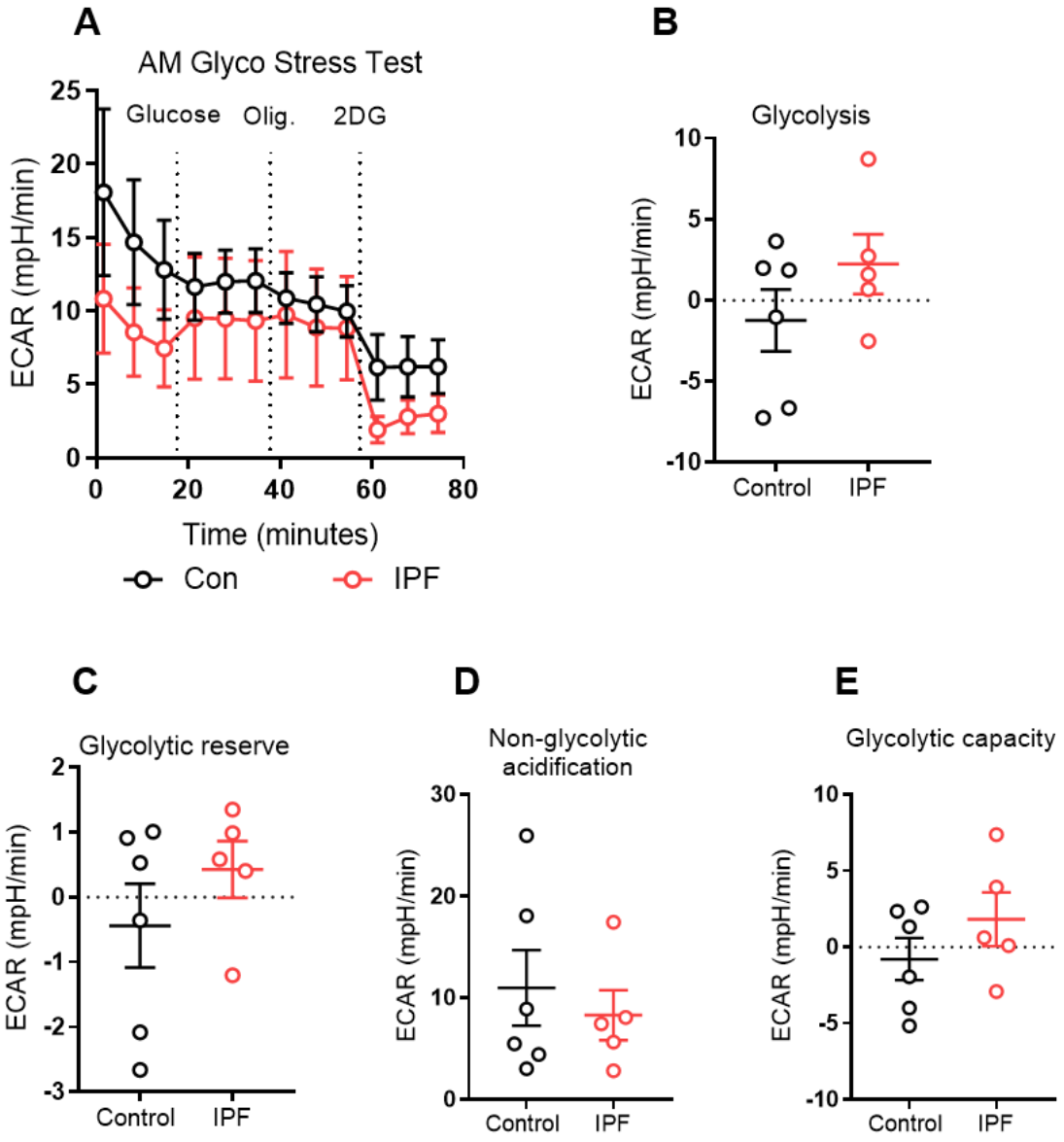

Figure 3.21. Unaltered glycolytic capacity in IPF AM. Glycolytic stress test of healthy (n = 6) and IPF (n = 5) BAL AM; assessed after injection of glucose, oligomycin and 2-deoxy-glucose (2DG). 150 000 MACS-sorted CD206$^+$ AM were plated on Cell-Tak coated plates. A) Analysis of extracellular acidification rate (ECR). B) Glycolysis C) Glycolytic reserve D) Non-glycolytic acidification E) Glycolytic capacity. Data presented as mean ± S.E.M. Significance tested by Mann Whitney U test.

3.3.9 Targeted GC-MS analysis of CD206+ macrophages

Finally, the expression of metabolites involved in glycolysis and OXPHOS was analysed in MACS sorted $CD206^{+}$ AM using a similar targeted GC-MS approach as described in 3.3.2 for the analysis of BAL supernatant. Of the 20 metabolites investigated (marked in grey in Figure 3.22 C and D), only four reached detectable levels. These were mannose-6-phosphate, glucose-6-phosphate-1, 2-phosphoglycerate and fumarate. While there was a trend for increased accumulation of these four metabolites in both IPF (Figure 3. 22 A) and CHP (Figure 3.22 B) compared to control, only 2-phosphoglycerate and fumarate were statistically significant; further CHP samples are necessary to achieve a sufficiently powered analysis.

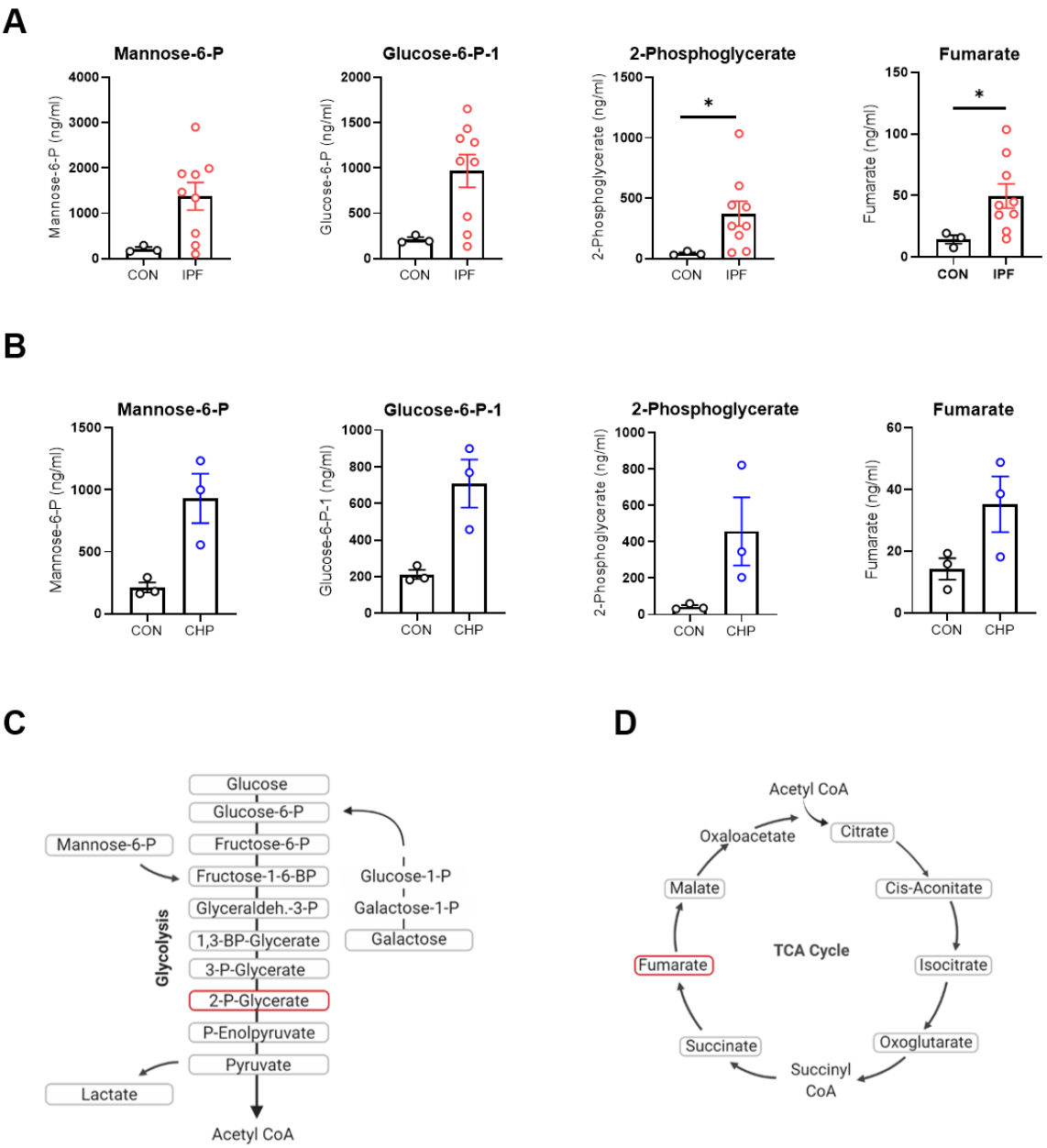

Figure 3.22. Specific increase of metabolites in IPF AM. A - B) Metabolites measured by targeted GC-MS in IPF (n = 9), CHP (n = 3) and healthy control (n = 3) CD206⁺ AM. C – D) Schematics of glycolysis (C) and TCA cycle (D) indicating significant changes in red. Data presented as mean ± S.E.M. Statistical significance tested by Mann Whitney U test, * $P < 0.05$.

3.3.10 Correlation between metabolic signature and lung function in IPF and CHP

To investigate the relationship between the distinct metabolic signature in IPF/CHP airway macrophages/BAL and lung function, the following Spearman Rank correlations were performed against lung function parameters forced expiratory volume in one second (FEV_1), FEV_1 percent predicted, forced vital capacity (FVC), FVC percent predicted and diffusing capacity of lung carbon monoxide (D_{LCO}):

1. The relative gene expression of metabolic enzymes in IPF and CHP AMs compared to *ACTB* as measured by gene array (3.3.6)
2. Metabolic parameters of IPF AMs measured by Seahorse mitochondrial stress test (3.3.7)
3. BAL metabolite content in IPF and CHP measured by targeted GC-MS (3.3.2)

Spearman Rank correlation between relative gene expression and lung function parameters yielded several significant correlations in the IPF dataset (n = 21). In the glycolysis pathway, *HK3* correlated negatively with FEV_1, FVC and D_{LCO}, while *PFKL* showed significant negative correlation to D_{LCO} (Figure 3.23 A). Within the TCA cycle, first half TCA cycle genes *ACO1, IDH1* and *SUCLA2* correlated positively with lung function parameters. Furthermore, several components of pyruvate metabolism correlated to lung function. While *dihydrolipoamide dehydrogenase (DLD),* a component of the pyruvate dehydrogenase and *pyruvate dehydrogenate kinase (PDK)*, which inactivates pyruvate kinase, correlated positively with lung function parameters, *pyruvate dehydrogenase phosphatase regulatory subunit (PDPR)* was negatively correlated with FEV_1 (% predicted) and FVC (% predicted, Figure 3.23 A). Of the genes which were significantly altered in IPF AM compared to healthy controls (as shown in section 3.3.6), only *ATP citrate lyase* (*ACLY*) and *phosphoenolpyruvate carboxykinase 2 (PCK2)* also showed a significant correlation with lung function. Both ACLY and *PCK2* were increased in IPF AMs compared to healthy controls and show a negative correlation to D_{LCO} as well as FEV_1 and FVC (*ACLY* only) (Figure 3.23 B – C). ATP citrate lyase converts citrate to either acetyl CoA as the first step

of fatty acid synthesis, or into oxaloacetate. *PCK2* converts oxaloacetate into phosphoenolpyruvate, which feeds back into glycolysis. Increased expression of both *ACLY* and *PCK2* in IPF AMs suggests that excess citrate is converted back into phosphoenolpyruvate to feed back into glycolysis and supply more pyruvate, which correlates with decline in lung function in IPF patients. However, when dividing the IPF cohort into $ACLY^{high/low}$ expressers or $PCK2^{high/low}$ expressers, there was no difference in survival (Figure 3.23 D – E).

While more genes were altered in the CHP dataset compared to controls than in the IPF dataset, fewer genes correlated with alterations in lung function parameters. In CHP, *ENO3* correlated negatively with FVC % predicted and *SDHD* correlated negatively with FEV_1, while *PDPR* correlated positively with FEV_1 and FVC. The low number of genes correlating with changes in lung function parameters might be due to the small sample size (n = 10) on the CHP dataset.

Equally, the IPF dataset for Seahorse metabolic parameters contained only n = 11 and did not yield any significant correlation to lung function parameters (Figure 3.24 A), while no correlation test could be performed for the CHP Seahorse parameters, as the sample size was only n = 3.

Correlating the BAL metabolite content measured by targeted GC-MS with lung function parameters showed a negative correlation between BAL lactate, succinate or 2-oxoglutarate and FEV1 % predicted in the IPF dataset (n = 70), while lactate also showed a negative correlation with FVC % predicted (Figure 3.24 B). However, no significant correlations were found in the CHP BAL metabolite dataset (n = 39, Figure 3.24 B).

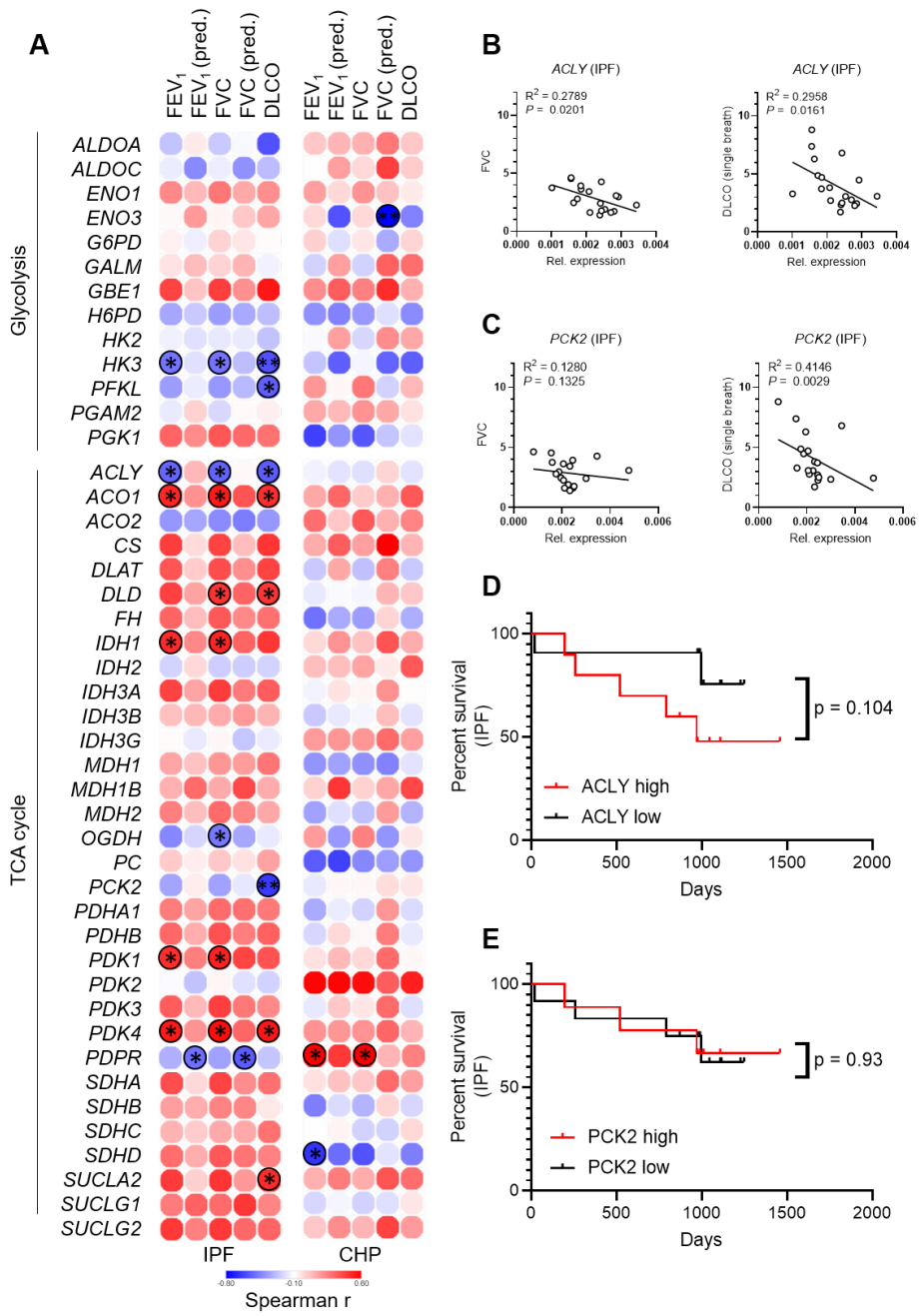

Figure 3.23. Correlation between altered metabolic gene expression in AM and lung function in IPF and CHP. A) Spearman Rank correlation between gene expression relative to *ACTB* (ΔΔCT) of metabolic genes in IPF (n = 21) or CHP (n = 10) AM assessed by gene array (Figures 3.11 – 3.14) and lung function parameters FEV_1, FEV_1 (% predicted), FVC, FVC (% predicted), DLCO. Positive correlation is shown in red, negative correlation in blue. B - C) Spearman Rank correlation between ACLY (B) or PCK2 (C) gene expression in IPF AM (n = 19) and FVC or DLCO. gene expression in IPF AM and FVC or DLCO. D) Survival analysis of IPF patients (n = 21) split into ACLY-high and ACLY-low expressing groups. E) Survival analysis of IPF patients (n = 21) split into PCK2-high and PCK2-low expressing groups. Statistical significance was tested by Spearman Rank correlation (A – C) or Gehan-Breslow-Wilcoxon test (D – E), * $P < 0.05$, ** $P < 0.01$. FEV_1 = forced expiratory volume in 1 second, FVC = forced vital capacity, DLCO = diffusing capacity of lung carbon monoxide.

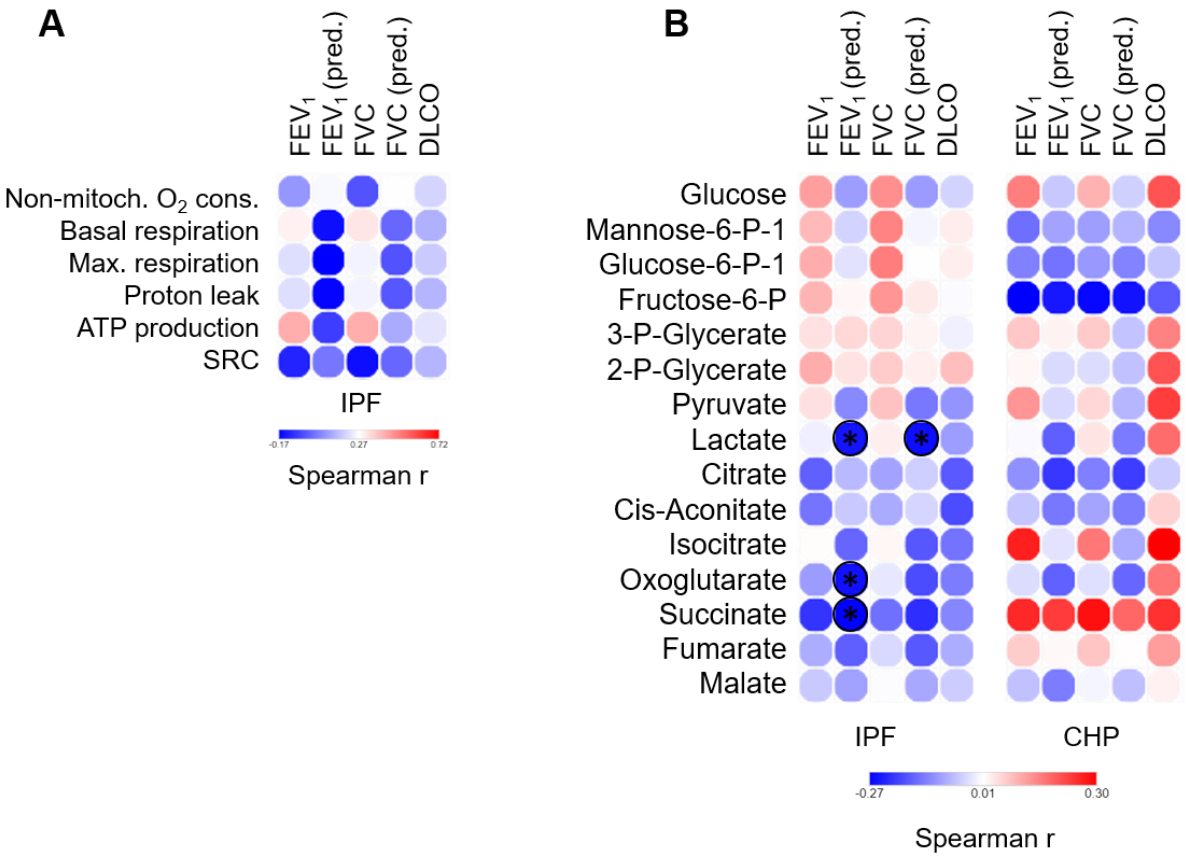

Figure 3.24. Correlation of AM metabolic activity and BAL metabolite content with lung function parameters. A) Spearman Rank correlation between metabolic parameters measured by Seahorse mitochondrial stress test in IPF AM (n = 11, Figure 3.15) and lung function parameters FEV_1, FEV_1 (% predicted), FVC, FVC (% predicted), DLCO. B) Spearman Rank between metabolite content in IPF (n = 70) or CHP (n = 39) BAL measured by targeted GC-MS (Figure 3.5 – 3.6) and lung function parameters FEV_1, FEV_1 (% predicted), FVC, FVC (% predicted), DLCO. Statistical significance was tested by Spearman Rank correlation, * $P < 0.05$. Positive correlation is shown in red, negative correlation in blue.

3.3.11 Rewiring AM fibrotic phenotype by treatment with metabolic inhibitors

To investigate the role of specific metabolic pathways, for pro-fibrotic AM phenotype during CHP and IPF, $CD206^+$ sorted AMs were incubated *ex vivo* with either 25mM 2DG (inhibits glycolysis), 100 μM UK5099 (inhibits mitochondrial pyruvate transport), 200 μM Etomoxir (inhibits fatty acid oxidation) or 250 μM DON (glutamine antagonist) and compared to a medium control. Gene expression of fibrosis effector and macrophage phenotype genes was assessed by qPCR and presented relative to the expression of *ACTB.*

In CHP AMs, the expression of fibrosis effector genes *CCL-2, CCL-18, IL-10*, *MMP-1, MMP-9, MMP-12* and *IL-1β* was analysed. A Wilcoxon matched-pairs signed rank test was performed between the treated and untreated groups, however no significant differences could be detected with the limited sample size of n = 3. Upon inhibition of glycolysis, trends were an increased expression of *CCL-18* and decreased expression of *CCL-2* and *IL-1β* (Figure 3.25 A). Inhibition of pyruvate transport into the mitochondria and fatty acid oxidation both resulted in trends towards an increased expression of *IL-1β* and *CCL-18*, while expression of *CCL-2* was decreased (Figure 3.25 B and C). Inhibition of the glutamine pathway did not alter expression of *CCL-2*, while again *IL-1β* was increased.

In the IPF samples, the following genes were analysed. *CCL-2, -18* and *-22*, which recruit monocytes, adaptive immune cells and T-regs, respectively. *MMP-1* (collagenase), *MMP-2* (Gelatinase A), *MMP-7* (matrilysin), *MMP-9* (Gelatinase B) and *MMP-12* (Elastase), which collectively break down extracellular matrix components such as collagens type I – V, fibronectin and elastin. The anti-inflammatory cytokine *IL-10* and pro-inflammatory cytokine *IL-1β*. The macrophage phenotype markers *CD86, IRF5* (pro-inflammatory AM) and *CD163* (anti-inflammatory) as well as expression of the transferrin receptor *CD71*. The experiment was better powered in the IPF group as samples from 12 patients were analysed and statistical significance was determined by a Wilcoxon matched-pairs signed rank test between treated and untreated groups.

Upon treatment with the glycolysis inhibitor 2DG, *CCL-18* was significantly increased, while gene expression of *CCL-2, CCL-22, MMP-1, MMP-7, MMP-9, MMP-12, IL-10, IL-1β* and *CD71* were decreased (Figure 3.26 A). Treatment with UK5099, an inhibitor of mitochondrial pyruvate transport, resulted in increased expression of *MMP-1* and *CCL-22* and decreased gene expression *of CCL-2, MMP-7* and *CD163* (Figure 3.26 B). Inhibition of fatty acid oxidation by treatment with Etomoxir resulted in increased expression of pro-inflammatory genes *CCL-18, MMP-2* and pro-inflammatory *interferon regulatory factor 5 (IRF5),* while expression of *CCL-2, MMP-12* and anti-inflammatory *IL-10* was decreased (Figure 3.27 A). Upon treatment with glutamine antagonist DON however, only gene expression of *CD86* was increased while *CCL-2* was decreased (Figure 3.27 B).

These results suggest that expression of matrix metalloproteases and anti-inflammatory IL-10 and CD163 are dependent on glycolysis, pyruvate transport (TCA cycle) and fatty acid oxidation (feeding into the TCA cycle), as these were decreased upon inhibition of these pathways. IPF AMs however seem to be independent of glutaminolysis, as treatment with glutamine antagonist DON did not affect fibrosis related gene expression.

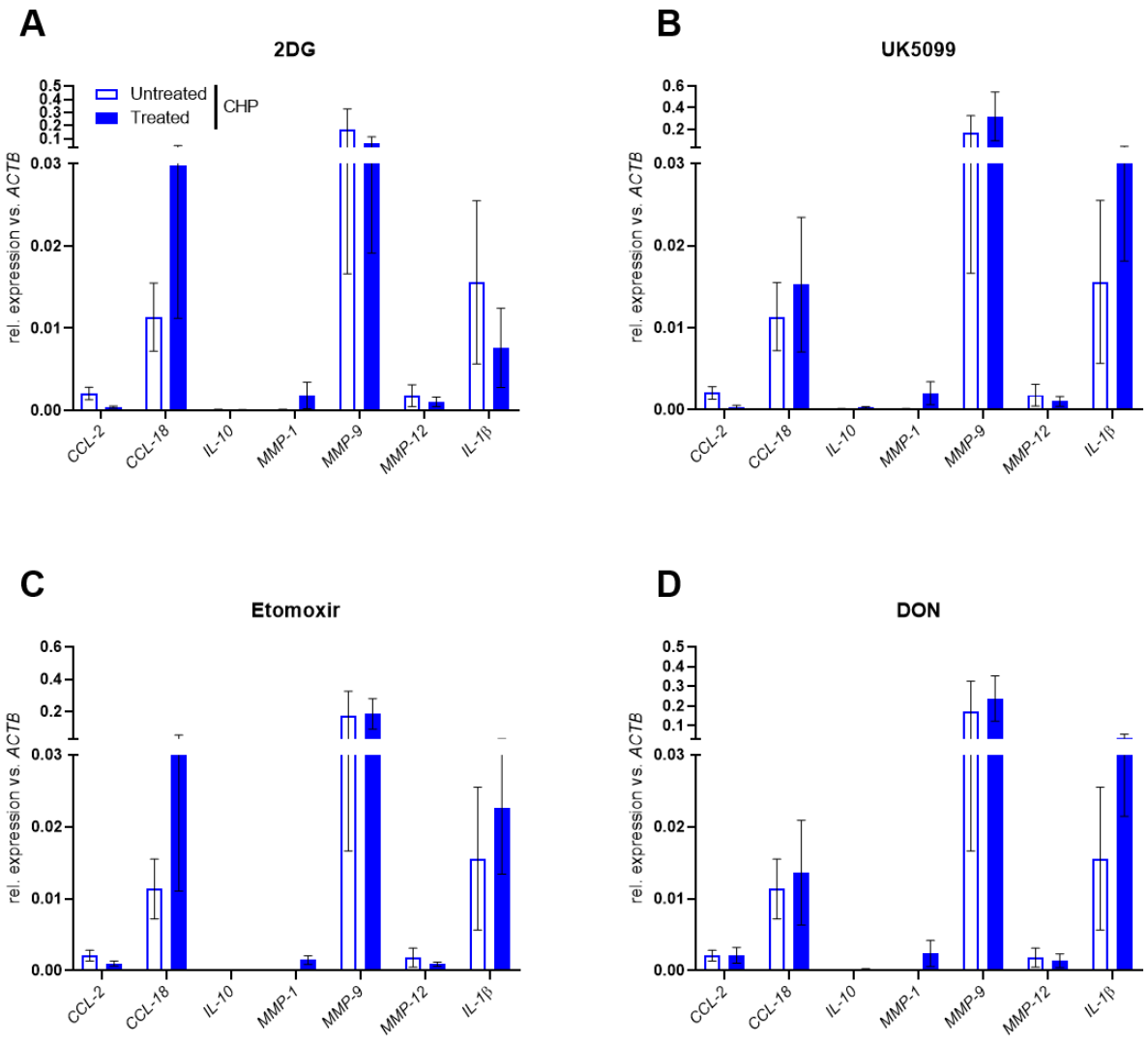

Figure 3.25. Gene expression of key effector genes in CHP AMs upon incubation with metabolic inhibitors. A – D) Gene expression analysis of fibrosis effector function and AM phenotype genes in CD206^{+} sorted AMs from CHP patients, after 24 h culture with 25 mM 2DG (A), 100 µM UK5099 (B), 200 µM Etomoxir (C) or 250 µM DON (D) (n = 3) compared to medium control; *ACTB* was used as housekeeping gene. Data presented as mean ± S.E.M of $2^{-(\Delta CT)}$ showing relative gene expression. Statistical significance tested by Wilcoxon matched-pairs signed rank test between treated and medium control groups.

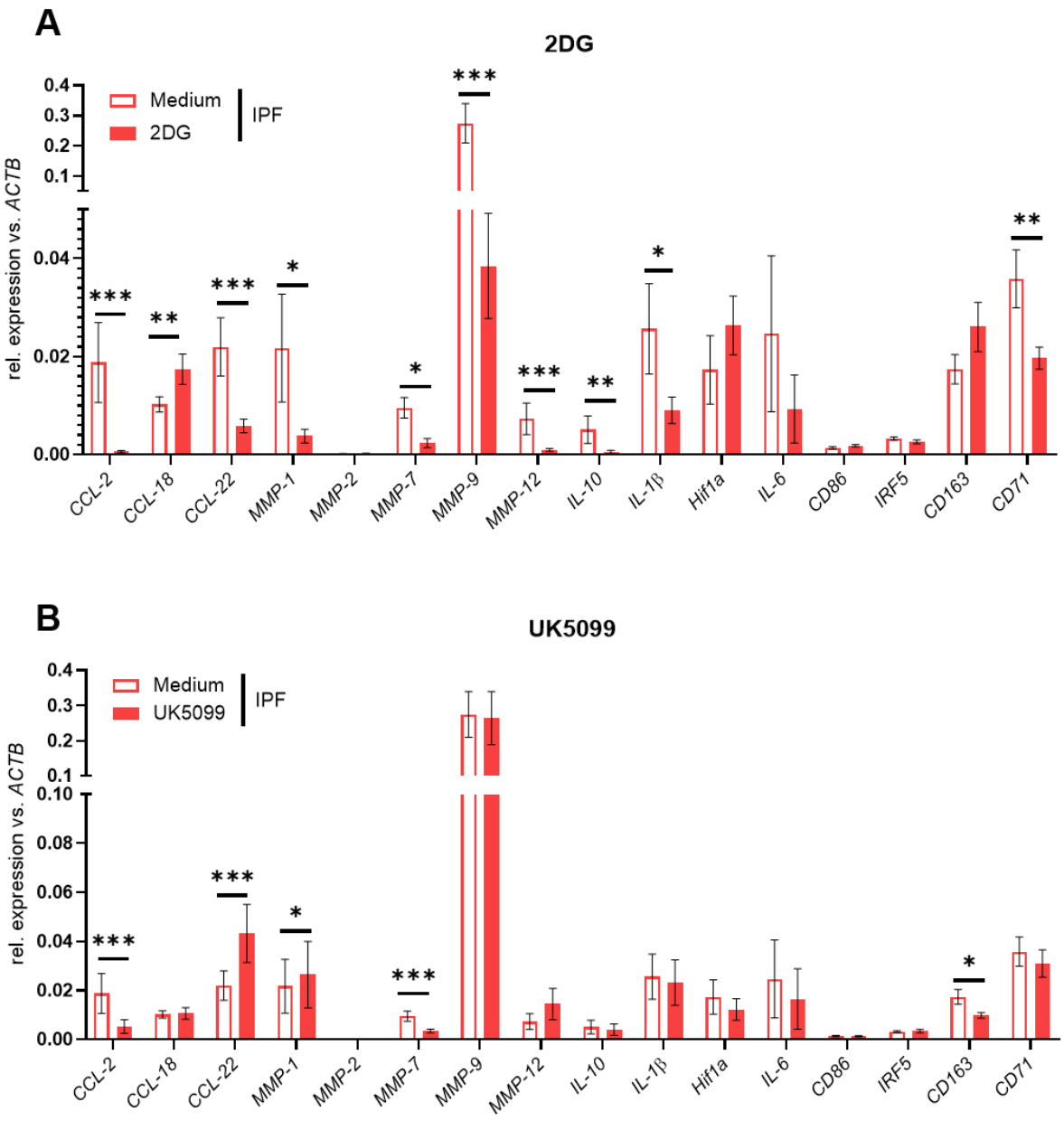

Figure 3.26. Treatment with 2DG and UK5099 alters effector gene expression in IPF AM. A – B) Gene expression analysis of AM key effector function genes in CD206+ sorted AMs from IPF patients, after 24 h incubation with 25 mM 2DG (A), 100 µM UK5099 (B) (n = 12) compared to medium control; *ACTB* was used as housekeeping gene. Data presented as mean ± S.E.M of $2^{-(\Delta CT)}$ showing relative gene expression. Statistical significance tested by Wilcoxon matched-pairs signed rank test between treated and medium control groups, * P < 0.05, ** P < 0.01, *** P < 0.005.

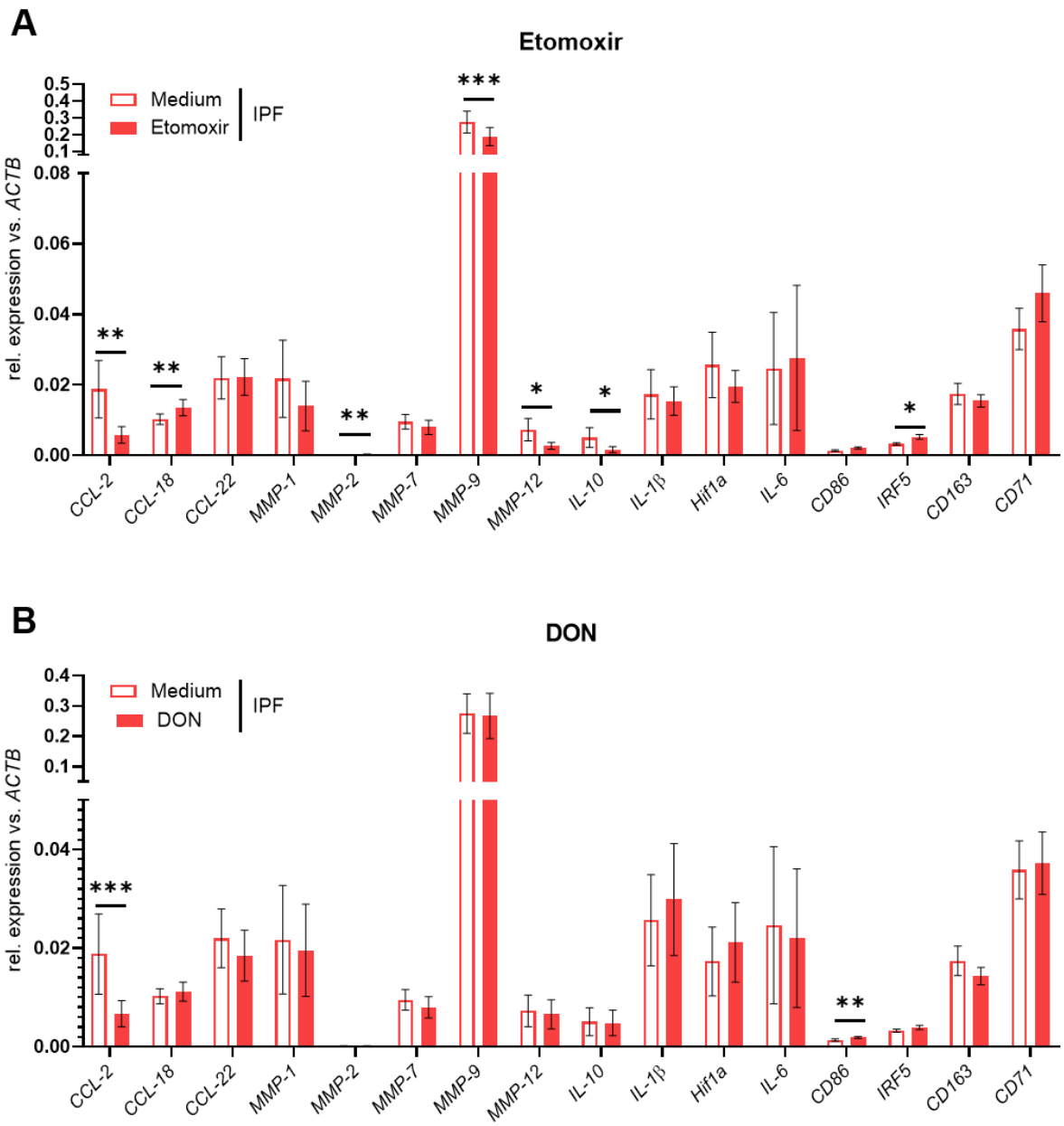

Figure 3.27. Inhibition by Etomoxir and DON alters effector gene expression in IPF AM. A – D) Gene expression analysis of AM key effector function genes in CD206^{+} sorted AMs from IPF patients, after 24 h culture with 200 µM Etomoxir (A) or 250 µM DON (B) (n = 12) compared to medium control; *ACTB* was used as housekeeping gene. Data presented as mean ± S.E.M of $2^{-(\Delta CT)}$ showing relative gene expression. Statistical significance tested by Wilcoxon matched-pairs signed rank test between treated and medium control groups, * P < 0.05, ** P < 0.01, *** P < 0.005.

3.4 Discussion

The overall aim of this chapter was to analyse AM metabolic phenotypes in IPF and CHP, assess how this underlies disease pathology and to determine whether inhibition of AM metabolic pathways can alter pro-fibrotic phenotypes. To achieve this, IPF, CHP and healthy control BAL samples were first characterised by FACS and GC-MS targeted at glycolysis and TCA cycle metabolites. Subsequently, AMs were sorted using the MACS system and their metabolic phenotype was analysed by a metabolic gene array, GC-MS analysis of metabolic intermediates as well as Seahorse metabolic assays. To bring these findings into context with clinical pathologies, metabolic phenotype was related to clinical parameters. Finally, metabolic inhibitors were administered to IPF and CHP AMs *ex vivo* to identify metabolic pathways, which were critical for fibrosis pathways.

Recruitment of Mo-AMs during pulmonary fibrosis has been reported both in mouse models[212,236] as well as in clinical studies[237], while an increased number of AMs has also been observed in our IPF cohort. Similarly, an increased number of lymphocytes is a well-described feature of CHP[23,217], which was recapitulated in our cohort. Consistent with previous reports[224,238], both cohorts had increased total numbers of granulocytes as well as NK cells. As BAL was performed for diagnosis and further used for this research, the IPF and CHP patients recruited for this study represent an early disease time point. As the time point of sample acquisition varies between studies, results need to be interpreted in the appropriate context. While samples obtained at a late time point e.g. during lung transplantation show a more established pro-fibrotic phenotype[239], samples obtained for diagnostic purposes can be more heterogeneous, less fibrotic and better suited to understand early signalling dysregulation[76,240]. All hypersensitivity pneumonitis patients recruited for this study had been diagnosed with the chronic form of the disease (chronic hypersensitivity pneumonitis). Both IPF and CHP groups had significantly reduced lung function compared to healthy controls as measured by FVC, FEV_1 and D_{LCO}.

GC-MS analysis targeted at glycolysis and TCA cycle metabolites showed an increase of lactate, isocitrate and malate in IPF compared to healthy control BAL samples, while TCA

cycle metabolites citrate, cis-aconitate, succinate and fumarate as well as glycolytic 2- and 3-phosphpoglycerate correlated positively with the numbers of neutrophils in BAL. These results may suggest that neutrophils either secrete more of these metabolites or take up less than in healthy controls. Furthermore, BAL concentration of succinate correlated negatively with AM numbers, similarly indicating that IPF AMs either consume more succinate than during homeostasis or secrete less. Succinate has been identified recently as a signalling metabolite, as it can signal to dendritic cells, post-translationally modify proteins and regulate pro-inflammatory factors Hif1α and IL-1β[241] and might therefore be involved in rewiring AM phenotype during IPF. While the CHP cohort showed a similar relationship between BAL metabolites and immune cells, these changes were less significant due to a smaller samples size and larger variation.

As AMs play an important regulatory role during wound healing and during pulmonary fibrosis and are the largest immune cell population in BAL, this chapter subsequently focused on the metabolic phenotype in AMs in IPF and CHP compared to healthy controls. Cellular characterisation showed that in both IPF and CHP AMs expression of CD86, which provides costimulatory signals necessary for T cell activation was decreased. Furthermore, in CHP AMs, expression of the CSF receptor (CSF1R), which recognises macrophage-activating colony stimulating factor, was significantly decreased, while expression of the pro-inflammatory integrin CD11b was increased. Indeed, increased expression of CD11b on AMs during pulmonary fibrosis has been reported and linked to superoxide production[242].

Several studies have recently investigated mitochondria and metabolism in AMs during pulmonary fibrosis. Using samples from IPF patients, Larson-Casey *et al*. have shown that mitophagy is altered in IPF AM[170], while Tsitoura *et al*. found that mitochondria are dysmorphic[237]. Furthermore, El-Chemaly *et al*. have shown that the glucose transporter GLUT1 is increased in inflammatory BAL cells, which are the majority of AMs in IPF[168]. Similarly, increased glucose uptake and glycolysis as well as fatty acid oxidation was observed in AMs during mouse models of pulmonary fibrosis (bleomycin and TGF-β overexpression) and Xie *et al*. have shown a dependency on glycolysis in fibrotic AMs[169].

While mouse models for pulmonary fibrosis are useful to investigate molecular mechanism of the disease, they also have drawbacks and findings often do not translate well into human disease. The aim of this chapter was therefore to investigate metabolic reprogramming of AMs during pulmonary fibrosis in primary cells obtained from IPF and CHP patients.

Gene expression analysis of key metabolic enzymes in AMs showed an increased expression of first half TCA cycle genes in IPF AM compared to healthy controls, as well increased expression of *ACLY* and *PCK2*. While ACLY breaks down citrate into acetyl CoA as the first step of fatty acid synthesis and oxaloacetate[243] in the cytosol, PCK1 converts cytosolic oxaloacetate into phosphoenolpyruvate. PCK2 on the other hand converts mitochondrial oxaloacetate into phosphoenolpyruvate[244]. The increased expression of both genes suggests that excess citrate is converted into acetyl CoA in the cytosol and enters fatty acid synthesis for energy storage, while mitochondrial oxaloacetate enters glycolysis again as phosphoenolpyruvate, which can contribute to protein synthesis.

In the CHP cohort, expression of all major glycolysis genes was increased, as well as the first half TCA cycle genes and *ACLY* and *PCK2*, while expression of the second half TCA cycle genes was decreased compared to healthy controls. Seahorse analysis confirmed this phenotypic change, as CHP AMs showed increased levels of ECAR and maximal OXPHOS while IPF AMs did not show a change in glycolysis or OXPHOS utilisation compared to healthy controls. Direct comparison between IPF and CHP AMs confirmed this as glycolysis genes *GPI* and *ENO1* were increased in CHP AMs and the second half TCA cycle genes were decreased, while overall CHP AMs had increased OXPHOS capacity and ATP production.

These findings highlight the importance of using primary human cells when studying complex human diseases such as IPF and CHP, as they differ profoundly from the results shown in murine studies[169]. While post bleomycin both ECAR (glycolysis) and maximal respiration were increased, this was not observed in IPF primary AMs[169]. The results shown here indicate that although gene expression of the second half TCA cycle was decreased in CHP AMs, this phenotype can still support a significant increase in OXPHOS utilisation if

only enough NADH is produced in the first half of the TCA cycle and if enough input is provided to the TCA cycle, such as through increased glycolysis. These results further suggest that solely an increase in first half TCA cycle expression is not enough to support an overall increase in OXPHOS, as this does not necessarily increase the throughput through the TCA cycle and subsequent NADH production to fuel the electron transport chain. To add to these findings, glucose tracing experiments could show where glucose ends up and whether alternative energy sources for the TCA cycle are utilised, such as fatty acid oxidation or glutaminolysis. Furthermore, this chapter focused on central carbon metabolism, but investigating fatty acid consumption, synthesis and oxidation would further add to the understanding of AM metabolism during pulmonary fibrosis.

While targeted GC-MS for glycolysis and TCA cycle metabolites was also performed in sorted AMs, samples size was quite small in all groups (n = 3 - 6) and more samples are needed to draw conclusions.

Correlation analysis of alterations identified by gene array, GC-MS or seahorse with lung function parameters showed a significantly negative correlation between gene expression of *ACLY* and *PCK2* and lung function parameters in IPF. A similar trend emerged in the CHP cohort, however this was not statistically significant as the sample size was only n = 10. Furthermore, no change in survival could be detected when splitting the IPF cohort into $ACLY^{high/low}$ or $PCK2^{high/low}$ groups. ACLY is a key enzyme of de novo fatty acid synthesis, generating cytosolic acetyl CoA and oxaloacetate and has been reported to be increased during tumorigenesis, including during lung cancer[245]. As inhibition of ACLY improved tumour pathogenesis[246], it may be of interest to investigate ACLY inhibitors, such as MiR-22[247] in the context of IPF, especially targeted to AMs.

Finally, sorted AMs from IPF and CHP were incubated with metabolic inhibitors *ex vivo* to determine which pathway is required to sustain a fibrotic phenotype. Therapies which target AM metabolism would be an interesting new treatment strategy for pulmonary fibrosis. Four established inhibitors of metabolic pathways were chosen for this experiment as these have been used *ex vivo*, *in vivo*, in the lung and on macrophages: 2-DG (glycolysis)[248–250],

UK5099 (mitochondrial pyruvate transport)[251–253], Etomoxir (fatty acid oxidation)[254,255] and DON (glutaminolysis)[256,257]. Concentrations to use on primary AMs were determined by a previous MSc student in the lab (Wolf, MSc Thesis 2018). To analyse the impact of metabolic inhibition, the following functional genes were analysed before and after metabolic inhibition. Monocyte attracting chemokine ligand-2 (CCL-2, also known an MCP-1), lymphocyte attracting chemokine ligand-18 (CCL-18) and chemokine ligand-22, which attracts monocytes, NK cells and DCs are increased during IPF and CHP[73,75,258] and contribute to inflammation. Furthermore, matrix metalloproteases are increased during pulmonary fibrosis, influencing matrix turnover and deposition[258,259]. Matrix metalloproteases-1, -2, -7, -9, and -12 were selected for this assay as between them they can digest all classes of collagens and elastins[260]. The pro-inflammatory signalling and metabolic regulatory molecules IL-1β and Hif1α are increased in AMs during pulmonary fibrosis[177,261] and were selected as targeted genes as well pro-inflammatory cytokine IL-6 and anti-inflammatory IL-10. Additionally, M1-like macrophage markers CD86 and IRF5 were investigated as well as M2-like macrophage marker CD163, which is increased in AM during pulmonary fibrosis[185,237] and transferrin receptor CD71, which has recently been shown by our group to be altered in IPF[226].

Inhibition of glycolysis by 2-DG resulted in the largest functional change, decreasing expression of CCL-22, IL-1β and CD71 as well as MMP-1, -7, -9 and -12. This is in line with the study by Xie *et al*, which showed a decrease of MMP-12 in AMs upon inhibition of glycolysis by 2DG in the bleomycin model for pulmonary fibrosis[169]. Treatment with UK5099, inhibiting pyruvate transport into the mitochondria resulted in a similar trend – increased CCL-22 and decreased MMP-7, while here MMP-1 was increased. Furthermore, expression of CD163, which has previously been shown to be upregulated in IPF AMs[185,237], was decreased. Similarly, inhibition of FAO by Etomoxir resulted in increased CCL-18 and decreased MMP-9, however MMP-2 was increased as well as the M1-macrophage marker IRF5. Similar conclusions were drawn in the bleomycin model, as inhibition of fatty acid synthesis and oxidation by FAO inhibitors Etomoxir, Orlistat and TOFA did not rewire AM functional phenotype[169]. Until recently the paradigm held that long chain fatty acid oxidation

is essential for M(IL-4) activation (*in vitro*)[255], but a recent study has highlighted that 3µM Etomoxir is sufficient to inhibit enzyme activity, while higher concentrations of Etomoxir deplete intracellular coenzyme A (CoA) and do not specifically inhibit FAO[262]. It would therefore be interesting to investigate the impact of lower concentrations of Etomoxir or other FAO inhibitors such as Orlistat in the context of IPF AMs. Inhibition of glutamine metabolism by treatment with DON only decreased the expression of CCL-2, while the M1-like macrophage marker CD86 was increased. These findings suggest that inhibiting glycolysis in IPF AMs is most effective for rewiring AM functional phenotype, while inhibition of pyruvate transport or FAO had similar but less pronounced effects. Glutaminolysis however seems to be negligible for AM functional phenotype during IPF, as treatment with DON did not alter functional phenotype. These findings are in line with similar observations made in the bleomycin model of pulmonary fibrosis[169].

Since significant alterations in metabolic phenotype were observed in CHP AMs, the treatment with metabolic inhibitors may have yielded very important insights into CHP AM function and determined differences from IPF AMs. However, despite best efforts to recruit patients, only three CHP samples could be used for the inhibitor experiment. While I had hoped to recruit more CHP patients for this experiment as well as for the Seahorse assay during the last year, the outbreak of the COVID-19 pandemic resulted in a stop in bronchoscopies for the near future. Therefore, *ex vivo* inhibition of metabolic pathways could only be performed on three CHP samples and no statistics could be performed. It would be very interesting to repeat this experiment with a larger sample size to be able to draw conclusions about how metabolic pathways influence AM functional phenotype in CHP.

3.5 Conclusion

Overall, analysis of the metabolic phenotype of AMs during IPF and CHP revealed a number of distinct alterations which could be further targeted and highlighted the different metabolic phenotypes underlying IPF and CHP AMs. While these two interstitial lung diseases may be pathologically indistinguishable, their AM metabolic profile is distinct and offers specific treatment opportunities. Treatment with metabolic inhibitors *ex vivo* has shown that it is possible to rewire AM fibrotic phenotype by targeting specific metabolic pathways. This experiment identified the glycolysis pathway, rather than glutaminolysis as essential for AM fibrotic phenotype.

4. AM metabolic reprogramming during bleomycin induced pulmonary fibrosis

4.1 Introduction

Several different animal models have been developed to model pulmonary fibrosis to understand disease pathology and test candidate therapies. The most used models include pulmonary fibrosis induced by bleomycin, silica, asbestos or fluorescein isothionate or the overexpression of fibrotic factors such as IL-1β or TGF-β. These models are applied in rodents such as rats, guinea pigs and mice. Murine models of fibrosis are by far the most commonly used as these animals are relatively inexpensive and many tools, reagents and modified strains are available. Silica induced pulmonary fibrosis is a robust model of lung injury and causes persistent fibrotic lesions[263], however the long time to develop fibrosis, difficult mode of delivery and problems with reproducibility make it a less favourable model[264]. The asbestos induced pulmonary fibrosis model takes at least four weeks to develop fibrosis and suffers from uneven distribution and central rather than subpleural fibrosis[265]. Similarly, fluorescein isothionate induced pulmonary fibrosis causes persistent fibrosis, however not usual interstitial pneumonia or inflammatory infiltrates. The bleomycin induced pulmonary fibrosis model in adult male mice produces a phenotype most similar to the acute phase of IPF in humans[266] and is therefore the most clinically relevant model and used most often for preclinical studies[267]. The disadvantage of the model is its patchy fibrosis development and spontaneous resolution in younger mice[268]. However, the bleomycin model was selected here as it enabled the use of specific tools for investigation of mechanisms of pulmonary fibrosis.

Bleomycin is a chemotherapeutic antibiotic, which causes chelation of metal ions resulting in ROS production[269] and epithelial cell death (d1– 3), inflammatory infiltrate (d3-9) and ultimately development of fibrosis (d10-21) in mice[270–272], while in young mice spontaneous resolution is observed after d21[273]. Most commonly 6 – 8 week old mice are used, however recent studies suggest that aged mice (15 – 24 months) reflect human pulmonary fibrosis better[266]. As these are also more expensive and frail, 10 – 12 week old mice were utilised for the majority of experiments. In the literature, the dose of bleomycin and mode of delivery varies widely between 0.4 to 4 U/kg[274–279], although 2.0 – 2.5U/kg delivers the most effective

model of pulmonary fibrosis and some key studies in the field have used up to 30U per mouse[280,281].

The bleomycin mouse model has helped to better understand the role of monocyte and macrophages during pulmonary fibrosis. Both the depletion of lung macrophages and circulating monocytes reduced pulmonary fibrosis[282–284], while adoptive transfer of M2-like YM1-positive AMs exacerbated pulmonary fibrosis[285]. Misharin *et al.* developed a flow cytometry panel to identify macrophage populations during steady state and during the bleomycin mouse model, in which they characterised a distinct population of SigF^{low} macrophages that infiltrate the lungs after bleomycin exposure[41]. These were identified as monocyte recruited AMs (Mo-AM), expressing high levels of CD11b, CD11c, CD14, CD36 and low levels of SiglecF[212]. While Tr-AM populate the lung during early embryogenesis and are maintained with minimal replenishment from bone marrow or circulating monocytes[36,53], they can be depleted during lung injury and are then restored by Mo-AMs[286,287]. Recently, a single cell RNAseq study identified this emerging population during the bleomycin mouse model as transitional between monocytes and AMs, over time expressing more SiglecF[239]. In a later study, Misharin *et al*. show that specific gene deletion of Mo-AMs after recruitment to the lungs ameliorated pulmonary fibrosis, while depletion of Tr-AMs did not alter disease severity. Furthermore, single cell RNAseq showed an upregulation of fibrosis related genes in Mo-AMs post bleomycin and a subset of Mo-AMs could be detected in the lungs up to one-year post bleomycin exposure, highlighting the driving role of Mo-AMs during pulmonary fibrosis[288].

Xie *et al*. investigated AM metabolic phenotype in the bleomycin and TGF-β overexpression models. Using enrichment of AMs by adherence, they observed increased glucose uptake, glycolysis and fatty acid oxidation during pulmonary fibrosis *in vivo*[289]. Furthermore, the M2-like AM profile was dependent on glycolysis, but not FAO or glutaminolysis. While this study highlighted important underlying metabolic pathways in AMs during pulmonary fibrosis, it did not differentiate between Tr-AMs and Mo-AMs and only investigated a limited number of glycolysis and few fibrosis related genes. Thus, the metabolic phenotype of Tr-AMs and

Mo-AMs and the role of central carbon metabolism during pulmonary fibrosis remain unknown.

Succinate in particular has been identified as not only being involved in energy generation in the TCA cycle, but also as an important signalling molecule, driving IL-1β production[290] and stabilising Hif1α in macrophages[96]. Via its four subunits, SDH catalyses the oxidation of succinate and furthermore links the TCA cycle to the electron transport chain. While the subunits SDHA and SDHB drive the enzymatic activity and catalyse the oxidation of succinate to fumarate, subunits SDHC and SDHD are anchored into the inner mitochondrial membrane, bind ubiquinone, and facilitate the reduction to ubiquinol and therefore electron transfer. Succinate regulates critical immune responses such as NO, prostaglandin and extracellular signal regulated kinase (ERK)[291,292] via Hif1α and the succinate receptor and is also chemotactic for DC migration[293]. Furthermore, succinate can post translationally modify lysines in other metabolic enzymes, including GAPDH, IDH and PDH[241]. SDH, which oxidises succinate to generate fumarate, but is also linked to the ETC and drives ROS production, is therefore a critical regulator of macrophage phenotypes. Inhibition of SDH, such as by administration of dimethyl malonate (DMM)[294], which is hydrolysed into malonate intracellularly, results in an accumulation of succinate. This may induce glycolytic reprogramming via Hif1α and reduce ROS production, thereby rewiring macrophage phenotype.

Targeted delivery of metabolic inhibitor drugs such as DMM to AMs specifically improves efficacy, sustained drug release and prevents capture by mucus[295]. Systems for inhaled AM targeted drug delivery include the use of micro- and nanocarriers, such as liposomes, which are phagocytosed by AMs. Recently, aerosolised delivery of small interfering RNA (siRNA), which post-translationally downregulates gene expression, has been developed to target AMs specifically[296], while mannose coated microspheres were developed to be recognised and phagocytosed by AMs[297]. Targeted delivery of microspheres loaded with antibiotics such as rifampicin to target intracellular *Mycobacterium Tuberculosis (Mtb)* inside AMs is

well developed[295,298,299] and opens the door for delivery of other drugs, including metabolic inhibitors.

The overall aim of this chapter was to use the bleomycin mouse model to analyse the underlying metabolic phenotype of Tr-AMs and Mo-AMs during pulmonary fibrosis and to investigate AM targeted therapy with metabolic inhibitors, in particular the SDH inhibitor DMM.

4.1.1 Hypothesis & Aims

Murine Tr-AMs and Mo-AMs have distinct metabolic phenotypes underlying function during pulmonary fibrosis. Inhibiting SDH in AMs can rewire their phenotype and ameliorate bleomycin induced pulmonary fibrosis.

Aims:

1. To measure central carbon metabolites in BAL during bleomycin induced pulmonary fibrosis
2. To investigate the metabolic phenotype of Tr-AMs and Mo-AMs during bleomycin induced pulmonary fibrosis
3. To utilize dimethyl-malonate loaded liposomes for targeted SDH inhibition in AMs in the bleomycin mouse model

4.2 Methods

4.2.1 The bleomycin model of pulmonary fibrosis

Adult, male C57Bl/6J mice were exposed to 0.05U bleomycin (50µl) or 50µl PBS by oropharyngeal administration on d0 of the model and lung and BAL were harvested at day 7 (inflammatory phase), d21 (peak fibrosis phase) or d42 (resolution phase in mice; figure 4.1A). Subsequent analysis of immune infiltrate and fibrotic phenotype was performed as described in detail in chapter 2.

4.2.2 Sorting Tr-AMs and Mo-AMs from bleomycin exposed mice

The PKH26 Red Fluorescent Cell dye for phagocytic cells was used to stain Tr-AMs in naïve mice before exposure to bleomycin (Figure 4.1B), as described in section 2.4.3, which confirmed SiglecF^{high} expression as a marker for Tr-AM, while Mo-AMs were SiglecF^{int}. Tr-AMs and Mo-AMs were subsequently FACS sorted from BAL at d7 or d21 post bleomycin based on the expression of SigF as described in section 2.4.5 and previously published by Misharin *et al*.[212].

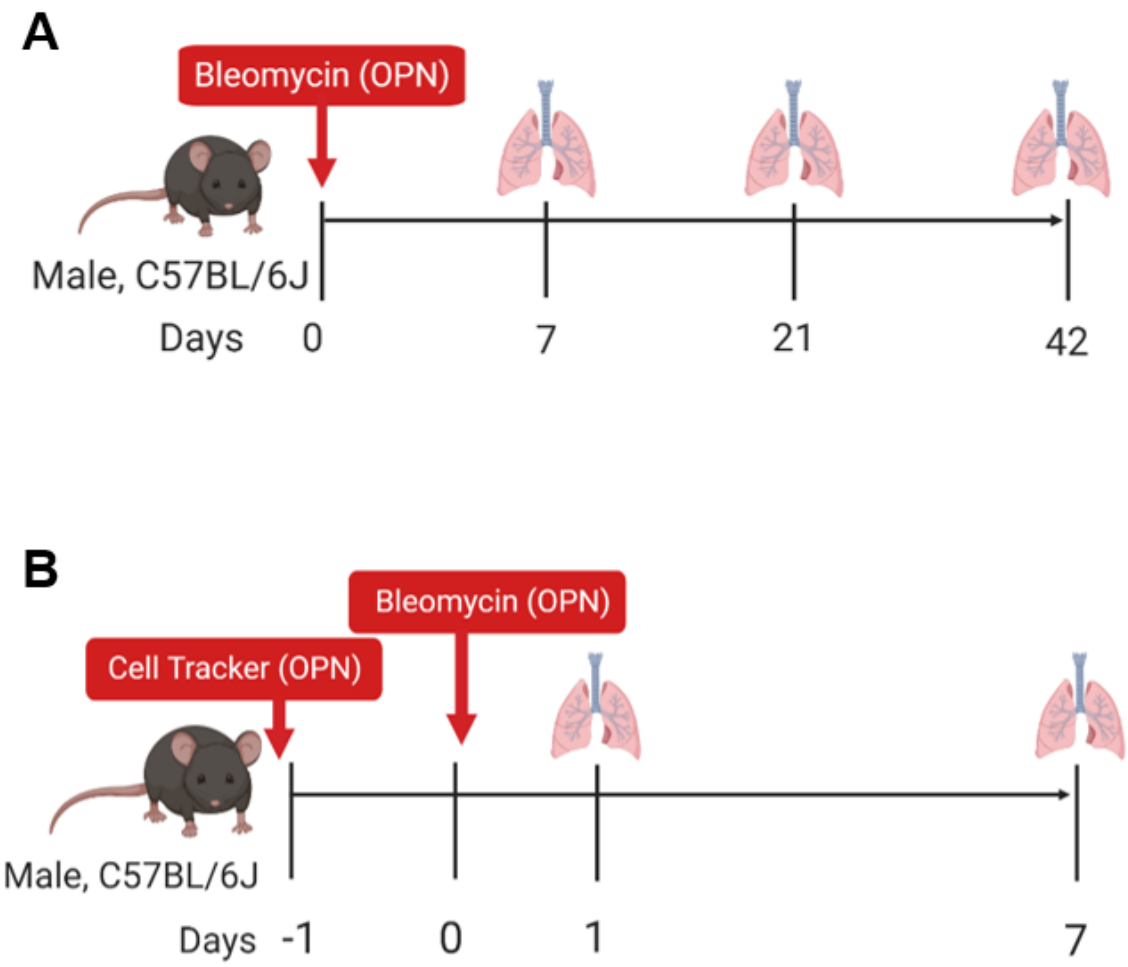

Figure 4.1. Schematic overview of bleomycin mouse model and *in vivo* cell tracker staining. A) Adult male C57BL/6 WT mice were exposed to either 0.05U bleomycin or 50µl phosphate buffered saline (PBS) on d0. Lungs were harvested at d7, d21 or d42 post bleomycin. B) Adult male C57BL/6 WT mice were exposed to either 50µl cell tracker or 50µl PBS on d-1. On d0, either 0.05U bleomycin or 50µl PBS were administered and lungs were harvested on d1 or d7.

4.2.3 Treatment with DMM-liposomes during bleomycin induced PF

Vehicle or DMM loaded liposomes, coupled to a DiD dye for tracking (Encapsula nanosciences) were titrated and ultimately administered oropharyngeal at 1:4 dilution in PBS (50µl), while an equal amount of PBS was used as control. DMM-liposomes, vehicle-liposomes or PBS was administrated either at d0, together with exposure to bleomycin (Figure 4.2A), at d10 during peak fibrosis (Figure 4.2B) or repeatedly every third day from d10 onwards (d10, d13, d16, d19) until harvest at d21 post bleomycin (Figure 4.2C). BAL and lungs were harvested to assess the impact of preventative or therapeutic AM-targeted SDH inhibition during bleomycin induced pulmonary fibrosis.

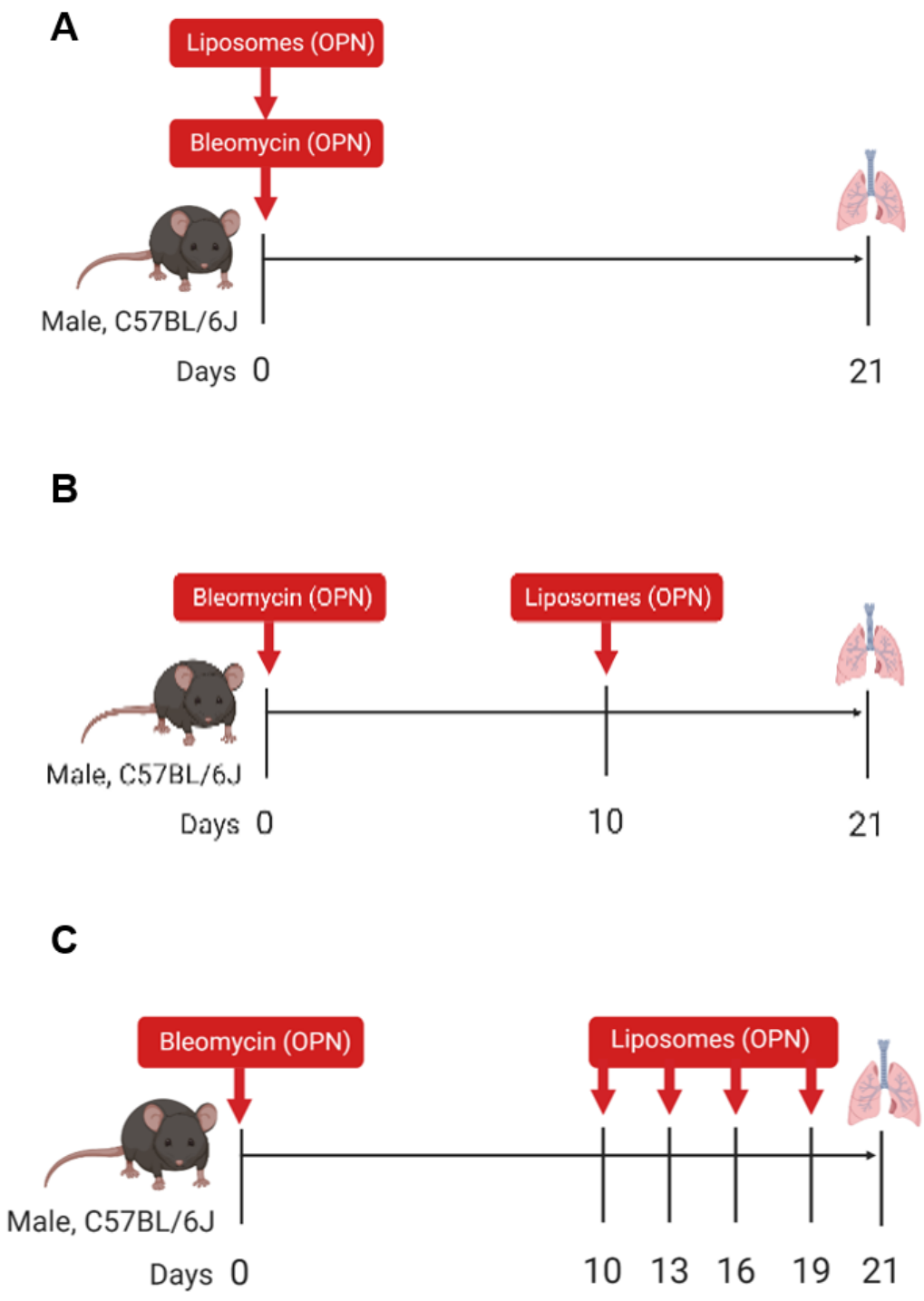

Figure 4.2. Treatment strategy of DMM-liposomes in murine pulmonary fibrosis. A) Adult male C57BL/6 WT mice were exposed to either 0.05U bleomycin or 50µl PBS as well as 40µl of either empty liposomes, DMM-filled liposomes or PBS on d0. Lungs were harvested at d21. B) Adult male C57BL/6 WT mice were exposed to either 0.05U bleomycin or 50µl PBS on d0 and 40µl of either empty liposomes, DMM-filled liposomes or PBS on day 10. Lungs were harvested at d21. C) Adult male C57BL/6 WT mice were exposed to either 0.05U bleomycin or 50µl PBS on d0 and administered 40µl of either empty liposomes, DMM-filled liposomes or PBS every third day from d10 onwards. Lungs were harvested at d21.

4.3 Results

4.3.1 Lung function during bleomycin mouse model

To characterise the bleomycin mouse model of pulmonary fibrosis, dynamic lung function parameters as well as BAL and lung cell numbers were assessed at the inflammatory (d7), peak fibrosis (d21) and resolution (d42) time points. Dynamic resistance and elastance were significantly increased at d21 post bleomycin compared to PBS treated mice (Figure 4.3 A-B), while dynamic compliance was decreased at the 21-day time point (Figure 4.3C). These changes returned back to baseline by d42. Furthermore, BAL cell numbers were increased in the bleomycin dosed group at d7 (Figure 4.3D), indicating immune cell infiltration, while total lung cell counts were increased in bleomycin dosed mice at the 7d and 21d time point (Figure 4.3E) and recovered to baseline at d42. These results suggest inflammatory infiltration during the early phase and severe lung function changes three weeks after bleomycin exposure, while these parameters recovered in mice by 6 weeks post bleomycin.

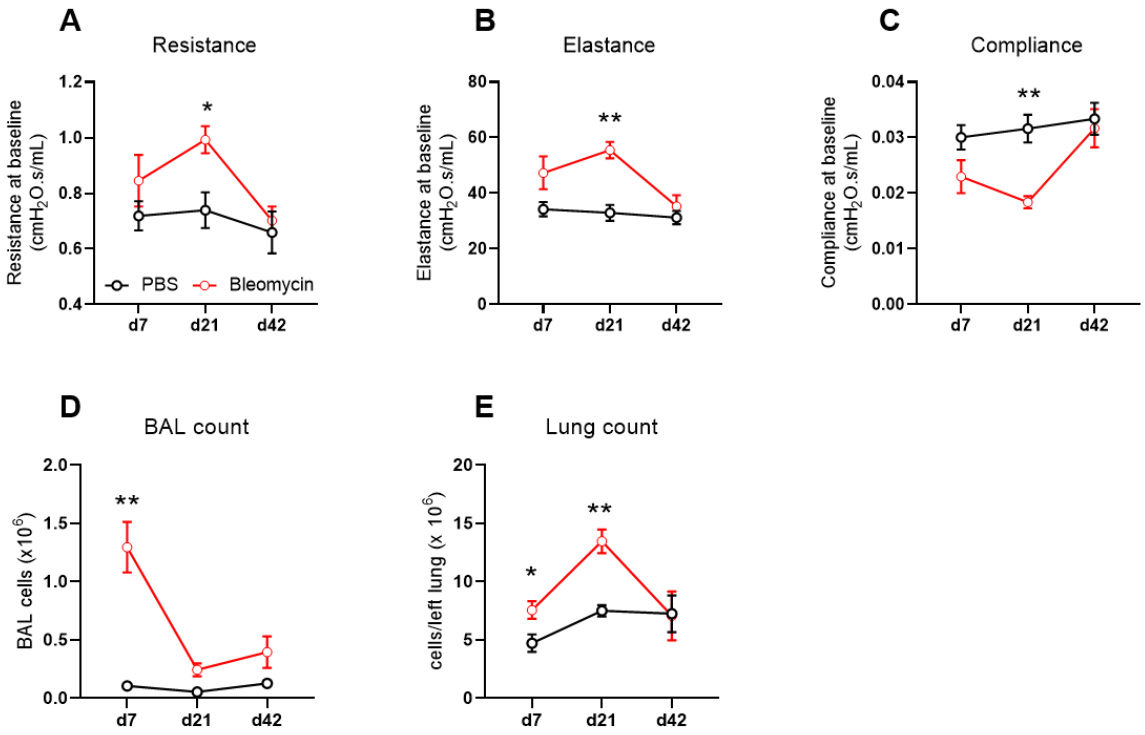

Figure 4.3. Lung function parameters during the bleomycin mouse model. A - C) Dynamic resistance (A), elastance (B) and compliance (C) measured at baseline by FlexiVent in PBS or Bleo dosed mice at d7, d21 and d42. D – E) BAL count (D) and lung count (E) in PBS or Bleo dosed mice. D7, n = 6; d21 n = 6-7 pooled from two independent experiment; d42 n = 7-10 mice per group pooled from two independent experiments. Data presented as mean ± S.E.M. Statistical significance tested by Mann Whitney U test between PBS and Bleo groups per time point; *P < 0.05, ** P < 0.01.

4.3.2 Immune populations during bleomycin mouse model

To further investigate the inflammatory infiltrate at the different time points of the bleomycin mouse model, flow cytometry was performed on BAL and lung at d7, d21 and d42 and the major immune cell populations involved in pulmonary fibrosis were identified using the gating strategy shown in Figure 4.4. Briefly, live, CD45+ cells were selected to identify SiglecF^{+}/ CD11c^{+} AMs, SiglecF^{+}/CD11c^{-} eosinophils and SiglecF^{-}/Ly6G^{+} neutrophils. SiglecF^{-}/Ly6G^{-} cells were further identified as MHCII^{+}/CD11c^{+}/CD103^{+} DCs and CD64^{+}/CD11b^{+}/Ly6C^{+} monocytes. Using separate staining panels, CD8 T-cells were identified as live, CD45^{+}/CD3^{+}/CD8^{+}. Furthermore, Tr-AMs were selected as live, CD45^{+}/CD64^{+}/CD11c^{+}/SiglecF^{high}, while Mo-AMs were SiglecF^{int}.

At the inflammatory time point 7d post bleomycin exposure, total numbers of AMs, both resident and recruited, as well as monocytes, eosinophils and neutrophils were significantly increased in BAL, but decreased back to baseline levels by d21 (Figure 4.5A-F). In lung, total numbers of monocytes, Mo-AMs, eosinophils and T cells were increased seven days after bleomycin exposure, while neutrophils and T cells were significantly increased at the three-week time point and NK cells and Mo-AMs were increased even at the 6 week time point (Figure 4.6A – H).

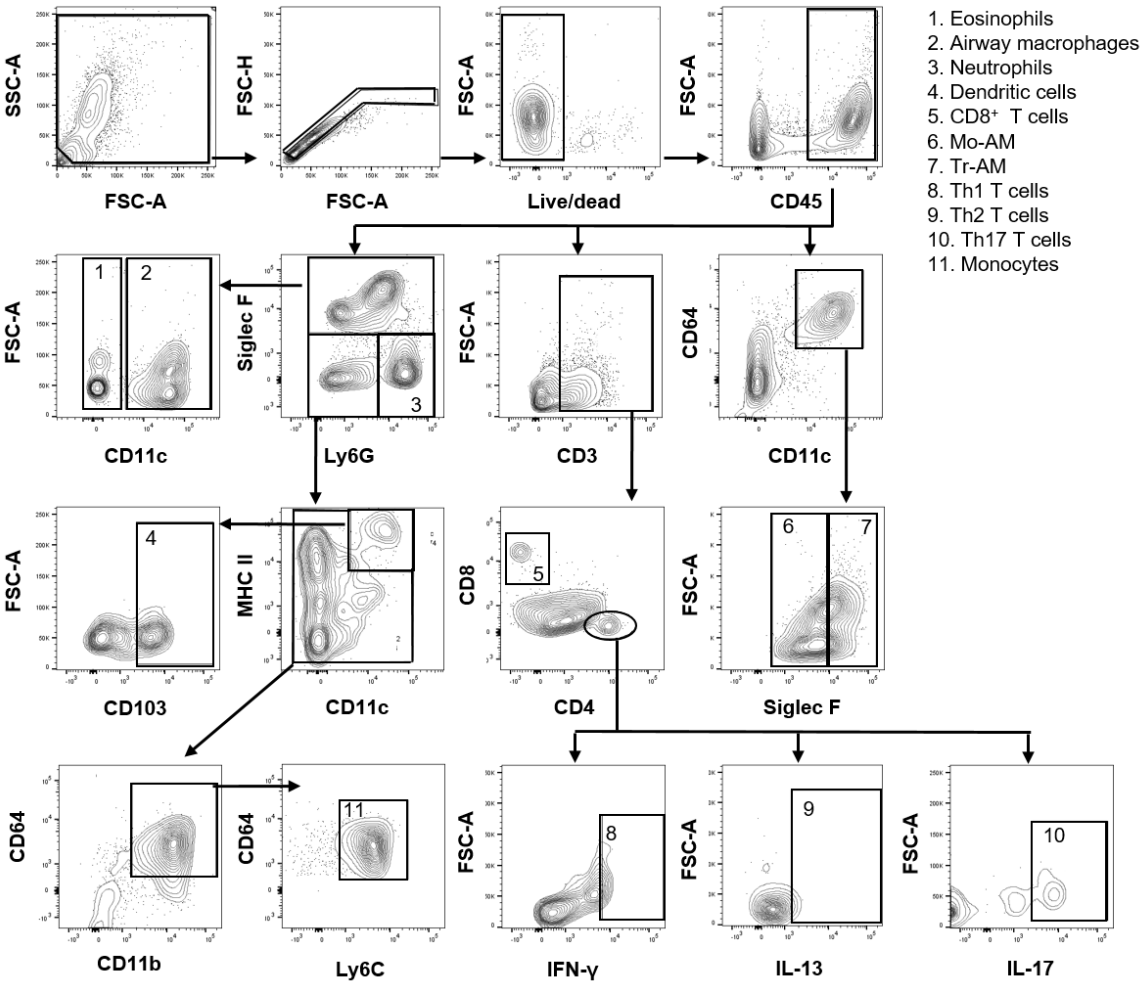

Figure 4.4. Gating strategy for immune populations in BAL and lung during bleomycin induced pulmonary fibrosis. Representative FACS plots showing gating strategy to determine the following immune cell populations in murine BAL and lung: eosinophils, neutrophils, monocytes, airway macrophages (AM), including monocyte-recruited AMs ($SigF^{int}$), and tissue-resident AMs ($SigF^{high}$), neutrophils, dendritic cells (DCs), T cells, including Th1-T-cells, Th2-T-cells and Th-17-T-cells.

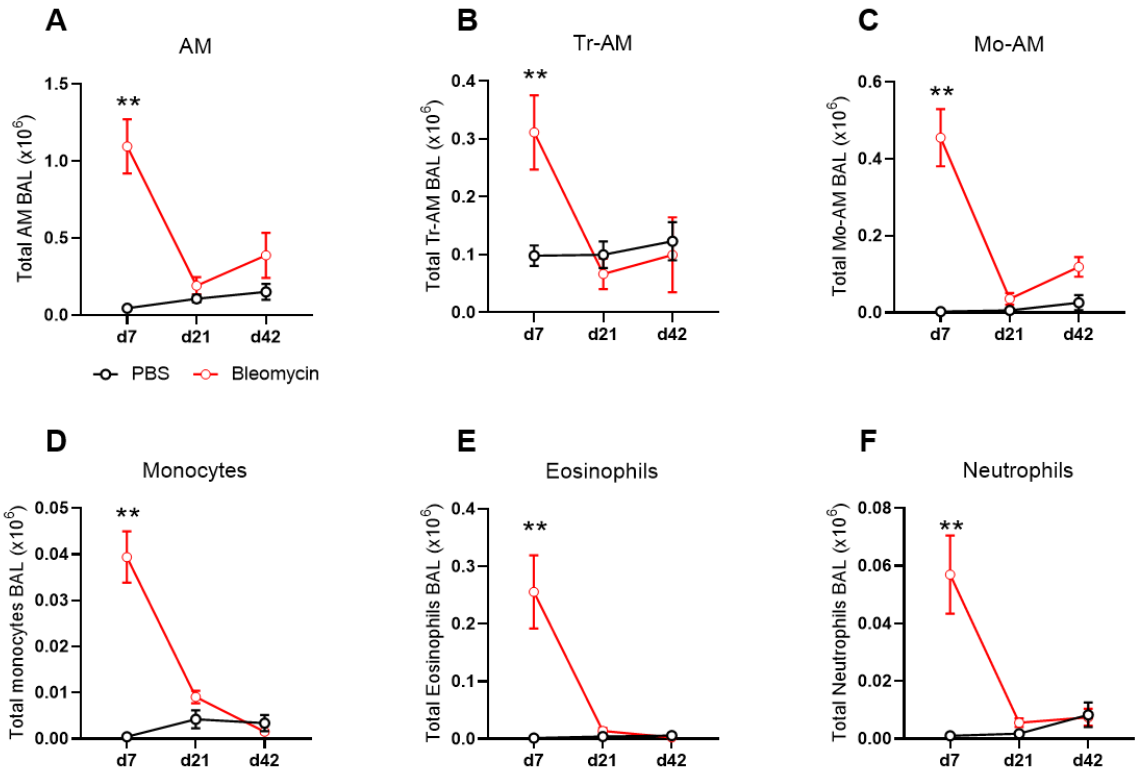

Figure 4.5. Immune cell populations in BAL during bleomycin induced pulmonary fibrosis. A – F) Total numbers of AMs (A), tissue-resident AMs (B), monocyte-recruited AMs (C), monocytes (D), eosinophils (E) and neutrophils (F) in BAL at d7, d21 or d42 after exposure to bleomycin or PBS. D7, n = 6; d21 n = 6-7 pooled from two independent experiment; d42 n = 7-10 mice per group pooled from two independent experiments. Data presented as mean ± S.E.M. Statistical significance tested by Mann Whitney U test between PBS and Bleo groups per time point; *P < 0.05, ** P < 0.01.

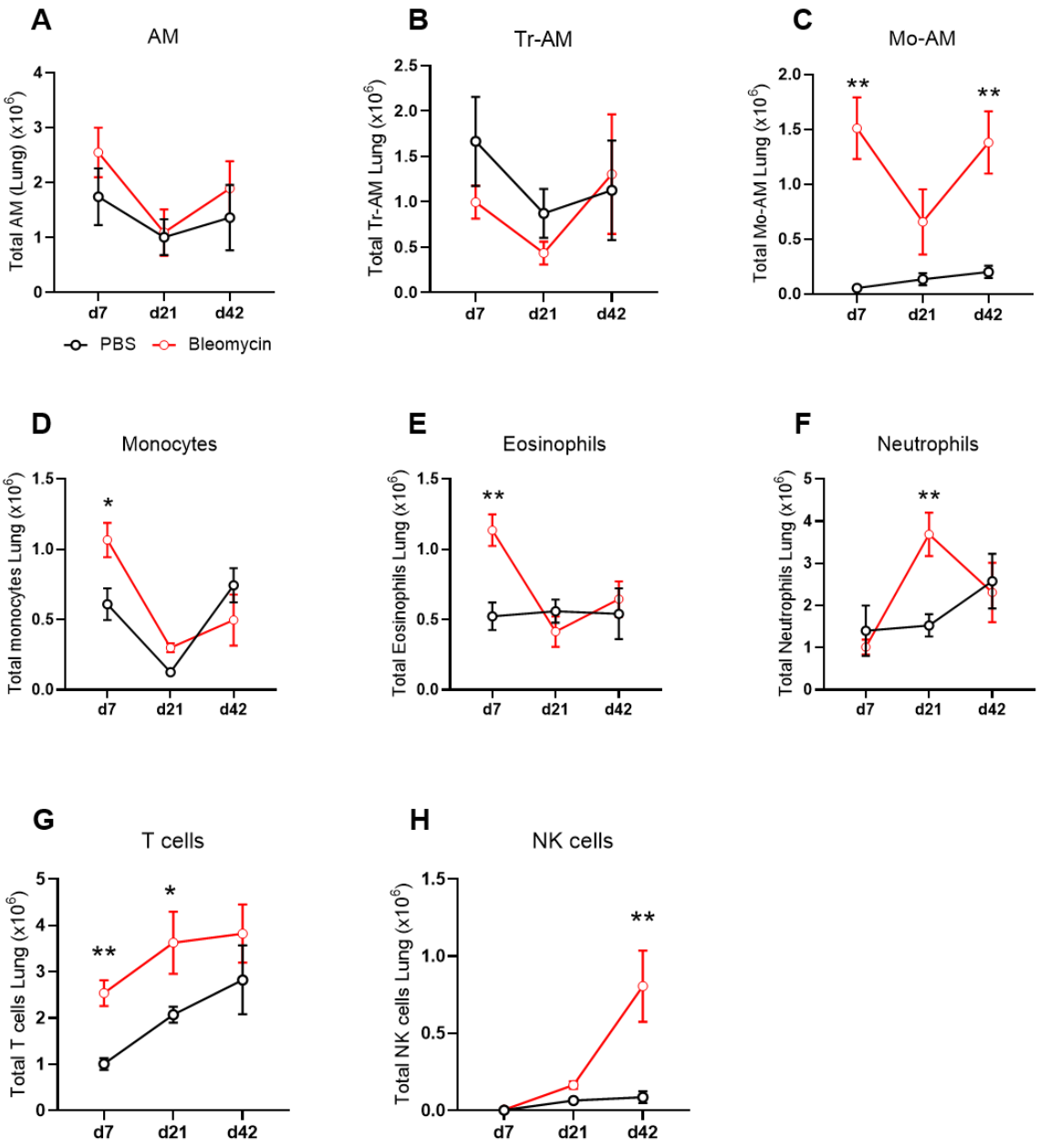

Figure 4.6. Immune cell populations in lung during bleomycin induced pulmonary fibrosis. A – H) Total numbers of AMs (A), tissue-resident AMs (B), monocyte-recruited AMs (C), monocytes (D), eosinophils (E), neutrophils (F), T cells (G) and NK cells (H) in BAL at d7, d21 or d42 after exposure to bleomycin or PBS. D7, n = 6; d21 n = 6-7 pooled from two independent experiment; d42 n = 7-10 mice per group pooled from two independent experiments. Data presented as mean ± S.E.M. Statistical significance tested by Mann Whitney U test between PBS and bleo groups per time point; *P < 0.05, ** P < 0.01.

4.3.3 Fibrotic phenotype of bleomycin mouse model

To assess the fibrotic phenotype after bleomycin exposure, gene expression of *Col1α1*, *Col3α1, Col4α1* and *Fn1* was measured in lung homogenates. Expression of *Col1α1*, *Col3α1* and *Col4α1* was significantly increased at the 21d time point and returned to baseline by d42 (Figure 4.7 A – C), while *Fn1* gene expression was already significantly increased at d7 post bleomycin. Furthermore, analysis of fibrosis score using the modified Ashcroft scoring system based on Sirius Red staining of lung slices showed increased fibrosis at the 7d and 21d time point and indicates recovery towards the late time point (Figure 4.7 E – F). Overall, the results shown in Figures 4.3 – 4.7 confirm the establishment of the bleomycin model for pulmonary fibrosis, which is in line with studies published by other groups using this model[300–302]. While the d7 time point is marked by inflammatory infiltration of the lungs, d21 represents the fibrotic phase with severely decreased lung function, increased collagen deposition and gene expression. At the 6-week time point lung function, immune cell infiltration and collagen gene expression have diminished.

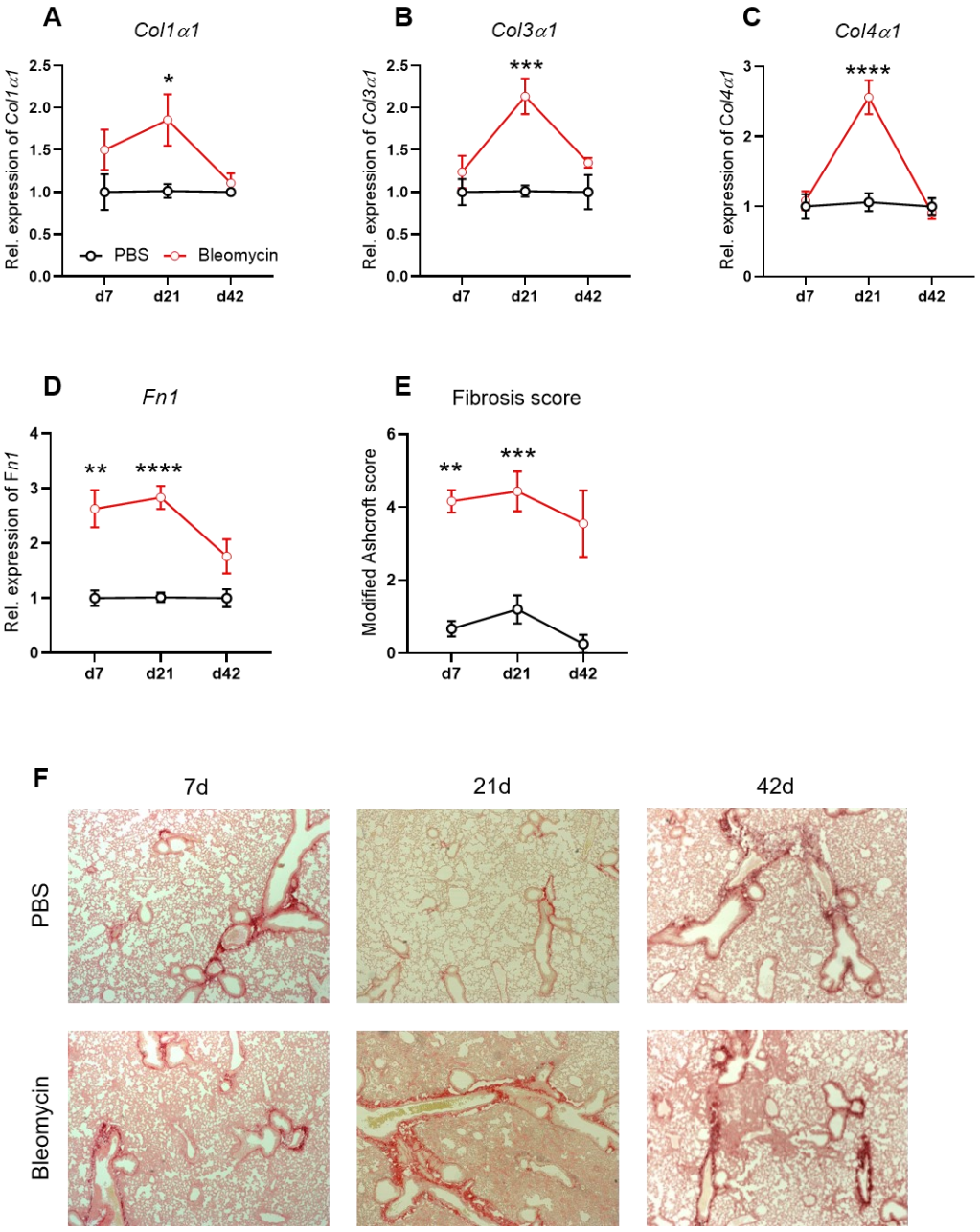

Figure 4.7. Fibrotic phenotype during bleomycin induced pulmonary fibrosis. A – D) Gene expression analysis of *Col1α1* (A), *Col3α1* (B), *Col4α1* (C) and *Fn1* (D) in lung homogenate of PBS or bleo dosed mice at d7, d21 and d42. *Actb* was used as housekeeping gene. E – F) Ashcroft score (E) and representative images (F) of lung slices of PBS or bleo dosed mice stained with Sirius Red, scored blinded by 3-5 individuals. Day 7, n = 6; d21 n = 6-7 pooled from two independent experiment; d42 n = 7-10 mice per group pooled from two independent experiments. Data presented as mean ± S.E.M. Statistical significance tested by Mann Whitney U test between PBS and bleo groups per time point; *P < 0.05, ** P < 0.01, *** P < 0.005, **** P < 0.001.

4.3.4 Targeted GC-MS analysis of BAL

To analyse the glycolysis and Krebs cycle associated metabolite content in BAL during the pathogenesis of pulmonary fibrosis, we utilised a targeted GC-MS assay. BAL from d7, d21 and d42 post bleomycin was used to capture the metabolite content during inflammation, peak fibrosis and resolution. Analysis was performed in collaboration with the King's College Mass Spectrometry facility. The assay effectively detected glucose, glucose-6-phosphate, fructose-6-phosphate, 3-phosphoglycerate, 2-phosphoglycerate, pyruvate and lactate as glycolysis associated metabolites and citrate, cis-aconitate, isocitrate, 2-oxoglutarate, succinate, fumarate and malate as Krebs cycle associated metabolites. Interestingly, all these targeted metabolites were significantly increased in the bleomycin treated group at d7 compared to the PBS group (Figure 4.8 and Figure 4.9). During peak fibrosis, glucose (Figure 4.8A), pyruvate (Figure 4.8F) and lactate (Figure 4.8G) were significantly increased in the bleomycin treated group, while at the resolution time point all measured glycolysis associated metabolite levels returned to baseline levels. Furthermore, first-half Krebs cycle metabolites citrate (Figure 4.9A), cis-aconitate (Figure 4.9B) and isocitrate (Figure 4.9C) were significantly increased at peak fibrosis in the bleomycin treated group, while the other targeted Krebs cycle metabolites returned to baseline. Strikingly, citrate and cis-aconitate were significantly higher at d42 in the bleomycin treated group compared to the PBS treated group, although total levels declined over the time course of the bleomycin mouse model. Taken together these data show that during bleomycin induced inflammation, most glycolysis and Krebs cycle associated metabolites are highly increased, and levels of key glycolysis and first-half Krebs cycle metabolites are maintained during the fibrotic phase. For citrate and cis-aconitate, levels were maintained even during the resolution stage of bleomycin induced pulmonary fibrosis.

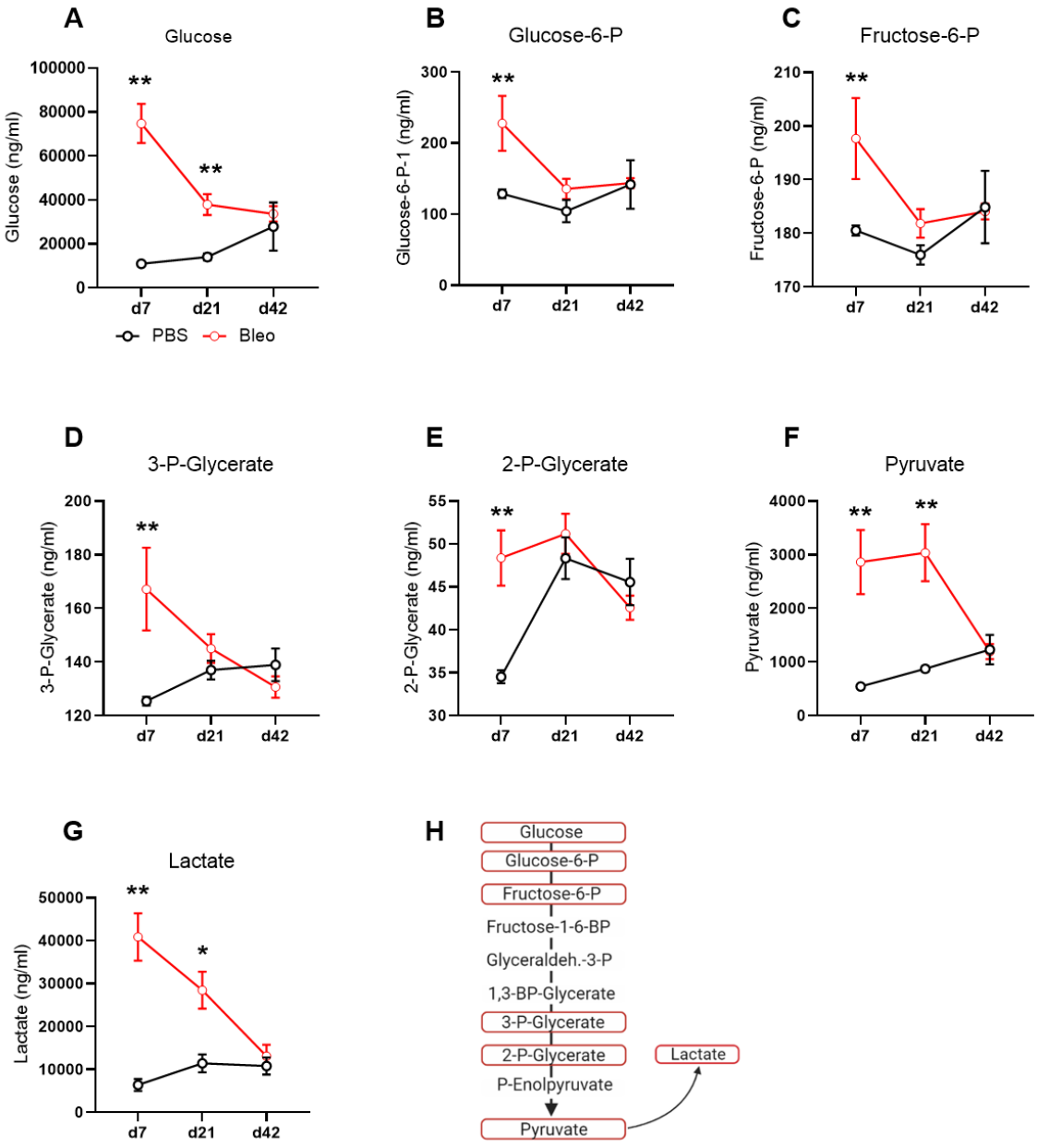

Figure 4.8. Glycolysis metabolites in BAL increase after bleomycin exposure. Targeted GC-MS analysis of glycolysis associated metabolites in BAL of PBS or bleo dosed mice at d7, d21 and d42. A) Glucose. B) Glucose-6-phosphate. C) Fructose-6-phosphate. D) 3-Phosphoglycerate. E) 2-Phosphoglycerate. F) Pyruvate. G) Lactate. H) Schematic of the glycolysis pathway showing significantly increased changes in red. D7, n = 6; d21, n = 4- 8; d42 n = 7-11. Data presented as mean ± S.E.M. Statistical significance tested by Mann Whitney U test between PBS and bleo groups per time point, *P < 0.05, ** P < 0.01.

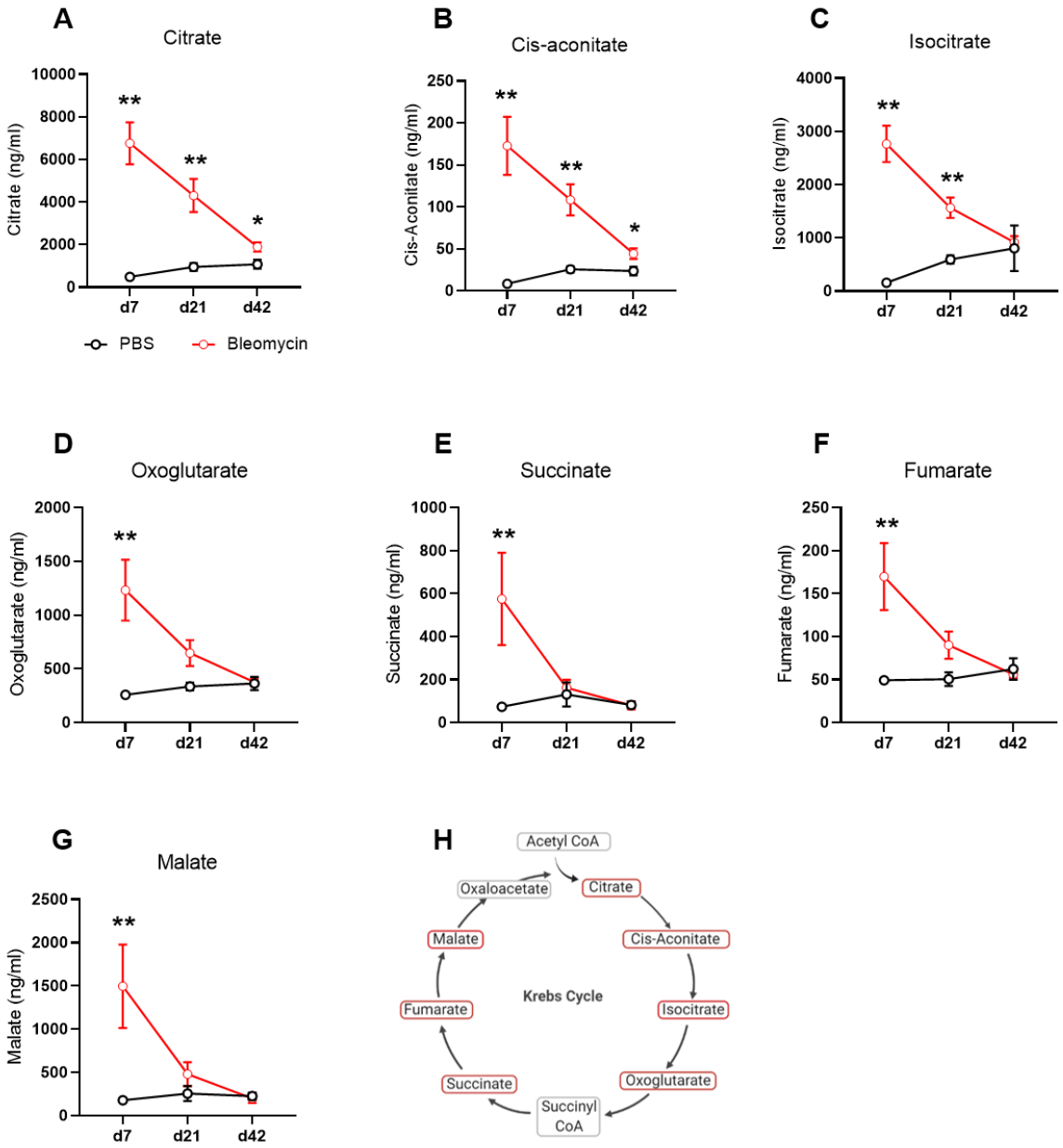

Figure 4.9. Krebs cycle metabolites increase after bleomycin exposure in BAL. Targeted GC-MS analysis of Krebs cycle associated metabolites in BAL of PBS or bleo dosed mice at d7, d21 and d42. A) Citrate. B) Cis-aconitate. C) Isocitrate. D) 2-Oxoglutarate. E) Succinate. F) Fumarate. G) Malate. H) Schematic of the TCA cycle showing significantly increased changes in red. D7, n = 6; d21, n = 4-8; d42 n = 7-11. Data presented as mean ± S.E.M. Statistical significance tested by Mann Whitney U test between PBS and bleo groups per time point, *P < 0.05, ** P < 0.01.

4.3.5 Cell tracker analysis of recruited Mo-AMs

To study the role of AMs and underlying metabolic alterations during pulmonary fibrosis in more detail, Tr-AM and Mo-AM were identified based on expression of SiglecF as shown in the gating strategy in Figure 4.4. and published by Misharin *et al*.[212]. To confirm this method of identifying the two AM subsets, the phagocytic cell tracker dye PKH26 was administered via the oropharyngeal route to mice to stain tissue resident AMs and flow cytometry was performed to assess cell tracker staining in SiglecF^{high} and SiglecF^{int} AMs as well as neutrophils and monocytes. To identify as suitable concentration of PKH26, three doses (0.05μM, 0.1 μM and 0.5 μM) were administered and total BAL cell recruitment as well as numbers of AMs, neutrophils and monocytes were assessed. Of the three doses tested neither induced BAL cell infiltration nor an increase of AMs, neutrophils or monocytes (Figure 4.10A – D). Furthermore, at lower doses (0.05 μM and 0.1 μM) circa 60% of AMs were positive for the dye, while at the highest dose (0.5 μM) over 80% of AMs stained consistently (Figure 4.10 E – F). However, some neutrophils (Figure 4.10 G) and monocytes (Figure 4.10 H) also took up the dye, although the total numbers of these were minimal. Overall, none of the tested concentrations of cell tracker caused inflammatory infiltration of BAL and 0.5 μM was selected for subsequent experiments and administered prior to dosing with PBS or bleomycin. Mo-AM and Tr-AM were analysed by flow cytometry at d7 post bleomycin. Over 90% of SiglecF^{high} Tr-AMs were celltracker^{+}, while the large majority of SiglecF^{int} Mo-AMs were celltracker^{-} (Figure 4.11 A), confirming the delineation of Tr-AM/Mo-AMs using Siglec-F expression. SiglecF expression was subsequently used as a marker to differentiate between Tr-AM and Mo-AM *in vivo*. Analysis of Mo-AM and Tr-AM at different time points throughout the bleomycin model showed that Mo-AMs make up about 60% of AMs at d7 post bleomycin and then slowly decrease, while they are absent in PBS dosed control mice (Figure 4.11 B).

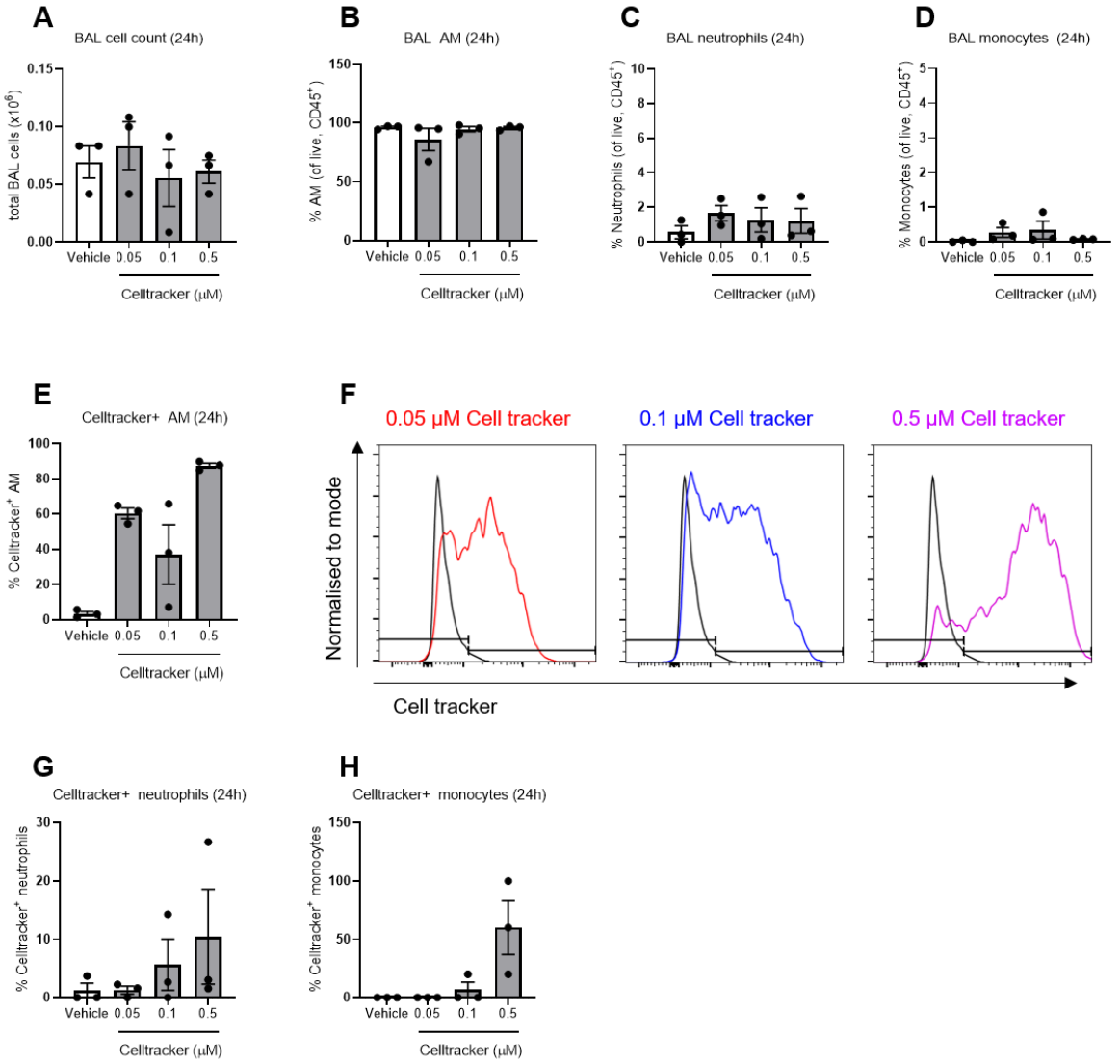

Figure 4.10. Optimization of cell tracker PKH26 *in vivo*. A) Total BAL cell count 24h after administration of 0.05 μM cell tracker, 0.1 μM cell tracker, 0.5 μM cell tracker or PBS vehicle. B – D) % AMs (B), neutrophils (C) and monocytes (C) of live, CD45⁺ BAL cells 24h after administration of 0.05 μM cell tracker, 0.1 μM cell tracker, 0.5 μM cll tracker or PBS vehicle. E – F) % Cell tracker⁺ AM 24h after administration of 0.05 μM cell tracker, 0.1 μM cell tracker, 0.5 μM cell tracker or PBS vehicle and representative histograms (F). G – H) % Cell tracker⁺ neutrophils (G) and monocytes (H) 24h after administration of 0.05 μM cell tracker, 0.1 μM cell tracker, 0.5 μM cell tracker or PBS vehicle. All groups n = 3. Data presented as mean ± S.E.M. Statistical significance tested by One Way ANOVA.

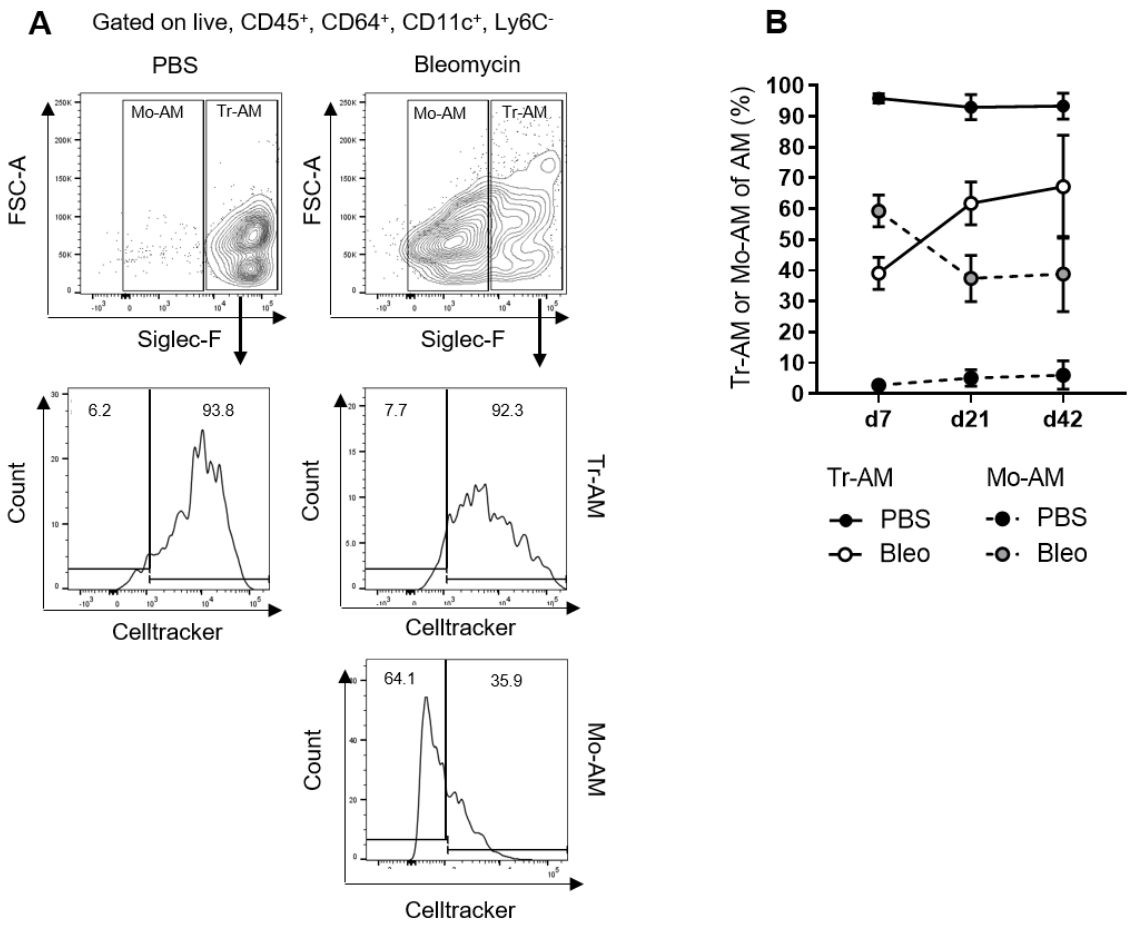

Figure 4.11. Mo-AM and Tr-AM populations during bleomycin mouse model. A) Representative FACS plots of Cell tracker stained Mo-AM and Tr-AM in BAL of PBS or bleomycin dosed mice at d7. B) % Tr-AM and Mo-AM of total AM in PBS or bleomycin dosed mice at d7, d21 and d42 post bleomycin. D7, n = 6; d21, n = 10-11; d42, n = 6-10. Data presented as mean ± S.E.M.

4.3.6 Seahorse mitochondrial stress test of sorted Mo-AM and Tr-AM

To investigate the metabolic phenotype of Mo-AM and Tr-AM during bleomycin induced pulmonary fibrosis, these populations were FACS sorted and analysed by Seahorse mitochondrial stress test. Our analysis showed that during peak fibrosis at d21 post bleomycin, Tr-AMs from bleomycin exposed mice have highly increased baseline OCR (Figure 4.12 A and E), maximal oxidative respiration (Figure 4.12 C) and SRC compared to PBS dosed control mice (Figure 4.12 D). Furthermore, ATP production as well as baseline ECAR were increased in Tr-AM from bleomycin exposed mice compared to those from PBS control mice (Figure 4.12 F and G) indicating an overall 'energetic' phenotype (Figure 4.12 B). Comparison of Tr-AM and Mo-AM from bleomycin exposed mice showed increased maximal respiration and baseline OCR in fibrotic Tr-AMs (Figure 4.12 C and E), as well as increased ATP production (Figure 4.12 G) and proton leak (Figure 4.12 H), making fibrotic Mo-AMs more similar in metabolic phenotype to PBS Tr-AM than to fibrotic Tr-AMs.

A similar trend emerged at the inflammatory time point, at d7 post bleomycin. Here, comparison between Mo-AM and Tr-AM from bleomycin exposed mice showed a highly increased maximal respiration and SRC in Tr-AMs (Figure 4.13 A, C and D), while there was no significant difference in baseline OCR or ECAR, ATP production or proton leak (Figure 4.13 E–H). As Mo-AMs are only recruited upon lung injury and exist in naïve lungs only in very small numbers, it was not possible to include Mo-AMs from PBS dosed mice into the analysis. Overall, these results show that during bleomycin induced pulmonary fibrosis, Tr-AMs have a more energetic metabolic phenotype compared to naïve Tr-AMs, which is more pronounced at d21 post bleomycin with trends already emerging during the inflammatory phase at d7. Mo-AMs on the other hand maintain a quiescent metabolic phenotype both during the inflammatory and fibrotic stages of the bleomycin mouse model.

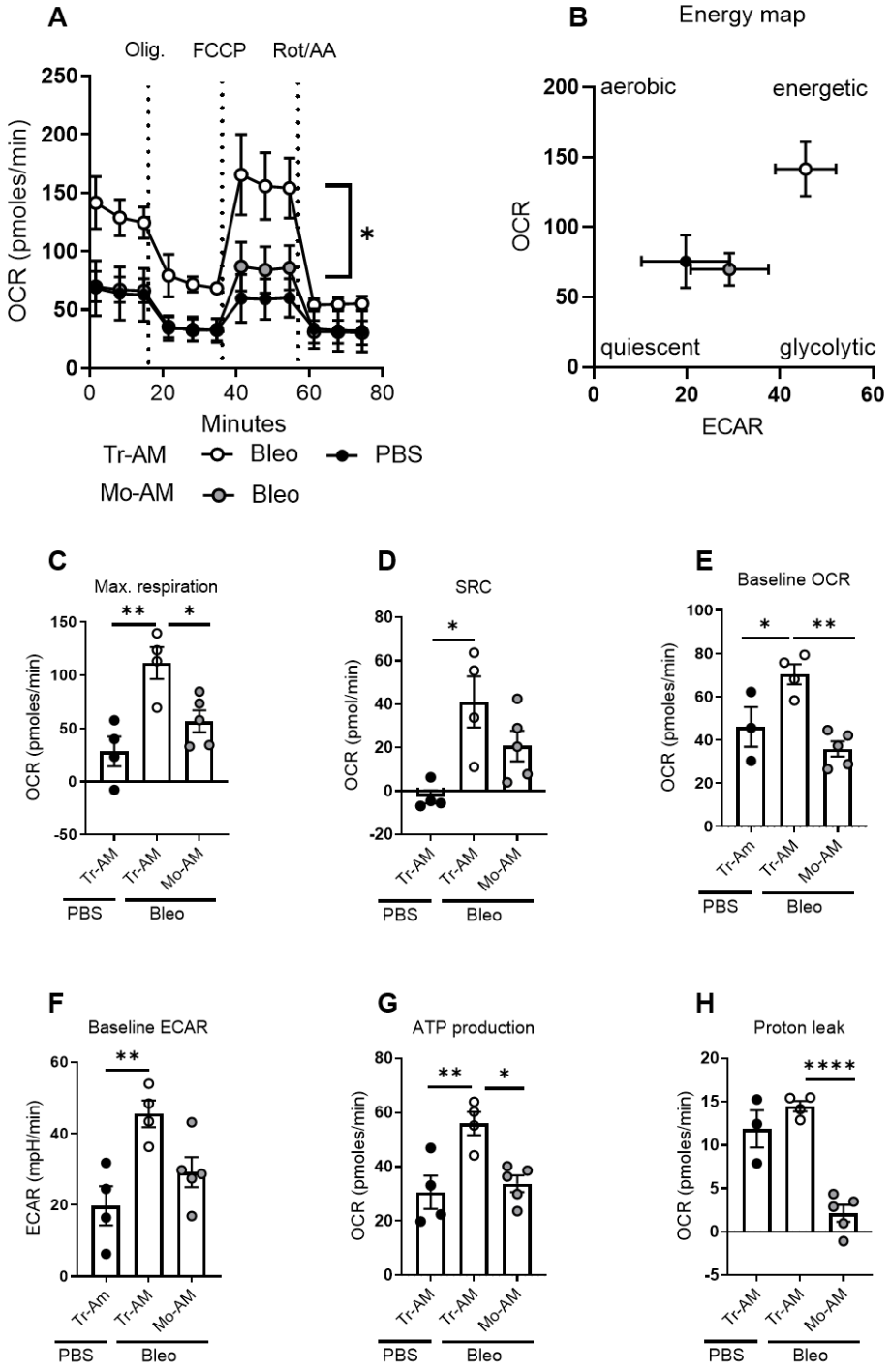

Figure 4.12. Seahorse mitochondrial stress test of Mo-AM and Tr-AM at d21 post bleomycin. Mitochondrial stress test of Mo-AM and Tr-AM in PBS or bleomycin dosed mice at d21, assessed after injection of Oligomycin, FCCP and Rotenone/Antimycin A. A) Analysis of oxygen consumption rate (OCR). B) Energy map showing four energy states: quiescent, energetic, aerobic and glycolytic. C) Maximal respiration D) Spare respiratory capacity (SRC) E) Basal respiration F) Non-mitochondrial oxygen consumption G) ATP production H) Proton leak. PBS Tr-AM n = 4, bleo Tr-AM n = 4, bleo Mo-AM n = 5; representative of three independent experiments. Data presented as mean ± S.E.M. Significance tested by One-Way ANOVA with Dunn's multiple comparison test, * P < 0.05, ** P< 0.01, *** P < 0.005, *** P < 0.001.

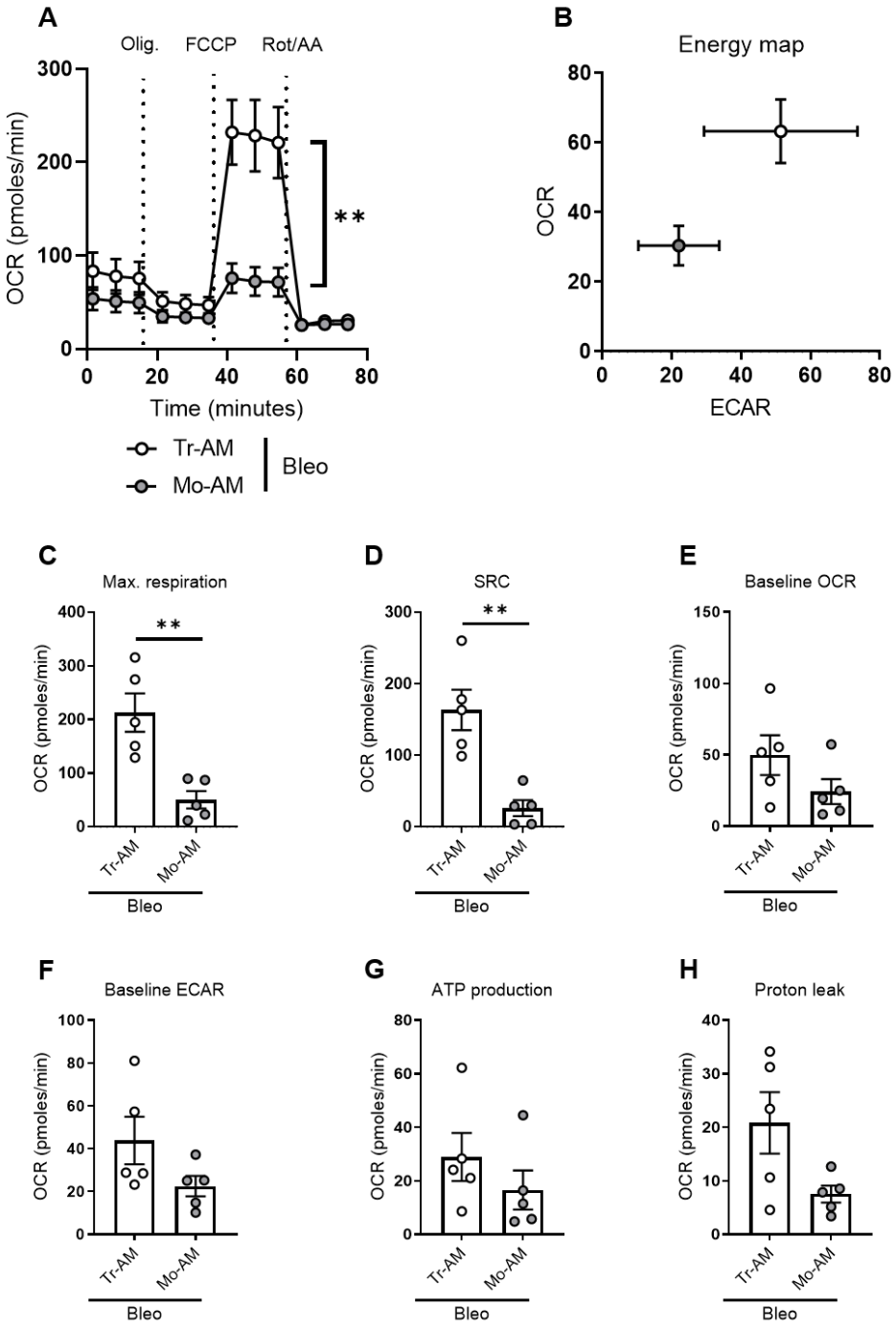

Figure 4.13. Seahorse mitochondrial stress test of Mo-AM and Tr-AM at d7 post bleomycin. Mitochondrial stress test of Mo-AM and Tr-AM in bleomycin dosed mice at d7, assessed after injection of Oligomycin, FCCP and Rotenone/Antimycin A. A) Analysis of oxygen consumption rate (OCR). B) Energy map showing four energy states: quiescent, energetic, aerobic and glycolytic. C) Maximal respiration D) Spare respiratory capacity (SRC) E) Basal respiration F) Non- mitochondrial oxygen consumption G) ATP production H) Proton leak. bleo Tr-AM n = 5, bleo Mo-AM n = 5; representative of three independent experiments. Data presented as mean ± S.E.M. Significance tested by Mann Whitney U test, * P < 0.05, ** P< 0.01.

4.3.7 Targeting SDH in AMs with liposomes

The finding shown here suggest that during the pathogenesis of pulmonary fibrosis Tr-AMs acquire an energetic phenotype, characterised by high rates of OXPHOS. We next assessed how manipulation of this phenotype impacts the pathogenesis of lung fibrosis. Succinate dehydrogenase (SDH) links the TCA cycle to the electron transport chain and is a key enzyme in oxidative phosphorylation. Gene expression analysis in AMs of IPF patients and healthy controls has shown that SDHC is significantly decreased in IPF AMs (Figure 4.14 C), suggesting a potential target site to rewire AM metabolic phenotype.

To better understand the impact of AM targeted SDH inhibition during pulmonary fibrosis, liposomes containing the specific SDH inhibitor dimethyl malonate (DMM) and empty (vehicle) liposomes were utilised. DMM was selected as it is a succinate analogue and results in SDH competitive inhibition and succinate accumulation, while incubation with succinate increases the overall available succinate pool, which can also have signalling functions in addition to its role in oxidative phosphorylation. The utilised liposomes were 1.5 – 2.0 µm in diameter, allowing phagocytosis by AMs and were tagged with a DiD dye, to facilitate tracking by flow cytometry. Titration experiments in naïve mice showed that 1:1 and 1:2 dilutions of liposomes with PBS (DMM concentrations 9.6mM and 4.8mM, respectively) resulted in a high proportion of neutrophils and DCs taking up liposomes, while this markedly decreased at a dilution of 1:4 (DMM concentration 2.4mM) and still resulted in uptake by over 90% of AMs (Figure 4.15 A). The 1:4 dilution of liposomes in PBS (DMM concentration 2.4mM) was therefore selected for further experiments. This concentration of DMM-liposomes or vehicle-liposomes was subsequently administered to PBS or bleomycin dosed mice (at the same time). Lungs were harvested on d1, d3 and d7 and downstream effectors of succinate accumulation, *Hif1α* and *IL-1β* were analysed by gene expression analysis. Indeed, *Hif1α* gene expression was significantly increased in AMs 3 days after administration of bleomycin and DMM-liposomes, compared to PBS mice (Figure 4.15 C), although vehicle-liposomes induced a similar trend. Furthermore there was a trend of

increased *Il-1β* expression at d7 post bleomycin and DMM-liposome treatment, compared to the PBS group (Figure 4.15 B).

Finally, lungs were harvested 21 days post bleomycin and liposome administration and liposome uptake by AMs, neutrophils, DCs and monocytes was analysed by flow cytometry. This showed that even 21 days after administration, 80 – 90% of AMs were positive for the DiD liposome fluorophore (Figure 4.16 A), indicating liposome uptake. In bleomycin dosed mice this was only about 70% due to recruitment of Mo-AMs from the periphery, which had not been exposed to the liposomes (Figure 4.16 A). Furthermore, up to 50% neutrophils in bleomycin dosed mice indicated liposome uptake (Figure 4.16 B) as well as about 20% DCs (Figure 4.16 C) and 10% monocytes (Figure 4.16 D), however total numbers of these populations were low (Figure 4.16 F-H).

Taken together, these results suggest that administration of 2.4mM DMM in liposomes to target AMs induces downstream effector genes of succinate accumulation and targets mainly AMs, although a small proportion is taken up by neutrophils, monocytes and DCs. However, these populations are only present in very small proportions at d0 when liposomes were administered.

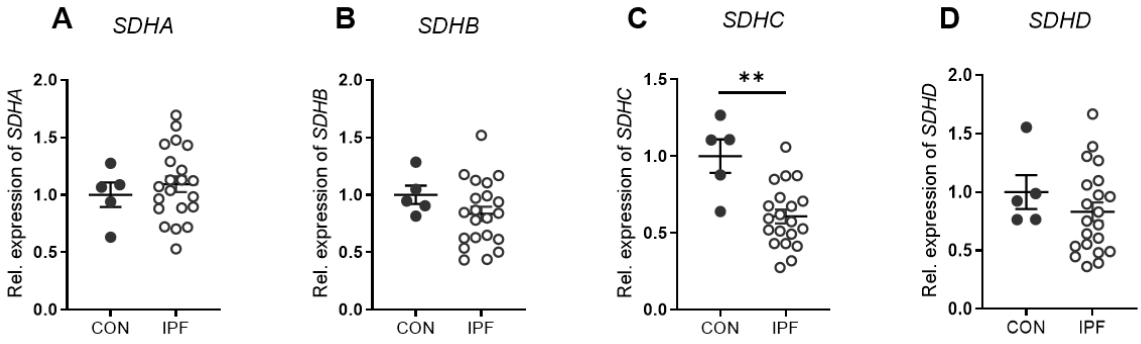

Figure 4.14. SDHC gene expression is decreased in IPF AMs. A – D) Gene expression analysis of SDH subunits *SDHA* (A), *SDHB* (B), *SDHC* (C) and *SDHD* (D) in AMs from IPF patients (n = 21) and healthy controls (n = 5), *ACTB* was used as housekeeping genes. Data presented as mean ± S.E.M. Significance tested by Mann Whitney U test, ** P < 0.01.

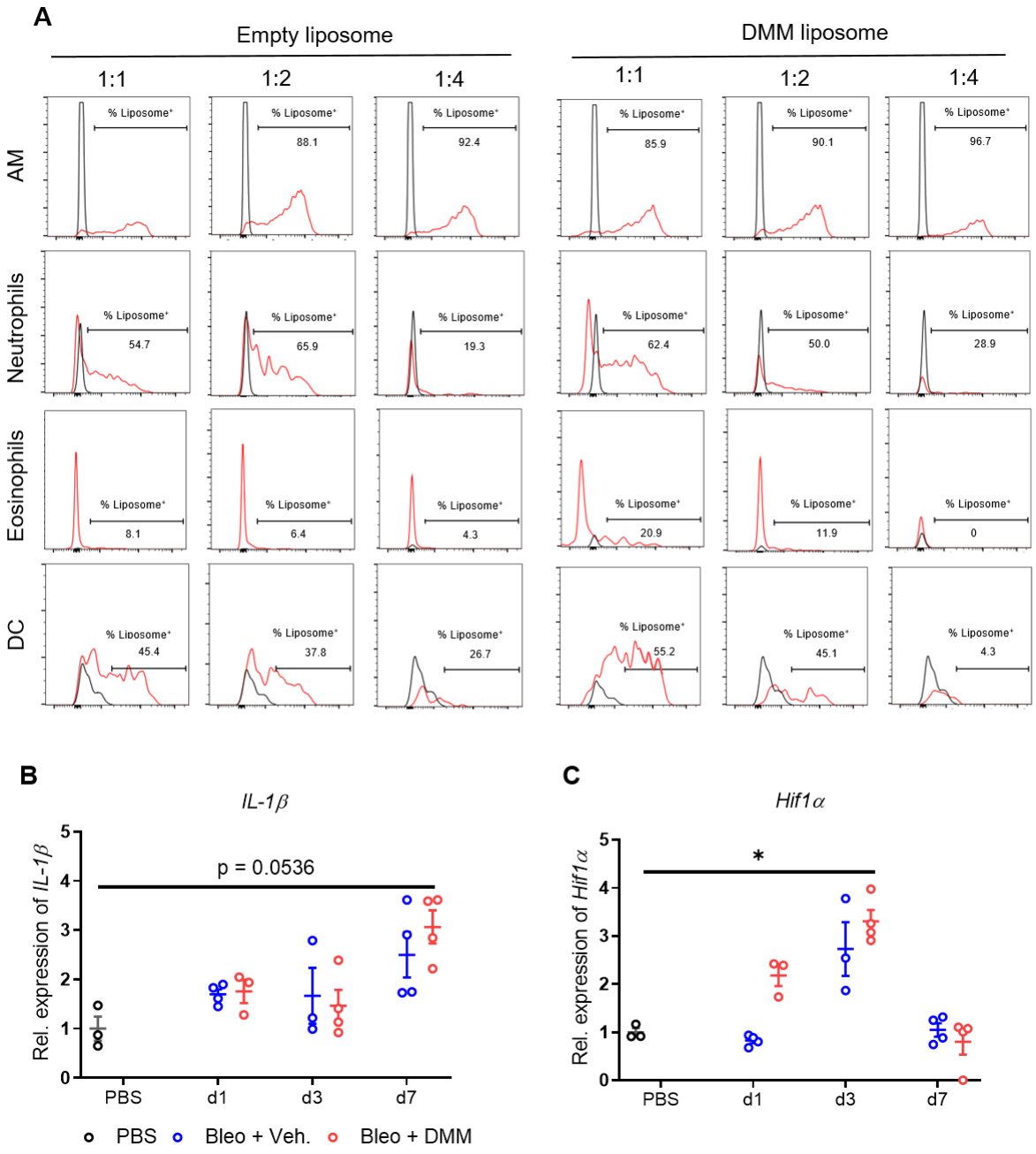

Figure 4.15. Dose and time titration of DMM-liposomes *in vivo*. A) Representative flow cytometry plots of liposome uptake (red) in AMs, neutrophils, eosinophils and DCs 21 days after administration of 1:1 (9.6mM), 1:2 (4.8mM), 1:4 diluted (2.4mM) liposomes or PBS (black). B – C) Gene expression analysis of *Il-1β* (B) and *Hif1α* (C) in AMs at d1, d3 or d7 after administration of PBS or bleomycin and vehicle-liposomes or DMM-liposomes. Data presented as mean ± S.E.M. Significance tested by Kruskal Wallis test plus Dunn's multiple comparison test per time point, * $P < 0.05$.

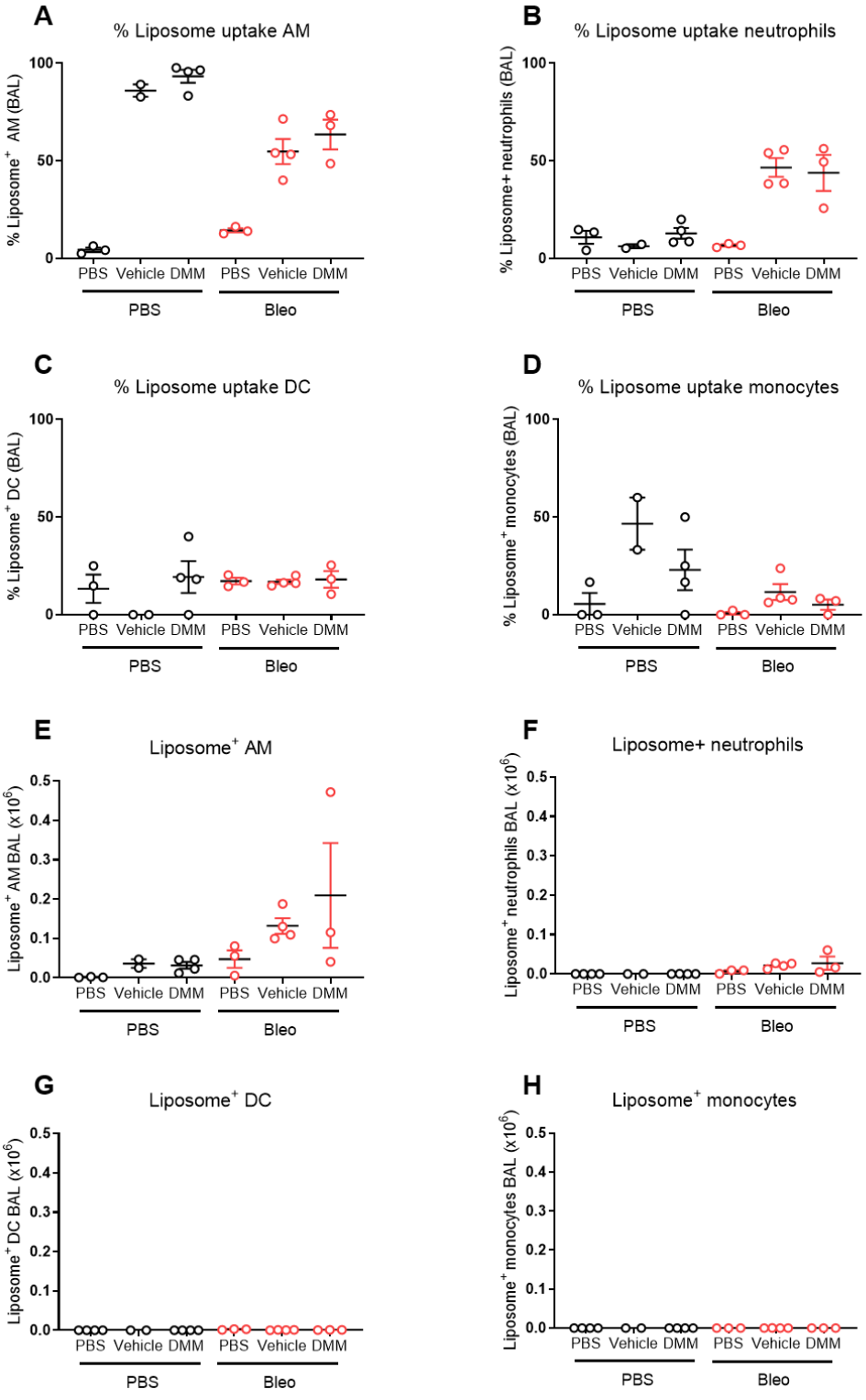

Figure 4.16. Liposome uptake by immune cell populations during bleomycin induced pulmonary fibrosis. A – D) % liposome⁺ AM (A), neutrophils (B), DCs (C) and monocytes (D) in BAL at d21 post administration of PBS or bleomycin (0.05U) and PBS, vehicle-liposomes or DMM-liposomes (2.4mM). E – H) Total liposome⁺ AMs (E), neutrophils (F), eosinophils (G), monocytes (H) in BAL at d21 post administration of PBS or bleomycin (0.05U) and PBS, vehicle-liposomes or DMM-liposomes (2.4mM). Data presented as mean ± S.E.M.

4.3.8 Preventative treatment with DMM-liposomes improves pulmonary fibrosis

Next, the effect of AM-targeted SDH inhibition by DMM-liposomes on bleomycin induced pulmonary fibrosis pathogenesis was assessed. DMM-liposomes (2.4mM), vehicle-liposomes or PBS was administered to PBS or bleomycin treated mice (Figure 4.2A) and lungs were harvested at d21. While preventative treatment with DMM-liposomes did not alter total numbers of BAL or lung cells (Figure 4.17 A-B), elastance and compliance were significantly improved, compared to vehicle treated bleomycin exposed mice (Figure 4.17 D-E). Furthermore, preventative treatment with DMM-liposomes decreased gene expression of *Col1α1* and *Tgfβ-1* compared to the PBS treated bleomycin exposed group, although vehicle-liposomes also had an intermediate effect (Figure 4.17 F and J). There was no change in gene expression of *Col3α1*, *Col4α1* or *Fn1*.

Next, therapeutic AM-targeted SDH inhibition by DMM-liposomes was assessed. Mice were exposed to bleomycin or PBS on d0 and treated with DMM-liposomes (2.4mM), vehicle liposomes or PBS once during peak fibrosis, on d10 and lungs were assessed at day 21. However, one-time treatment with DMM-liposomes at d10 during the bleomycin mouse model of pulmonary fibrosis did not significantly alter BAL or lung cell count (Figure 4.18 A-B), lung function (Figure 4.18 C – E) or fibrosis related gene expression in AMs (Figure 4.18 F-J). Similarly, repeated treatment with DMM-liposomes (every 3rd day from d10 onwards) did not significantly improve lung function or fibrotic phenotype (Figure 4.19).

Overall, AM-targeted SDH inhibition is promising as it improved pulmonary fibrosis when administered preventatively and showed promising trends when administered therapeutically, however these need to be further investigated to draw final conclusions.

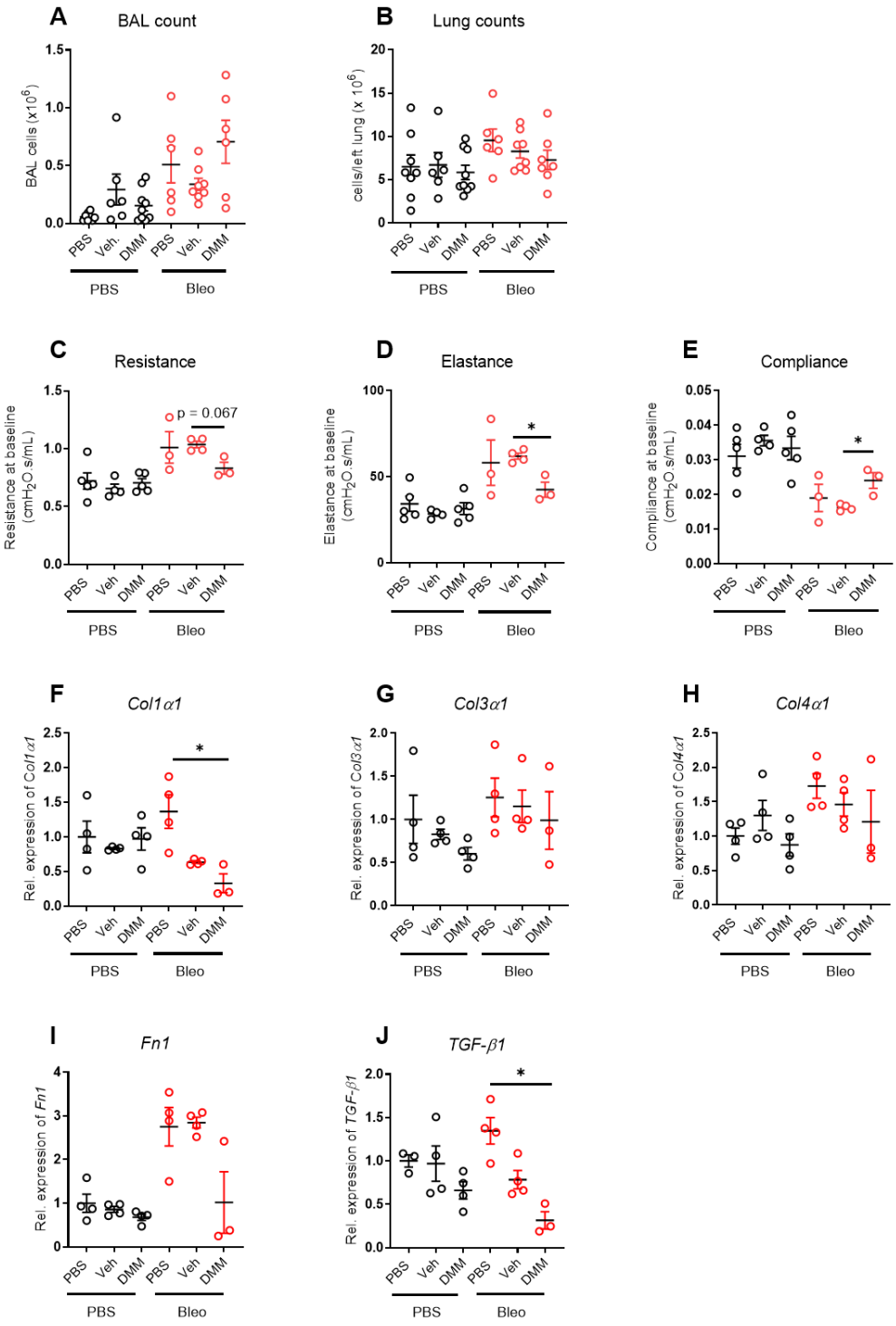

Figure 4.17. Preventative treatment with DMM-liposomes improves lung function during pulmonary fibrosis. PBS or bleomycin exposed mice were treated with DMM-liposomes, vehicle-liposomes or PBS on d0 and lungs were harvested on d21. A – B) BAL (A) and lung cell counts (B). C – E) Dynamic resistance (C), elastance (D) and compliance (E). F – J) Gene expression analysis of *Col1α1*, *Col3α1, Col4α1, Fn1* and *Tgfβ-1*, *Actb* was used as housekeeping gene. N = 3 – 4 per group, A – B two independent experiments pooled. Data presented as mean ± S.E.M. Significance tested by Kruskal Wallis test and Dunn's multiple comparison test, * $P < 0.05$.

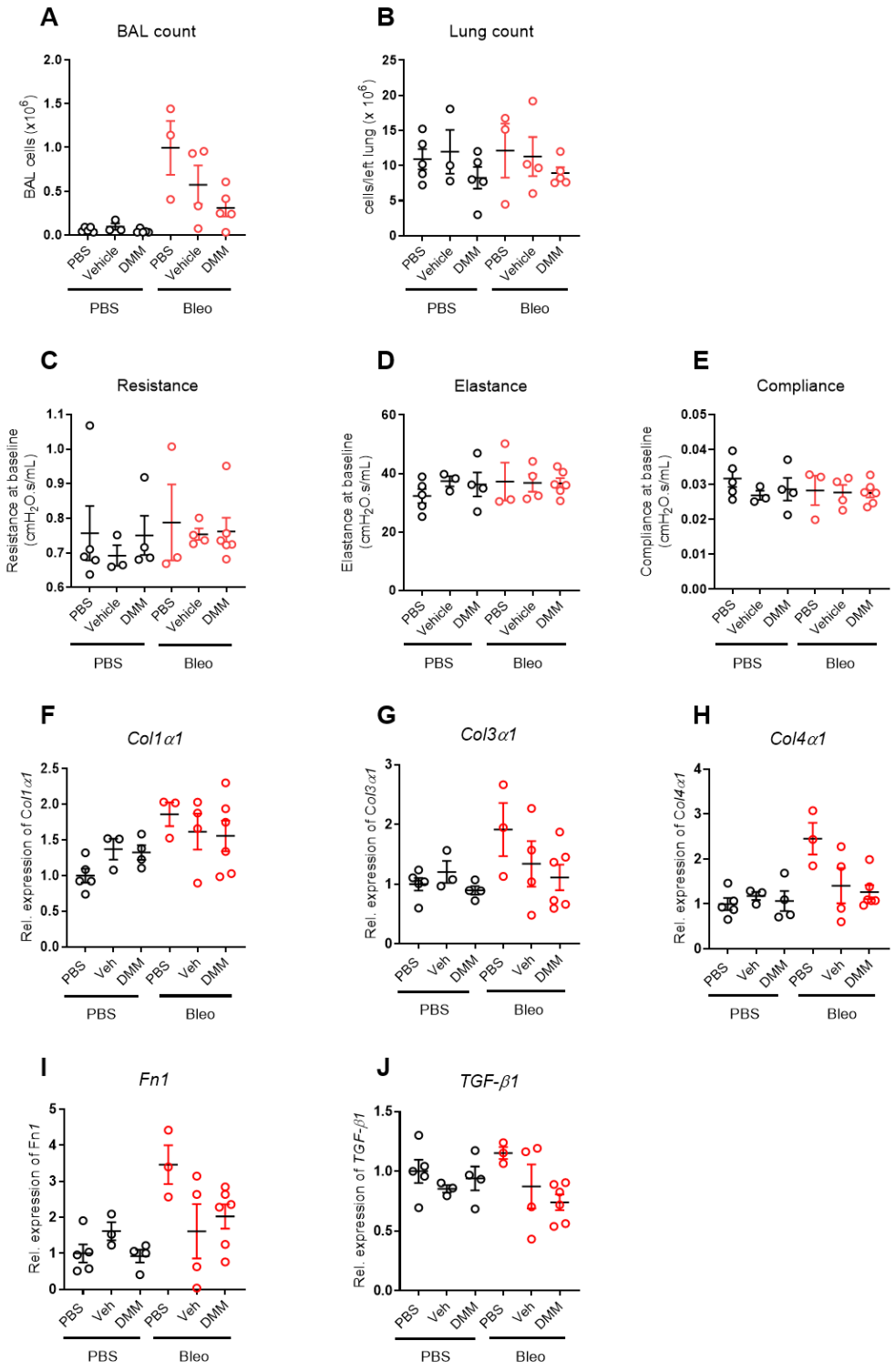

Figure 4.18. Therapeutic treatment with DMM-liposomes during pulmonary fibrosis. Mice were exposed to PBS or bleomycin on d0, treated with DMM-liposomes, vehicle-liposomes or PBS on d10 and lungs were harvested on d21. A – B) BAL (A) and lung cell counts (B). C – E) Dynamic resistance (C), elastance (D) and compliance (E). F – J) Gene expression analysis of *Col1α1*, *Col3α1, Col4α1, Fn1* and *Tgfβ1*, *Actb* was used as housekeeping gene. N = 3 – 6 per group, A – B two independent experiments pooled. Data presented as mean ± S.E.M. Significance tested by Kruskal Wallis test and Dunn's multiple comparison test.

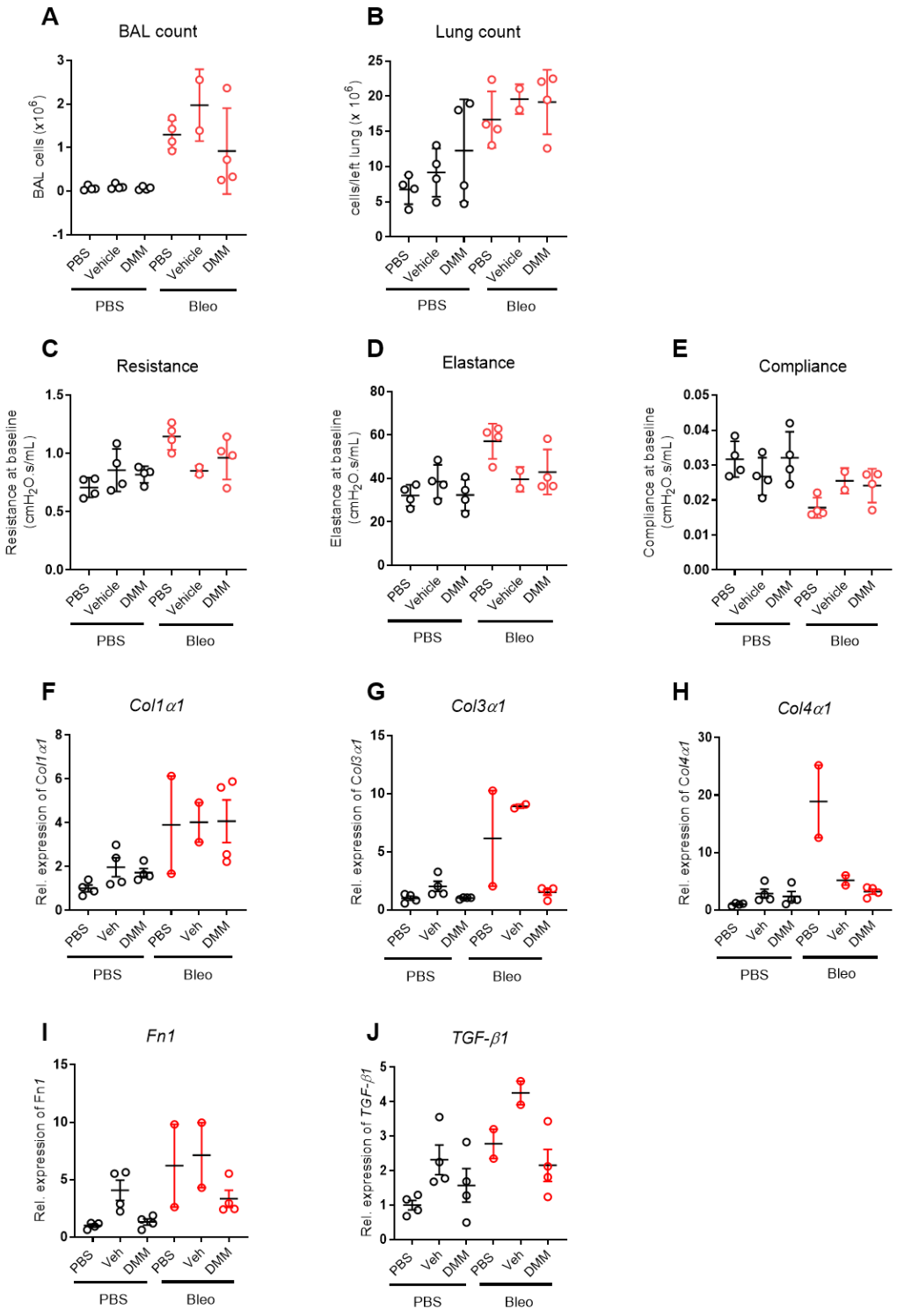

Figure 4.19. Repeated therapeutic treatment with DMM-liposomes during pulmonary fibrosis. Mice were exposed to PBS or bleomycin on d0, treated with DMM-liposomes, vehicle-liposomes or PBS every third day from d10 onwards and lungs were harvested on d21. A – B) BAL (A) and lung cell counts (B). C – E) Dynamic resistance (C), elastance (D) and compliance (E). F – J) Gene expression analysis of *Col1α1*, *Col3α1, Col4α1, Fn1* and *Tgfβ1*, *Actb* was used as housekeeping gene. N = 2 – 4 per group, A – B two independent experiments pooled. Data presented as mean ± S.E.M. Significance tested by Kruskal Wallis test and Dunn's multiple comparison test.

4.3.9 DMM inhibition and succinate administration in IPF AMs *ex vivo*

In parallel, DMM and succinate were administered to sorted AMs from IPF patients *ex vivo* and AM functional gene expression was assessed by qPCR. Incubation with DMM *ex vivo* resulted in decreased gene expression of *MMP-1, MMP-2, MMP-9* and *MMP-12*, while pro-inflammatory AM marker *CD86* was increased (Figure 4.20 A), indicating a reduced wound-healing oriented AM phenotype overall.

Exposure to succinate similarly decreased the gene expression of *MMP-1, MMP-2, MMP-9 and MMP-12*, as well as *MMP-7, CCL-22* and *TGFβ-1,* while *CD86* and *CCL-18* were increased, indicating an even stronger effect of rewiring AM phenotype than SDH inhibition by DMM.

Together these data suggest a promising effect of SDH inhibition and treatment with succinate on AM phenotype during pulmonary fibrosis.

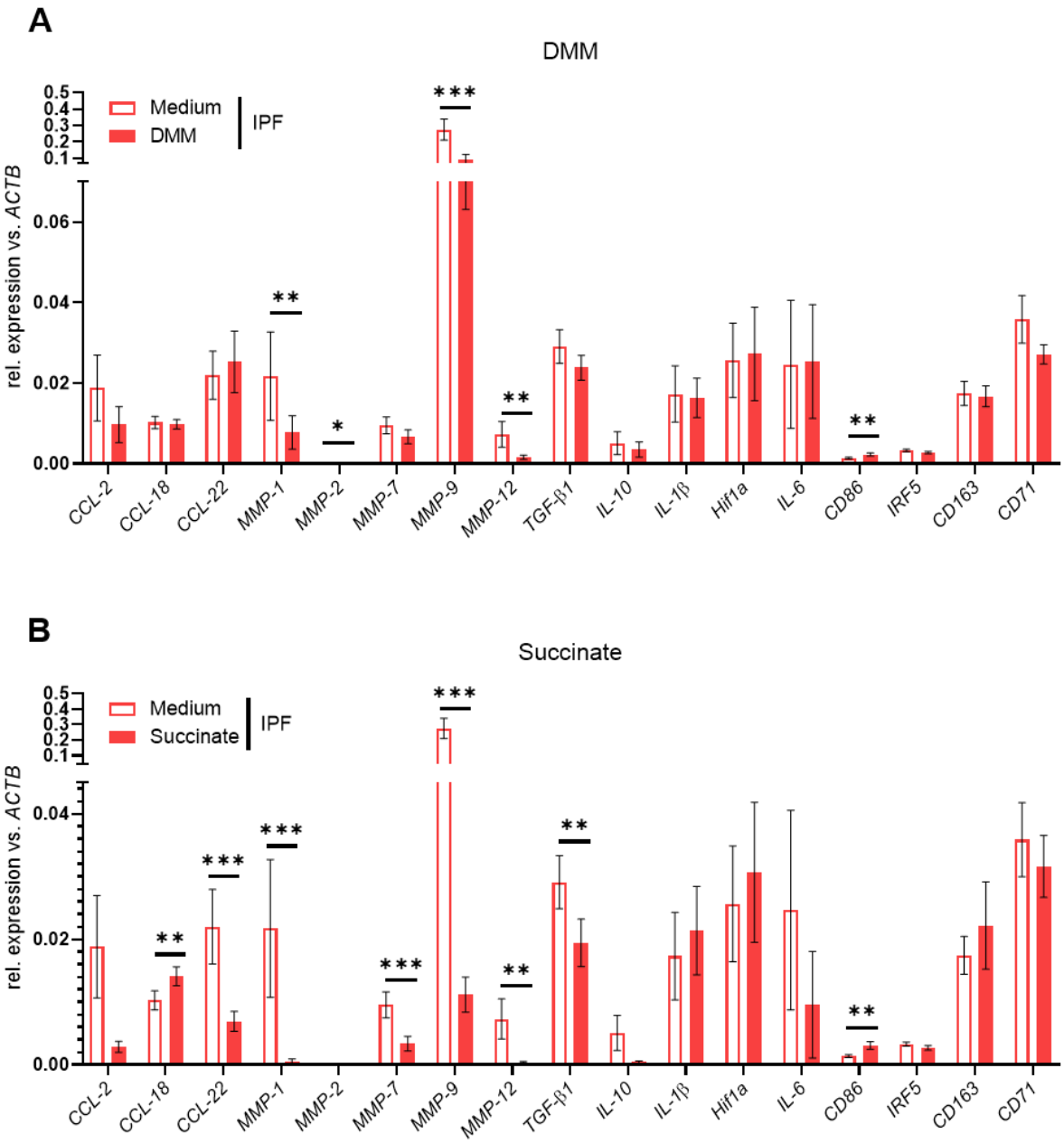

Figure 4.20. *Ex vivo* culture with DMM and succinate alters IPF AM phenotype. A – B) Gene expression analysis of AM key effector function genes in CD206^{+} sorted AMs from IPF patients, after 24 hours culture with 10mM DMM (A) or 10mM succinate (B) (n = 12) compared to medium control; *ACTB* was used as housekeeping gene. Data presented as mean ± S.E.M of $2^{-(\Delta CT)}$ showing relative gene expression. Statistical significance tested by Wilcoxon matched-pairs signed rank test between treated and medium control groups, * P < 0.05, ** P < 0.01, *** P < 0.005.

4.4 Discussion

The overall aim of this chapter was to establish the bleomycin mouse model of pulmonary fibrosis, in order to investigate the metabolic phenotype of Tr-AM and Mo-AM during pulmonary fibrosis. Furthermore, the use of AM targeted metabolic inhibitors, particularly inhibiting SDH, was assessed using liposome delivery.

In our studies, we utilised male, 10-12 week old C57Bl/6 mice, administering a one-time dose of 2.5U/kg bleomycin oropharyngeal[276–279], which induced robust and reproducible pulmonary fibrosis. Based on the recommendations of the American Thoracic Society for the use of animal models for pulmonary fibrosis, a combination of readouts was applied to determine the inflammatory, fibrotic and pathological phenotype[303]. These include assessment of collagen deposition by histological staining with Sirius Red and fibrosis score using the modified Ashcroft score, gene expression analysis of collagens *Col1α1, Col3α1, Col4α1* and *Fibronectin-1*, analysis of BAL and lung immune infiltrates by flow cytometry and assessment of respiratory mechanics (dynamic resistance, elastance and compliance) by FlexiVent. These readouts confirmed that this model recapitulates many features of human disease and is comparable to published data on this model[300–302]. Here, increased total BAL and lung cell counts were increased at d7 and d21 (lung only), while AM, monocytes, eosinophils and neutrophils were increased in BAL at d7, as previously reported, contributing to the fibrotic phenotype by secreting TGF-β, MMPs, TNF-α, IL-1β and endothelin-1[304–309]. In accordance with the published model, peak fibrosis score, fibrosis gene expression and impaired elastance and compliance were observed at d21 post bleomycin[300] and these changes were decreased or resolved by d42, highlighting that bleomycin induced fibrosis is not a model for irreversible, persistent fibrosis[310].

Central carbon metabolites had not previously been investigated over the time course of the bleomycin mouse model and while initially, it was planned to analyse all key metabolites in glycolysis and the Krebs cycle, several were excluded from the final target list as they were not stable enough to be detected or their peaks overlapped. The increased glycolysis and TCA cycle intermediates at d7 is in parallel to the large influx of immune cells and

increased activity and highlights inflammation at this time point. It is in line with immune infiltration of the lungs and indicates increased energy demand to support cytokine production, including TNF-α, IL-6, IL-1β, CCL-3 and MCP1[261]. Furthermore, central carbon metabolites, such as succinate or fumarate, may be released for signalling purposes[96,140,241] or secreted by apoptotic cells. At d21 post bleomycin, only the first half TCA metabolites were still significantly increased, as well as glucose, pyruvate and lactate, paralleling the metabolite profile in IPF BAL, where only lactate, isocitrate and malate were increased (Figure 3.5).

To further investigate the underlying metabolic phenotypes of AMs during pulmonary fibrosis Tr-AM and Mo-AM were sorted based on the expression of SiglecF. To confirm this marker in the model utilised here, a dye staining phagocytic cells (PKH26) was administered one day before exposure to bleomycin, to label tissue resident AMs. First, however, PKH26 concentration for oropharyngeal staining was optimised. Previous studies used 0.5μM – 2.5μM PKH26 for intraperitoneal staining[311–313] and 10 - 15μM for intravenous staining[314,315]. As oropharyngeal dosing was considered even more sensitive and AMs make up the majority BAL cells, concentrations between 0.05μM and 0.5μM were tested here, and staining with 0.5μM cell tracker proved most reliable. Subsequent staining with PKH26 prior to bleomycin exposure confirmed SiglecF^{high} expression as a marker for Tr-AM and SiglecF^{low} expression as a marker for Mo-AM as suggested by Misharin *et al*.[41,212], which infiltrated the lungs upon injury induced by bleomycin. While both Tr-AM and Mo-AM can adopt a fibrotic phenotype[285], Misharin *et al*. showed that Mo-AMs downregulate fibrosis genes related genes over time as they differentiate into Tr-AMs[212]. The underlying metabolic phenotype of Tr-AM and Mo-AM had not been investigated in detail previously and surprisingly the Tr-AMs showed a high increase of OXPHOS and glycolysis upon injury by bleomycin, while Mo-AMs had much lower levels in comparison. One reason for this might be that Tr-AMs had been exposed to the lung environment for longer, which critically shapes AM phenotype[283]. It would therefore be interesting to correlate fibrosis gene expression to metabolism genes and phenotype over pseudo time as Mo-AMs differentiate into Tr-AMs post bleomycin, to investigate how the two trajectories correlate.

One key metabolic enzyme is SDH, which links the TCA cycle to the electron transport chain with its four subunits. As this is one location where the TCA cycle breaks during macrophage polarization[127] and the accumulation of succinate leads to macrophage metabolic rewiring *via* the induction of Il-1β and Hif1α[136], SDH is essential in regulating the macrophage metabolic programme. The SDH subunit C, which binds ubiquinone and initiates electron transfer, is downregulated in IPF AMs, indicating alteration in this pathway during IPF. DMM is hydrolysed into malonate intracellularly, which is a competitive inhibitor for SDH, resulting in succinate accumulation[294]. To target SDH in AMs specifically, DMM encapsulated in liposomes was administered oropharyngeal to mice, either preventatively before exposure to bleomycin, or therapeutically afterwards. Therefore, a similar system to the traditionally used chlodronate liposomes was applied, utilising empty liposomes as vehicle controls. Previously published studies for chlodronate encapsulating liposomes used volumes ranging from 20µl to 100 µl[316–319]. Titration studies shown here indicated a concentration of 2.4mM DMM (10µl liposomes diluted 1:4 in PBS) does not induce inflammation and was chosen as 90% of BAL AMs were positive for the DiD fluorophore tagged to the liposomes. Furthermore, expression of downstream effectors of succinate, *Il-1β* and *Hif1α* was detected using this concentration. Preventative treatment with DMM-liposomes, vehicle control or PBS showed that 21 days post bleomycin over 90% of AMs from mice which did not receive bleomycin stained positive for the DiD dye, while in the bleomycin treated group it was only around 60%, indicating influx of Mo-AMs as described earlier. While gene expression of *Col1α1* and *Tgfβ1* were significantly decreased compared to the PBS control group, the vehicle group also exhibited decreased expression. This vehicle effect has been observed in other studies, inducing cytokines[316] and altering lung function[320], and needs to be taken into account when drawing conclusions. This is difficult however as some groups administer PBS as control and some administer empty liposomes, however not many groups use both controls[316,317,321]. To overcome this effect, liposomes may need to be titrated to even lower concentrations.

While over 500 studies have been published in the last 35 years investigating potential drugs in the bleomycin mouse model, less than 5% administered the drugs after d7[322]. For

better translation into human disease and to investigate the potential to reverse fibrosis, therapeutic administration during peak fibrosis is essential[323]. Here, DMM-liposomes, vehicle control or PBS control was administered as a single dose at d10 post bleomycin or as repetitive treatment every third day between d10 and d21. While neither significantly improved pulmonary fibrosis at d21, sample numbers for these experiments are very limited, which makes it difficult to draw final conclusions. As only a limited amount of liposomes was secured for these experiments, it would be interesting to repeat these to assess reproducibility. Another caveat, which is highlighted by the liposome provider (encapsula nanoscience) include fluorescent lipid being incorporated into the cell wall during phagocytosis, which during apoptosis is then taken up by other phagocytes indicating a false-positive liposome staining. As already discussed, the vehicle effect needs to be considered when drawing conclusions and may be prevented by further titrating down the liposome concentration. Finally, mannosylated liposomes may be useful for future experiments to target AMs specifically and prevent uptake by other phagocytes such as neutrophils, which is particularly relevant for therapeutic treatment when immune cell numbers are increased. To circumvent the vehicle effect of liposomes, administration of free succinate could also be considered, as well as novel targeting strategies such as siRNAs.

To complement the *in vivo* DMM studies, DMM was also administered to human IPF AMs *ex vivo*. Based on the study by Mills *et al*., using BMDMs[136], IPF AMs were incubated with 10mM DMM for 24 hours, which resulted in decreased MMP gene expression and increased expression of M1 macrophage marker CD86, indicating a more pro-inflammatory phenotype overall. MMPs are elastolytic and have been implicated in the pathogenesis of pulmonary fibrosis[77,324], therefore decreased DMM expression may indicate an improved phenotype. Similarly, incubation with succinate resulted in decreased DMM expression, as well as decreased CCL-22, TGF-β1 and CD86, while lymphocyte attracting chemokine CCL-18 was increased. While these changes are less pronounced than after culture with other metabolic inhibitors such as 2-DG (Chapter 3), they still indicate that rewiring of IPF AM phenotype is possible through metabolic inhibition.

4.5 Conclusion

Overall, the bleomycin mouse model of pulmonary fibrosis was established and was consistent with published data. Metabolic phenotyping of Mo-AMs and Tr-AMs during the bleomycin mouse model revealed significantly increased utility of both OXPHOS and glycolysis pathways for Tr-AMs but not Mo-AMs with most pronounced changes occurring during peak fibrosis. These findings prove distinct metabolic programmes underlying AM phenotype, the link of which warrants further investigation. Furthermore, preliminary experiments highlighted the use of liposomes encapsulating metabolic inhibitor drugs to target AMs in particular, which will require further testing of reproducibility and potential combination treatment.

5. Itaconate controls the severity of pulmonary fibrosis

5.1 Introduction

In chapter 3, we assessed the metabolic alterations in airway macrophages in patients with interstitial lung disease, compared to healthy controls. Following this, in chapter 4 AM-targeted delivery of SDH-inhibitor DMM by liposomes was examined and its impact on bleomycin induced pulmonary fibrosis was analysed. Recently, the endogenous metabolite itaconate has been suggested as a potent AM regulator: in this chapter we aimed to define the role of itaconate during pulmonary fibrosis.

Treatment options for IPF are still limited to disease-slowing pharmaceuticals Nintedanib and Pirfenidone, with a median survival of three years after diagnosis[325,326], encouraging the search for novel therapeutic strategies. As discussed in more detail in earlier chapters, AMs play an important role in regulating mechanisms underlying IPF[226] and are suitable as targets to initiate phenotype rewiring as their high level of plasticity enables AMs to acquire phenotypes which can either drive or resolve fibrotic responses to lung injury[327,328]. Our group has recently shown that AM phenotype is tightly linked to disease outcome in IPF patients, as increased numbers of transferrin receptor-negative ($CD71^-$) AMs were associated with worse disease outcome[226]. Macrophage activation is furthermore tightly linked to underlying cellular metabolism[83]. Several laboratories have shown that activation of bone-marrow derived macrophages results in TCA cycle disruption and accumulation of metabolites, ultimately resulting in metabolic rewiring and functional change[78,123,127,146,329].

Synthesis of itaconate is catalysed by cis-aconitate decarboxylase (CAD), which mediates the decarboxylation of cis-aconitate (from isocitrate) to itaconate[330]. This enzyme is encoded by the gene *ACOD1*, which was previously called immune-responsive gene-1 (*IRG1*)[331]. While itaconate has been shown to have antimicrobial properties by inhibiting the glyoxylate cycle in bacteria[332–335], it is the most highly induced metabolite in murine RAW 264.7 macrophages[331,336,337] and BMDMs[133] upon LPS stimulation *in vitro* and also in human BMDMs[134]. By inhibiting SDH, itaconate can decrease the production of pro-inflammatory cytokines[133,336]. In addition, itaconate has been shown to activate an anti-inflammatory response pathway *in vitro* via the transcription factor NRF2 and the adapter protein

KEAP1[338,339]. While itaconate has been shown to regulate macrophage phenotype and function during pro-inflammatory activation *in vitro*, its function *in vivo* such as during chronic lung disease and role in regulating macrophage pro-fibrotic responses remains largely unknown. This chapter aims to provide insight into the role of itaconate in the context of pulmonary fibrosis.

5.1.1 Hypothesis & Aims

AM derived itaconate regulates wound healing during pulmonary fibrosis and exogenous itaconate ameliorates disease *in vivo*.

Aims:

1. To assess gene expression of *ACOD1* and itaconate levels in IPF and healthy control BAL and sorted AMs
2. To investigate the role of itaconate in a mouse model of pulmonary fibrosis using *Acod1*$^{-/-}$ mice
3. To elucidate how itaconate regulates the pulmonary environment during the fibrotic responses

5.2 Methods

5.2.1 Bleomycin mouse model of pulmonary fibrosis in *Acod1*$^{-/-}$ mice

Male adult (10 – 12 week) *Acod1*$^{-/-}$ or wild type (WT) littermates were exposed via the oropharyngeal (o.p.) route, to a single dose of bleomycin (0.05U; 50µl) or PBS (50 µl). To examine bleomycin induced inflammation, fibrosis and resolution of disease, lungs were harvested at d7 (inflammation), d21 (fibrosis) or d42 (resolution) (Figure 3.1 A) post bleomycin. Lung function was assessed using the FlexiVent system, cells were counted (lung and BAL) and assessed by flow cytometry. Severity of fibrosis was assessed by collagen gene expression, Sirius red staining for collagen, modified Ashcroft score and hydroxyproline assay.

5.2.2 Adoptive transfer of Mo-AMs into *Acod1*$^{-/-}$ mice

Female adult (10 – 12 week) *Acod1*$^{-/-}$ or WT littermates and male adult *Acod1*$^{-/-}$ mice were exposed to a single dose of bleomycin (0.05U; 50 µl, o.p.) or a PBS control (50 µl). On d7 post bleomycin, BAL was harvested from the female mice (*Acod1*$^{-/-}$ and WT) Mo-AMs were sorted by flow cytometry based on expression of Siglec F. Sorted Mo-AMs were pooled per group and 50,000 cells were adoptively transferred (o.p.) into the lungs of male *Acod1*$^{-/-}$ mice (PBS or bleomycin dosed). On d21 and on d42 post bleomycin (2 or 5 weeks after adoptive transfer) lungs were harvested (Figure 3.1 B). Lung function, cell counts, flow cytometry and assessment of fibrosis severity were performed as described in chapter 2.

5.2.3 Therapeutic dosing of itaconate during the bleomycin model

Male adult (10 – 12 week) WT mice were exposed to a single dose of bleomycin (0.05U; 50 µl) or a control of PBS (50 µl). Itaconate (0.25mg/kg; 50 µl) or PBS control (50 µl) were administered o.p. every third day from d10 (d10, d13, d16, d19). On d21 lungs were harvested (Figure 3.1 C). Lung function, cell counts, flow cytometry and assessment of fibrosis severity were performed as described in chapter 2.

5.2.4 Treatment of aged WT mice with itaconate during the bleomycin model

Male aged (52 weeks) WT mice were exposed to a single dose of bleomycin (0.05U; 50 µl) or PBS control (50 µl). Itaconate (0.25mg/kg; 50 µl) or PBS control (50 µl) were administered o.p. every second day from d9. On d14 lungs were harvested (Figure 3.1 C). Lung function, cell counts, flow cytometry and assessment of fibrosis severity were performed as described in chapter 2.

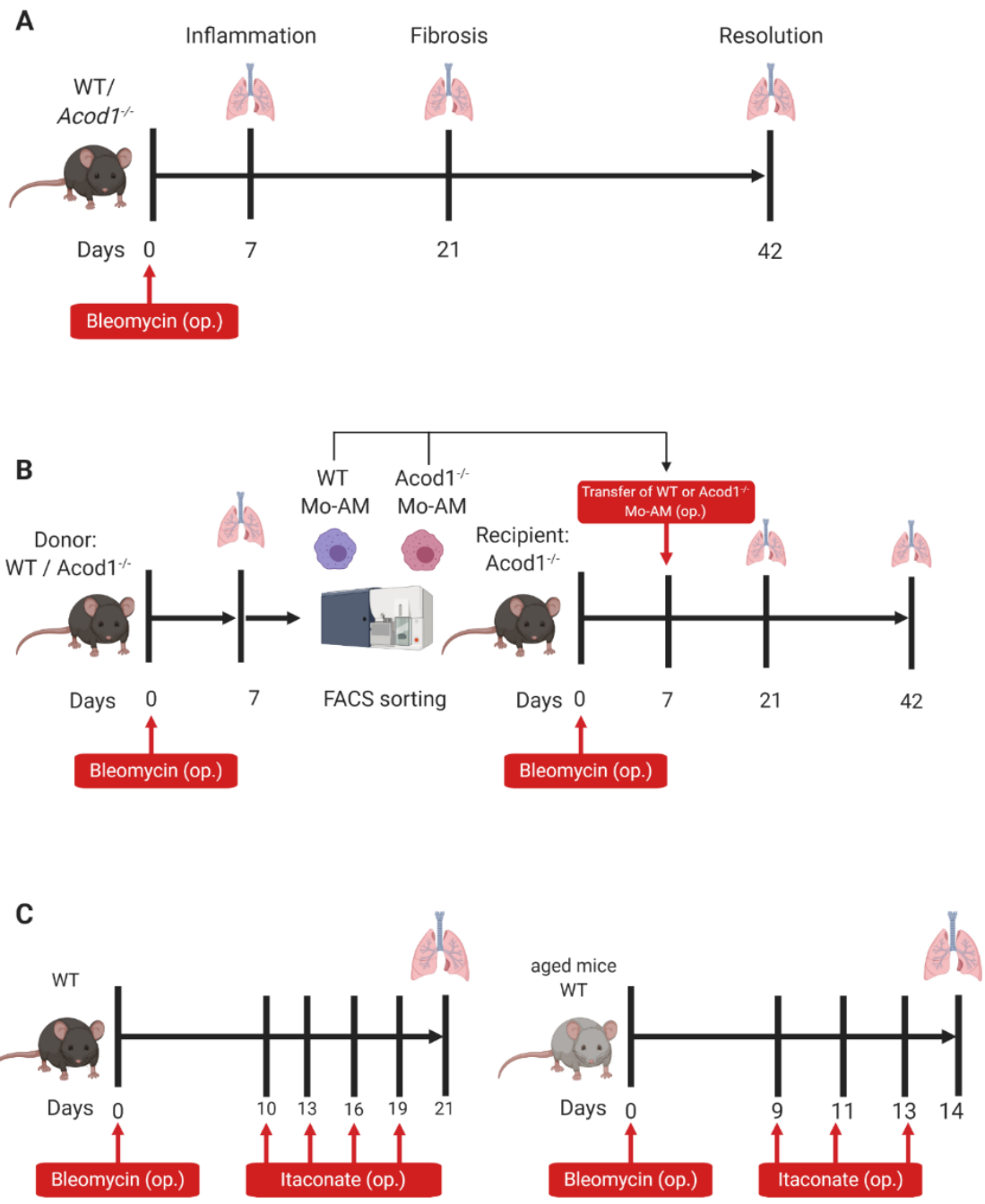

Figure 5.1: Schematic overview of mouse models used in chapter 5. A) Adult male C57BL/6 WT or *Acod1*$^{-/-}$ mice were exposed to either 0.05U bleomycin or 50µl phosphate buffered saline (PBS) on d0. Lungs were harvested at d7, d21 or d42 post bleomycin. B) Adult female C57BL/6 WT or *Acod1*$^{-/-}$ donors and male *Acod1*$^{-/-}$ recipient mice were exposed to either 0.05U bleomycin or 50µl PBS on d0. Lungs were harvested from donor mice at d7, monocyte-recruited AMs were isolated by FACS sorting and 50 000 cells were transferred into lungs of recipient mice. Recipient mice were culled at d21 or d42 post initial bleomycin exposure. C) Adult or aged (52 weeks) male C57BL/6 WT mice were exposed to 0.05U bleomycin or 50µl PBS on d0. Itaconate (0.25mg/kg) was administered as indicated either every 2nd or every 3rd day. Mice were culled at d21 (adult mice) or d14 (aged mice). Op. = oropharyngeal administration.

5.3 Results

5.3.1 The ACOD1/itaconate axis in human and murine pulmonary fibrosis

To determine the expression of *ACOD1* mRNA in the human lung, expression levels were assessed in primary AMs, lung fibroblasts (HLF), bronchial epithelial cells (HBE) and peripheral blood mononuclear cells (PBMCs) from healthy volunteers and IPF patients, however, *ACOD1* levels were below the detection limit in these cell types. Demographics for patient samples used to generate Figures 5.2 A – B are shown in Table 5.1 – 5.2. Although healthy controls used for this study were significantly younger than IPF patients, there was not significant correlation between itaconate in BAL and age (Figure 5.3 A), while there was also no difference in *Acod1* expression upon bleomycin treatment in aged compared to young mice (Figure 5.3 B). AMs were enriched from BAL by magnetic bead sorting on CD206 expression, as this marker is highly expressed on human AMs[235]. Analysis by qPCR (Figure 5.2 A) showed that in healthy control AMs, *ACOD1* was highly expressed and this was significantly decreased in AMs from IPF patients. Itaconate levels in BAL were measured by targeted GC-MS and normalised to cell count. In IPF patients, itaconate levels in BAL were decreased compared to healthy controls (Figure 5.2 B). In contrast*, ACOD1* expression was undetectable by qPCR in HLFs (Figure 5.2 C), HBEs (Figure 5.3 D) or PBMCs (Figure 5.2 E). In the bleomycin mouse model of pulmonary fibrosis, gene expression of *Acod1* was measured by qPCR at d7, d21 and d42 post bleomycin, to assess expression during the inflammatory, fibrotic and resolution stage. While *Acod1* expression levels were significantly increased at d7 in the bleomycin treated group, levels increased even higher at d21 and reduced back to baseline by d42 (Figure 5.2 F). Similarly, itaconate was measured in whole lung homogenates at these time points by targeted GC-MS and was found to be significantly increased at d7 and d21 in the bleomycin treated group, reducing back to baseline levels by d42 (Figure 5.2 G). Taken together, these results indicate significant alteration of the *ACOD1/*itaconate axis in IPF patients and this axis is induced during bleomycin induced pulmonary fibrosis in mice.

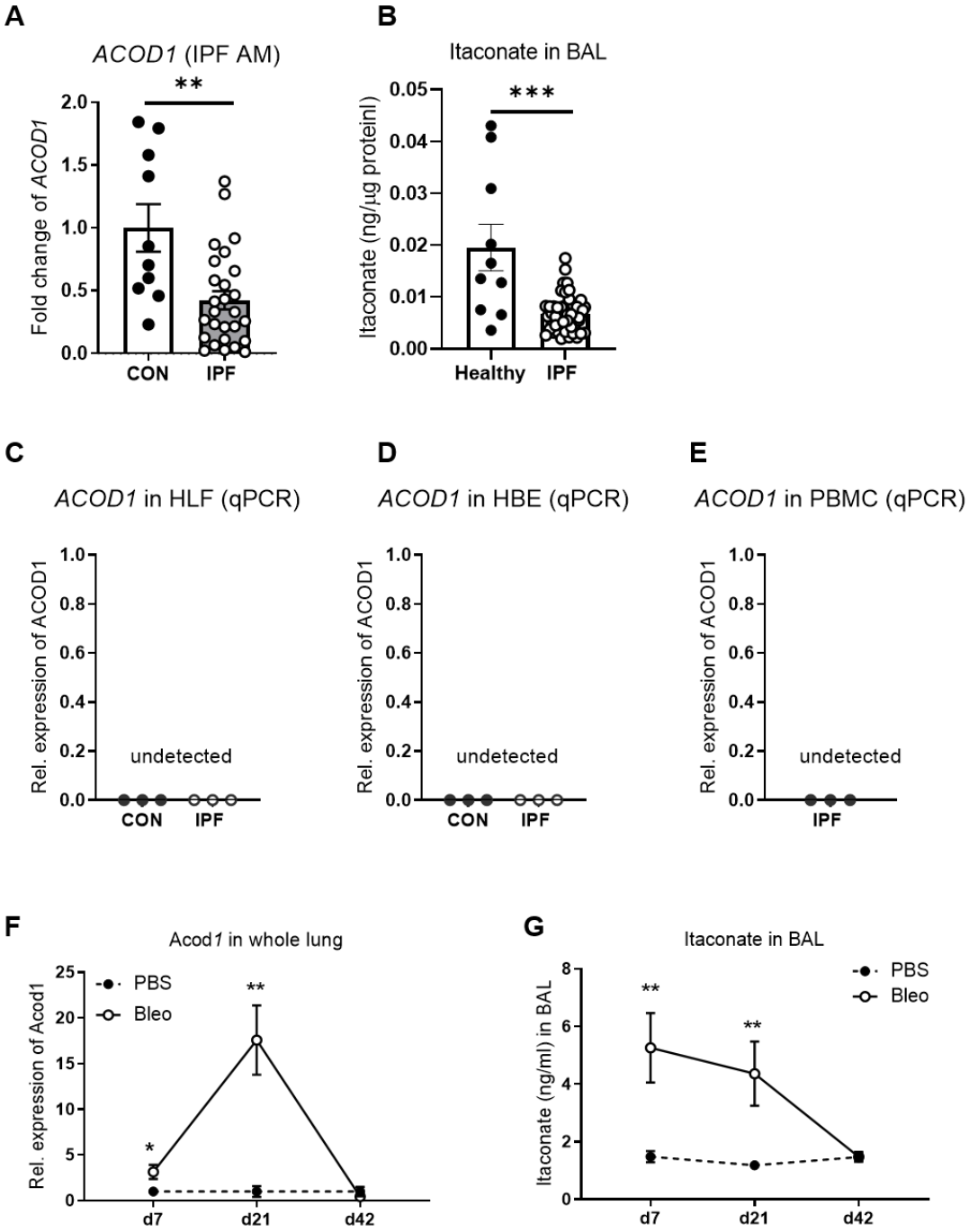

Figure 5.2. The *ACOD1*/itaconate axis is altered in IPF and increased during bleomycin induced pulmonary fibrosis. A) Gene expression analysis of ACOD1 in CD206^{+} sorted AMs from control (n = 5) and IPF (n = 21) donors. *ACTB* was used as housekeeping gene. **B)** Targeted GC-MS analysis of itaconate in bronchoalveolar lavage (BAL) or control (n = 5) and IPF (n = 62) donors, normalised to total protein. **C – E)** Gene expression analysis of *ACOD1* in human lung fibroblasts **(C)**, human bronchial epithelial cells **(D)** and human peripheral blood mononuclear cells **(E)** from control (n = 3) and IPF (n = 3) donors. *ACTB* was used as housekeeping gene. **F)** Gene expression analysis of *Acod1* in lung homogenates of PBS or Bleo dosed mice at d7, d21 and d42 post bleomycin administration; n = 3–8 per group, pooled from two independent experiments. **G)** Targeted GC-MS analysis of itaconate in BAL of PBS or Bleo dosed mice at d7, d21 and d42 post bleomycin administration; n = 3 – 8 per group, pooled from two independent experiments. Data presented as mean ± S.E.M. Significance tested by Mann-Whitney U test *P < 0.05, ** P < 0.01, *** P < 0.001.

Table 5.1: Subject demographics of samples used for qPCR analysis (Figure 5.2 A).

Table showing sex, age, drug-treatment, FEV1, FEV1 % predicted, forced vital capacity (FVC), % predicted FVC, D_{LCO} and smoking status of healthy (n = 5) and IPF (n = 21) samples used for qPCR of *ACOD1* (Figure 5A). Data presented as mean ± S.D.

	IPF (n = 27) Mean ± S.D.	Healthy (n = 10) Mean ± S.D.	T-test
Sex (M/F)	21M / 6F	5M / 5F	
Age	69.5 ± 9.0	43.6 ± 11.0	***
Anti-fibrotic treatment Nintedanib Pirfenidone	41% 45% 55%	N/A	
FEV1	2.3 ± 0.7	2.8 ± 0.8	n.s.
FEV1 (predicted)	85.4 ± 18.5	N/A	
FVC	2.8 ± 0.9	3.5 ± 1.1	n.s.
FVC (predicted)	81.8 ± 18.1	N/A	
D_{LCO} (single breath)	4.0 ± 1.7	N/A	
Ever smoked Ex-smoker Current smoker	77% 90% 10%	20% 100%	

Table 5.2: Subject demographics of samples used for GC-MS analysis (Figure 5.2 B).

Table showing sex, age, drug-treatment, FEV1, FEV1 % predicted, forced vital capacity (FVC), % predicted FVC, D_{LCO} and smoking status of healthy (n = 6) and IPF (n = 62) samples used for GC-MS of itaconate (Figure 5B). Data presented as mean ± S.D.

	IPF (n = 47) Mean ± S.D.	Healthy (n = 10) Mean ± S.D.	T-test
Sex (M/F)	37M / 10F	6M / 4F	
Age	72.9 ± 7.7	46.6 ± 12.1	***
Anti-fibrotic treatment Nintedanib Pirfenidone	70% 36% 78%	N/A	
Steroid treatment	8.5%	N/A	
FEV1	2.2 ± 0.6	3.0 ± 0.6	*
FEV1 (predicted)	84.6 ± 14.2	N/A	
FVC	2.7 ± 0.8	3.7 ± 0.9	n.s.
FVC (predicted)	80.6 ± 13.6	N/A	
D_{LCO} (single breath)	3.8 ± 1.4	N/A	
Ever smoked Ex-smoker Current smoker	64% 87% 13%	33% 100%	

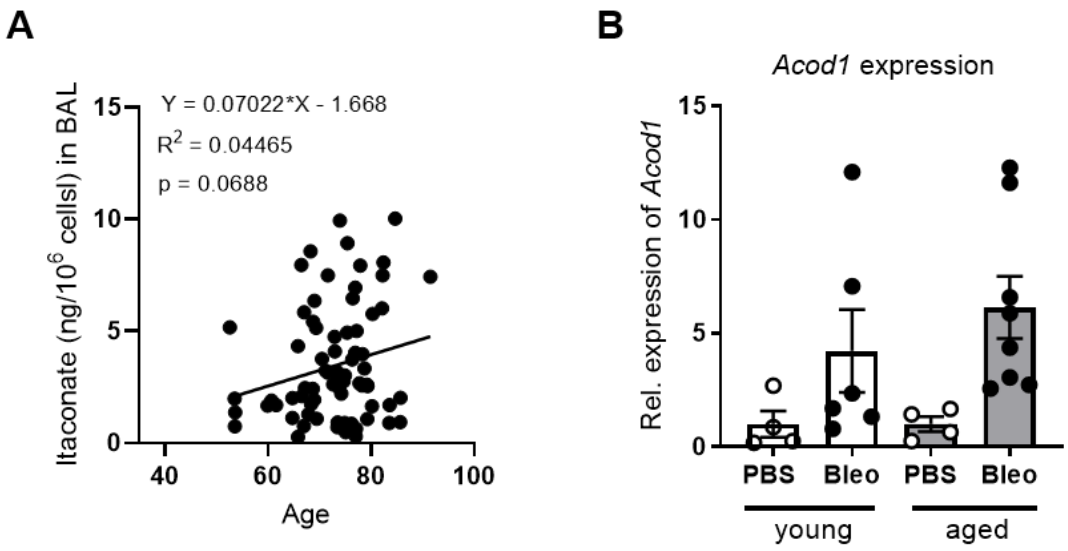

Figure 5.3. Correlation of the ACOD1/itaconate axis to age. A) Pearson correlation between itaconate measured in BAL (ng/10^6 cells) and age of IPF patients (n = 75). B) Gene expression analysis of *Acod1* in lung homogenate of PBS or bleomycin dosed, young (10 week) or aged (52 week) mice. *Actb* was used as housekeeping control. PBS groups n = 4, bleo/young n = 6, bleo/aged n = 8. Data presented as mean ± S.E.M. Significance tested by Pearson correlation (A) or One-Way-ANOVA with Dunn's multiple comparison test (B).

5.3.2 Acod1-deficiency results in worse lung function during PF

To further assess the role of itaconate during pulmonary fibrosis, we dosed WT or *Acod1*$^{-/-}$ mice (which globally do not express *Acod1)* with bleomycin. *Acod1*$^{-/-}$ or WT littermates were exposed o.p. to one dose of bleomycin (0.05U in 50µl) or 50µl PBS as control. To investigate the impact of loss of itaconate during the inflammatory, fibrotic and resolution stage of bleomycin induced pulmonary fibrosis, mice were harvested at d7, d21 or d42 and lung function parameters were assessed using the FlexiVent system. *Acod1*$^{-/-}$ mice had worsened dynamic resistance compared with WT controls at d42 post-bleomycin exposure (Figure 5.4 G-I). However, in comparison to WT controls, *Acod1*-deficient mice did not show altered lung function (Figure 5.4 A-F) at d7 or d21 post-injury, suggesting that itaconate does not play a role in the initiation of fibrosis. Overall, these results suggest that Acod1-deficiency results in worsened lung function and more severe pulmonary fibrosis.

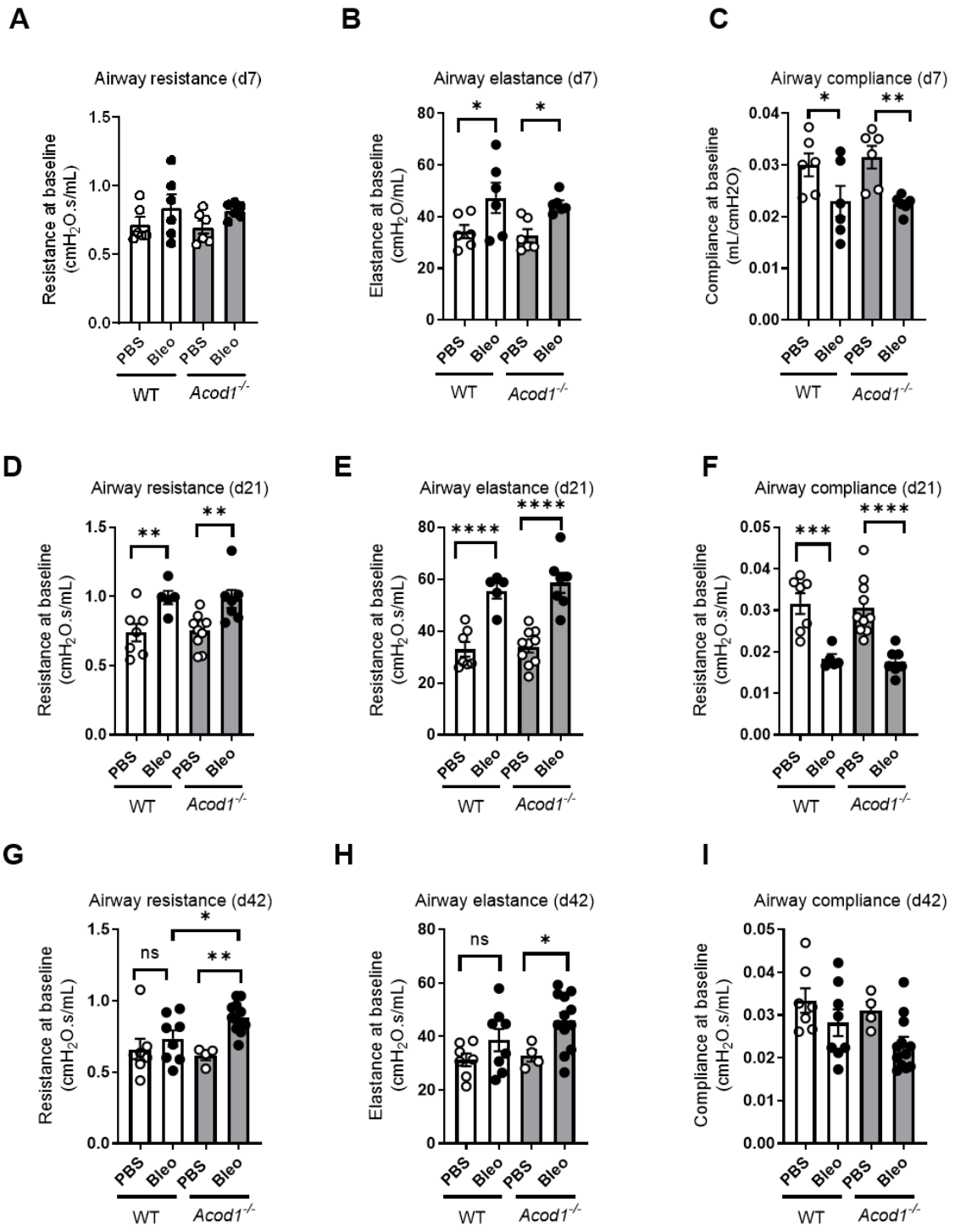

Figure 5.4. Lung function parameters of bleomycin model do not resolve during Acod1 deficiency. Resistance, elastance and compliance measured at baseline by FlexiVent in PBS or bleo dosed WT and *Acod1*$^{-/-}$ mice. A – C) D7 post bleomycin; n = 6 per group. D – F) D21 post bleomycin; n = 5 – 10 mice per group; pooled from two independent experiments. G – I) D42 post bleomycin; n = 4 – 12 mice per group; pooled from two independent experiments. Data presented as mean ± S.E.M. Statistical significance tested by One-Way ANOVA + Dunn's multiple comparison test; *P < 0.05, ** P < 0.01, *** P < 0.005, **** P < 0.001.

5.3.3 Increased total and myeloid BAL cell numbers in *Acod1*$^{-/-}$ mice

To determine the impact of *Acod1* deficiency on cell numbers in BAL and lung, total cells were counted in BAL and whole lung homogenate and subsequently immune cell populations were assessed by multi-parameter flow cytometry based on the gating strategy shown in Figure 4.4. No change in number of total BAL and lung cells or immune cell populations was detected between *Acod1*$^{-/-}$ and WT bleomycin groups at d7 or d21 post bleomycin. At the resolution time point however, at d42, total BAL cell numbers were significantly increased in *Acod1*$^{-/-}$ bleomycin treated mice compared to WT (Figure 5.5 A). Total BAL AM numbers were increased (Figure 5.5 B), with a significant increase in Mo-AMs in the Acod1 deficient mice, while the number of Tr-AMs was unchanged (Figure 5.5 C – D). Furthermore, the total number of BAL monocytes and dendritic cells were increased in *Acod1*$^{-/-}$ bleomycin treated mice at d42, compared to WT mice, while the numbers of eosinophils and neutrophils remained unchanged (Figure 5.5 E – H). In contrast, there was no difference in total lung cell numbers or total numbers of granulocytes and myeloid populations in lung homogenate between *Acod1*$^{-/-}$ and WT bleomycin treated mice at d42 (Figure 5.6 A – H). No change in CD3^{+} lymphocyte (Figure 5.7 A) or NK cell numbers (Figure 5.7 B) was detected at any time during the bleomycin model in the *Acod1*$^{-/-}$ group compared to bleomycin dosed WT.

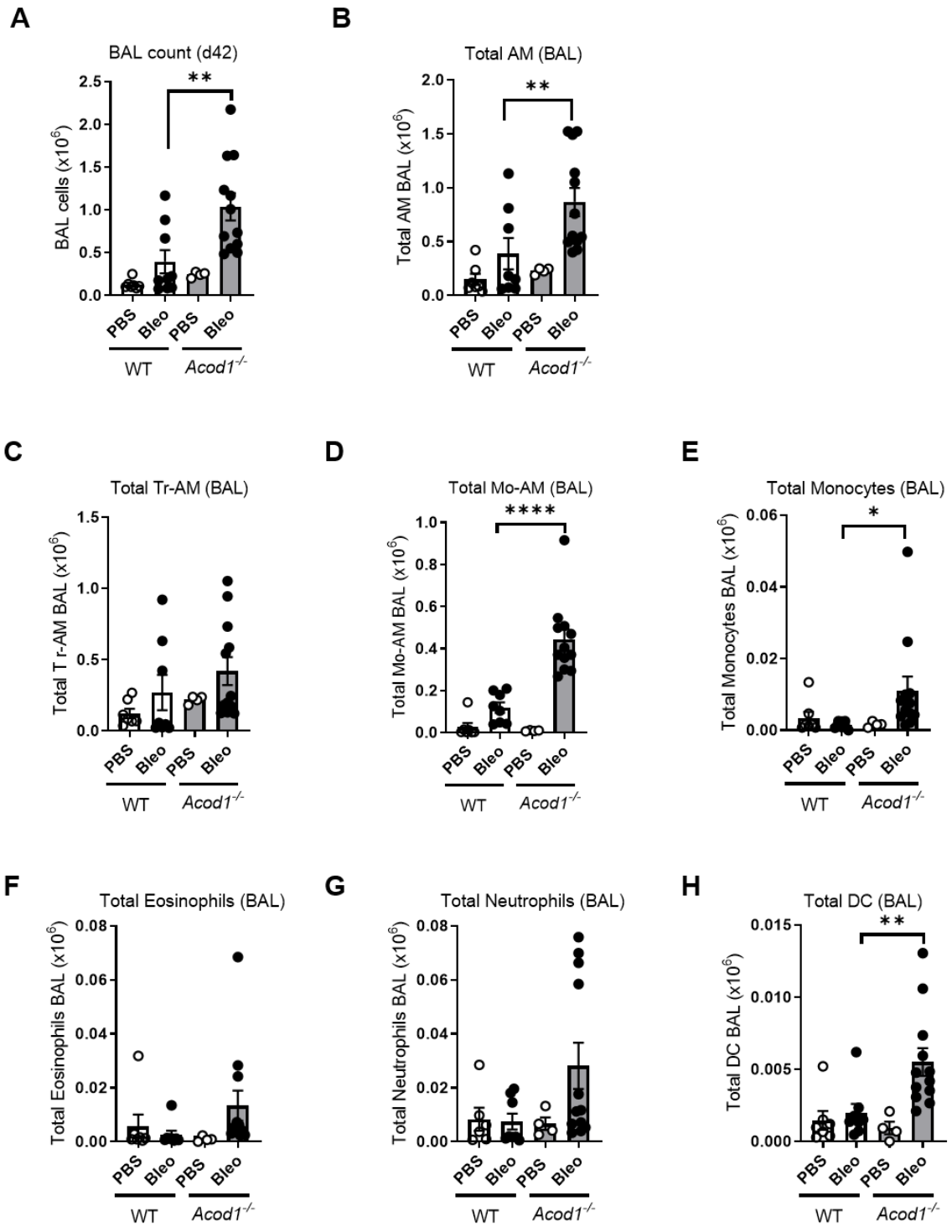

Figure 5.5. Increased total and myeloid BAL cell numbers in *Acod1*$^{-/-}$ mice at d42 post bleomycin. A) Total BAL cells. B) Total BAL airway macrophages. C) Total BAL tissue-resident airway macrophages. D) Total BAL monocyte-recruited airway macrophages. E) Total BAL monocytes. F) Total BAL eosinophils. G) Total BAL neutrophils. H) Total BAL dendritic cells. WT or *Acod1*$^{-/-}$ mice were dosed with 0.05U bleomycin or 50µl PBS at d0 and harvested at d42. WT/PBS n = 7, WT/bleomycin n = 9, *Acod1*$^{-/-}$/PBS n = 4, *Acod1*$^{-/-}$/bleomycin n = 12; pooled from two independent experiments. Data presented as mean ± S.E.M. Statistical significance tested by One-Way ANOVA + Dunn's multiple comparison test; *P < 0.05, ** P < 0.01, *** P < 0.005, **** P < 0.001.

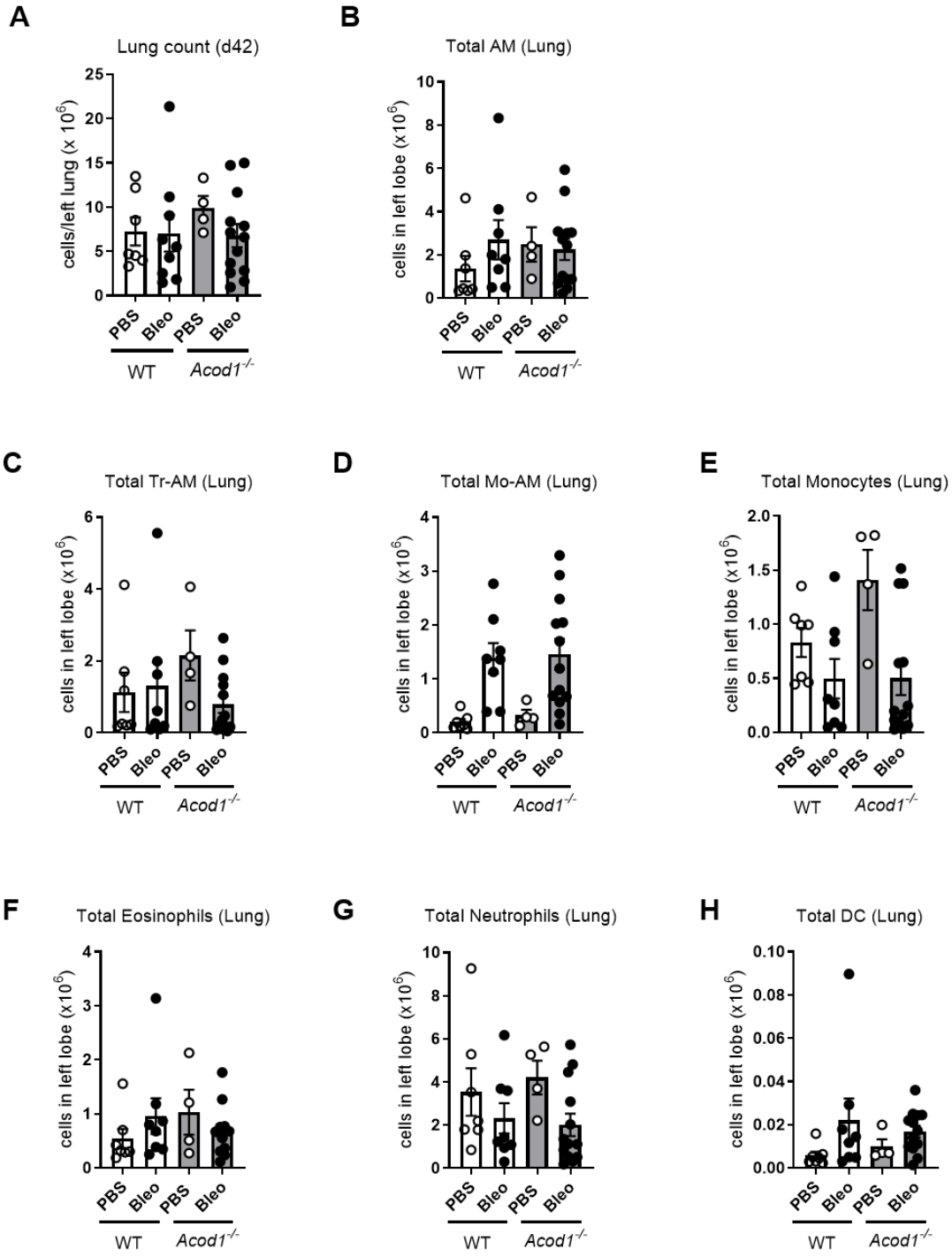

Figure 5.6. Total and myeloid lung cell numbers are unchanged in *Acod1*$^{-/-}$ mice at d42 post bleomycin. A) Total lung cells. B) Total lung airway macrophages. C) Total lung Tr-AM. D) Total lung Mo-AM. E) Total lung monocytes. F) Total lung eosinophils. G) Total lung neutrophils. H) Total lung dendritic cells. WT or *Acod1*$^{-/-}$ mice were dosed with 0.05U bleomycin or 50µl PBS at d0 and harvested at d42. WT/PBS n = 7, WT/bleomycin n = 9, *Acod1*$^{-/-}$/PBS n = 4, *Acod1*$^{-/-}$/bleomycin n = 12; pooled from two independent experiments. Data presented as mean ± S.E.M. Statistical significance tested by One-Way ANOVA + Dunn's multiple comparison test; *P < 0.05, ** P < 0.01, *** P < 0.005, **** P < 0.001.

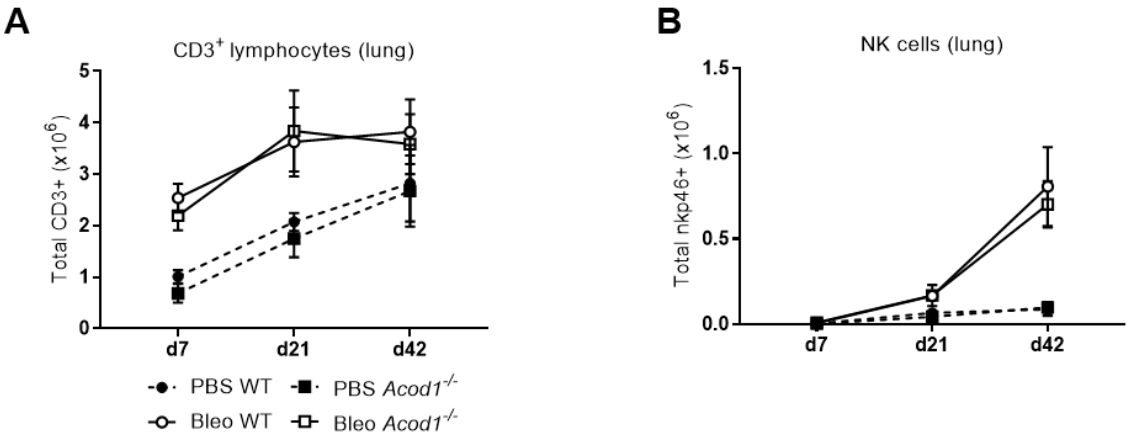

Figure 5.7. Acod1-deficiency does not change lymphocytes in bleomycin model. A) Total lung CD3⁺ lymphocytes. B) Total lung NK cells. WT or *Acod1*$^{-/-}$ mice were dosed with 0.05U bleomycin or 50µl PBS at d0 and harvested at d7, d21 and d42. Data presented as mean ± S.E.M. Statistical significance tested per time point by One-Way ANOVA + Dunn's multiple comparison test.

5.3.4 *Acod1* expression controls the severity of lung fibrosis

To investigate the impact of *Acod1* expression on fibrotic phenotype after bleomycin exposure, gene expression of *collagen1α1 (col1α1), collagen3 α1 (col3α1), collagen4α1 (col4α1)* and *fibronectin-1 (fn1)* was measured by qPCR in WT and *Acod1*$^{-/-}$ bleomycin exposed mice. Whilst collagen type I and type III are most abundant in extracellular matrix during fibrosis and form part of the interstitial matrix, collagen type VI and type V are involved in repair of the basement membrane and drastically increase in abundancy during remodelling[340]. Fibronectin-1 is a glycoprotein of the extracellular matrix, binding both collagens and integrins ultimately facilitating extracellular matrix accumulation. Furthermore, histology slices were stained with Sirius red for collagen and quantified using the modified Ashcroft scoring system and hydroxyproline content was analysed using a spectrometric assay. In the bleomycin mouse model of pulmonary fibrosis, significant changes in collagen gene expression in *Acod1*$^{-/-}$ mice were detected at d21 post bleomycin, while collagen staining and scoring was most changed at d42. At d21 post bleomycin, gene expression of interstitial *collagen type III (col3α1)* and connecting *fibronectin-1* was increased in *Acod1*$^{-/-}$ mice compared to WT, while *collagen type I (col1α1)* and basal *collagen type IV (col4α1)* remained unchanged (Figure 5.8 A – D). At d42 post bleomycin, *Acod1*$^{-/-}$ mice showed higher modified Ashcroft scores of fibrosis based on Sirius red staining (Figure 5.8 E - F) and higher hydroxyproline expression, compared to the WT groups (Figure 5.8 G). These results indicate that Acod1-deficiency results in more severe pulmonary fibrosis in response to inhaled bleomycin, in comparison to WT controls.

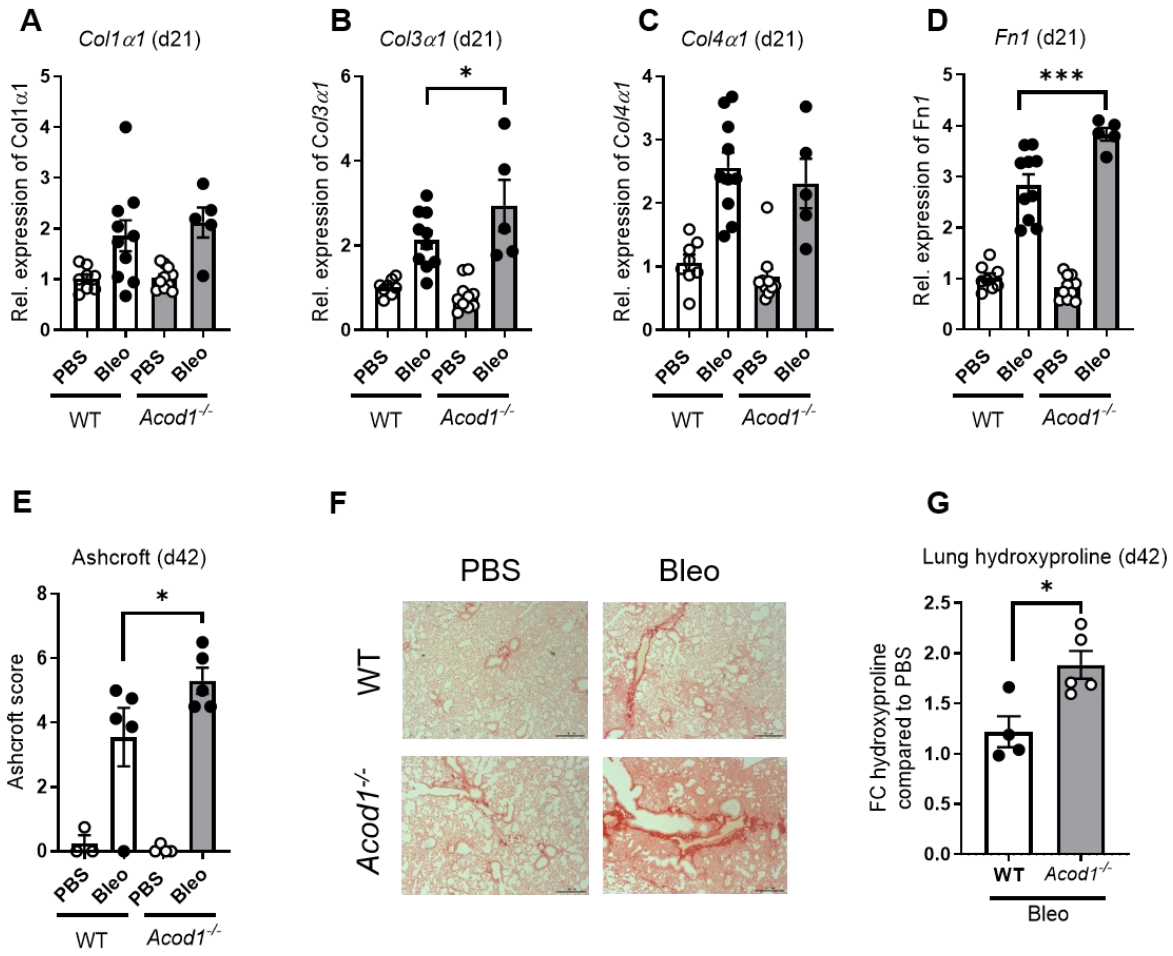

Figure 5.8. Collagen gene expression and fibrotic phenotype in Acod1 deficient mice. A – D) Gene expression analysis of col1α1 (A), col3α1 (B), col4α1 (C) and fn-1 (D) in lung homogenate of PBS or bleo dosed WT and *Acod1*$^{-/-}$ mice at d21; WT/PBS n = 8, WT/bleomycin n = 10, *Acod1*$^{-/-}$/PBS n = 10, *Acod1*$^{-/-}$/bleomycin n = 5; pooled from two independent experiments. *Actb* was used as housekeeping gene. E – F) Ashcroft score (K) and representative images (L) of lung slices of PBS or bleo dosed mice at d42 post bleomycin stained with Sirius Red, scored blinded by 3-5 individuals. G) Fold change hydroxyproline increase in bleomycin compared to PBS in WT and *Acod1*$^{-/-}$ mice at d42 post bleomycin (n = 4 – 5 per group). Data presented as mean ± S.E.M. Statistical significance tested by One-Way ANOVA + Dunn's multiple comparison test; *P < 0.05, *** P < 0.005.

5.3.5 Impact of *Acod1* on superoxide expression in macrophages

Production of ROS is a major function of AMs and part of the lungs innate defence system. ROS production however needs to be tightly controlled as it is necessary to fight pathogens, but oxidative stress is detrimental to pulmonary cells and lung structure. MitoSOX red staining was used to measure superoxide, a subtype of ROS, in BAL during the bleomycin mouse model for pulmonary fibrosis in WT and *Acod1*$^{-/-}$ mice. MitoSOX red dye is targeted at mitochondria and oxidised by superoxide, producing red fluorescence which can be detected by flow cytometry. In BAL, total superoxide was analysed, as well as the mean fluorescent intensity (MFI) of mitoSOX in CD45^{+} and AM (Figure 5.9 A – D). There was no difference in any of these parameters at d7 or d21 post bleomycin when comparing WT and *Acod1*$^{-/-}$ mice. At d42 post bleomycin, the *Acod1*$^{-/-}$ bleomycin treated group showed a significantly increased intensity of mitoSOX staining in CD45^{+} cells compared to WT (Figure 5.9 F) although the proportions staining positive for mitoSOX remained unchanged (Figure 5.9 E). While there was a similar trend in the AM compartment, these changes were not statistically significant (Figure 5.9 G and H). These results show that after bleomycin treatment, superoxide production is increased in Acod1-deficient mice during the resolution phase. While only a limited set of markers was used to identify AMs within CD45^{+} cells, it would be interesting to investigate other BAL cells in more detail to find out if other cell compartments contributes to this increased mitoSOX intensity at d42.

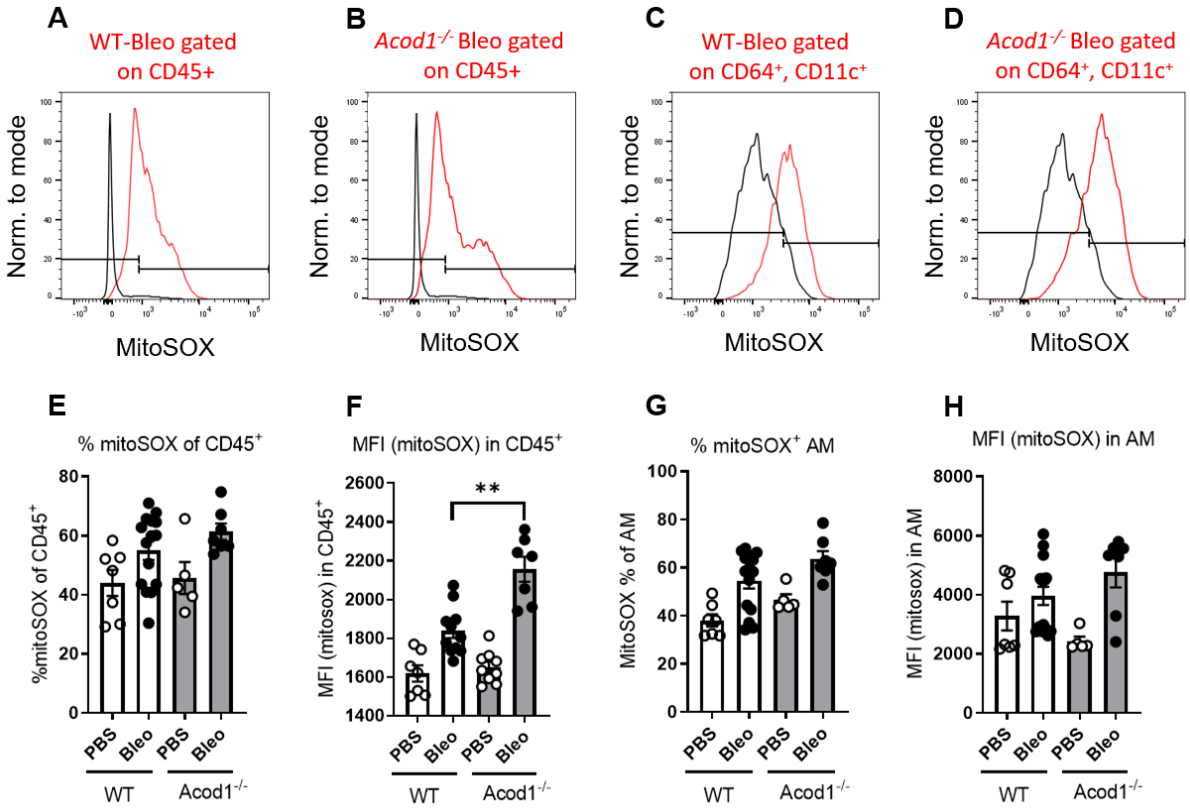

Figure 5.9. MitoSOX mean fluorescent intensity increased in *Acod1*$^{-/-}$ CD45+ population. A – D) Representative Flowjo plots of mitoSOX staining in CD45^{+} population in WT (A) and *Acod1*$^{-/-}$ (B) bleomycin treated group and mitoSOX staining in AMs (gated on CD64^{+}, CD11c^{+}, Ly6C^{-}) in WT (C) and *Acod1*$^{-/-}$ (D) at d42. Black = unstained control, red = mitoSOX stained. E) Percentage of CD45^{+} cells staining positive for mitSOX at d42. F) Mean fluorescent intensity (MFI) of mitoSOX staining in CD45^{+} cells at d42. G) Percentage of AMs staining positive for mitSOX at d42. H) MFI of mitoSOX staining in AMs at d42. PBS/WT n = 7, bleo/WT n = 16, PBS/*Acod1*$^{-/-}$ n = 5,bBleo/*Acod1*$^{-/-}$ n = 7; pooled from two independent experiments. Data presented as mean ± S.E.M. Statistical significance tested by One-Way ANOVA + Dunn's multiple comparison test; **P < 0.01.

5.3.6 Acod1 deficiency impairs maximal respiration in Tr-AM

To further investigate the metabolic phenotype of different macrophage subsets in *Acod1*$^{-/-}$ and WT mice during the bleomycin mouse model, Tr-AM and Mo-AM were FACS sorted based on SiglecF expression, as described in chapter 4.3.7 at d7 post bleomycin. 100,000 sorted macrophages (2 – 3 mice pooled) were plated on cell-Tak coated 8-well seahorse plates and respiration parameters were analysed using the mitochondrial stress test as described in chapter 2. In Tr-AMs, Acod1-deficiency resulted in significantly decreased maximal and spare respiratory capacity (Figure 5.10 A, C and D), while basal respiration (Figure 5.10 E), ATP production (Figure 5.10 G), proton leak (Figure 5.10 G) and non-mitochondrial OCR (Figure 5.10 F) remained unchanged. In Mo-AMs however, no differences could be determined in any of the respiratory parameters assessed (Figure 5.11). Overall, these findings suggest that Acod1-deficiency results in impaired respiration in Tr-AMs, while it does not affect mitochondrial respiration in Mo-AMs.

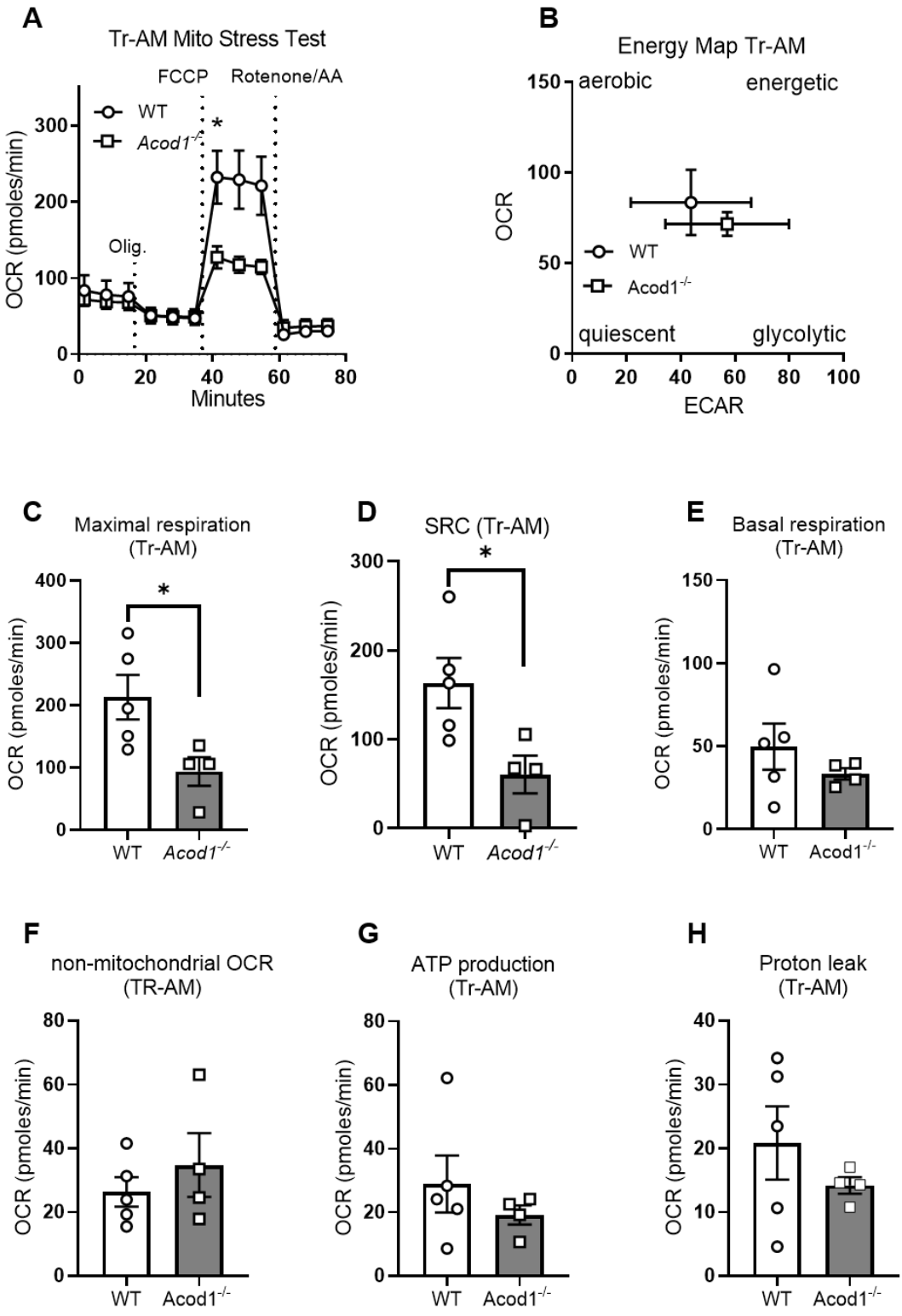

Figure 5.10. Respiratory capacity is decreased in *Acod1*$^{-/-}$ Tr-AM. Mitochondrial stress test of WT (n = 5) and *Acod1*$^{-/-}$ (n = 4) Tr-AM at d7 post bleomycin treatment; assessed after injection of Oligomycin, FCCP and Rotenone/Antimycin A. 100 000 sorted Tr-AMs, pooled from 2 – 3 mice, were plated on Cell-Tak coated plates. A) Analysis of OCR. B) Energy map of WT and *Acod1*$^{-/-}$ Tr-AM showing four energy states: quiescent, energetic, aerobic and glycolytic. C) Maximal respiration D) Spare respiratory capacity E) Basal respiration F) Non mitochondrial oxygen consumption G) ATP production H) Proton leak. Data presented as mean ± S.E.M. Significance tested by Mann Whitney U test, *P < 0.05.

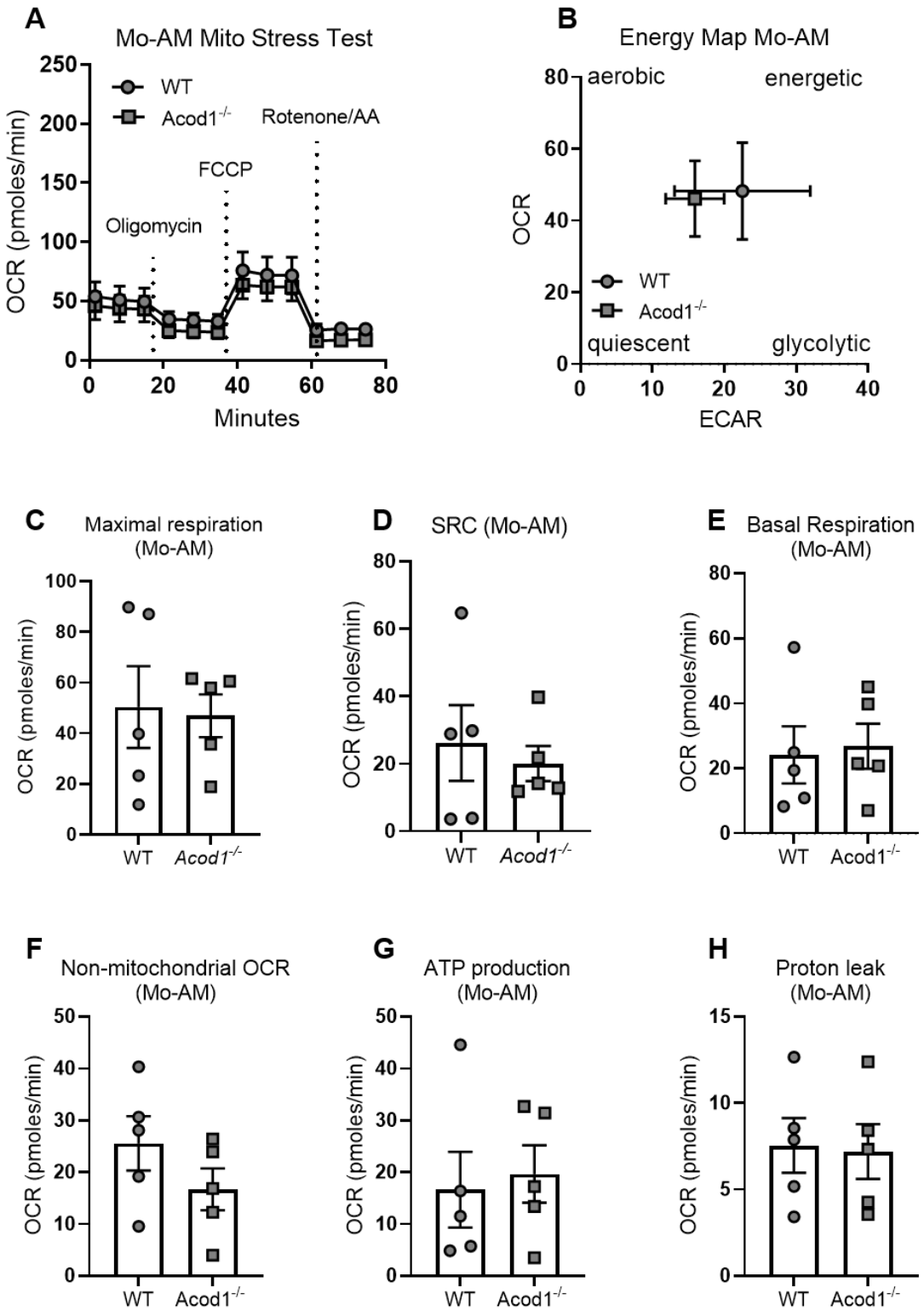

Figure 5.11. Respiratory capacity in *Acod1*$^{-/-}$ Mo-AMs. Mitochondrial stress test of WT (n = 5) and *Acod1*$^{-/-}$ (n = 5) Mo-AMs at d7 post bleomycin treatment; assessed after injection of Oligomycin, FCCP and Rotenone/Antimycin A. 100 000 sorted Tr-AMs, pooled from 2 – 3 mice, were plated on Cell-Tak coated plates. A) Analysis of OCR. B) Energy map of WT and *Acod1*$^{-/-}$ Mo-AM showing four energy states: quiescent, energetic, aerobic, and glycolytic. C) Maximal respiration D) Spare respiratory capacity (E) Basal respiration F) Non mitochondrial oxygen consumption G) ATP production H) Proton leak. Data presented as mean ± S.E.M. Significance tested by Mann Whitney U test, *P < 0.05.

5.3.7 Acod1-deficiency increases pro-fibrotic phenotype in Tr-AM

Next, the impact of Acod1-deficiency on the functional phenotype of AMs, particularly in a fibrotic context, was investigated using a Qiagen gene array to analyse the expression of 84 genes involved in the fibrosis cascade. These included integrins, matrix metalloproteases, the TGF-β superfamily as well as chemokines and cytokines (full gene list shown in table 2.6). These data show that Acod1-deficiency leads to an increased pro-fibrotic gene expression in Tr-AM (Figure 5.12 A), while in Mo-AM, only two genes were significantly differentially expressed (Figure 5.12 B). Figure 5.12 C and 5.12 D show the genes that were significantly changed (significance annotated by *) or changed at least 10-fold compared to WT controls. In Mo-AMs, *interleukin (Il)-1β* and *integrin linked kinase (Ilk)* were significantly decreased in *Acod1*$^{-/-}$ compared to WT mice (Figure 5.12 B and D), while no pro-fibrotic factors were found to be significantly increased. In contrast, in Tr-AMs a range of pro-fibrotic mediators including *CCAAT enhancer binding protein (Cebpb), transforming growth factor beta receptor 1 (Tgfbr1), Smad7* and the *integrin beta-1-binding protein 1 (Itbp1*) were increased in Acod1-deficient compared to WT mice (Figure 5.12 A and C). Genes that were increased by at least 10-fold in *Acod1*$^{-/-}$ Tr-AM but did not reach statistical significance include *angiotensin (Agt), bone morphogenic protein 7 (Bmp7)* a ligand of the TGF-β superfamily, *Smad6* and *vascular endothelial growth factor A (Vegfa)*. Cytospin images of the FACS sorted cells showed that while Mo-AMs are smaller than Tr-AMs, due to their recent recruitment from the peripheral monocyte pool, there is no difference in cellular morphology between *Acod1*$^{-/-}$ and WT Tr-AM and Mo-AM (Figure 5.12 E). Interestingly, while Acod1-deficiency affected the pro-fibrotic phenotype of Tr-AMs more than that of Mo-AMs, gene expression analysis of *Acod1* showed that Mo-AMs show higher expression of *Acod1* post bleomycin exposure (Figure 5.12 F) and therefore might contribute itaconate to the site of recruitment where it acts on Tr-AMs. Taken together, these results indicate that during Acod1-deficiency, Tr-AM and Mo-AM are metabolically, transcriptionally and phenotypically distinct, while size and granularity is unchanged.

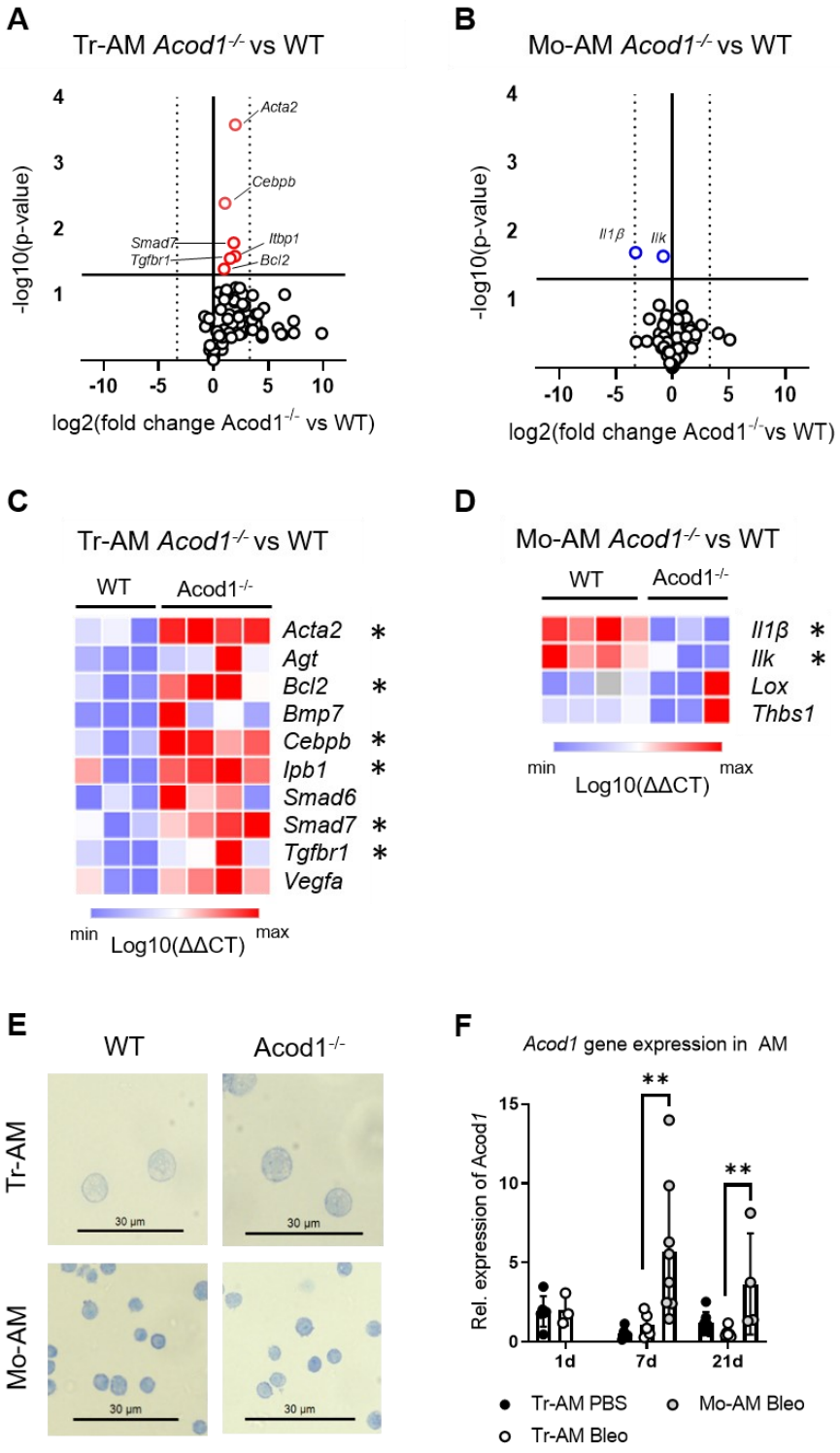

Figure 5.12. Upregulation of pro-fibrotic pathways in *Acod1*$^{-/-}$ Tr-AM. A – B) Volcano plots showing differentially expressed genes in WT vs *Acod1*$^{-/-}$ Tr-AM (A) and Mo-AM (B), at d7 post bleomycin exposure (n = 3–4 per group). Genes significantly ($p < 0.05$) up-regulated in WT vs *Acod1*$^{-/-}$ highlighted in red, while genes significantly downregulated are shown in blue. C – D) Heat map representation of murine fibrosis gene array of FACS sorted Mo-AM (C) and Tr-AM (D) from WT and *Acod1*$^{-/-}$ mice. Data shown as log10 of ΔΔCT WT vs *Acod1*$^{-/-}$. E) Representative images of FACS sorted Tr-AM and Mo-AM WT and *Acod1*$^{-/-}$ mice after cytospin and Diff-Quick staining. F) Gene expression analysis of *Acod1* in BAL PBS Tr-AM, bleo Tr-AM and bleo Mo-AM at d1, d7 and d21 (n = 4–7 per group) post bleomycin. *Actb* was used as housekeeping control. Pooled from three independent experiments. Data presented as mean ± S.E.M. Significance tested by two-tailed Student's t-test (A – D) or One-Way ANOVA (F), *P < 0.05, **P < 0.001.

5.3.8 Lung function and BAL composition in *Acod1*$^{-/-}$ mice after adoptive transfer

The data shown so far may indicate a mechanism whereby Mo-AMs deliver itaconate to the site of injury and regulate the phenotype of Tr-AMs; to investigate this we utilised an adoptive transfer approach. As shown in Figure 5.1 B, WT and *Acod1*$^{-/-}$ donor mice were exposed to bleomycin (0.05U) and Mo-AMs were FACS sorted from BAL at d7 following the gating strategy shown in Figure 4.4. Recipient *Acod1*$^{-/-}$ were also exposed to either bleomycin (0.05U) or 50µl PBS at d0 and received oropharyngeal adoptive transfer of 50,000 either WT or *Acod1*$^{-/-}$ Mo-AMs at d7. Recipient mice were subsequently sacrificed at d21 or d42 post bleomycin and lung function, fibrosis parameters and macrophage phenotype was analysed. While resistance and elastance were decreased and compliance was increased in mice that received an adoptive transfer of WT (itaconate-expressing) Mo-AMs compared to mice receiving Acod1-deficient Mo-AMs at d42 post initial bleomycin exposure, this was not statistically significant (Figure 5.13 A – C). This trend was similar at d21 post bleomycin exposure (Figure 5.13 D – F). Next, the composition of BAL was investigated following adoptive transfer. Bleomycin dosed *Acod1*$^{-/-}$ mice that received adoptive transfer of WT Mo-AMs showed an increased number of total BAL cells (Figure 5.14 A) at d42, as well as an increased number of BAL AMs (Figure 5.14 B), both Tr-AMs (Figure 5.14 C) and Mo-AMs (Figure 5.14 D) and monocytes (Figure 5.14 E), compared to mice receiving a transfer of *Acod1*$^{-/-}$. Furthermore, numbers of eosinophils (Figure 5.14 F) and dendritic cells (Figure 5.14 H) were increased in mice that received WT cells, while the number of neutrophils remained unchanged. Similar trends were observed at d21 post bleomycin (after adoptive transfer), although except for the numbers of monocytes and dendritic cells, these changes were not significant (Figure 5.14 I – P). Adoptive transfer of WT or *Acod1*$^{-/-}$ Mo-AMs did not affect BAL composition in PBS dosed mice.

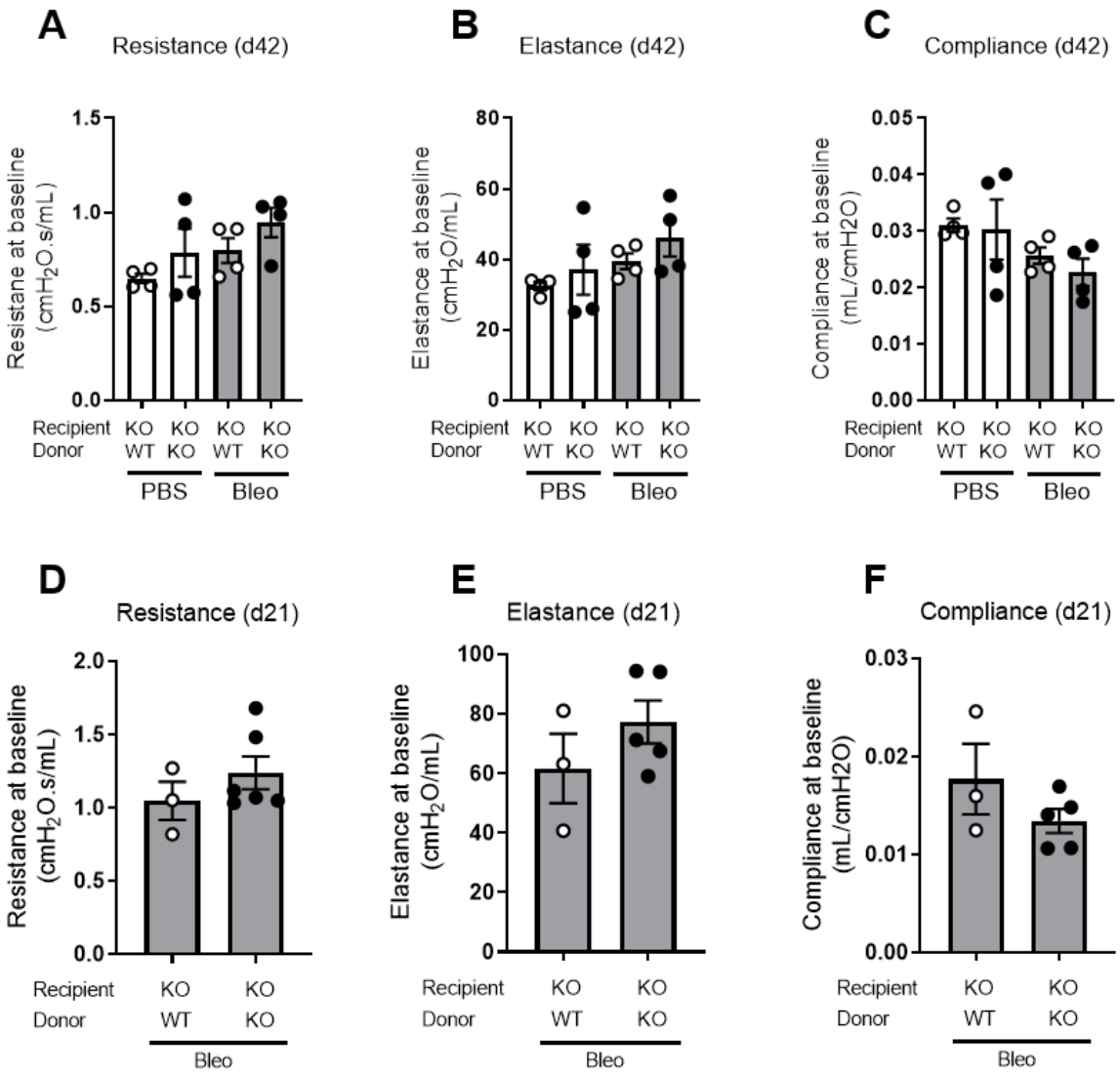

Figure 5.13. Lung function remains unchanged after adoptive transfer of WT Mo-AM into *Acod1*$^{-/-}$ mice. A – C) Resistance, elastance and compliance measured at d42 post bleomycin at baseline by FlexiVent in PBS or bleo dosed mice that received transfer of either WT or *Acod1*$^{-/-}$ Mo-AM at d7 post bleomycin. All groups n = 4. D – F) Resistance, elastance and compliance measured at d21 post bleomycin at baseline by FlexiVent in Bleomycin dosed mice that received transfer of either WT or *Acod1*$^{-/-}$ Mo-AMs at d7 post bleomycin. WT-adoptive transfer n = 3, *Acod1*$^{-/-}$ adoptive transfer n = 5. Statistical significance tested by One-Way ANOVA + Dunn's multiple comparison test (A – C) or Mann-Whitney U test (D – F).

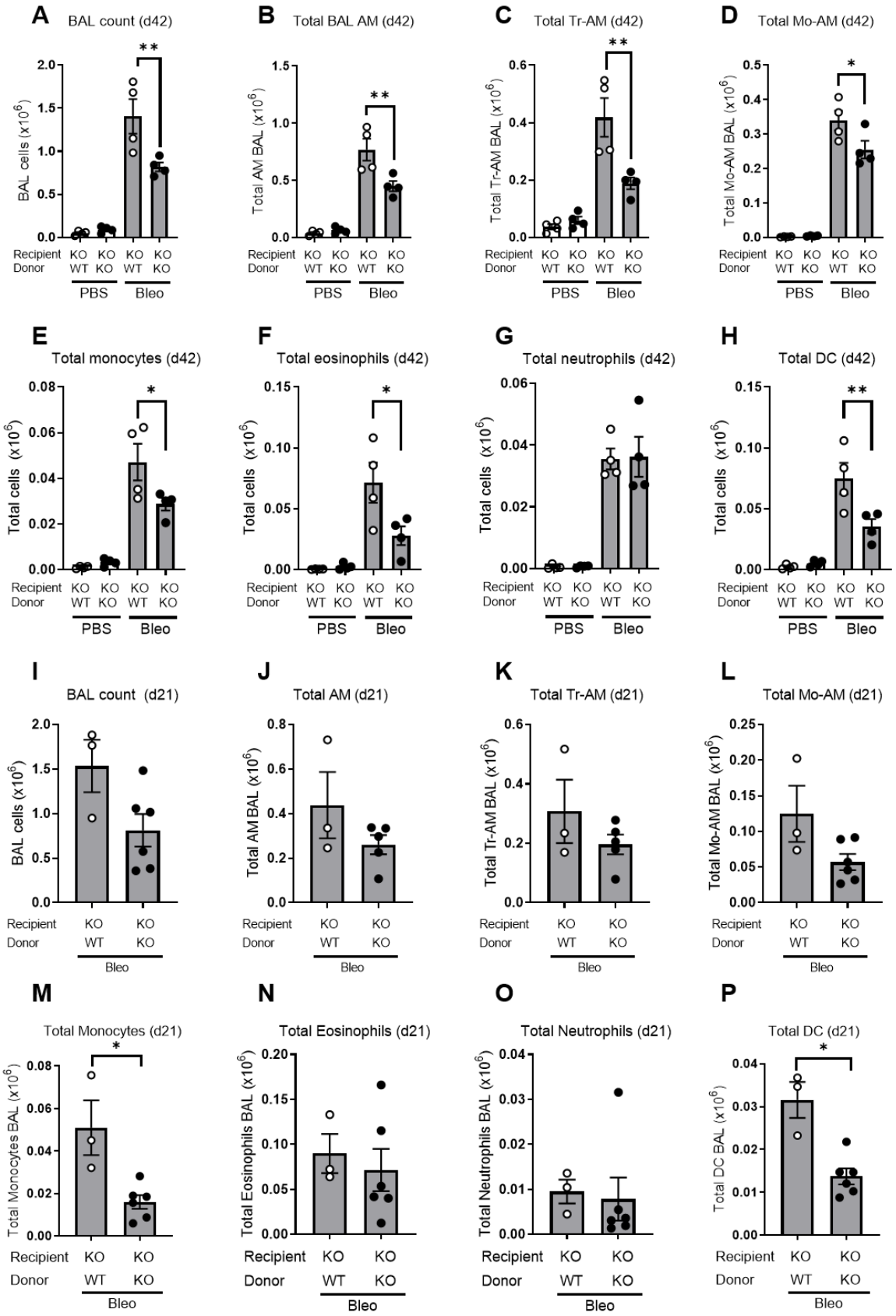
A
BAL count (d42)
BAL cells (x10^6)
B
Total BAL AM (d42)
Total AM BAL (x10^6)
C
Total Tr-AM (d42)
Total Tr-AM BAL (x10^6)
D
Total Mo-AM (d42)
Total Mo-AM BAL (x10^6)
E
Total monocytes (d42)
Total cells (x10^6)
F
Total eosinophils (d42)
G
Total neutrophils (d42)
H
Total DC (d42)
I
BAL count (d21)
J
Total AM (d21)
K
Total Tr-AM (d21)
L
Total Mo-AM (d21)
M
Total Monocytes (d21)
Total Monocytes BAL (x10^6)
N
Total Eosinophils (d21)
Total Eosinophils BAL (x10^6)
O
Total Neutrophils (d21)
Total Neutrophils BAL (x10^6)
P
Total DC (d21)
Total DC BAL (x10^6)
Recipient KO KO KO KO
Donor WT KO WT KO
PBS
Bleo
Recipient KO KO
Donor WT KO
Bleo

Figure 5.14. Immune cell profile in BAL after adoptive transfer with WT or *Acod1*$^{-/-}$ Mo-AMs. A – H) BAL cell populations at d42 in PBS or bleo dosed mice that received transfer of either WT or *Acod1*$^{-/-}$ Mo-AMs at d7 post bleomycin. A) Total BAL count. B) Total BAL AM count. C) Total BAL tissue-resident AM count. D) Total BAL monocyte-recruited AM count. E) Total BAL monocyte count. F) Total BAL eosinophil count. G) Total BAL neutrophil count. H). Total BAL dendritic cell (DC) count. All groups n = 4. I – P) BAL cell populations at d21 in bleomycin-dosed mice that received transfer of either WT or *Acod1*$^{-/-}$ Mo-AMs at d7 post bleomycin. I) Total BAL count. J) Total BAL airway macrophage count. K) Total BAL Tr-AM count. L) Total BAL Mo-AAM count. M) Total BAL monocyte count. N) Total BAL eosinophil count. O) Total BAL neutrophil count. P) Total BAL dendritic cell (DC) count. WT-adoptive transfer n = 3, *Acod1*$^{-/-}$ adoptive transfer n = 5. Data presented as mean ± S.E.M. Statistical significance tested by One-Way ANOVA + Dunn's multiple comparison test (A - H) or Mann-Whitney U test (I –P), *P < 0.05, **P < 0.001.

5.3.9 Fibrotic phenotype improved after adoptive transfer of WT Mo-AM

The fibrotic phenotype of mice receiving adoptive transfer of Mo-AMs was assessed at d21 or d42 post bleomycin by gene expression analysis and scoring of Sirius-red stained histology slices. At d42 post bleomycin (adoptive transfer at d7), there was no difference in collagen or fibronectin gene expression comparing bleomycin-dosed groups that received WT or *Acod1*$^{-/-}$ adoptive transfer (Figure 5.15 A – D). Furthermore, there was no difference in Ashcroft score based on Sirius-red staining for deposited collagen in histology slices (Figure 5.15 E – F). At peak fibrosis (d21) however, clear differences are detectable: Bleomycin-dosed *Acod1*$^{-/-}$ mice that received an adoptive transfer of itaconate-expressing WT Mo-AMs show decreased expression of *Col3α1* (Figure 5.15 H) and *Fn-1* (Figure 5.15 J) compared to those that received an adoptive transfer of *Acod1*$^{-/-}$ Mo-AMs at d7. Furthermore, these mice also show decreased modified Ashcroft score based on Sirius-red staining (Figure 5.15 K – L). Overall, these results suggest that transfer of itaconate-expressing Mo-AMs can improve pulmonary fibrosis pathology, especially during peak fibrosis.

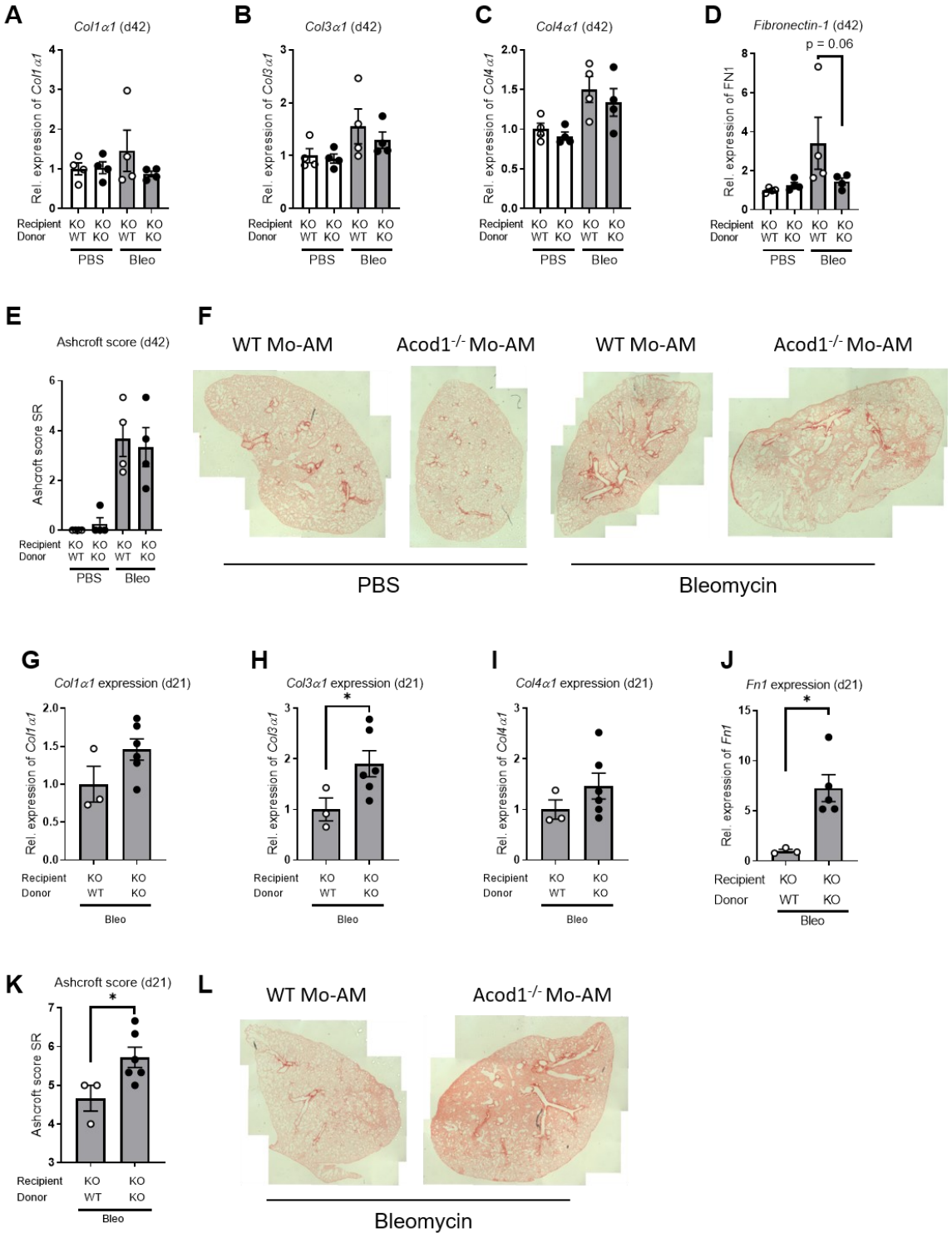

Figure 5.15. Fibrotic phenotype improved after adoptive transfer of WT Mo-AM into Acod1$^{-/-}$ mice. A – D) Gene expression analysis of *Col1α1* (A), *Col3α1* (B), *Col4α1* (C) and *Fn-1* (D) in lung homogenate at d42 in PBS or bleo dosed mice after transfer of either WT or *Acod1*$^{-/-}$ Mo-AMs at d7 post bleomycin. E) Modified Ashcroft score of fibrosis based on Sirius red staining of histology slices. A – E) all groups n = 4. F) Representative images of Sirius red stain. G – J) Gene expression analysis of *Col1α1* (G), *Col3α1* (H), *Col4α1* (I) and *Fn-1* (J) in lung homogenate at d21 in bleo dosed mice after transfer of either WT or *Acod1*$^{-/-}$ Mo-AMs at d7 post bleomycin. K) Modified Ashcroft score of fibrosis based on Sirius red staining of histology slices. L) Representative images of Sirius red stain. WT-adoptive transfer n = 3, *Acod1*$^{-/-}$ adoptive transfer n = 5. Data presented as mean ± S.E.M. Statistical significance tested by One-Way ANOVA + Dunn's multiple comparison test (A - H) or Mann-Whitney U test (I –P), *P < 0.05, **P < 0.001.

5.3.10 AM phenotype after adoptive transfer

Next, AM phenotype in an adoptive transfer model (Figure 5.15.) was assessed by flow cytometry using the markers CD11b (activated macrophages) and MHC II (M1-like macrophages) to distinguish between AM phenotypes. First, live, single, $CD45^+$, $CD11c^+$, $CD64^+$ AMs were gated. Then, Tr-AM and Mo-AM were separated by gating on SiglecF. Within Mo-AM and Tr-AM populations, the $CD11b^+$, MHC II^+ cells were identified, which were grouped as activated, M1-like AMs and $CD11b^-$, MHC II^- cells, which were grouped as less activated, not-M1-like cells (Figure 5.16 A). This analysis showed that after adoptive transfer of WT, itaconate-expressing Mo-AMs into *Acod1*$^{-/-}$ mice, a higher proportion of Tr-AMs exhibited an activated, M1-like profile compared to mice that received *Acod1*$^{-/-}$ Mo-AMs (Figure 5.16 B), while a lower proportion showed a $CD11b^-$, MHC II^- phenotype (Figure 5.16 C). These trends were similar in Mo-AMs; however, this was not statistically significant (Figure 5.16 D-E).

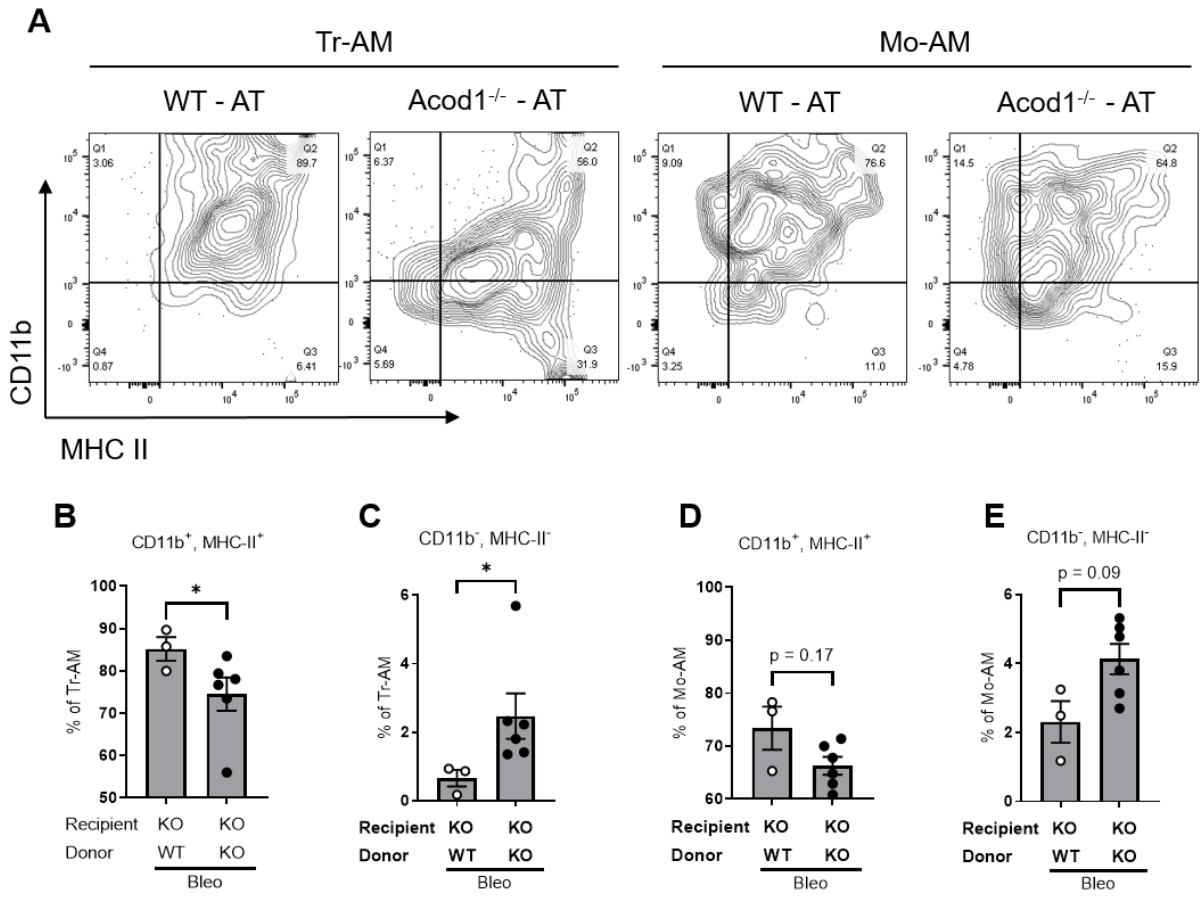

Figure 5.16. Increased proportion of CD11b^{+}/MHC-II^{+} Tr-AM in *Acod1*$^{-/-}$ mice after adoptive transfer of WT Mo-AM. A) Representative FACS plots of CD11b/MHC II gating (pre-gated on live, CD45^{+}, CD11c^{+}, CD64^{+}). B – E) Fraction of CD11b^{+}/MHC II^{+} (M1-like) and CD11b^{-}/MHC II^{-} (M2-like) Tr-AM (B – C) and Mo-AM (D - E) in BAL of *Acod1*$^{-/-}$ mice adoptively transferred with WT or *Acod1*$^{-/-}$ Mo-AMs; d21 post bleomycin. Data presented as mean ± S.E.M. Significance tested by Mann Whitney U test, *P < 0.05.

5.3.11 Itaconate ameliorates metabolic reprogramming of primary HLF *in vitro*

During pulmonary fibrosis, fibroblasts are recruited to the site of injury and differentiate into myofibroblasts and secrete ECM components. To investigate the mechanism by which itaconate improved pulmonary fibrosis and to translate these murine findings to a human system, primary HLF were isolated from healthy or IPF lung tissue and cultured up to passage 2. To identify the optimal dose for culture with itaconate *in vitro*, proliferation of HLFs was assessed during 72h incubation with three different concentrations of itaconate (0.1mM, 1mM and 10mM) as well as a media control and a negative control (10% DMSO). All concentrations tested decreased HLF proliferation in a dose dependent manner (Figure 5.17 A). Furthermore, a crystal violet survival assay was performed 24 hours after exposure to 1mM, 10mM itaconate or a vehicle control. Neither concentration tested impacted HLF survival (Figure 5.17 B). For subsequent experiments, a concentration of 10mM itaconate was selected as this had the strongest effect on proliferation. Next, HLFs were incubated for 24 hours with either 10mM itaconate or a vehicle control, in complete DMEM medium, followed by assessment of their respiratory capacity using the Seahorse Mito Stress test. Similar to the previously reported increased glycolytic phenotype upon activation by TGF-β[230], primary IPF fibroblasts showed an increased respiratory capacity compared to healthy HLFs (Figure 5.18 A – B). However, the basal respiration, maximal respiration, spare respiratory capacity (Figure 5.18 C – E) and ATP production (Figure 5.18 G) decreased in IPF HLFs upon incubation with 10mM itaconate, while it remained unchanged in healthy HLFs.

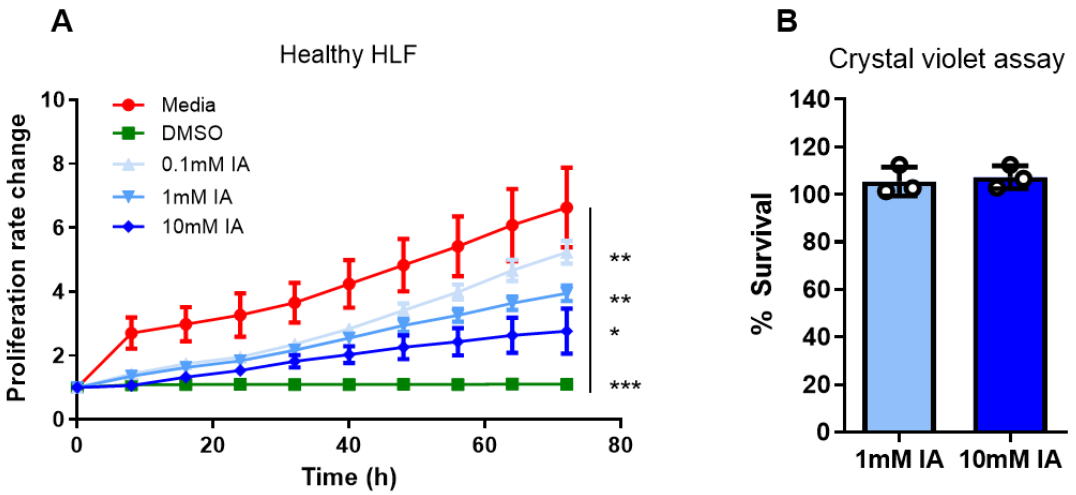

Figure 5.17. Dose titration of itaconate *in vitro*. A) Proliferation of primary human lung fibroblasts (HLF) over 72 hours during incubation with vehicle control (media), 10% DMSO (negative control), 0.1mM itaconate (IA), 1mM IA or 10mM IA. All groups n = 3. B) Crystal Violet survival assay of healthy HLFs, percentage calculated compared to vehicle control treated group; both groups n = 3. Data presented as mean ± S.E.M. Significance tested by Mann Whitney U test of area under the curve, *P < 0.05, **P < 0.01, ***P < 0.005.

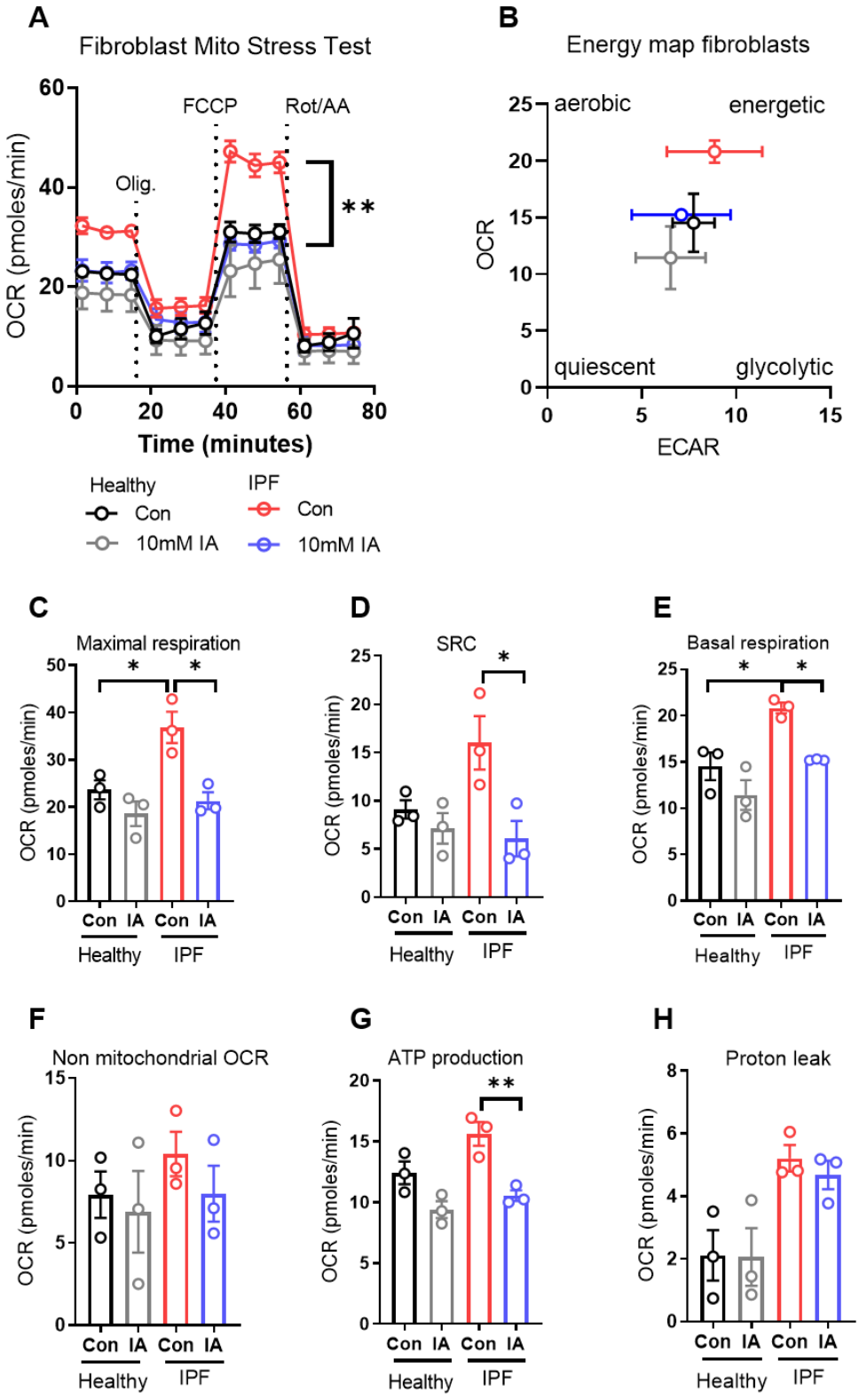

Figure 5.18. Metabolic phenotype rewired in human lung fibroblasts after culture with itaconate. Mitochondrial stress test of healthy and IPF primary human lung fibroblasts after 24h culture with 10mM itaconate or vehicle control (all groups n = 3); assessed after injection of Oligomycin, FCCP and Rotenone/Antimycin A. A) Analysis of OCR. B) Energy map showing four energy states: quiescent, energetic, aerobic, and glycolytic. C) Maximal respiration D) Spare respiratory capacity E) Basal respiration F) Non-mitochondrial oxygen consumption G) ATP production H) Proton leak. Data presented as mean ± S.E.M. Significance tested by One-Way ANOVA with Dunn's multiple comparison test, *P < 0.05, ** P< 0.01.

5.3.12 Itaconate alters primary human lung fibroblast phenotype *in vitro*

The influence of itaconate on the functional phenotype of healthy and IPF HLF was next assessed *in vitro*. Proliferation rate and wound healing capacity of healthy and IPF HLFs was assessed using the JuLI stage imaging system. HLFs were seeded in 96-well plates and incubated with 10mM itaconate or vehicle control for 72 hours, during which images were taken every 30 minutes at three positions in the well to calculate confluence. Treatment with 10mM itaconate *in vitro* significantly decreased HLF fibroblast proliferation in healthy, but even more so in IPF derived cells (Figure 5.19 A). To assess wound healing capacity, a scratch assay was performed next. A standardised scratch was applied in the middle of the well and wound width was monitored by taking a picture every 30 minutes over the subsequent 48 hours. In healthy HLFs, incubation with 10mM itaconate resulted in a slower scratch closure compared to vehicle control treatment, while in IPF HLF there was no change (Figure 5. 19 B and D). Gene expression analysis showed furthermore that culture with 10mM itaconate resulted in decreased expression of *Fn-1* and *IL-1β* (Figure 5.19 C). Together, these results show that treatment with itaconate *in vitro* can slow HLF proliferation, decrease wound healing capacity and lower gene expression of pro-fibrotic genes, indicating that itaconate could have anti-fibrotic properties.

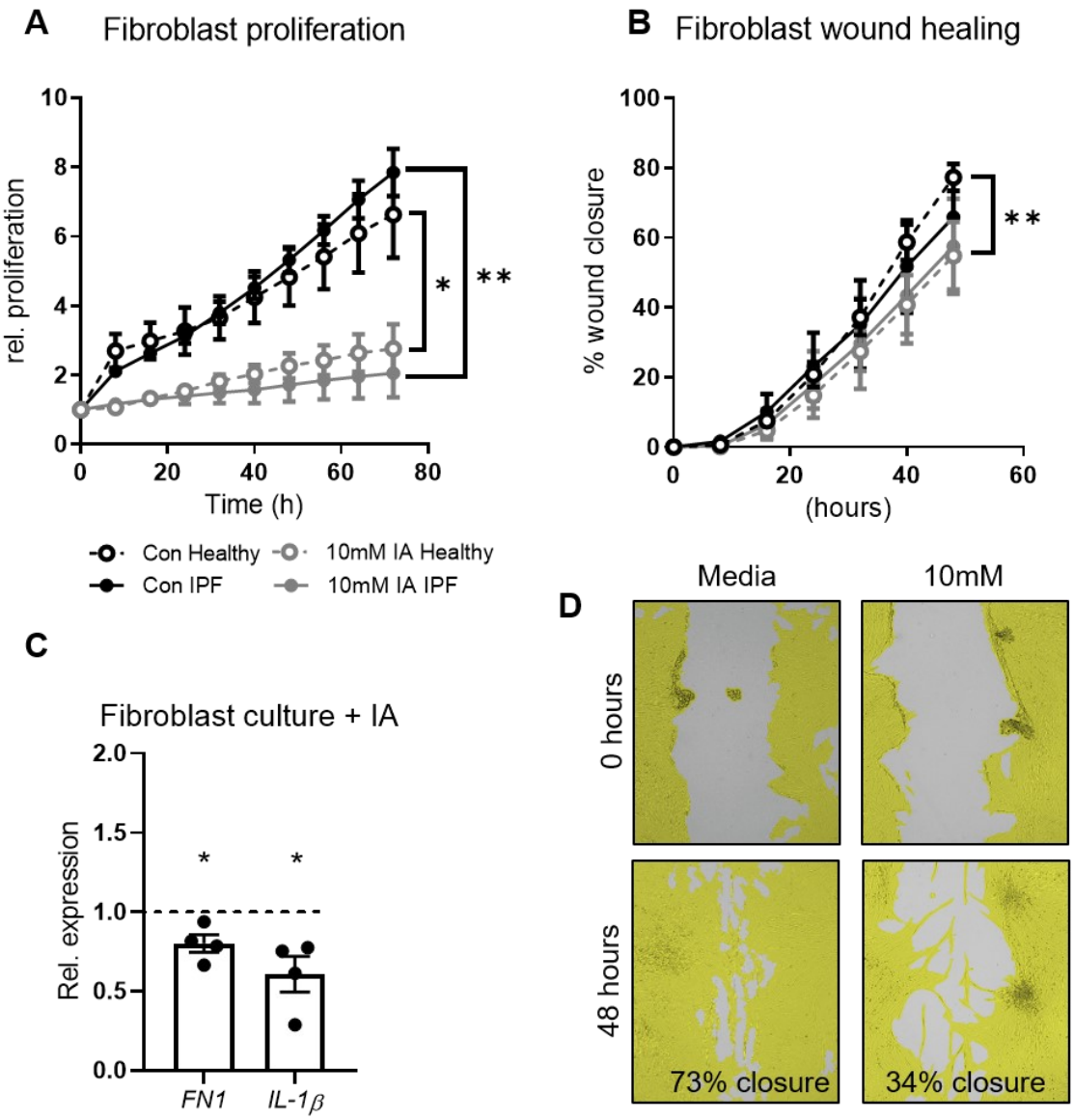

Figure 5.19. Decreased fibrotic phenotype of primary human lung fibroblasts treated with itaconate *in vitro*. A) Proliferation rate of healthy HLF incubated with 10mM itaconate (IA) or vehicle control measured using the JULI Stage system; (all groups n = 3). B) Wound healing capacity of healthy HLFs incubated with 10mM itaconate or vehicle control measured using the JuLI Stage system; (all groups n = 4). C) Gene expression analysis of *FN1* and *Il-1β* in healthy human primary lung fibroblasts incubated for 24h with 10mM itaconate or vehicle control. D) Representative images of fibroblast wound healing during culture with 10mM itaconate or vehicle control, acquired using the JULI stage system. D) Data presented as mean ± S.E.M. Significance was tested by two-tailed T-test of area under the curve (A – B), or one-sample T-test (C) *P < 0.05, ** P < 0.01.

5.3.13 Inhaled itaconate improves pulmonary fibrosis phenotype *in vivo*

The results presented here show that *ACOD1* expression is reduced in IPF AMs (Figure 5.2), *Acod1*$^{-/-}$ mice have worsened fibrotic phenotype in comparison to controls (Figures 5.4 and 5.8) and that itaconate can limit fibroblast wound healing capacities (Figure 5.18). These data raise the intriguing possibility that exogenous itaconate could improve the severity of lung fibrosis. To address whether inhaled itaconate is anti-fibrotic, we determined the dose of itaconate that would not provoke an inflammatory response in murine airways. We evaluated four different doses of itaconate (0.25mg/kg, 1mg/kg, 2.5mg/kg and 10mg/kg) or a PBS control (50 µl), which were administered via the oropharyngeal route to 10-week-old male WT mice. Mice were sacrificed after 24 hours; lung and BAL cells were counted and the immune infiltrate into BAL was analysed by flow cytometry. The highest dose of itaconate (10mg/kg) caused significant weight loss within 24 hours (Figure 5.20 A), as well as infiltration of large numbers of neutrophils, eosinophils and monocytes into the BAL (Figure 5.20 D–F). Furthermore, treatment with 2.5mg/kg resulted in significant increase of BAL cell numbers (Figure 5.20 C). We therefore selected a dose of 0.25mg/kg for subsequent experiments. This dose was also used by Daniels *et al*. *in vivo* in the brain[341]. To investigate whether treatment with itaconate could improve bleomycin induced pulmonary fibrosis, 0.25mg/kg itaconate was administered every third day after d10 via the oropharyngeal route to 10-week-old male mice (see Figure 5.1 C). Treatment with itaconate was started after the inflammatory phase had subsided, to test its particular potential as an anti-fibrotic treatment[267]. Repeated treatment with inhaled itaconate ameliorated all major hallmarks of lung fibrosis, including improved lung function (Figure 5.21 B-C), reduced gene expression of *Col4α1* (Figure 5.22 C) and *Fn-1* (Figure 5.22 D) and decreased collagen deposition (Figure 5.22 E–F). Taken together, these results demonstrate that inhaled itaconate improves bleomycin induced pulmonary fibrosis.

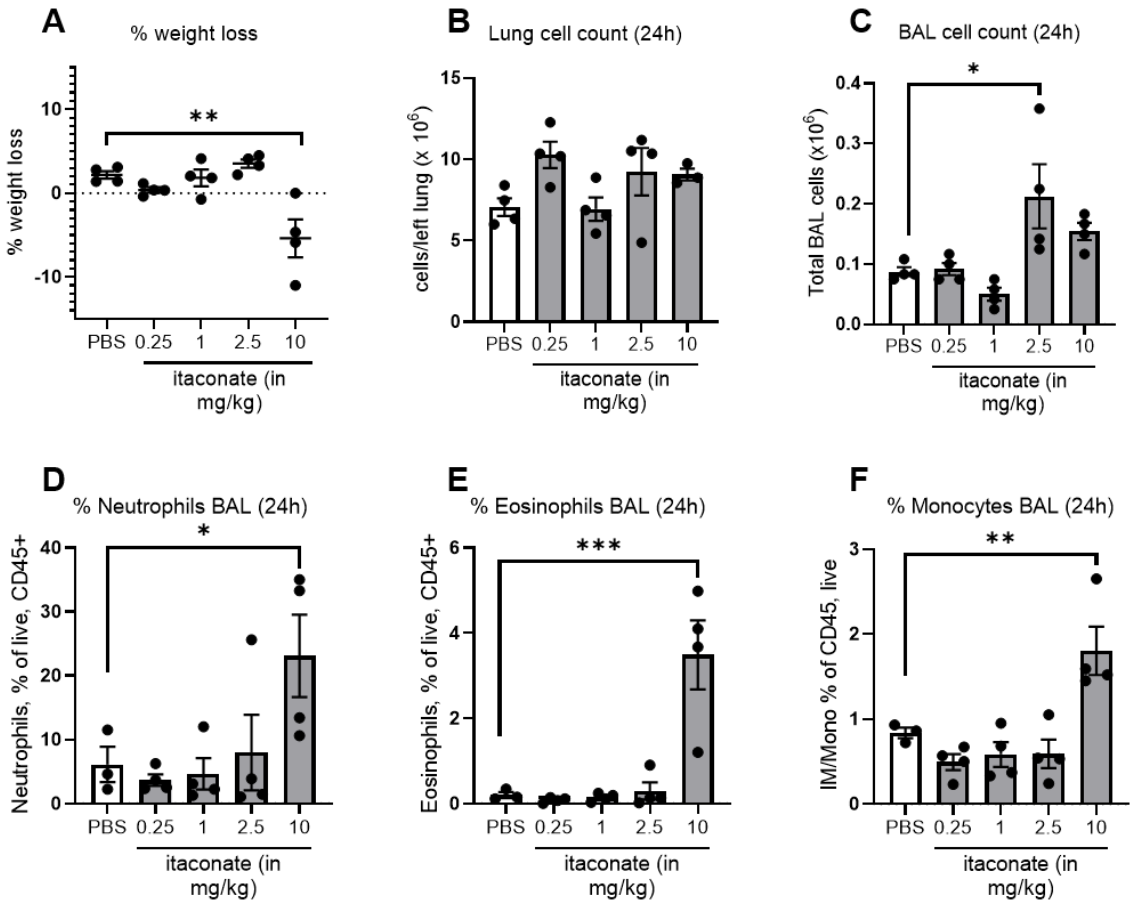

Figure 5.20. Titration of itaconate dose *in vivo*. WT mice were treated with 0.25 mM – 10mM itaconate or PBS oropharyngeal *in vivo* (all groups n = 4) and harvested at 24 hours post administration. A) Percent weight loss. B) Lung cell count in lung homogenate. C) BAL cell count. D) Percent BAL neutrophils of $CD45^+$ cells. E) Percent BAL eosinophils of $CD45^+$ cells. F) Percent BAL monocytes of $CD45^+$ cells. Data presented as mean ± S.E.M. Significance tested by One-Way ANOVA with Dunn's multiple comparison test, *P < 0.05, ** P< 0.01, ***P < 0.005.

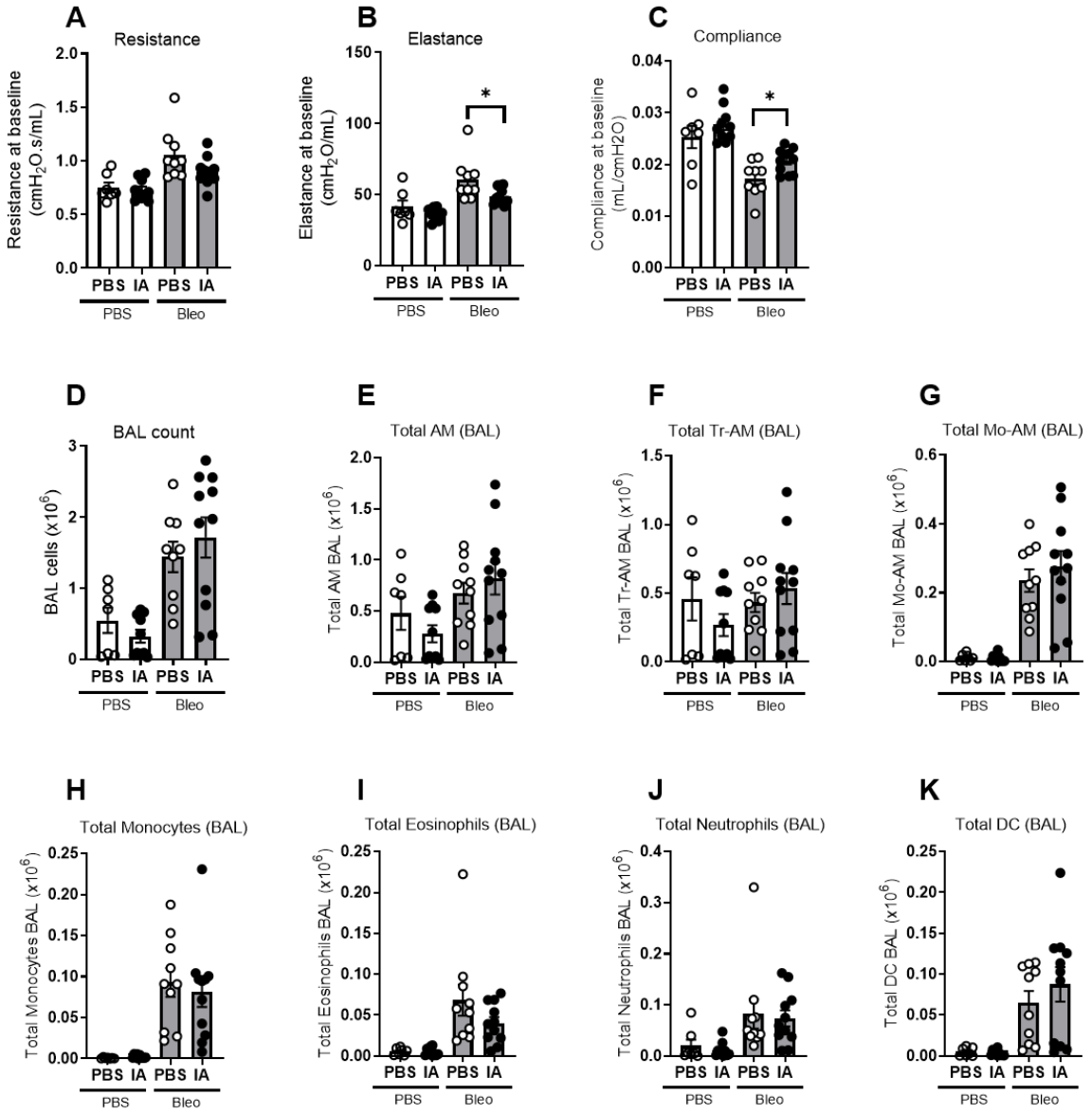

Figure 5.21. Lung function and immune cell infiltrate in BAL after treatment with inhaled itaconate. A – C) Resistance, elastance and compliance measured at baseline by FlexiVent in PBS or bleomycin dosed mice treated repeatedly with 0.25mg/kg itaconate (IA) or PBS. D) Total BAL count. E) Total AM in BAL F) Total Tr-AM in BAL G) Total Mo-AM in BAL H) Total monocytes in BAL I) Total eosinophils in BAL J) Total neutrophils in BAL K) Total dendritic cells (DC) in BAL. PBS/PBS n = 7, PBS/IA n = 10, bleo/PBS n = 9, bleo/IA n = 10. Data presented as mean ± S.E.M. Significance tested by One-Way ANOVA with Dunn's multiple comparison test, *P < 0.05.

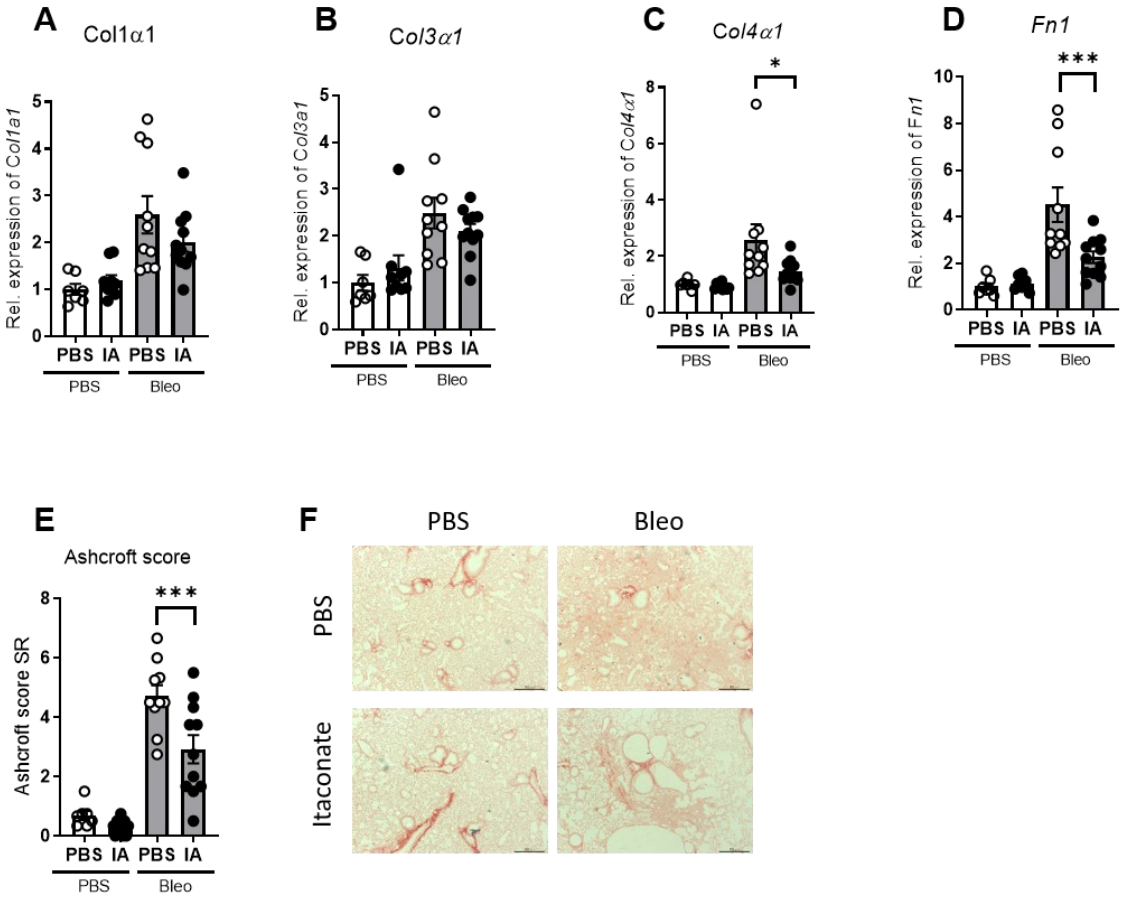

Figure 5.22. Fibrotic phenotype after treatment with inhaled itaconate. A – D) Gene expression analysis of *Col1α1, Col3α1, Col4α1* and *Fn-1* in lung homogenate at d21 post bleomycin after repeated treatment with inhaled itaconate (0.25mg/kg) or PBS. *Actb* was used as housekeeping control. E) Modified Ashcroft score based on Sirius red staining on histology slices. F) Representative images of Sirius red staining. PBS/PBS n = 7, PBS/IA n = 10, bleo/PBS n = 9, bleo/IA n = 10. Data presented as mean ± S.E.M. Significance tested by One-Way ANOVA with Dunn's multiple comparison test, *P < 0.05, ***P < 0.005.

5.3.14 Itaconate therapy in aged mice

As age is a risk factor for IPF, the anti-fibrotic potential of inhaled itaconate was investigated in aged (52-week-old) mice. While a repeat of the exact experiment as described in 5.3.13 was anticipated using the aged mice, they were a lot more susceptible to bleomycin and lost weight more rapidly than observed in the younger mice (Figure 5.23 A). Therefore, itaconate was administered every second day between d9 and d13 and harvested the mice at d14 post bleomycin. Assessment of lung function parameters at d14 post bleomycin showed that repeated administration of 0.25mg/kg itaconate had no effect on lung function parameters in either young or old mice at this time point (Figure 5.23 B –D). Furthermore, there was no difference in BAL cell count (Figure 5.24 A) and flow cytometry analysis showed no change in BAL cell composition (Figure 5.24 B – H) upon treatment with itaconate between d9 and d14 of the bleomycin model. Gene expression analysis showed that in aged mice, expression of *Col1α1* and *Col3α1* (Figure 5.25 A – B) was significantly increased after treatment with itaconate, whereas there was no change in *Col4α1* or *Fn-1* (Figure 5.25 C–D). However, collagen deposition did not change at this time point, as assessed by modified Ashcroft score based on Sirius red staining for collagen (Figure 5.25 E–F).

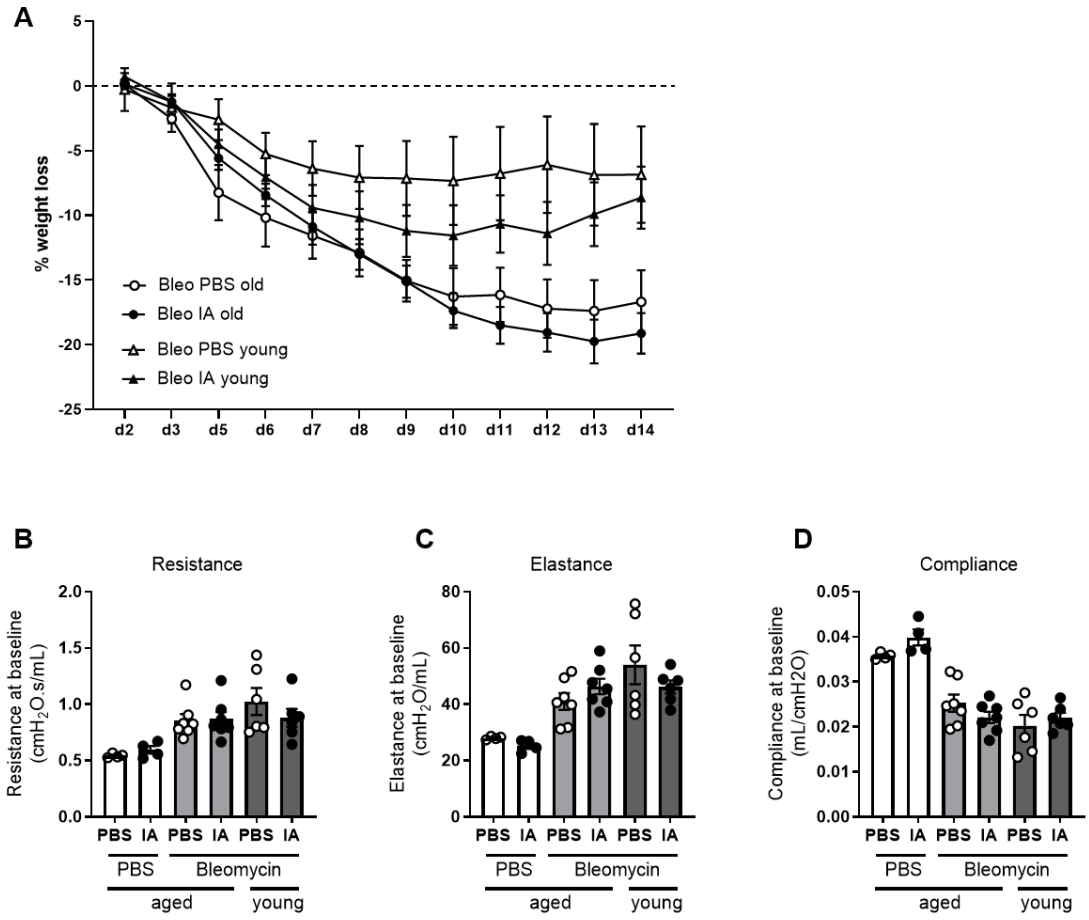

Figure 5.23. Weight loss and lung function parameters in young and aged mice at d14 post bleomycin after treatment with inhaled itaconate. A) Percent weight loss of young (10 weeks) or aged (52 weeks) PBS or bleomycin dosed mice treated repeatedly with 0.25mg/kg itaconate (IA) or PBS. B – D) Resistance, elastance and compliance measured at baseline by FlexiVent. PBS/PBS n = 4, PBS/IA n = 4, aged Bleomycin/PBS n = 7, aged Bleomycin/IA n = 7, young Bleomycin/PBS n = 6, young Bleomycin/IA n = 6. Data presented as mean ± S.E.M. Significance tested by One-Way ANOVA with Dunn's multiple comparison test.

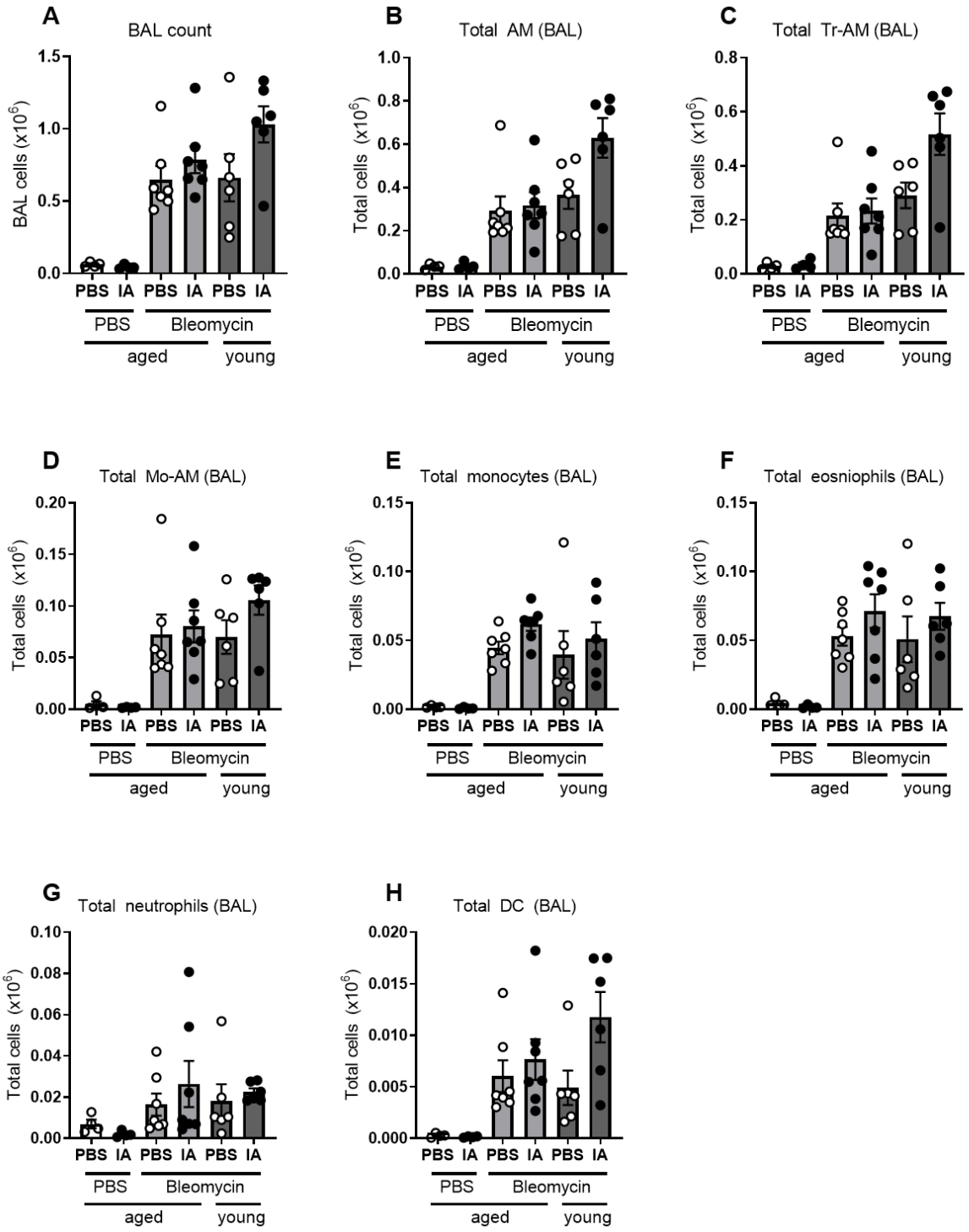

Figure 5.24. BAL cell composition in young and aged mice after treatment with itaconate. A) Total BAL count in young (10 weeks) or aged (52 weeks) PBS or bleomycin dosed mice treated repeatedly with 0.25mg/kg itaconate (IA) or PBS. E) Total airway macrophages (AM) in BAL F) Total Tr-AM in BAL G) Total Mo-AM in BAL H) Total monocytes in BAL I) Total eosinophils in BAL J) Total neutrophils in BAL K) Total dendritic cells (DC) in BAL. PBS/PBS n = 4, PBS/IA n = 4, aged Bleomycin/PBS n = 7, aged Bleomycin/IA n = 7, young Bleomycin/PBS n = 6, young Bleomycin/IA n = 6. Data presented as mean ± S.E.M. Significance tested by One-Way ANOVA with Dunn's multiple comparison test.

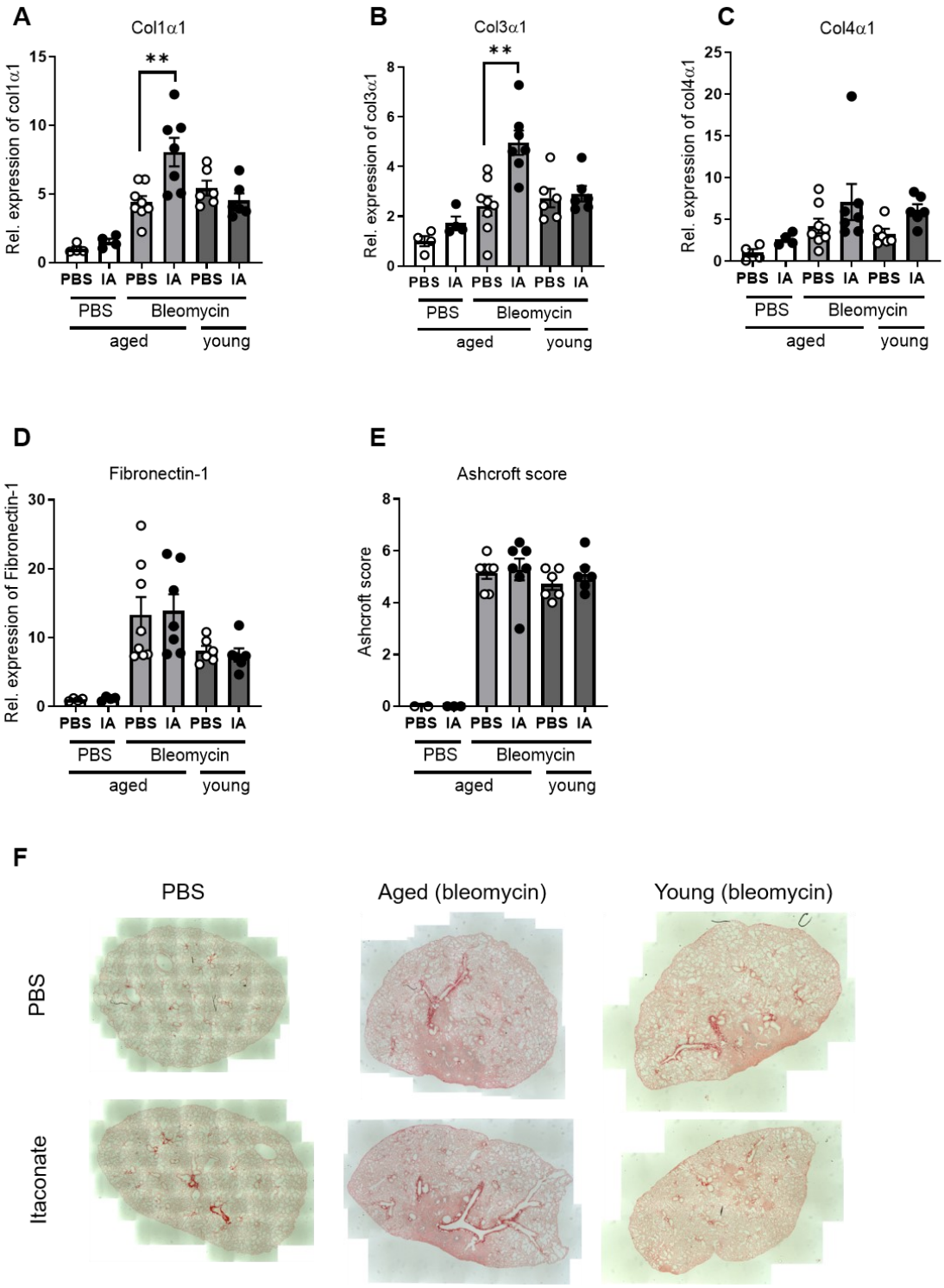

Figure 5.25. Fibrotic phenotype in young and old mice after treatment with inhaled itaconate. A – D) Gene expression analysis of *Col1α1, Col3α1, Col4α1* and *Fn1* in lung homogenate at d14 post bleomycin after repeated treatment with inhaled itaconate (0.25mg/kg) or PBS. *Actb* was used as housekeeping control. E) Ashcroft score based on Sirius red staining on histology slices. F) Representative images of Sirius red staining. PBS/PBS n = 4, PBS/IA n = 4, aged Bleomycin/PBS n = 7, aged Bleomycin/IA n = 7, young Bleomycin/PBS n = 6, young Bleomycin/IA n = 6. Data presented as mean ± S.E.M. Significance tested by One-Way ANOVA with Dunn's multiple comparison test.

5.3.15 Itaconate exposure alters pro-fibrotic pathways in IPF AMs

To investigate whether *ex vivo* treatment with itaconate could rewire IPF AM functional phenotype, CD206^{+} AMs were sorted from patient BAL, then incubated with 10mM itaconate for 24 hours and gene expression of key effector genes was analysed by qPCR (Figure 5.26). Gene expression relative to *ACTB* was compared between itaconate treated and untreated medium control groups. Treatment with itaconate decreased the gene expression of chemokines *CCL-2* and *CCL-22, MMP1, -9* and *-12* as well as *TGF-β1*, while the gene expression of *CD86* and *CD163* was increased. These results suggest that treatment with itaconate can rewire the pro-fibrotic phenotype of AMs not just in the bleomycin mouse model (Figure 5.16) but also in IPF patients and therefore opens a novel therapeutic possibility.

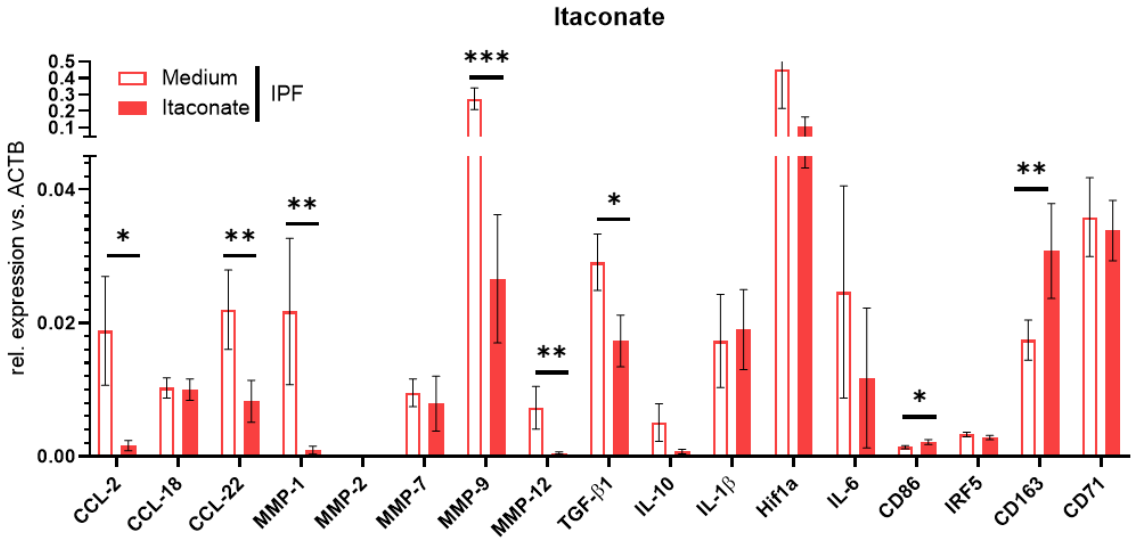

Figure 5.26. Culture with itaconate *ex vivo* alters IPF AM fibrotic phenotype. Gene expression analysis of fibrosis effector and AM phenotype genes in IPF airway macrophages (n = 12) treated with 10 mM itaconate or medium control for 24 hours *ex vivo*; *ACTB* was used as housekeeping control. Data presented as mean ± S.E.M. Statistical significance tested by Wilcoxon matched-pairs signed rank test, * P < 0.05, ** P < 0.01, *** P < 0.005.

5.4 Discussion

The mammalian metabolite itaconate was discovered as an antimicrobial agent by inhibiting isocitrate lyase in bacteria and thereby blocking the glycoxylate shunt[332] in the 1970s. Subsequent studies have shown that bacteria such as *Y.pestis* and *A. pseudomonas* degrade itaconate in a three-step reaction utilizing itaconate co-enzyme A (CoA) transferase, itaconyl-CoA hydratase and (s)-citramalyl-CoA lyase, thereby evading antimicrobial activity[342]. Moreover, production of itaconate is induced by interferons[343]. Michelucchi *et al*. have linked the gene *immune responsive gene-1* (*Irg1*) to transcribing cis-aconitate decarboxylase (CAD), which synthesises itaconate from cis-aconitate[344]. Due to a recent change in nomenclature, *Irg1* will here be referred to as *Acod1*. Recent studies have shown that itaconate is highly increased in macrophages upon activation[337]. It has been demonstrated to inhibit the TCA cycle enzyme SDH, thereby altering succinate levels[336] and decreasing expression of IL-6 and IL-12[345]. Lampropoulou *et al*. described an anti-inflammatory and antimicrobial role for itaconate[133], while another group showed that itaconate induces electrophilic stress and reacts with gluthathione as well as inhibiting IκBζ protein induction via activating transcription factor 3 (ATF3)[346]. This NRF2 independent pathway might therefore be a target for treatments for autoimmune diseases such as skin psoriasis, in which IκBζ is a key driver[347]. Additionally, itaconate has also been shown to induce anti-inflammatory pathways via the alkylation of KEAP1 and subsequent activation of NRF2[134], a basic leucine zipper protein that blocks pro-inflammatory cytokine transcription and triggers anti-inflammatory pathways, thereby reducing the macrophage inflammatory response[348]. Using RAW264.7 macrophages it has been shown that itaconate can modify cysteine in KEAP1 but also in glutathione and covalently modify key glycolytic enzymes leading to impaired glycolytic flux[349]. For its anti-microbial as well as anti-inflammatory potential, itaconate has been suggested as a therapeutic strategy in different diseases including *Mycobacterium Tuberculosis* infection[350], ischemic muscle injury[351], psoriasis[346] and Zika virus infection[341].

Based on these immunomodulatory functions, the role of itaconate in AMs during lung fibrosis was investigated here. In this chapter, a critical role for the *ACOD1*/itaconate pathway was identified in the pathogenesis of pulmonary fibrosis. We show that the *ACOD1*/itaconate pathway is disrupted in IPF, and that *Acod1*$^{-/-}$ mice have more severe disease phenotype in a murine model of pulmonary fibrosis. *Acod1* influences fibrotic responses in AMs as *Acod1*$^{-/-}$ Tr-AMs demonstrate impaired metabolism and enhanced expression of pro-fibrotic genes, whereas adoptive transfer of WT monocyte-recruited AMs into the lungs of *Acod1*$^{-/-}$ improved bleomycin induced pulmonary fibrosis and altered Tr-AM phenotype. *Ex vivo* culture of primary human lung fibroblasts with itaconate reversed metabolic reprogramming in IPF and decreased both proliferation and wound healing capacity. It is also shown here that therapeutic administration of inhaled itaconate *in vivo* ameliorates bleomycin-induced pulmonary fibrosis in mice. Thus, this work suggests the *ACOD1*/itaconate axis as an endogenous anti-fibrotic pathway that is dysregulated during IPF. These data highlight the prospect of therapeutic strategies, which directly promote *ACOD1*/itaconate and pharmacological approaches that deliver itaconate or its derivatives as anti-fibrotic agents.

It is well established that lung-resident AMs in mice maintain their populations via proliferation *in situ* during homeostasis[352,353], and that a second population of ontologically distinct Mo-AMs are recruited from peripheral monocytes during ongoing inflammatory responses[32]. It has recently been shown that Mo-AMs rather than Tr-AMs were essential for the development of pulmonary fibrosis in murine models, whereas deletion of tissue-resident AMs had no effect on disease[212]. The data presented here indicate that *Acod1* is differentially expressed in Tr-AMs and Mo-AMs, and that these cell types are metabolically distinct. Itaconate synthesis *via Acod1* is an anti-fibrotic pathway expressed in Mo-AMs, and this cell population has been shown to contribute to pulmonary fibrosis[212]: our data indicates that there is some functional diversity within Mo-AM populations, which may be determined in part by *Acod1* expression. A recent study by our group with lineage-traced AM populations in the human lung using BAL from sex-mismatched lung transplant patients showed that the majority of AMs in the adult lung post-transplant are monocyte-derived

rather than tissue resident cells[68]. Therefore, the finding that *Acod1* is highly expressed in Mo-AM populations in mice is particularly relevant. While *Acod1* expression was altered in Mo-AMs during pulmonary fibrosis, phenotypic changes such as decreased OXPHOS capacity and increased expression of fibrosis related genes presented in Tr-AMs in *Acod1*$^{-/-}$ mice, suggesting paracrine signalling of itaconate between Mo-AMs and Tr-AMs in the lungs. Adoptive transfer of Acod1 expressing Mo-AMs into *Acod1*$^{-/-}$ mice altered Tr-AM, but not Mo-AM phenotype, further highlighting the interaction between these two macrophage subsets in the lungs. Future studies may benefit from investigating Mo-AM and Tr-AM phenotype at later time points during the bleomycin model. It would furthermore be of interest to analyse, which proportions of Tr-AMs and Mo-AMs express *Acod1*, for example by single cell sequencing. This may further identify a subset of Mo-AMs, which is not driving fibrosis but supressing the pro-fibrotic phenotype through expression of itaconate.

As the fibrotic phenotype was more severe in *Acod1*$^{-/-}$ mice at d42 post bleomycin, a time point where this model usually resolves in young mice[266], this indicates that either fibrosis was not cleared efficiently or a second surge of collagen deposition occurred at a later point (after d21). Gene expression of *Col3α1* and *Fn-1* was increased in Acod1-deficient mice at d21 post bleomycin, which indicates that further collagen deposition may have occurred subsequently, contributing to more severe fibrosis at the later time point. It would be interesting to investigate a time point such as d28 or d32 in future experiments in *Acod1*$^{-/-}$ and WT mice to further understand whether Acod1-deficiency results in impaired resolution of pulmonary fibrosis or to prolonged collagen deposition.

In human AMs *ACOD1* is highly expressed under homeostatic conditions and disrupted during pulmonary fibrosis. This is particularly pertinent as not much is known regarding the role of itaconate during human disease. Meiser *et al.* recently reported that itaconate was not detectable in plasma or urine of septic patients or in BAL of patients with pulmonary inflammation, including patients with COPD and sarcoidosis[354]. Furthermore, *Acod1* expression was not detected by several single cell sequencing studies in the lung[239,355] whereas here, expression of *Acod1* in healthy control BAL and decreased expression in IPF

BAL is reported. This might be due to several factors regarding sample processing protocols, sequencing depth of single cell approaches and the severity of fibrosis patients investigated. IPF Cell Atlas datasets were generated from enzymatic digestion of whole lung homogenates rather than from lavage, which is likely a major confounder for the study of metabolic processes. Furthermore, IPF Cell Atlas patients were end-stage IPF (or other ILD) patients, but the present study evaluated expression of *ACOD1* in patients undergoing diagnostic bronchoscopy. Finally, the control lungs reported in the IPF Cell Atlas studies were either declined for organ donation or transplant donors, whereas control samples from our study were obtained from BAL of healthy volunteers.

Primary HLF showed increased levels of OXPHOS and metabolic activity, similar to previously reported increases in glycolytic phenotype after incubation with TGF-β[230]. Treatment with itaconate ameliorated the increased OXPHOS and rewired HLF metabolic phenotype, directly influencing human lung fibroblast phenotype and function *in vitro*. Incubation with itaconate altered HLF fibrotic phenotype by decreasing proliferation rate and wound healing capacity compared to sham-treated controls. These findings indicate that itaconate could mediate paracrine effects on other stromal or immune cells types as it is actively secreted at homeostasis and may have implications for chronic diseases of the lung or other tissues in which fibrosis plays a role.

Finally, the anti-fibrotic potential of itaconate was investigated by administering itaconate *in vivo* during peak fibrosis of the bleomycin model. The utilised dose was selected based on studies published by Daniels *et al*. in a model of neuronal Zika virus infection[341] and titration experiments. Treatment with itaconate improved lung function, but did not change the immune cell profile in BAL. However, the biggest change in immune cell profile between WT and *Acod1*$^{-/-}$ mice was previously observed at d42 post bleomycin, which was not investigated here. While the aim of this experiment was to investigate whether itaconate administered during peak fibrosis could improve the fibrotic phenotype, it would be of interest to also assess later time points and use longer administration of itaconate.

5.5 Conclusion

The results shown in this chapter indicate that the *ACOD1*/itaconate axis is decreased in IPF patients and that Acod1-deficiency in mice results in more severe fibrosis at d42, in the bleomycin mouse model. Furthermore, Mo-AMs are highest expressers of *Acod1* in mice and Acod1-deficiency in Tr-AMs resulted in lower OXPHOS and increased pro-fibrotic gene expression, indicating anti-fibrotic potential of itaconate. Indeed, adoptive transfer of WT, itaconate-expressing, Mo-AMs into *Acod1*$^{-/-}$ mice improved fibrotic phenotype, while treatment with itaconate *in vitro* decreased lung fibroblast proliferation and wound healing capacity and ameliorated fibrotic phenotype in mice upon repeated administration *in vivo*. These findings suggest that itaconate is produced by Mo-AMs and released locally at the site of injury where it decreases both Tr-AM pro-fibrotic transcriptional profile and fibroblast fibrotic phenotype. While treatment with itaconate on HLFs *in vitro* reduces OXPHOS and therefore indicates inhibition of succinate dehydrogenase, the exact mechanism of action of itaconate in this context needs to be further investigated. Future experiments could investigate whether itaconate acts on Tr-AMs and HLFs by inhibiting SDH or activating NRF2. In conclusion, this work defines a regulatory pathway, which is impaired during fibrotic lung disease. The relationships between *ACOD*1, airway macrophages and fibrosis reported here have the potential to impact therapies for IPF and highlight *ACOD1*, itaconate or its metabolites as molecular targets for the treatment of fibrotic lung diseases.

6. Final Discussion and conclusions

6.1 Final discussion and future work

Airway macrophages (AMs) are specialised niche cells, which regulate inflammatory and wound-healing responses in the airways and play a key role during the pathogenesis of pulmonary fibrosis[31]. Recently, it has become clear that underlying metabolic programmes tightly control macrophage functions. Seminal studies have shown *in vitro* that pro-inflammatory macrophages upregulate glycolysis and thereby NADPH production in the pentose phosphate pathway, while the TCA cycle is broken to accumulate citrate, succinate, fumarate and malate[90,129,356,357]. These metabolites contribute to ROS production, cytokine release (IL-1β, IL-18) and immune cell recruitment and are therefore essential in supporting the pro-inflammatory macrophage function. M(IL-4) macrophages on the other hand rely on increased OXPHOS and FAO to generate sufficient energy to launch an anti-inflammatory and wound repair programme by secreting collagens, TGF-β and anti-inflammatory cytokines[51,117,357,358]. Whilst *in vitro* derived cells model the possible spectrum of macrophage activation, these do not fully recapitulate the pulmonary environment, with its unique features such as low glucose levels, constant exposure to environmental particles and inhaled pathogens as well as complex interactions between immune and stromal cells. This thesis therefore focused on elucidating the metabolic phenotypes which underlie primary AMs from the murine/human airways during ongoing fibrotic lung disease. Indeed, the data presented in this thesis highlights that *in situ* AM phenotypes are complex and distinct from *in vitro* models. The metabolic phenotype of AMs observed during pulmonary fibrosis does not recapitulate that of 'wound-healing' M(IL-4) macrophages[357,359], but instead showed a dependency on glycolysis as well as minimal spare respiratory capacity (chapter 3).

The overall focus of this thesis was to identify the underling metabolic programmes of AMs during interstitial lung diseases such as IPF and CHP. One particular aim was to determine how ontological origins of AM populations (Tr-AM and Mo-AM), might dictate metabolic phenotypes. In addition, it has become clear that specific metabolites have signalling functions outside of their roles as metabolic intermediates. However, the role of TCA cycle

metabolites contributing to the fibrotic phenotype is not well described. A major outcome of the work described here is the identification of the immunomodulatory metabolite itaconate as an endogenous anti-fibrotic in the human and murine lung.

6.1.1 How does metabolic alteration in AMs underlie fibrotic lung disease?

Metabolic reprogramming has been identified as a major driver of pulmonary fibrosis and confounding factor of aging related diseases. While increased glucose uptake was detected in fibrotic foci[360], glycolysis has been shown to be necessary for the differentiation of fibroblasts into myo-fibroblasts[230]. Furthermore, mitochondrial dysfunction and increased ROS production have been observed in lung fibroblasts during IPF[229]. However, metabolic reprogramming has been reported not only in fibroblasts but also in other key cell types involved in the pathogenesis of IPF, such as epithelial cells and AMs. In epithelial cells, the pro-fibrotic cytokine TGF-β has been shown to induce mitochondrial depolarisation, resulting in increased ROS production[361], while mitochondria in IPF AMs showed morphological defects and mtROS was increased[237]. Other studies reported increased expression of the glucose transporter GLUT1 in AMs during IPF[360] as well as increased glycolysis[362] and glucose uptake in AMs in the murine bleomycin model[231], suggesting glycolytic reprogramming in human and murine AMs during pulmonary fibrosis. However, many questions remain open such as a more detailed understanding of AM metabolic reprogramming *in situ* and its connection to functional change. While *in vitro* experiments have identified signalling functions for many metabolites, including succinate, fumarate and citrate[358,363–365], these had not been investigated in the context of lung fibrosis.

In chapter 3, both the metabolic and functional phenotype of AMs derived from healthy controls and patients with ILD was assessed. Although the activation phenotype of AMs from IPF and CHP patients were similar, interestingly AMs from these groups had distinct metabolic phenotypes. Specifically, there was increased lactate, isocitrate and malate in BAL as well as increased expression of first half TCA cycle genes in IPF AMs compared to healthy controls. These findings add more detail to the understanding of AM metabolic

phenotype during pulmonary fibrosis and show that *in vitro* models of macrophage 'wound healing' phenotypes[51,356,366], characterised by increases in OXPHOS and FAO do not recapitulate primary cell phenotypes[83]. Furthermore, incubation with metabolic inhibitors showed that IPF AMs are particularly susceptible to inhibition of glycolysis, which decreased pro-fibrotic gene expression, but also to inhibition of pyruvate transport and FAO, while inhibition of glutaminolysis did not alter AM fibrotic phenotype. These results confirm findings derived from murine models of pulmonary fibrosis where inhibition of glycolysis had the largest effect on AM functional rewiring[231]. However, whilst in the bleomycin mouse model increased ECAR and OCR levels were detected during the seahorse assay upon the development of pulmonary fibrosis[231], this was not the case in primary human AMs from IPF patients. This may be due to greater heterogeneity within fibrosis pathogenesis at the time point of BAL procedure or may reflect the acute nature of murine models, in which fibrosis is established and resolved within a relatively short period of time.

In contrast, metabolic reprogramming was more pronounced in CHP AMs compared to healthy controls, clearly showing increased utilisation of glycolysis and OXPHOS, although the second half of the TCA cycle was disrupted. These results suggest that even with a downregulation of the TCA cycle enzymes following SDH, OXPHOS can function and sustain AM phenotype. Furthermore, the metabolic profile of CHP AMs resembles that of pro-inflammatory *in vitro* macrophages[367], highlighting the pro-inflammatory environment in CHP lungs due to chronic antigen exposure[18]. While not much is known about AMs during CHP and their metabolic profile in particular, it is important to realise the stark alterations in metabolic programme in comparison to healthy, but also IPF AMs. AM metabolic phenotype may therefore serve as a potential biomarker to better differentiate between IPF and CHP pathogenesis. However, due to the rarity of CHP it was only possible to recruit a small cohort of CHP patients for the experiments presented here and a validation cohort would be valuable. It remains to be investigated why IPF and CHP have such distinct metabolic phenotypes, although contributing factors could be differences in the inflammatory environment as well as changes in the epigenetic regulatory profile.

The data presented here has highlighted the importance of underlying metabolic pathways on AM function during fibrotic lung disease and opens new avenues for the understanding and manipulation of metabolic pathways and signalling factors in other chronic lung diseases. Indeed, recent advances have been made in identifying mitochondrial dysfunction in AMs during COPD[202], altered fatty acid metabolism during Asthma[368] and utilisation of AM metabolites as nutrients by *P. Aeruginosa* during cystic fibrosis[369]. The field of chronic lung research would greatly benefit from identifying further metabolic dysfunctions in AMs and other key cell types and to target these therapeutically as has been outlined for pulmonary fibrosis in this thesis.

6.1.2 Targets to rewire AM metabolic phenotype and function

Gene expression analysis, targeted GC-MS and *ex vivo* culture with metabolic inhibitors revealed targets suitable to rewire AM metabolism and potentially pro-fibrotic phenotypes. Citrate, succinate and fumarate in particular have been identified recently to be connected to immune function and were assessed as potential targets. Citrate can move from mitochondrion to cytoplasm via the citrate carrier (CIC) and is an essential substrate for FAS, production of NO, ROS and prostaglandins[128]. Furthermore, it is the primary substrate for the production of itaconate, which has been shown to have immunomodulatory function in AMs by inhibiting SDH[336] and triggering an anti-inflammatory programme via NRF2[134]. Fumarate in turn has been linked to epigenetic reprogramming in trained immunity and inflammation, by inhibiting histone demethylases and inducing methylation of the promotors of *Tnf* and *Il6*, resulting in increased expression[137]. Succinate induces IL-1β, via Hif1α stabilisation, while also driving posttranscriptional modification of proteins through succinylation[90,370].

The present work has shown that succinate was negatively correlated to AM number in BAL, while it was not detectable in sorted AMs (chapter 3), suggesting either increased uptake by other cell types or decreased production in AMs. Succinate signals through the succinate receptor (SUCNR1) to regulate immune function, such as modulating inflammatory cytokine release, macrophage polarisation and fibroblast activation[371]. As

such, SDH was selected as a target for inhibition by DMM *in vivo*, during bleomycin induced pulmonary fibrosis and *ex vivo* in IPF AMs. Results from these experiments (chapter 4) suggest that *ex vivo* treatment with DMM, or supplementation with succinate improved pro-fibrotic AM phenotype, by decreasing expression of MMPs. Treatment with DMM *in vivo* was particularly effective as a preventative measure, before lung injury, while additional data is needed to draw conclusions about the therapeutic administration of DMM during pulmonary fibrosis.

Interestingly, we observed the increased expression of *IDH2* in both IPF and CHP AMs, as well as increased expression of *ACLY* (chapter 3). ACLY converts citrate to acetyl CoA and oxaloacetate in the cytosol and thereby contributes to FAS, while inducing the production of NO, ROS and prostaglandins in response to LPS treatment *in vivo*[130]. Furthermore, ACLY regulates histone modification and loss of ACLY results in decreased glycolysis gene expression and glucose consumption[130]. Targeting ACLY in AMs during pulmonary fibrosis with specific inhibitors[246] may prevent the feedback of oxaloacetate into the glycolysis pathway and decrease FAS from acetyl CoA, therefore presenting a promising approach to reduce substrate availability in fibrotic AMs.

Other ways to reduce glycolysis and OXPHOS include inhibition of hexokinase by 2-DG and the mitochondrial pyruvate carrier by UK5099. Results from these *ex vivo* experiments (chapter 3) showed a strong dependency of IPF AMs on glycolysis, but also pyruvate utilisation to sustain release of MMPs and chemokines. Furthermore, inhibition of FAO by Etomoxir resulted in decreased expression of MMPs and *IL-10* and increased expression of the pro-inflammatory transcription factor *IRF5*, while the inhibition of glutamine transport by DON did not affect AM phenotype. These results are in line with previous findings obtained in the bleomycin mouse model of pulmonary fibrosis[231]. While here, Etomoxir was used at a concentration of 200μM[254], recent studies have shown that a concentration of 3μM is sufficient to inhibit enzyme activity and larger concentrations deplete intracellular free coenzyme A (CoA) in AMs[262] and induce oxidative stress in T cells[372]. Also taking the increased expression of *ACLY* in IPF AMs into account (chapter 3), it would be interesting

to investigate the role of FAO on AM fibrotic phenotype in more detail. Of the TCA cycle metabolites analysed, only fumarate was significantly increased in IPF AMs compared to controls (chapter 3); further research is necessary to delineate its impact on AM fibrotic phenotype, potentially through epigenetic modulation.

In summary, inhibition of glycolysis (hexokinase), pyruvate transport and SDH have shown to rewire AM fibrotic phenotype, while citrate (ACLY) and fumarate may have potential as therapeutic targets in fibrotic lung disease.

6.1.3 Tr-AM and Mo-AMs have distinct metabolic characteristics

As it became increasingly clear that two distinct AM populations populate the lungs (Tr-AM and Mo-AM)[212,236,373], one aim of this thesis was to investigate the metabolic phenotype of these to better understand their distinct roles during pulmonary fibrosis. Tr- AMs are derived from yolk sac or foetal liver monocytes, which seed the lung before birth and develop into long lived, self-maintaining AMs, expressing $CD11c^{hi}$ and $SigF^{hi}$ [53,352,374]. However, when this niche is empty, for example due to lung injury, adult peripheral monocytes may be recruited[55]. Indeed, single cell RNAseq analysis after sex mismatched lung transplant has shown that the vast majority of AMs several months after the transplant was recipient-derived and therefore recruited from the periphery[375]. This study suggests that a much higher proportion of Mo-AMs populate the lungs in aged individuals than previously understood from murine studies. These findings are now supported by another single cell RNAseq study, showing that only Mo-AMs are localised in fibrotic regions and express molecules driving fibroblast proliferation[376], while another study identified a fibrosis-localised pro-fibrotic transitional AM subpopulation intermediate between Mo-AM and Tr-AM[236]. Several studies have recently investigated transcriptomic and metabolic reprogramming during monocyte to Tr-AM differentiation[377,378] and metabolic requirements for efferocytosis of AMs[379,380]. However, all of these studies have focused on AMs in pro-inflammatory disease models.

Here, Mo-AM and Tr-AM metabolic phenotypes were investigated in the context of pulmonary fibrosis in the bleomycin mouse model. Indeed, a SigF^{low} Mo-AM population emerged after lung injury with bleomycin as previously published[212,239,376]. However, while Tr-AMs showed significantly increased OXPHOS upon bleomycin injury, this was not the case for Mo-AMs at d7 and d21 post bleomycin, compared to PBS control mice (chapter 4). It therefore remains to be determined how Mo-AMs sustain their differentiation and suggested pro-fibrotic potential metabolically during pulmonary fibrosis. One solution could be to investigate more time points to form a more complete picture of the kinetics of Mo-AM recruitment. Another explanation for this distinct metabolic phenotype of Mo-AMs and Tr-AMs could be the different nutritional environment in the lungs compared to the periphery, resulting in distinct (epigenetic) priming of Mo-AMs and Tr-AMs[381].

Overall, the present work has demonstrated a distinct metabolic phenotype of Tr-AMs and Mo-AMs during the bleomycin model of pulmonary fibrosis, in which OXPHOS was significantly increased in Tr-AMs, while Mo-AMs were quiescent.

6.1.4 The role of itaconate during pulmonary fibrosis

As our preliminary work had identified the ACOD1/itaconate axis to be dysfunctional in IPF AMs, the aim of the final chapter of this thesis was to investigate the role of itaconate in the context of pulmonary fibrosis. Itaconate has previously been described as an antimicrobial substrate, inhibiting isocitrate lyase in bacteria and thereby blocking the glyoxylate shunt[382,383]. Recently, itaconate has emerged as a regulator of AM metabolism and function[331,384], as it has the potential to inhibit SDH[385], leading to an accumulation of succinate, as well as activating the NRF2 anti-inflammatory programme by binding KEAP1[134]. Furthermore, itaconate covalently modifies glycolytic proteins due to its weak elecrophilicity and impairs glycolytic flux through inhibition of fructose-bisphosphate aldolase A (ALDOA)[349]. While itaconate has been shown to restrict Zika virus replication in neurons[341], it is induced during respiratory syncytial virus (RSV) infection and contributes to ROS production[386]. Furthermore, itaconate is the most highly expressed metabolite during

stimulation with LPS[345] *in vitro* and also highly expressed in TB infected AMs, where it can reduce immune pathology[387], but also be exploited by *Mtb* as nutrient[383]. Here, the role of itaconate was investigated in the context of pulmonary fibrosis. While some reports used itaconate-analogues to improve cellular uptake, it has become increasingly clear that neither dimethyl itaconate, nor 4-octyl itaconate are metabolised to itaconate intracellularly[388,389]; therefore itaconate was utilised in its natural form for this study.

As decreased expression of itaconate and *ACOD1* gene expression was detected in IPF BAL and AMs, respectively (chapter 5), a global itaconate knockout mouse model was utilised to determine the role of itaconate during bleomycin induced pulmonary fibrosis. *Acod1*$^{-/-}$ mice had a more severe fibrotic phenotype at d42 post bleomycin, a time point where, in WT mice, the resolution of bleomycin induced pulmonary fibrosis is underway[266]. Further studies are required to delineate whether itaconate indeed promotes the resolution of pulmonary fibrosis or whether it slows pathogenesis or alters the fibrotic milieu in another way. Itaconate was administered during peak fibrosis of the murine bleomycin model and ameliorated fibrotic phenotype, which is more relevant for translation into the clinic than preventative administration[267]. A caveat however was the use of comparably young mice, 10 – 12 weeks old, as the experiments with the available aged mice had to be terminated early due to increased severity of the bleomycin model. This should be improved with a lower dose of bleomycin for aged mice.

Furthermore, some questions remain regarding the mechanism of action of itaconate during pulmonary fibrosis. The present results show that culture with itaconate reprograms fibroblast metabolic phenotype[230], suggesting a paracrine effect of AM-derived itaconate (not detected in fibroblasts and epithelial cells) on fibroblasts. It remains to be determined how itaconate is taken up intracellularly by fibroblasts and whether it acts by inhibition of SDH, induction of NRF2 or via another pathway. Finally, culture of primary human AMs with itaconate resulted in increased expression of CD86 and CD163 *ex vivo* (chapter 5), which would be interesting to investigate further at a transcriptional and regulatory level. Caveats of the present experiments include the fact that the hydroxyproline assay could not be

completed due to the outbreak of the coronavirus pandemic and furthermore, itaconate levels were only measured in BAL and not in isolated AMs, due to the sensitivity of the assay. Both experiments would add to the present research.

This thesis research has furthermore identified differences in Mo-AMs and Tr-AMs in the context of the signalling metabolite itaconate (chapter 5). In itaconate-deficient mice (*Acod1*$^{-/-}$), Tr-AMs showed increased pro-fibrotic gene expression compared to WT, while this was not the case for Mo-AMs. However, Mo-AMs had significantly higher expression of *Acod1* compared to Tr-AMs, suggesting they might deliver itaconate to the site of injury where it then dampens the AM and fibroblast phenotype. As the experiments shown here have identified itaconate as an anti-fibrotic factor and Mo-AMs as the main expressers of *Acod1*, these results are in contrast to previous publications suggesting Mo-AMs solely as drivers of fibrotic pathogenesis[212,239,376] and rather support a new hypothesis of an itaconate-expressing anti-fibrotic Mo-AM sub-population. Indeed, adoptive transfer of itaconate-expressing Mo-AMs during peak fibrosis improved the bleomycin induced fibrotic phenotype (chapter 5) and offers new therapeutic possibilities. Combining the knowledge obtained from the recent RNAseq advances in humans, it will hopefully soon be possible to identify Mo-AMs from Tr-AMs by flow cytometry in humans, which will be necessary to explore these new concepts in the context of human IPF.

In summary, results from chapter 5 suggest that itaconate is an anti-fibrotic factor, which is dysregulated during IPF and decreases the severity of pulmonary fibrosis through reduction of fibroblast metabolic phenotype and the fibrotic phenotype is ameliorated after therapeutic treatment with inhaled itaconate or adoptive transfer of itaconate-sufficient Mo-AMs.

6.2 Future experiments

Several avenues were not directly addressed in this thesis, due to the scope of the project. It is now accepted that during pro-inflammatory macrophage activation and metabolic reprogramming *in vitro*, the TCA cycle is broken at the position of IDH and SDH, leading to

an accumulation of succinate and citrate, while it is intact and actively contributing to ATP production in alternatively activated M(IL-4) macrophages[51]. Here, *IDH* gene expression was found to be increased in IPF and CHP AMs, while *SDH* gene expression was decreased. However, no accumulation of citrate or succinate could be detected by targeted GC-MS in isolated AMs from these patient groups, while both were increased in BAL in CHP but not IPF patients (chapter 3). These data support the hypothesis that CHP AMs more closely resemble the pro-inflammatory macrophage phenotype described *in vitro*, sustained by the pro-inflammatory environment surrounding them. However, it will be necessary to further delineate this concept to understand the differences between IPF and CHP AM metabolic programme, its connection to *in vitro* observed states and related functional changes. In particular, investigating the link between accumulation of isocitrate in IPF BAL, increased expression of first half TCA cycle genes and decreased expression of *ACOD1*, which is branching off at this point could yield a better understanding of the dynamics and impact of alterations in the first half of the TCA cycle in AMs.

Gene expression of ACLY, which is one of the starting points for FAS, was found to be highly increased in IPF and CHP AMs. It would be of interest to analyse FAS in AMs during pulmonary fibrosis and to trace citrate to determine its contribution to FAS/FAO and energy levels. This could be achieved by inhibiting ACLY, in IPF AMs *ex vivo*, as several ACLY inhibitors are available and are currently investigated as anti-cancer treatments[246].

Acetyl CoA obtained via ACLY from citrate has furthermore been suggested to contribute to histone acetylation and related gene expression modulation[243,390]. Investigating the role of acetyl CoA, but also fumarate, which is significantly increased in IPF AMs and has been suggested as an epigenetic modulator[137,140], on epigenetic reprogramming during IPF may therefore provide new insights into the mechanisms of phenotypic alteration through metabolites.

Since the focus of this thesis was on central carbon metabolism, primarily glycolysis and OXPHOS, the pentose phosphate pathway was not investigated in detail. The increased utilisation of the glycolysis pathway in IPF and CHP AMs however suggests that there might

also be an increased flux through the pentose phosphate pathway, yielding NADPH for the production of superoxide, which is increased in AMs during pulmonary fibrosis[173,242]. The pentose phosphate pathway and its NADPH production could therefore be another target to be assessed for AM metabolic therapy during pulmonary fibrosis.

One caveat of this thesis is the low number of recruited CHP patients across the different assays due to the rare occurrence of the disease and as bronchoscopies had stopped during the COVID-19 pandemic. The results are included here nevertheless as they show a clear contrast in AM metabolic phenotype compared to IPF AMs. It will however be important to validate the CHP results shown here in a separate cohort and perform assays such as the seahorse glycolysis stress test to compare it to that of IPF patients. This could give further insights into whether BAL or AM metabolic reprogramming could be used to distinguish between IPF and CHP patients during the diagnostic process.

As recent advances have been made in characterising AM populations in the lungs by single cell RNAseq[239,355,376], it will hopefully soon be possible to distinguish between and sort Mo-AMs and Tr-AMs from human BAL. This method would be of great value to translate the findings on Mo-AM and Tr-AM metabolic phenotype during pulmonary fibrosis obtained in mice into the human disease and could provide new insights into Mo-AM dysfunction, pro-fibrotic phenotype and the itaconate pathway during IPF. Furthermore, treatment of IPF patients with itaconate-expressing Mo-AMs could then be considered.

It has been shown here that targeting AMs specifically with metabolic inhibitors delivered in liposomes is a viable option. Other metabolic inhibitors that have been shown here to rewire IPF AM phenotype could be considered for liposome treatment, in particular 2-DG or UK5099. Another option could be siRNA therapy targeting these pathways, which has recently been suggested for the treatment of respiratory diseases[296].

Here, expression of collagen I, III, IV and fibronectin was used as a readout for the pathogenesis of pulmonary as suggested by the American Thoracic Society guidelines for the use of animal models for pulmonary fibrosis[266]. As other studies however highlight the importance of collagen VI in myeloid cells in the context of pulmonary fibrosis[391], it would

be important to add this as a readout to future studies and especially to investigate a potential link between itaconate and collagen VI in macrophages.

Finally, many questions remain open regarding the immunomodulatory role of itaconate in AMs during pulmonary fibrosis. Itaconate has been the subject of considerable research interest, as well in an *in vitro* context to understand basic concepts, as during disease and particularly respiratory diseases such as Tuberculosis and RSV infection. However, some basic concepts such as the uptake of itaconate are not fully understood. The results presented here show that itaconate has a direct impact on human lung fibroblasts, supporting a paracrine signalling mechanism such as suggested by Zhou *et al*. between macrophages and fibroblasts[392]. Understanding this interaction better and also identifying the mechanism of action of itaconate on human lung fibroblasts would enable to pinpoint dysfunction of the itaconate pathway during IPF and allow for more precise therapeutic targeting.

6.3 Concluding remarks

Collectively, the research reported here contributes to a better understanding of AM metabolic reprogramming during lung fibrosis. Whilst IPF AMs show increased utility of the first half of the TCA cycle and a dependency on glycolysis for fibrotic phenotype, CHP AMs have highly increased glycolysis and OXPHOS utility, resulting in a pro-inflammatory metabolic phenotype. Detailed analysis of the two AM subsets Mo-AM and Tr-AM in the bleomycin mouse model has highlighted the distinct metabolic phenotype underlying their functional phenotype. While Tr-AMs showed increased utilisation of glycolysis and OXPHOS during the bleomycin mouse model, this was not the case for Mo-AMs. The immunomodulatory metabolite itaconate may have potential as an anti-fibrotic therapy. Further investigation in the *Acod1*$^{-/-}$ mouse model showed a role for itaconate in controlling the development of pulmonary fibrosis, as *Acod1*$^{-/-}$ had more severe fibrosis and were rescued by inhalation of itaconate and adoptive transfer of itaconate expressing Mo-AMs during the fibrotic phase. Taken together, this thesis highlights the importance of metabolic

pathways regulating the functional phenotype of AMs during pulmonary fibrosis and identified several targets for innovative treatment options.

Reference list

1. Raghu, G. Idiopathic pulmonary fibrosis: Guidelines for diagnosis and clinical management have advanced from consensus-based in 2000 to evidence-based in 2011. *Eur. Respir. J.* **37**, 743–746 (2011).

2. Raghu, G. Idiopathic pulmonary fibrosis: Guidelines for diagnosis and clinical management have advanced from consensus-based in 2000 to evidence-based in 2011. *Eur. Respir. J.* **37**, 743–746 (2011).

3. Maher, T. M., Wells, A. U. & Laurent, G. J. Idiopathic pulmonary fibrosis: Multiple causes and multiple mechanisms? *Eur. Respir. J.* **30**, 835–839 (2007).

4. Selman, M. & Pardo, A. Revealing the pathogenic and aging-related mechanisms of the enigmatic idiopathic pulmonary fibrosis: An integral model. *Am. J. Respir. Crit. Care Med.* **189**, 1161–1172 (2014).

5. King, T. E. Clinical advances in the diagnosis and therapy of the interstitial lung diseases. *Am. J. Respir. Crit. Care Med.* **172**, 268–279 (2005).

6. Martinez, F. J., Andrade, J. A. De, Anstrom, K. J., King, T. E. & Raghu, G. Randomized trial of acetylcysteine in idiopathic pulmonary fibrosis. *N. Engl. J. Med.* **370**, 2093–2101 (2014).

7. Raghu, G., Anstrom, K. J., King, T. E., Lasky, J. A. & Martinez, F. J. Prednisone, azathioprine, and N-acetylcysteine for pulmonary fibrosis. *N. Engl. J. Med.* **366**, 1968–1977 (2012).

8. Wollin, L. *et al.* Mode of action of nintedanib in the treatment of idiopathic pulmonary fibrosis. *Eur. Respir. J.* **45**, 1434–1445 (2015).

9. Richeldi, L. *et al.* Efficacy and Safety of Nintedanib in Idiopathic Pulmonary Fibrosis. *N. Engl. J. Med.* **370**, 2071–2082 (2014).

10. Flaherty, K. R. *et al.* Nintedanib in progressive fibrosing interstitial lung diseases. *N. Engl. J. Med.* **381**, 1718–1727 (2019).

11. Woodcock, H. V, Molyneaux, P. L. & Maher, T. M. Reducing lung function decline in patients with idiopathic pulmonary fibrosis : potential of nintedanib. 503–510 (2013).doi:10.2147/DDDT.S38833

12. Noble, P. W. *et al.* Pirfenidone for idiopathic pulmonary fibrosis: Analysis of pooled data from three multinational phase 3 trials. *Eur. Respir. J.* **47**, 243–253 (2016).

13. Ogura, T. *et al.* Safety and pharmacokinetics of nintedanib and pirfenidone in idiopathic pulmonary fibrosis. *Eur. Respir. J.* **45**, 1382–1392 (2015).

14. Datta, A., Scotton, C. J. & Chambers, R. C. Novel therapeutic approaches for pulmonary fibrosis. *Br. J. Pharmacol.* **163**, 141–172 (2011).

15. Schaefer, C. J., Ruhrmund, D. W., Pan, L., Seiwert, S. D. & Kossen, K. Antifibrotic activities of pirfenidone in animal models. *Eur. Respir. Rev.* **20**, 85–97 (2011).

16. Behr, J. *et al.* Safety and tolerability of acetylcysteine and pirfenidone combination therapy in idiopathic pulmonary fibrosis: A randomised, double-blind, placebo-controlled, phase 2 trial. *Lancet Respir. Med.* **4**, 445–453 (2016).

17. Pepys, J., Riddell, R. W., Citron, K. M. & Clayton, Y. M. Precipitins Against Extracts of Hay and Moulds in the Serum of Patients with Farmer's Lung, Aspergillosis, Asthma, and Sarcoidosis. *Thorax* **17**, 366–374 (1962).

18. Riario Sforza, G. G. & Marinou, A. Hypersensitivity pneumonitis: A complex lung disease. *Clin. Mol. Allergy* **15**, 1–8 (2017).

19. Varone, F. *et al.* Fibrotic Hypersensitivity Pneumonitis: Diagnosis and Management. *Lung* **198**, 429–440 (2020).

20. Meyer, K. C. *et al.* An official American Thoracic Society clinical practice guideline: The clinical utility of bronchoalveolar lavage cellular analysis in interstitial lung disease. *Am. J. Respir. Crit. Care Med.* **185**, 1004–1014 (2012).

21. Salisbury, M. L. *et al.* Diagnosis and treatment of fibrotic hypersensitivity pneumonia: Where we stand and where we need to go. *Am. J. Respir. Crit. Care Med.* **196**, 690–699 (2017).

22. Walsh, S. L. F. *et al.* Multicentre evaluation of multidisciplinary team meeting agreement on diagnosis in diffuse parenchymal lung disease: a case-cohort study. *Lancet Respir. Med.* **4**, 557–565 (2016).

23. Morisset, J. *et al.* Identification of diagnostic criteria for chronic hypersensitivity pneumonitis: An international modified Delphi survey. *Am. J. Respir. Crit. Care Med.* **197**, 1036–1044 (2018).

24. Thomeer, M. J., Costabel, U., Rizzato, G., Poletti, V. & Demedts, M. Comparison of registries of interstitial lung diseases in three. 114–118 (2001).

25. Lacasse, Y. & Cormier, Y. Hypersensitivity pneumonitis. *Orphanet J. Rare Dis.* **1**, 1–9 (2006).

26. Hyldgaard, C., Hilberg, O., Muller, A. & Bendstrup, E. A cohort study of interstitial lung diseases in central Denmark. *Respir. Med.* **108**, 793–799 (2014).

27. Pérez, E. R. F. *et al.* Identifying an inciting antigen is associated with improved survival in patients with chronic hypersensitivity pneumonitis. *Chest* **144**, 1644–1651 (2013).

28. Selman, M., Pardo, A. & King, T. E. Hypersensitivity pneumonitis: Insights in diagnosis and pathobiology. *Am. J. Respir. Crit. Care Med.* **186**, 314–324 (2012).

29. Kokkarinen, J. I., Tukiainen, H. O. & Terho, E. O. Effect of Corticosteroid Treatment on the Recovery of Pulmonary Function in Farmer's Lung. *Am. Rev. Respir. Dis.* **145**, 3–5 (1992).

30. Maher, T. M. Chronic hypersensitivity pneumonitis; an enigmatic and frequently fatal disease. *Eur. Respir. Rev.* **29**, 1–3 (2020).

31. Byrne, A. J., Mathie, S. A., Gregory, L. G. & Lloyd, C. M. Pulmonary macrophages: key players in the innate defence of the airways. *Thorax* **70**, 1189–96 (2015).

32. Ginhoux, F. & Jung, S. Monocytes and macrophages: Developmental pathways and tissue homeostasis. *Nat. Rev. Immunol.* **14**, 392–404 (2014).

33. Fricker, M. Macrophage dysfunction in the pathogenesis and treatment of asthma. (2017).doi:10.1183/13993003.00196-2017

34. Ginhoux, F. & Jung, S. Monocytes and macrophages: Developmental pathways and tissue homeostasis. *Nat. Rev. Immunol.* **14**, 392–404 (2014).

35. Hussell, T. & Bell, T. J. Alveolar macrophages: plasticity in a tissue-specific context. *Nat. Rev. Immunol.* **14**, 81–93 (2014).

36. Yona, S. *et al.* Fate Mapping Reveals Origins and Dynamics of Monocytes and Tissue Macrophages under Homeostasis. *Immunity* **38**, 79–91 (2013).

37. Chawla, A., Nguyen, K. D. & Goh, Y. P. S. Macrophage-mediated inflammation in metabolic disease. *Nat. Rev. Immunol.* **11**, 738–749 (2011).

38. Lambrecht, B. N. Alveolar Macrophage in the Driver's Seat. *Immunity* **24**, 366–368 (2006).

39. Koivisto, L., Bi, J., Häkkinen, L. & Larjava, H. Integrin αvβ6: Structure, function and role in health and disease. *Int. J. Biochem. Cell Biol.* **99**, 186–196 (2018).

40. Byrne, A. J., Maher, T. M. & Lloyd, C. M. Pulmonary Macrophages: A New Therapeutic Pathway in Fibrosing Lung Disease? *Trends Mol. Med.* **22**, 303–316 (2016).

41. Misharin, A. V., Morales-Nebreda, L., Mutlu, G. M., Budinger, G. R. S. & Perlman, H. Flow cytometric analysis of macrophages and dendritic cell subsets in the mouse lung. *Am. J. Respir. Cell Mol. Biol.* **49**, 503–510 (2013).

42. Zaynagetdinov, R. *et al.* Identification of myeloid cell subsets in murine lungs using flow cytometry. *Am. J. Respir. Cell Mol. Biol.* **49**, 180–189 (2013).

43. Guth, A. M. *et al.* Lung environment determines unique phenotype of alveolar macrophages. *Am. J. Physiol. Cell. Mol. Physiol.* **296**, L936–L946 (2009).

44. Snelgrove, R. J. *et al.* A critical function for CD200 in lung immune homeostasis and the severity of influenza infection. *Nat. Immunol.* **9**, 1074–1083 (2008).

45. Murray, P. J. *et al.* Macrophage activation and polarization: nomenclature and experimental guidelines. *Immunity* **41**, 14–20 (2014).

46. Lee, I. T. & Yang, C. M. Role of NADPH oxidase/ROS in pro-inflammatory mediators-induced airway and pulmonary diseases. *Biochem. Pharmacol.* **84**, 581–590 (2012).

47. Lawrence, T., immunology, G. N.-N. reviews & 2011, undefined Transcriptional regulation of macrophage polarization: enabling diversity with identity. *nature.com* at <https://www.nature.com/articles/nri3088>

48. Martinez, F. O. & Gordon, S. The M1 and M2 paradigm of macrophage activation: Time for reassessment. *F1000Prime Rep.* **6**, 1–13 (2014).

49. Stein, B. M., Keshav, S., Harris, N. & Gordon, S. Interleukin 4 Potently Enhances Murine Macrophage Mannose Receptor Activity: A Marker of Alternative Immunologic Macrophage Activation By Michael Stein, Satish Keshav, Neil Harris,* and Siamon Gordon. *J Exp Med* **176**, 287–292 (1992).

50. Varin, A. & Gordon, S. Alternative activation of macrophages: Immune function and cellular biology. *Immunobiology* **214**, 630–641 (2009).

51. Bossche, J. Van den, O'Neill, L. A. & Menon, D. Macrophage Immunometabolism: Where Are We (Going)? *Trends Immunol.* **xx**, 1–12 (2017).

52. Schulz, C. *et al.* A Lineage of Myeloid Cells Independent of Myb and Hematopoietic Stem Cells. 2–7 (2012).

53. Guilliams, M. *et al.* Alveolar macrophages develop from fetal monocytes that differentiate into long-lived cells in the first week of life via GM-CSF. **210**, 1977–1992 (2013).

54. Hashimoto, D. *et al.* Tissue-resident macrophages self-maintain locally throughout adult life with minimal contribution from circulating monocytes. *Immunity* **38**, 792–804 (2013).

55. Laar, L. van de *et al.* Yolk Sac Macrophages, Fetal Liver, and Adult Monocytes Can Colonize an Empty Niche and Develop into Functional Tissue-Resident Macrophages. *Immunity* **44**, 755–768 (2016).

56. Svedberg, F. R. *et al.* The lung environment controls alveolar macrophage metabolism and responsiveness in type 2 inflammation. *Nat. Immunol.* **20**, 571–580 (2019).

57. Ginhoux, F. & Guilliams, M. Tissue-Resident Macrophage Ontogeny and Homeostasis. *Immunity* **44**, 439–449 (2016).

58. Tan, S. Y. S. & Krasnow, M. A. Developmental origin of lung macrophage diversity. *Development* **143**, 1318–1327 (2016).

59. Belperio, J. A. *et al.* Critical role for the chemokine MCP-1/CCR2 in the pathogenesis of bronchiolitis obliterans syndrome. *J. Clin. Invest.* **108**, 547–556 (2001).

60. Patel, A. A. *et al.* The fate and lifespan of human monocyte subsets in steady state and systemic inflammation. *J. Exp. Med.* **214**, 1913–1923 (2017).

61. Shi, C. & Pamer, E. G. Monocyte recruitment during infection and inflammation. *Nat. Rev. Immunol.* **11**, 762–774 (2011).

62. Gibbings, S. L. *et al.* Transcriptome analysis highlights the conserved difference between embryonic and postnatal-derived alveolar macrophages. *Blood* **126**, 1357–1366 (2015).

63. Bittmann, I. *et al.* Cellular chimerism of the lung after transplantation: An interphase cytogenetic study. *Am. J. Clin. Pathol.* **115**, 525–533 (2001).

64. Eguíluz-Gracia, I. *et al.* Long-Term persistence of human donor alveolar macrophages in lung transplant recipients. *Thorax* **71**, 1006–1011 (2016).

65. Nayak, D. K. *et al.* Long-term persistence of donor alveolar macrophages in human lung transplant recipients that influences donor specific immune responses. *Am J Transplant.* **16**,

2300–2311 (2017).

66. Hunninghake, G. W. *et al.* The Human Alveolar Macrophage. *Methods Cell Biol.* **21**, 95–112 (1980).

67. Thomas, E. D., Ramberg, R. E., Sale, G. E., Sparkes, R. S. & Golde, D. W. Direct evidence for a bone marrow origin of the alveolar macrophage in man. *Science* **192**, 1016–8 (1976).

68. Byrne, A. J. *et al.* Dynamics of human monocytes and airway macrophages during healthy aging and after transplant. *J. Exp. Med.* **217**, 1–11 (2020).

69. Metcalf, T. U. *et al.* Human Monocyte Subsets Are Transcriptionally and Functionally Altered in Aging in Response to Pattern Recognition Receptor Agonists. *J. Immunol.* **199**, 1405–1417 (2017).

70. Hearps, A. C. *et al.* Aging is associated with chronic innate immune activation and dysregulation of monocyte phenotype and function. *Aging Cell* **11**, 867–875 (2012).

71. Seidler, S., Zimmermann, H. W., Bartneck, M., Trautwein, C. & Tacke, F. Age-dependent alterations of monocyte subsets and monocyte-related chemokine pathways in healthy adults. *BMC Immunol.* **11**, 30 (2010).

72. Zhang, L. *et al.* Macrophages: Friend or foe in idiopathic pulmonary fibrosis? *Respir. Res.* **19**, 1–10 (2018).

73. Cai, M. *et al.* CCL18 in serum, BAL fluid and alveolar macrophage culture supernatant in interstitial lung diseases. *Respir. Med.* **107**, 1444–1452 (2013).

74. Prasse, A. *et al.* A vicious circle of alveolar macrophages and fibroblasts perpetuates pulmonary fibrosis via CCL18. *Am. J. Respir. Crit. Care Med.* **173**, 781–792 (2006).

75. Pechkovsky, D. V. *et al.* Alternatively activated alveolar macrophages in pulmonary fibrosis-mediator production and intracellular signal transduction. *Clin. Immunol.* **137**, 89–101 (2010).

76. Schupp, J. C. *et al.* Macrophage activation in acute exacerbation of idiopathic pulmonary fibrosis. *PLoS One* **10**, 1–11 (2015).

77. Mahalanobish, S., Saha, S., Dutta, S. & Sil, P. C. Matrix metalloproteinase: An upcoming therapeutic approach for idiopathic pulmonary fibrosis. *Pharmacol. Res.* **152**, 104591 (2020).

78. Bossche, J. Van den, O'Neill, L. A. & Menon, D. Macrophage Immunometabolism: Where Are We (Going)? *Trends Immunol.* **38**, 395–406 (2017).

79. Masters, C. J., Reid, S. & Don, M. Glycolysis - new concepts in an old pathway. *Mol. Cell. Biochem.* **76**, 3–14 (1987).

80. Akram, M. Mini-review on glycolysis and cancer. *J. Cancer Educ.* **28**, 454–457 (2013).

81. Abbaszadeh, Z., Çeşmeli, S. & Biray Avcı, Ç. Crucial players in glycolysis: Cancer progress. *Gene* **726**, 3–8 (2020).

82. Lunt, S. Y. & Heiden, M. G. Vander Aerobic glycolysis: Meeting the metabolic requirements of cell proliferation. *Annu. Rev. Cell Dev. Biol.* **27**, 441–464 (2011).

83. O'Neill, L. A. J., Kishton, R. J. & Rathmell, J. A guide to immunometabolism for immunologists. *Nat. Rev. Immunol.* **16**, 553–65 (2016).

84. Newsholme, P., Curi, R., Gordon, S. & Newsholme, E. A. Metabolism of glucose, glutamine, long-chain fatty acids and ketone bodies by murine macrophages. *Biochem. J.* **239**, 121–5 (1986).

85. Krawczyk, C. M. *et al.* Toll-like receptor-induced changes in glycolytic metabolism regulate dendritic cell activation. *Blood* **115**, 4742–4749 (2010).

86. Donnelly, R. P. *et al.* mTORC1-Dependent Metabolic Reprogramming Is a Prerequisite for NK Cell Effector Function. *J. Immunol.* **193**, 4477–4484 (2014).

87. Michalek, R. D. *et al.* Cutting Edge: Distinct Glycolytic and Lipid Oxidative Metabolic Programs Are Essential for Effector and Regulatory CD4 + T Cell Subsets . *J. Immunol.* **186**, 3299–3303 (2011).

88. Michl, J., Ohlbaum, D. J. & Silverstein, S. C. 2-Deoxyglucose selectively inhibits Fc and complement receptor-mediated phagocytosis in mouse peritoneal macrophages. I. Description of the inhibitory effect. *J. Exp. Med.* **144**, 1465–1483 (1976).

89. Babior, B. M. NADPH oxidase. *Curr. Opin. Immunol.* **16**, 42–47 (2004).

90. Tannahill, G. M. *et al.* Succinate is an inflammatory signal that induces IL-1β through HIF-1α. *Nature* **496**, 238–242 (2013).

91. Nazaret, C., Heiske, M., Thurley, K. & Mazat, J. P. Mitochondrial energetic metabolism: A simplified model of TCA cycle with ATP production. *J. Theor. Biol.* **258**, 455–464 (2009).

92. Raimundo, N., Baysal, B. E. & Shadel, G. S. Revisiting the TCA cycle: Signaling to tumor formation. *Trends Mol. Med.* **17**, 641–649 (2011).

93. Jha, A. K. *et al.* Network integration of parallel metabolic and transcriptional data reveals metabolic modules that regulate macrophage polarization. *Immunity* **42**, 419–430 (2015).

94. Everts, B. *et al.* TLR-driven early glycolytic reprogramming via the kinases TBK1-IKKε supports the anabolic demands of dendritic cell activation. *Nat. Immunol.* **15**, 323–332 (2014).

95. Martínez-Reyes, I. & Chandel, N. S. Mitochondrial TCA cycle metabolites control physiology and disease. *Nat. Commun.* **11**, 1–11 (2020).

96. Tannahill, G. M. *et al.* Succinate is an inflammatory signal that induces IL-1β through HIF-1α. *Nature* **496**, 238–242 (2013).

97. Heiden, M. Vander, Cantley, L. & Thompson, C. Understanding the Warburg effect: The metabolic Requiremetns of cell proliferation. *Science (80-.).* **324**, 1029–1033 (2009).

98. Sengupta, S., Peterson, T. R. & Sabatini, D. M. Regulation of the mTOR Complex 1 Pathway by Nutrients, Growth Factors, and Stress. *Mol. Cell* **40**, 310–322 (2010).

99. Rong, X. *et al.* LXRs regulate ER stress and inflammation through dynamic modulation of membrane phospholipid composition. *Cell Metab.* **18**, 685–697 (2013).

100. Bonnefont, J. P. *et al.* Carnitine palmitoyltransferases 1 and 2: Biochemical, molecular and medical aspects. *Mol. Aspects Med.* **25**, 495–520 (2004).

101. Huang, S. C.-C. *et al.* Cell-intrinsic lysosomal lipolysis is essential for alternative activation of macrophages. *Nat. Immunol.* **15**, 846–55 (2014).

102. Vats, D. *et al.* Oxidative metabolism and PGC-1β attenuate macrophage-mediated inflammation. *Cell Metab.* **4**, 13–24 (2006).

103. Posokhova, E. N., Khoshchenko, O. M., Chasovskikh, M. I., Pivovarova, E. N. & Dushkin, M. I. Lipid synthesis in macrophages during inflammation in vivo: Effect of agonists of peroxisome proliferator activated receptors α and γ and of retinoid X receptors. *Biochem.* **73**, 296–304 (2008).

104. Feingold, K. R. *et al.* Mechanisms of triglyceride accumulation in activated macrophages. *J. Leukoc. Biol.* **92**, 829–839 (2012).

105. Malandrino, M. I. *et al.* Enhanced fatty acid oxidation in adipocytes and macrophages reduces lipid-induced triglyceride accumulation and inflammation. *Am. J. Physiol. - Endocrinol. Metab.* **308**, E756–E769 (2015).

106. Ecker, J. *et al.* Induction of fatty acid synthesis is a key requirement for phagocytic differentiation of human monocytes. *Proc. Natl. Acad. Sci. U. S. A.* **107**, 7817–7822 (2010).

107. Hosios, A. M. *et al.* Amino Acids Rather than Glucose Account for the Majority of Cell Mass in Proliferating Mammalian Cells. *Dev. Cell* **36**, 540–549 (2016).

108. Altman, B. J., Stine, Z. E. & Dang, C. V. From Krebs to clinic: Glutamine metabolism to cancer therapy. *Nat. Rev. Cancer* **16**, 619–634 (2016).

109. Yuneva, M., Zamboni, N., Oefner, P., Sachidanandam, R. & Lazebnik, Y. Deficiency in glutamine but not glucose induces MYC-dependent apoptosis in human cells. *J. Cell Biol.* **178**, 93–105 (2007).

110. Pietrocola, F., Galluzzi, L., Bravo-San Pedro, J. M., Madeo, F. & Kroemer, G. Acetyl coenzyme A: A central metabolite and second messenger. *Cell Metab.* **21**, 805–821 (2015).

111. Santos, C. C. dos, Gopal, B. & Verma, S. Metformin: An Old Dog with a New Trick? *Cell Metab.* **28**, 334–336 (2018).

112. Sato, N. *et al.* Metformin attenuates lung fibrosis development via NOX4 suppression. *Respir. Res.* **17**, 1–12 (2016).

113. Rangarajan, S. *et al.* Metformin reverses established lung fibrosis in a bleomycin model. *Nat. Med.* **24**, 1121–1127 (2018).

114. Spagnolo, P. *et al.* Metformin Does Not Affect Clinically Relevant Outcomes in Patients with Idiopathic Pulmonary Fibrosis. *Respiration* **96**, 314–322 (2018).

115. Hecker, L. *et al.* Reversal of Persistent Fibrosis in Aging by Targeting Nox4-Nrf2 Redox Imbalance. **6**, (2014).

116. Mills, E. L. *et al.* Succinate Dehydrogenase Supports Metabolic Repurposing of Mitochondria to Drive Inflammatory Macrophages. *Cell* **167**, 457-470.e13 (2016).

117. Huang, S. C.-C. *et al.* Cell-intrinsic lysosomal lipolysis is essential for alternative activation of macrophages. *Nat. Immunol.* **15**, 846–855 (2014).

118. Kelly, B. & O'Neill, L. A. J. Metabolic reprogramming in macrophages and dendritic cells in innate immunity. *Cell Res.* **25**, 771–784 (2015).

119. Baker, E. H. *et al.* Hyperglycemia and cystic fibrosis alter respiratory fluid glucose concentrations estimated by breath condensate analysis. *J. Appl. Physiol.* **102**, 1969–1975 (2007).

120. Woods, P. S. *et al.* Tissue-resident alveolar macrophages do not rely on glycolysis for LPS-induced inflammation. *Am. J. Respir. Cell Mol. Biol.* **62**, 243–255 (2020).

121. Schneider, C. *et al.* Induction of the nuclear receptor PPAR-γ 3 by the cytokine GM-CSF is critical for the differentiation of fetal monocytes into alveolar macrophages. *Nat. Immunol.* **15**, 1026–1037 (2014).

122. Palmieri, E. M. *et al.* Nitric oxide orchestrates metabolic rewiring in M1 macrophages by targeting aconitase 2 and pyruvate dehydrogenase. *Nat. Commun.* **11**, (2020).

123. Palsson-Mcdermott, E. M. & O'Neill, L. A. J. The Warburg effect then and now: From cancer to inflammatory diseases. *BioEssays* **35**, 965–973 (2013).

124. Rodríguez-Prados, J.-C. *et al.* Substrate fate in activated macrophages: a comparison between innate, classic, and alternative activation. *J. Immunol.* **185**, 605–614 (2010).

125. Everts, B. *et al.* TLR-driven early glycolytic reprogramming via the kinases TBK1-IKKε supports the anabolic demands of dendritic cell activation. *Nat. Immunol.* **15**, 323–332 (2014).

126. Corcoran, S. E., Neill, L. A. J. O., Corcoran, S. E. & Neill, L. A. J. O. HIF1 a and metabolic reprogramming in inflammation Find the latest version : HIF1 α and metabolic reprogramming in inflammation. *J Clin Invest* **126**, 3699–3707 (2016).

127. O'Neill, L. A. J. A Broken Krebs Cycle in Macrophages. *Immunity* **42**, 393–394 (2015).

128. Infantino, V. *et al.* The mitochondrial citrate carrier: a new player in inflammation. *Biochem. J.* **438**, 433–6 (2011).

129. Ryan, D. G. & O'Neill, L. A. J. Krebs cycle rewired for macrophage and dendritic cell effector functions. *FEBS Lett.* **591**, 2992–3006 (2017).

130. Wellen, K. E. *et al.* ATP-citrate lyase links cellular metabolism to histone acetylation. *Science (80-.).* **324**, 1076–1080 (2009).

131. Wang, B. *et al.* Microtubule acetylation amplifies p38 kinase signalling and anti-inflammatory IL-10 production. *Nat. Commun.* **5**, (2014).

132. Hu, L. *et al.* Epigenetic regulation of interleukin 6 by histone acetylation in macrophages and its role in paraquat-induced pulmonary fibrosis. *Front. Immunol.* **7**, 1–17 (2017).

133. Lampropoulou, V. *et al.* Itaconate Links Inhibition of Succinate Dehydrogenase with Macrophage Metabolic Remodeling and Regulation of Inflammation. *Cell Metab.* **24**, 158–166 (2016).

134. Mills, E. L. *et al.* Itaconate is an anti-inflammatory metabolite that activates Nrf2 via alkylation of KEAP1. *Nature* **556**, 113–117 (2018).

135. Littlewood-Evans, A. *et al.* GPR91 senses extracellular succinate released from inflammatory macrophages and exacerbates rheumatoid arthritis. *J. Exp. Med.* jem.20160061 (2016).doi:10.1084/jem.20160061

136. Mills, E. L. *et al.* Succinate Dehydrogenase Supports Metabolic Repurposing of Mitochondria to Drive Inflammatory Macrophages. *Cell* 457–470 (2016).doi:10.1016/j.cell.2016.08.064

137. Arts, R. J. W. *et al.* Glutaminolysis and Fumarate Accumulation Integrate Immunometabolic and Epigenetic Programs in Trained Immunity. *Cell Metab.* **24**, 807–819 (2016).

138. Xiao, M. *et al.* Inhibition of α-KG-dependent histone and DNA demethylases by fumarate and succinate that are accumulated in mutations of FH and SDH tumor suppressors. *Genes Dev.* **26**, 1326–1338 (2012).

139. Bénit, P. *et al.* Unsuspected task for an old team: Succinate, fumarate and other Krebs cycle acids in metabolic remodeling. *Biochim. Biophys. Acta - Bioenerg.* **1837**, 1330–1337 (2014).

140. Sciacovelli, M. *et al.* Fumarate is an epigenetic modifier that elicits epithelial-to-mesenchymal transition. *Nature* **537**, 544–547 (2016).

141. Kaelin, W. G. & McKnight, S. L. Influence of metabolism on epigenetics and disease. *Cell* **153**, 56–69 (2013).

142. Bossche, J. Van Den *et al.* Mitochondrial Dysfunction Prevents Repolarization of Inflammatory Macrophages Article Mitochondrial Dysfunction Prevents Repolarization of Inflammatory Macrophages. *CellReports* **17**, 684–696 (2016).

143. Huang, S. C. C. *et al.* Metabolic Reprogramming Mediated by the mTORC2-IRF4 Signaling Axis Is Essential for Macrophage Alternative Activation. *Immunity* **45**, 817–830 (2016).

144. Tan, Z. *et al.* Pyruvate Dehydrogenase Kinase 1 Participates in Macrophage Polarization via Regulating Glucose Metabolism. *J. Immunol.* **194**, 6082–6089 (2015).

145. Bossche, J. Van den, Baardman, J. & Winther, M. P. J. de Metabolic characterization of polarized M1 and M2 bone marrow-derived macrophages using real-time extracellular flux analysis. *J. Vis. Exp.* **2015**, 1–7 (2015).

146. O'Neill, L. A. J. & Pearce, E. J. Immunometabolism governs dendritic cell and macrophage function. *J. Exp. Med.* jem.20151570 (2015).doi:10.1084/jem.20151570

147. Haschemi, A. *et al.* The sedoheptulose kinase CARKL directs macrophage polarization through control of glucose metabolism. *Cell Metab.* **15**, 813–826 (2012).

148. Namgaladze, D. & Brüne, B. Fatty acid oxidation is dispensable for human macrophage IL-4-induced polarization. *Biochim. Biophys. Acta - Mol. Cell Biol. Lipids* **1841**, 1329–1335 (2014).

149. Nomura, M. *et al.* Fatty acid oxidation in macrophage polarization. *Nat. Immunol.* **17**, 216–217 (2016).

150. Sano, H. *et al.* Pulmonary surfactant protein A modulates the cellular response to smooth and rough lipopolysaccharides by interaction with CD14. *J. Immunol.* **163**, 387–95 (1999).

151. Trapnell, B. C. & Whitsett, J. A. GM-CSF Regulates Pulmonary Surfactant Homeostasis and Alveolar Macrophage-Mediated Innate Host Defense. *Annu. Rev. Physiol.* **64**, 775–802 (2002).

152. Shibata, Y. *et al.* GM-CSF regulates alveolar macrophage differentiation and innate immunity in the lung through PU.1. *Immunity* **15**, 557–567 (2001).

153. Baker, A. D. *et al.* Targeted PPARγ deficiency in alveolar macrophages disrupts surfactant catabolism. *J. Lipid Res.* **51**, 1325–1331 (2010).

154. Suzuki, T. *et al.* Familial pulmonary alveolar proteinosis caused by mutations in CSF2RA. *J. Exp. Med.* **205**, 2703–2710 (2008).

155. Tanaka, T. *et al.* Adult-onset hereditary pulmonary alveolar proteinosis caused by a single-base deletion in CSF2RB. *J. Med. Genet.* **48**, 205–209 (2011).

156. Suzuki, T. *et al.* Hereditary pulmonary alveolar proteinosis caused by recessive CSF2RB mutations. *Eur. Respir. J.* **37**, 201–204 (2011).

157. Martinez-Moczygemba, M. *et al.* Pulmonary alveolar proteinosis caused by deletion of the GM-CSFRα gene in the X chromosome pseudoautosomal region 1. *J. Exp. Med.* **205**, 2711–2716 (2008).

158. Haczku, A. Protective role of the lung collectins surfactant protein A and surfactant protein D in airway inflammation. *J. Allergy Clin. Immunol.* **122**, 861–79; quiz 880–1 (2008).

159. Watford, W. T., Wright, J. R., Hester, C. G., Jiang, H. & Frank, M. M. Surfactant Protein A Regulates Complement Activation. *J. Immunol.* **167**, 6593–6600 (2001).

160. Yamada, C. *et al.* Surfactant protein A directly interacts with TLR4 and MD-2 and regulates inflammatory cellular response: Importance of supratrimeric oligomerization. *J. Biol. Chem.* **281**, 21771–21780 (2006).

161. Surowiec, I. *et al.* Multi-platform metabolomics assays for human lung lavage fluids in an air pollution exposure study. *Anal. Bioanal. Chem.* **408**, 4751–4764 (2016).

162. Gonzalez-Gonzalez, F. J., Chandel, N. S., Jain, M. & Budinger, G. R. S. Reactive oxygen species as signaling molecules in the development of lung fibrosis. *Transl. Res.* **190**, 61–68 (2017).

163. Soares, M. P. & Hamza, I. Macrophages and Iron Metabolism. *Immunity* **44**, 492–504 (2016).

164. Bedard, K. & Krause, K. H. The NOX family of ROS-generating NADPH oxidases: Physiology and pathophysiology. *Physiol. Rev.* **87**, 245–313 (2007).

165. Murthy, S. *et al.* Modulation of reactive oxygen species by Rac1 or catalase prevents asbestos-induced pulmonary fibrosis. *Am. J. Physiol. - Lung Cell. Mol. Physiol.* **297**, 846–855 (2009).

166. Saci, A., Cantley, L. C. & Carpenter, C. L. Rac1 Regulates the Activity of mTORC1 and mTORC2 and Controls Cellular Size. *Mol. Cell* **42**, 50–61 (2011).

167. Sylow, L. *et al.* Rac1 governs exercise-stimulated glucose uptake in skeletal muscle through regulation of GLUT4 translocation in mice. *J. Physiol.* **594**, 4997–5008 (2016).

168. El-Chemaly, S. *et al.* Glucose transporter-1 distribution in fibrotic lung disease: Association with [18F]-2-fluoro-2-deoxyglucose-PET scan uptake, inflammation, and neovascularization. *Chest* **143**, 1685–1691 (2013).

169. Xie, N. *et al.* Metabolic characterization and RNA profiling reveal glycolytic dependence of profibrotic phenotype of alveolar macrophages in lung fibrosis. *Am. J. Physiol. - Lung Cell. Mol. Physiol.* **313**, L834–L844 (2017).

170. Larson-Casey, J. L., Deshane, J. S., Ryan, A. J., Thannickal, V. J. & Carter, A. B. Macrophage Akt1 Kinase-Mediated Mitophagy Modulates Apoptosis Resistance and Pulmonary Fibrosis. *Immunity* **44**, 582–596 (2016).

171. Lewis, C. A. *et al.* Tracing Compartmentalized NADPH Metabolism in the Cytosol and Mitochondria of Mammalian Cells. *Mol. Cell* **55**, 253–263 (2014).

172. Saleh, D., Barnes, P. J. & Giaid, A. Increased production of the potent oxidant peroxynitrite in the lungs of patients with idiopathic pulmonary fibrosis. *Am. J. Respir. Crit. Care Med.* **155**, 1763–1769 (1997).

173. Yamazaki, C. *et al.* Production of superoxide and nitric oxide by alveolar macrophages in the bleomycin-induced interstitial pneumonia mice model. *Jpn. J. Pharmacol.* **78**, 69–73 (1998).

174. Fredholm, B. B., IJzerman, A. P., Jacobson, K. A., Linden, J. & Müller, C. E. International union of basic and clinical pharmacology. LXXXI. Nomenclature and classification of

adenosine receptors - An update. *Pharmacol. Rev.* **63**, 1–34 (2011).

175. Zhou, Y., Murthy, J. N., Zeng, D., Belardinelli, L. & Blackburn, M. R. Alterations in adenosine metabolism and signaling in patients with chronic obstructive pulmonary disease and idiopathic pulmonary fibrosis. *PLoS One* **5**, (2010).

176. Zhou, Y. *et al.* Distinct Roles for the A 2B Adenosine Receptor in Acute and Chronic Stages of Bleomycin-Induced Lung Injury . *J. Immunol.* **186**, 1097–1106 (2011).

177. Philip, K. *et al.* HIF1A up-regulates the ADORA2B receptor on alternatively activated macrophages and contributes to pulmonary fibrosis. *FASEB J.* **31**, 4745–4758 (2017).

178. Zhan, L. *et al.* Regulatory role of KEAP1 and NRF2 in PPARγ expression and chemoresistance in human non-small-cell lung carcinoma cells. *Free Radic. Biol. Med.* **53**, 758–768 (2012).

179. Reddy, A. T., Lakshmi, S. P., Zhang, Y. & Reddy, R. C. Nitrated fatty acids reverse pulmonary fibrosis by dedifferentiating myofibroblasts and promoting collagen uptake by alveolar macrophages. *FASEB J.* **28**, 5299–5310 (2014).

180. Burgess, H. A. *et al.* PPARγ agonists inhibit TGF-β induced pulmonary myofibroblast differentiation and collagen production: Implications for therapy of lung fibrosis. *Am. J. Physiol. - Lung Cell. Mol. Physiol.* **288**, 1146–1153 (2005).

181. Milam, J. E. *et al.* PPAR-γ agonists inhibit profibrotic phenotypes in human lung fibroblasts and bleomycin-induced pulmonary fibrosis. *Am. J. Physiol. - Lung Cell. Mol. Physiol.* **294**, 891–901 (2008).

182. Ye, Q. *et al.* Decreased expression of haem oxygenase-1 by alveolar macrophages in idiopathic pulmonary fibrosis. *Eur. Respir. J.* **31**, 1030–1036 (2008).

183. Araujo, J. A., Zhang, M. & Yin, F. Heme oxygenase-1, oxidation, inflammation, and atherosclerosis. *Front. Pharmacol.* **3 JUL**, 1–17 (2012).

184. Puxeddu, E. *et al.* Iron laden macrophages in idiopathic pulmonary fibrosis: The telltale of occult alveolar hemorrhage? *Pulm. Pharmacol. Ther.* **28**, 35–40 (2014).

185. Yamashita, M. *et al.* Distinct Profiles of CD163-Positive Macrophages in Idiopathic Interstitial Pneumonias. *J. Immunol. Res.* **2018**, (2018).

186. Ugocsai, P., Barlage, S., Dada, A. & Schmitz, G. Regulation of surface CD163 expression and cellular effects of receptor mediated hemoglobin-haptoglobin uptake on human monocytes and macrophages. *Cytom. Part A* **69**, 203–205 (2006).

187. Allden, S. J. *et al.* The transferrin receptor CD71 delineates functionally distinct airway macrophage subsets during idiopathic pulmonary fibrosis. *Am. J. Respir. Crit. Care Med.* **200**, 209–219 (2019).

188. Assoian, R. K. *et al.* Expression and secretion of type β transforming growth factor by activated human macrophages. *Proc. Natl. Acad. Sci. U. S. A.* **84**, 6020–6024 (1987).

189. Postlethwaite, A. E., Keski-Oja, J., Moses, H. L. & Kang, A. H. Stimulation of the chemotactic migration of human fibroblasts by transforming growth factor β. *J. Exp. Med.* **165**, 251–256 (1987).

190. Desmouliere, A., Geinoz, A., Gabbiani, F. & Gabbiani, G. Transforming growth factor-β1 induces α-smooth muscle actin expression in granulation tissue myofibroblasts and in quiescent and growing cultured fibroblasts. *J. Cell Biol.* **122**, 103–111 (1993).

191. Ueno, M. *et al.* Hypoxia-inducible factor-1 mediates TGF- -induced PAI-1 production in alveolar macrophages in pulmonary fibrosis. *AJP Lung Cell. Mol. Physiol.* **300**, L740–L752 (2011).

192. Invernizzi, R. *et al.* The Respiratory Microbiome in Chronic Hypersensitivity Pneumonitis is Distinct from that of Idiopathic Pulmonary Fibrosis. *Am. J. Respir. Crit. Care Med.* rccm.202002-0460OC (2020).doi:10.1164/rccm.202002-0460OC

193. Byrne, A. J., Mathie, S. A., Gregory, L. G. & Lloyd, C. M. Pulmonary macrophages : key players in the innate defence of the airways. 1189–1196 (2015).doi:10.1136/thoraxjnl-2015-

207020

194. Calhoun, W. J., Bush, R. K., Salisbury, S. M. & Stevens, C. A. Enhanced reactive oxygen species metabolism of airspace cells and airway inflammation follow antigen challenge in human asthma. *J. Allergy Clin. Immunol.* **86**, 306–313 (1990).

195. Lee, I. & Yang, C. Role of NADPH oxidase / ROS in pro-inflammatory mediators-induced airway and pulmonary diseases. *Biochem. Pharmacol.* **84**, 581–590 (2012).

196. Park, H. S., Kim, S. R. & Lee, Y. C. Impact of oxidative stress on lung diseases. *Respirology* **14**, 27–38 (2009).

197. Harju, T., Soini, Y., Pääkkö, P. & Kinnula, V. L. Up-regulation of heme oxygenase-1 in alveolar macrophages of newly diagnosed asthmatics. *Respir. Med.* **96**, 418–423 (2002).

198. Damon, M. *et al.* Increased generation of the arachidonic metabolites LTB4 and 5-HETE by human alveolar macrophages in patients with asthma: Effect in vitro of nedocromil sodium. *Eur. Respir. J.* **2**, 202–209 (1989).

199. Huynh, M. L. N. *et al.* Defective apoptotic cell phagocytosis attenuates prostaglandin E 2 and 15-hydroxyeicosatetraenoic acid in severe asthma alveolar macrophages. *Am. J. Respir. Crit. Care Med.* **172**, 972–979 (2005).

200. Vercelli, D. Arginase: Marker, effector, or candidate gene for asthma? *J. Clin. Invest.* **111**, 1815–1817 (2003).

201. Chang, C.-I., Zoghi, B., Liao, J. C. & Kuo, L. The Involvement of Tyrosine Kinases, Cyclic AMP/Protein Kinase A, and p38 Mitogen-Activated Protein Kinase in IL-13-Mediated Arginase I Induction in Macrophages: Its Implications in IL-13-Inhibited Nitric Oxide Production. *J. Immunol.* **165**, 2134–2141 (2000).

202. O'Beirne, S. L. *et al.* Alveolar macrophage immunometabolism and lung function impairment in smoking and chronic obstructive pulmonary disease. *Am. J. Respir. Crit. Care Med.* **201**, 735–738 (2020).

203. Rahman, I. & MacNee, W. Role of oxidants/antioxidants in smoking-induced lung diseases. *Free Radic. Biol. Med.* **21**, 669–681 (1996).

204. Xia, T., Kovochich, M. & Nel, A. E. Impairment of mitochondrial function by particulate matter (PM) and their toxic components: Implications for PM-induced cardiovascular and lung disease. *Front. Biosci.* **12**, 1238–1246 (2007).

205. Bewley, M. A. *et al.* Impaired mitochondrial microbicidal responses in chronic obstructive pulmonary disease macrophages. *Am. J. Respir. Crit. Care Med.* **196**, 845–855 (2017).

206. Harju, T., Kaarteenaho-Wiik, R., Soini, Y., Sormunen, R. & Kinnula, V. L. Diminished immunoreactivity of γ-glutamylcysteine synthetase in the airways of smokers' lung. *Am. J. Respir. Crit. Care Med.* **166**, 754–759 (2002).

207. Cloonan, S. M. *et al.* The iron-y of iron overload and iron deficiency in chronic obstructive pulmonary disease. *Am. J. Respir. Crit. Care Med.* **196**, 1103–1112 (2017).

208. Philippot, Q. *et al.* Increased iron sequestration in alveolar macrophages in chronic obtructive pulmonary disease. *PLoS One* **9**, 1–9 (2014).

209. Belchamber, K. B. R. *et al.* Defective bacterial phagocytosis is associated with dysfunctional mitochondria in COPD macrophages. *Eur. Respir. J.* **54**, 1802244 (2019).

210. Eapen, M. S., Sharma, P. & Sohal, S. S. Mitochondrial dysfunction in macrophages: a key to defective bacterial phagocytosis in COPD. *Eur. Respir. J.* **54**, 1901641 (2019).

211. Hübner, R. H. *et al.* Standardized quantification of pulmonary fibrosis in histological samples. *Biotechniques* **44**, 507–517 (2008).

212. Misharin, A. V. *et al.* Monocyte-derived alveolar macrophages drive lung fibrosis and persist in the lung over the life span. *J. Exp. Med.* **214**, 2387–2404 (2017).

213. King, T. E., Pardo, A. & Selman, M. Idiopathic pulmonary fibrosis. *Lancet* **378**, 1949–1961 (2011).

214. Raghu, G., Anstrom, K. J., King, T. E., Lasky, J. A. & Martinez, F. J. Prednisone, Azathioprine, and N -Acetylcysteine for Pulmonary Fibrosis. *N. Engl. J. Med.* **366**, 1968–1977 (2012).

215. Martinez, F. J. *et al.* Idiopathic pulmonary fibrosis. (2017).doi:10.1038/nrdp.2017.74

216. Richeldi, L., Collard, H. R. & Jones, M. G. Idiopathic pulmonary fibrosis. *Lancet* **389**, 1941–1952 (2017).

217. Lacasse, Y., Girard, M. & Cormier, Y. Recent advances in hypersensitivity pneumonitis. *Chest* **142**, 208–217 (2012).

218. Fink, J. N. *et al.* Needs and opportunities for research in hypersensitivity pneumonitis. *Am. J. Respir. Crit. Care Med.* **171**, 792–798 (2005).

219. Patel, A. M., Ryu, J. H. & Reed, C. E. Hypersensitivity pneumonitis: Current concepts and future questions. *J. Allergy Clin. Immunol.* **108**, 661–670 (2001).

220. Morell, F. *et al.* Chronic hypersensitivity pneumonitis in patients diagnosed with idiopathic pulmonary fibrosis: A prospective case-cohort study. *Lancet Respir. Med.* **1**, 685–694 (2013).

221. Morisset, J. *et al.* Use of Mycophenolate Mofetil or Azathioprine for the Management of Chronic Hypersensitivity Pneumonitis. *Chest* **151**, 619–625 (2017).

222. Pereira, C. A. C., Gimenez, A., Kuranishi, L. & Storrer, K. Chronic hypersensitivity pneumonitis. *J. Asthma Allergy* **9**, 171–181 (2016).

223. Barnes, H. *et al.* A Systematically Derived Exposure Assessment Instrument for Chronic Hypersensitivity Pneumonitis. *Chest* **157**, 1506–1512 (2020).

224. Lee, J. *et al.* Bronchoalveolar lavage (BAL) cells in idiopathic pulmonary fibrosis express a complex pro-inflammatory, pro-repair, angiogenic activation pattern, likely associated with macrophage iron accumulation. *PLoS One* **13**, 1–15 (2018).

225. Morimoto, K., Janssen, W. J. & Terada, M. Defective efferocytosis by alveolar macrophages in IPF patients. *Respir. Med.* **106**, 1800–1803 (2012).

226. Allden, S. J. *et al.* The Transferrin Receptor CD71 Delineates Functionally Distinct Airway Macrophage Subsets during Idiopathic Pulmonary Fibrosis. *Am. J. Respir. Crit. Care Med.* (2019).doi:10.1164/rccm.201809-1775OC

227. Bondue, B. *et al.* PET/CT with 18F-FDG- and 18F-FBEM-Labeled Leukocytes for Metabolic Activity and Leukocyte Recruitment Monitoring in a Mouse Model of Pulmonary Fibrosis. *J. Nucl. Med.* **56**, 127–132 (2014).

228. Malsin, E. S. & Kamp, D. W. The mitochondria in lung fibrosis: friend or foe? *Transl. Res.* **202**, 1–23 (2018).

229. Zank, D. C., Bueno, M., Mora, A. L. & Rojas, M. Idiopathic pulmonary fibrosis: Aging, mitochondrial dysfunction, and cellular bioenergetics. *Front. Med.* **5**, 1–9 (2018).

230. Xie, N. *et al.* Glycolytic reprogramming in myofibroblast differentiation and lung fibrosis. *Am. J. Respir. Crit. Care Med.* **192**, 1462–1474 (2015).

231. Xie, N. *et al.* Metabolic characterization and RNA profiling reveal glycolytic dependence of pro-fibrotic phenotype of alveolar macrophages in lung fibrosis. *Am. J. Physiol. - Lung Cell. Mol. Physiol.* ajplung.00235.2017 (2017).doi:10.1152/ajplung.00235.2017

232. Martinez, F. O. Macrophage activation and polarization. *Front. Biosci.* **13**, 453 (2008).

233. Stöger, J. L. *et al.* Distribution of macrophage polarization markers in human atherosclerosis. *Atherosclerosis* **225**, 461–468 (2012).

234. Ohashi, T. *et al.* M2-like macrophage polarization in high lactic acid-producing head and neck cancer. *Cancer Sci.* **108**, 1128–1134 (2017).

235. Bharat, A. *et al.* Flow Cytometry Reveals Similarities Between Lung Macrophages in Humans and Mice. *Am. J. Respir. Cell Mol. Biol.* **54**, 147–149 (2016).

236. Aran, D. *et al.* Reference-based analysis of lung single-cell sequencing reveals a transitional profibrotic macrophage. *Nat. Immunol.* **20**, 163–172 (2019).

237. Tsitoura, E. *et al.* Accumulation of damaged mitochondria in alveolar macrophages with reduced OXPHOS related gene expression in IPF. *Respir. Res.* **20**, 1–16 (2019).

238. Homolka, J. *et al.* Systemic immune cell activation in a subgroup of patients with idiopathic pulmonary fibrosis. *Respiration* **70**, 262–269 (2003).

239. Reyfman, P. A. *et al.* Single-cell transcriptomic analysis of human lung provides insights into the pathobiology of pulmonary fibrosis. *Am. J. Respir. Crit. Care Med.* **199**, 1517–1536 (2019).

240. O'Dwyer, D. N. *et al.* Lung microbiota contribute to pulmonary inflammation and disease progression in pulmonary fibrosis. *Am. J. Respir. Crit. Care Med.* **199**, 1127–1138 (2019).

241. Mills, E. & O'Neill, L. A. J. Succinate: A metabolic signal in inflammation. *Trends Cell Biol.* **24**, 313–320 (2014).

242. Schaberg, T., Rau, M., Stephan, H. & Lode, H. Increased number of alveolar macrophages expressing surface molecules of the CD11/CD18 family in sarcoidosis and idiopathic pulmonary fibrosis is related to the production of superoxide anions by these cells. *Am. Rev. Respir. Dis.* **147**, 1507–1513 (1993).

243. Williams, N. C. & O'Neill, L. A. ACLY-matizing Macrophages to Histone Modification during Immunometabolic Reprogramming. *Trends Immunol.* **41**, 93–94 (2020).

244. Luo, S. *et al.* Downregulation of PCK2 remodels tricarboxylic acid cycle in tumor-repopulating cells of melanoma. *Oncogene* **36**, 3609–3617 (2017).

245. Migita, T. *et al.* ATP citrate lyase: Activation and therapeutic implications in non-small cell lung cancer. *Cancer Res.* **68**, 8547–8554 (2008).

246. Granchi, C. ATP citrate lyase (ACLY) inhibitors: An anti-cancer strategy at the crossroads of glucose and lipid metabolism. *Eur. J. Med. Chem.* **157**, 1276–1291 (2018).

247. Xin, M. *et al.* MiR-22 inhibits tumor growth and metastasis by targeting ATP citrate lyase: Evidence in osteosarcoma, prostate cancer, cervical cancer and lung cancer. *Oncotarget* **7**, 44252–44265 (2016).

248. Zhong, W. J. *et al.* Inhibition of glycolysis alleviates lipopolysaccharide-induced acute lung injury in a mouse model. *J. Cell. Physiol.* **234**, 4641–4654 (2019).

249. Liu, R. T. *et al.* Enhanced glycolysis contributes to the pathogenesis of experimental autoimmune neuritis. *J. Neuroinflammation* **15**, 1–13 (2018).

250. Passalacqua, K. D. *et al.* Glycolysis is an intrinsic factor for optimal replication of a norovirus. *MBio* **10**, 1–18 (2019).

251. Zhong, Y. *et al.* Application of mitochondrial pyruvate carrier blocker UK5099 creates metabolic reprogram and greater stem-like properties in LnCap prostate cancer cells in vitro. *Oncotarget* **6**, 37758–37769 (2015).

252. Laliberte, R., Perregaux, D., Svensson, L., Pazoles, C. J. & Gabel, C. A. Tenidap modulates cytoplasmic pH and inhibits anion transport in vitro: II. Inhibition of IL-1β production from ATP-treated monocytes and macrophages. *J. Immunol.* **153**, 2168–2179 (1994).

253. Feng, J. *et al.* Mitochondrial pyruvate carrier 2 mediates mitochondrial dysfunction and apoptosis in high glucose-treated podocytes. *Life Sci.* **237**, 116941 (2019).

254. Moon, J. S. *et al.* NOX4-dependent fatty acid oxidation promotes NLRP3 inflammasome activation in macrophages. *Nat. Med.* **22**, 1002–1012 (2016).

255. Bossche, J. Van den & Windt, G. J. W. van der Fatty Acid Oxidation in Macrophages and T Cells: Time for Reassessment? *Cell Metab.* **28**, 538–540 (2018).

256. Yawata, I. *et al.* Macrophage-induced neurotoxicity is mediated by glutamate and attenuated by glutaminase inhibitors and gap junction inhibitors. *Life Sci.* **82**, 1111–1116 (2008).

257. Vigeland, C. L. *et al.* Inhibition of glutamine metabolism accelerates resolution of acute lung injury. *Physiol. Rep.* **7**, (2019).

258. Willems, S. *et al.* Multiplex protein profiling of bronchoalveolar lavage in idiopathic pulmonary fibrosis and hypersensitivity pneumonitis. *Ann. Thorac. Med.* **8**, 38–45 (2013).

259. Dancer, R. C. A., Wood, A. M. & Thickett, D. R. Metalloproteinases in idiopathic pulmonary fibrosis. *Eur. Respir. J.* **38**, 1461–1467 (2011).

260. Doren, S. R. Van Matrix metalloproteinase interactions with collagen and elastin. *Matrix Biol.* **44**–**46**, 224–231 (2015).

261. Scheule, R. K., Perkins, R. C., Hamilton, R. & Holian, A. Bleomycin stimulation of cytokine secretion by the human alveolar macrophage. *Am. J. Physiol. - Lung Cell. Mol. Physiol.* **262**, (1992).

262. Divakaruni, A. S. *et al.* Etomoxir Inhibits Macrophage Polarization by Disrupting CoA Homeostasis. *Cell Metab.* **28**, 490-503.e7 (2018).

263. Barbarin, V. *et al.* Characterization of the effect of interleukin-10 on silica-induced lung fibrosis in mice. *Am. J. Respir. Cell Mol. Biol.* **31**, 78–85 (2004).

264. Moore, B. B. & Hogaboam, C. M. Murine models of pulmonary fibrosis. *Am. J. Physiol. - Lung Cell. Mol. Physiol.* **294**, 152–160 (2008).

265. Tashiro, J. *et al.* Exploring Animal Models That Resemble Idiopathic Pulmonary Fibrosis. *Front. Med.* **4**, 1–11 (2017).

266. Jenkins, R. G. *et al.* An official American thoracic society workshop report: Use of animal models for the preclinical assessment of potential therapies for pulmonary fibrosis. *Am. J. Respir. Cell Mol. Biol.* **56**, 667–679 (2017).

267. Moeller, A., Ask, K., Warburton, D., Gauldie, J. & Kolb, M. The bleomycin animal model: A useful tool to investigate treatment options for idiopathic pulmonary fibrosis? *Int. J. Biochem. Cell Biol.* **40**, 362–382 (2008).

268. Moore, B. B. & Hogaboam, C. M. Murine models of pulmonary fibrosis. *Am. J. Physiol. - Lung Cell. Mol. Physiol.* **294**, 152–160 (2008).

269. Hay, J., Shahzeidi, S. & Laurent, G. Mechanisms of bleomycin-induced lung damage. *Arch. Toxicol.* **65**, 81–94 (1991).

270. Degryse, A. L. *et al.* Repetitive intratracheal bleomycin models several features of idiopathic pulmonary fibrosis. *Am. J. Physiol. - Lung Cell. Mol. Physiol.* **299**, 442–452 (2010).

271. Cai, Y. *et al.* Noninvasive monitoring of pulmonary fibrosis by targeting matrix metalloproteinases (MMPs). *Mol. Pharm.* **10**, 2237–2247 (2013).

272. Sueblinvong, V. *et al.* Predisposition for disrepair in the aged lung. *Am. J. Med. Sci.* **344**, 41–51 (2012).

273. Mouratis, M. a & Aidinis, V. Modeling pulmonary fibrosis with bleomycin. *Curr. Opin. Pulm. Med.* **17**, 355–361 (2011).

274. Ortiz, L. A. *et al.* Mesenchymal stem cell engraftment in lung is enhanced in response to bleomycin exposure and ameliorates its fibrotic effects. *Proc. Natl. Acad. Sci. U. S. A.* **100**, 8407–8411 (2003).

275. Rojas, M. *et al.* Bone marrow-derived mesenchymal stem cells in repair of the injured lung. *Am. J. Respir. Cell Mol. Biol.* **33**, 145–152 (2005).

276. Gurujeyalakshmi, G. & Giri, S. N. Molecular mechanisms of antifibrotic effect of interferon gamma in bleomycin-mouse model of lung fibrosis: Downregulation of TGF-β and procollagen I and III gene expression. *Exp. Lung Res.* **21**, 791–808 (1995).

277. Liu, L. *et al.* Wnt pathway in pulmonary fibrosis in the bleomycin mouse model. *J. Environ. Pathol. Toxicol. Oncol.* **28**, 99–108 (2009).

278. Koyama, K. *et al.* The tyrosine kinase inhibitor tas-115 attenuates bleomycin-induced lung fibrosis in mice. *Am. J. Respir. Cell Mol. Biol.* **60**, 478–487 (2019).

279. Burman, A. *et al.* Localized hypoxia links ER stress to lung fibrosis through induction of C/EBP

homologous protein. *JCI insight* **3**, 1–19 (2018).

280. Habgood, A. N. *et al.* Secretory leukocyte protease inhibitor gene deletion alters bleomycin-induced lung injury, but not development of pulmonary fibrosis. *Lab. Investig.* **96**, 623–631 (2016).

281. Tatler, A. L. *et al.* Reduced ets domain-containing protein Elk1 promotes pulmonary fibrosis via increased integrin αvβ6 expression. *J. Biol. Chem.* **291**, 9540–9553 (2016).

282. Moore, B. B. *et al.* Protection from Pulmonary Fibrosis in the Absence of CCR2 Signaling. *J. Immunol.* **167**, 4368–4377 (2001).

283. Lavin, Y., Mortha, A., Rahman, A. & Merad, M. Regulation of macrophage development and function in peripheral tissues. *Nat. Rev. Immunol.* **15**, 731–744 (2015).

284. Gautiar, E. L. *et al.* Gene-expression profiles and transcriptional regulatory pathways that underlie the identity and diversity of mouse tissue macrophages. *Nat. Immunol.* **13**, 1118–1128 (2012).

285. Gibbons, M. A. *et al.* Ly6C hi Monocytes Direct Alternatively Activated Profibrotic Macrophage Regulation of Lung Fibrosis. doi:10.1164/rccm.201010-1719OC

286. Hashimoto, D. *et al.* Tissue-resident macrophages self-maintain locally throughout adult life with minimal contribution from circulating monocytes. *Immunity* (2013).doi:10.1016/j.immuni.2013.04.004

287. Landsman, L. & Jung, S. Lung Macrophages Serve as Obligatory Intermediate between Blood Monocytes and Alveolar Macrophages. *J. Immunol.* **179**, 3488–3494 (2007).

288. Misharin, A. V. *et al.* Monocyte-derived alveolar macrophages drive lung fibrosis and persist in the lung over the life span. *J. Exp. Med.* **214**, 2387–2404 (2017).

289. Xie, N. *et al.* Metabolic characterization and RNA profiling reveal glycolytic dependence of profibrotic phenotype of alveolar macrophages in lung fibrosis. *Am. J. Physiol. - Lung Cell. Mol. Physiol.* **313**, L834–L844 (2017).

290. Luo, F. *et al.* Extracellular adenosine levels are associated with the progression and exacerbation of pulmonary fibrosis. *FASEB J.* **30**, 874–883 (2016).

291. He, W. *et al.* Citric acid cycle intermediates as ligands for orphan G-protein-coupled receptors. *Nature* **429**, 188–193 (2004).

292. Robben, J. H. *et al.* Localization of the succinate receptor in the distal nephron and its signaling in polarized MDCK cells. *Kidney Int.* **76**, 1258–1267 (2009).

293. Rubic, T. *et al.* Triggering the succinate receptor GPR91 on dendritic cells enhances immunity. *Nat. Immunol.* **9**, 1261–1269 (2008).

294. Dervartanian, D. V. & Veeger, C. Studies on succinate dehydrogenase. I. Spectral properties of the purified enzyme and formation of enzyme-competitive inhibitor complexes. *BBA - Enzymol. Subj.* **92**, 233–247 (1964).

295. Makled, S., Boraie, N. & Nafee, N. Nanoparticle-mediated macrophage targeting—a new inhalation therapy tackling tuberculosis. *Drug Deliv. Transl. Res.* (2020).doi:10.1007/s13346-020-00815-3

296. Dua, K. *et al.* The potential of siRNA based drug delivery in respiratory disorders: Recent advances and progress. *Drug Dev. Res.* **80**, 714–730 (2019).

297. Chen, J. *et al.* Glycan targeted polymeric antibiotic prodrugs for alveolar macrophage infections. *Biomaterials* **195**, 38–50 (2019).

298. Ohashi, K., Kabasawa, T., Ozeki, T. & Okada, H. One-step preparation of rifampicin/poly(lactic-co-glycolic acid) nanoparticle-containing mannitol microspheres using a four-fluid nozzle spray drier for inhalation therapy of tuberculosis. *J. Control. Release* **135**, 19–24 (2009).

299. Suarez, S. *et al.* Respirable PLGA microspheres containing rifampicin for the treatment of tuberculosis: Screening in an infectious disease model. *Pharm. Res.* **18**, 1315–1319 (2001).

300. Manali, E. D. *et al.* Static and dynamic mechanics of the murine lung after intratracheal bleomycin. *BMC Pulm. Med.* **11**, (2011).

301. Izbicki, G., Segel, M. J., Christensen, T. G., Conner, M. W. & Breuer, R. Time course of bleomycin-induced lung fibrosis. *Int. J. Exp. Pathol.* **83**, 111–119 (2002).

302. Chaudhary, N. I., Schnapp, A. & Park, J. E. Pharmacologic differentiation of inflammation and fibrosis in the rat bleomycin model. *Am. J. Respir. Crit. Care Med.* **173**, 769–776 (2006).

303. Jenkins, R. G. *et al.* An Of fi cial American Thoracic Society Workshop Report : Use of Animal Models for the Preclinical Assessment of Potential Therapies for Pulmonary Fibrosis. **56**, 667–679 (2017).

304. Mutsaers, S. E., Foster, M. L., Chambers, R. C., Laurent, G. J. & McAnulty, R. J. Increased endothelin-1 and its localization during the development of bleomycin-induced pulmonary fibrosis in rats. *Am. J. Respir. Cell Mol. Biol.* **18**, 611–619 (1998).

305. Okuma, T. *et al.* C-C chemokine receptor 2 (CCR2) deficiency improves bleomycin-induced pulmonary fibrosis by attenuation of both macrophage infiltration and production of macrophage-derived matrix metalloproteinases. *J. Pathol.* **204**, 594–604 (2004).

306. Gasse, P. *et al.* IL-1R1/MyD88 signaling and the inflammasome are essential in pulmonary inflammation and fibrosis in mice. *J. Clin. Invest.* **117**, 3786–3799 (2007).

307. Williamson, J. D., Sadofsky, L. R. & Hart, S. P. The pathogenesis of bleomycin-induced lung injury in animals and its applicability to human idiopathic pulmonary fibrosis. *Exp. Lung Res.* **41**, 57–73 (2015).

308. Gharaee-Kermani, M. *et al.* The role of IL-5 in bleomycin-induced pulmonary fibrosis. *J. Leukoc. Biol.* **64**, 657–666 (1998).

309. Hao, H., Cohen, D. A., Jennings, C. D., Bryson, J. S. & Kaplan, A. M. Bleomycin-induced pulmonary fibrosis is independent of eosinophils. *J. Leukoc. Biol.* **68**, 515–521 (2000).

310. Chua, F., Gauldie, J. & Laurent, G. J. Pulmonary fibrosis: Searching for model answers. *Am. J. Respir. Cell Mol. Biol.* **33**, 9–13 (2005).

311. Rajakariar, R. *et al.* Hematopoietic prostaglandin D 2 synthase controls through PGD 2 and 15-deoxy 12 – 14 PGJ 2. *Pnas* **104**, 20979–20984 (2007).

312. Bystrom, J. *et al.* Resolution-phase macrophages possess a unique inflammatory phenotype that is controlled by cAMP. *Blood* **112**, 4117–4127 (2008).

313. Bellingan, G. J. *et al.* Adhesion molecule-dependent mechanisms regulate the rate of macrophage clearance during the resolution of peritoneal inflammation. *J. Exp. Med.* **196**, 1515–1521 (2002).

314. Maus, U. *et al.* The role of CC chemokine receptor 2 in alveolar monocyte and neutrophil immigration in intact mice. *Am. J. Respir. Crit. Care Med.* **166**, 268–273 (2002).

315. Maus, U., Huwe, J., Maus, R., Seeger, W. & Lohmeyer, J. Alveolar JE/MCP-1 and endotoxin synergize to provoke lung cytokine upregulation, sequential. Neutrophil and monocyte influx, and vascular leakage in mice. *Am. J. Respir. Crit. Care Med.* **164**, 406–411 (2001).

316. Traeger, T. *et al.* Selective depletion of alveolar macrophages in polymicrobial sepsis increases lung injury, bacterial load and mortality but does not affect cytokine release. *Respiration* **77**, 203–213 (2009).

317. Said, N., Smith, S., Sanchez-Carbayo, M. & Theodorescu, D. Tumor endothelin-1 enhances metastatic colonization of the lung in mouse xenograft models of bladder cancer. *J. Clin. Invest.* **121**, 132–147 (2011).

318. Dorr, A. D. *et al.* Sources of alveolar soluble TNF receptors during acute lung injury of different etiologies. *J. Appl. Physiol.* **111**, 177–184 (2011).

319. Yang, M., Kumar, R. K. & Foster, P. S. Interferon-γ and pulmonary macrophages contribute to the mechanisms underlying prolonged airway hyperresponsiveness. *Clin. Exp. Allergy* **40**, 163–173 (2010).

320. Li, J. J. *et al.* IL-27/IFN-γ Induce MyD88-Dependent Steroid-Resistant Airway Hyperresponsiveness by Inhibiting Glucocorticoid Signaling in Macrophages. *J. Immunol.* **185**, 4401–4409 (2010).

321. Bem, R. A. *et al.* Depletion of resident alveolar macrophages does not prevent Fas-mediated lung injury in mice. *Am. J. Physiol. - Lung Cell. Mol. Physiol.* **295**, 314–325 (2008).

322. Antoniu, S. A. & Kolb, M. R. J. Update on models of pulmonary fibrosis therapy for preclinical drug research. *Expert Opin. Drug Discov.* **4**, 939–946 (2009).

323. Maher, T. M. & Wells, A. U. Lost in translation; from animal models of pulmonary fibrosis to human disease. *Respirology* **14**, 915–6 (2009).

324. Chakrabarti, S. & Patel, K. D. Matrix metalloproteinase-2 (MMP-2) and MMP-9 in pulmonary pathology. *Exp. Lung Res.* **31**, 599–621 (2005).

325. Hutchinson, J., Fogarty, A., Hubbard, R. & McKeever, T. Global incidence and mortality of idiopathic pulmonary fibrosis: A systematic review. *Eur. Respir. J.* **46**, 795–806 (2015).

326. Kreuter, M., Bonella, F., Wijsenbeek, M., Maher, T. M. & Spagnolo, P. Pharmacological Treatment of Idiopathic Pulmonary Fibrosis: Current Approaches, Unsolved Issues, and Future Perspectives. *Biomed Res. Int.* **2015**, (2015).

327. Murray, P. J. *et al.* Macrophage Activation and Polarization: Nomenclature and Experimental Guidelines. *Immunity* **41**, 14–20 (2014).

328. Wynn, T. A. & Vannella, K. M. Macrophages in Tissue Repair, Regeneration, and Fibrosis. *Immunity* **44**, 450–462 (2016).

329. Kelly, B. & O'Neill, L. A. Metabolic reprogramming in macrophages and dendritic cells in innate immunity. *Cell Res.* **25**, 771–84 (2015).

330. Domínguez-Andrés, J. *et al.* The Itaconate Pathway Is a Central Regulatory Node Linking Innate Immune Tolerance and Trained Immunity. *Cell Metab.* **29**, 211-220.e5 (2019).

331. Michelucci, A. *et al.* Immune-responsive gene 1 protein links metabolism to immunity by catalyzing itaconic acid production. *Proc. Natl. Acad. Sci. U. S. A.* **110**, 7820–5 (2013).

332. McFadden, B. A. & Purohit, S. Itaconate, an isocitrate lyase directed inhibitor in Pseudomonas indigofera. *J. Bacteriol.* **131**, 136–144 (1977).

333. Cordes, T., Michelucci, A. & Hiller, K. Itaconic Acid: The Surprising Role of an Industrial Compound as a Mammalian Antimicrobial Metabolite. *Annu. Rev. Nutr.* **35**, 451–473 (2015).

334. Lorenz, M. C. & Fink, G. R. The glyoxylate cycle is required for fungal virulence. *Nature* **412**, 83–86 (2001).

335. Luan, H. H. & Medzhitov, R. Food Fight: Role of Itaconate and Other Metabolites in Antimicrobial Defense. *Cell Metab.* **24**, 379–387 (2016).

336. Cordes, T. *et al.* Immunoresponsive gene 1 and itaconate inhibit succinate dehydrogenase to modulate intracellular succinate levels. *J. Biol. Chem.* **291**, 14274–14284 (2016).

337. Strelko, C. L. *et al.* Itaconic acid is a mammalian metabolite induced during macrophage activation. *J. Am. Chem. Soc.* **133**, 16386–16389 (2011).

338. Mills, E. L. *et al.* Itaconate is an anti-inflammatory metabolite that activates Nrf2 via alkylation of KEAP1. *Nature* **556**, 113–117 (2018).

339. Otto, G. Itaconate helps KEAP1's cool. *Nat. Rev. Immunol.* **18**, 294 (2018).

340. Karsdal, M. A. *et al.* The good and the bad collagens of fibrosis – Their role in signaling and organ function. *Adv. Drug Deliv. Rev.* **121**, 43–56 (2017).

341. Daniels, B. P. *et al.* The Nucleotide Sensor ZBP1 and Kinase RIPK3 Induce the Enzyme IRG1 to Promote an Antiviral Metabolic State in Neurons. *Immunity* **50**, 64-76.e4 (2019).

342. Sasikaran, J., Ziemski, M., Zadora, P. K., Fleig, A. & Berg, I. A. Bacterial itaconate degradation promotes pathogenicity. *Nat. Chem. Biol.* **10**, 371–377 (2014).

343. Naujoks, J. *et al.* IFNs Modify the Proteome of Legionella-Containing Vacuoles and Restrict Infection Via IRG1-Derived Itaconic Acid. *PLoS Pathog.* **12**, (2016).

344. Michelucci, A. *et al.* Immune-responsive gene 1 protein links metabolism to immunity by catalyzing itaconic acid production. *Proc. Natl. Acad. Sci.* **110**, 7820–7825 (2013).

345. Lampropoulou, V. *et al.* Itaconate Links Inhibition of Succinate Dehydrogenase with Macrophage Metabolic Remodeling and Regulation of Inflammation. *Cell Metab.* **24**, 158–66 (2016).

346. Bambouskova, M. *et al.* regulate the I κ B ζ – ATF3 inflammatory axis. *Nature* (2018).doi:10.1038/s41586-018-0052-z

347. Johansen, C. *et al.* IκBζ is a key driver in the development of psoriasis. *Proc. Natl. Acad. Sci. U. S. A.* **112**, E5825–E5833 (2015).

348. Kobayashi, E. H. *et al.* Nrf2 suppresses macrophage inflammatory response by blocking proinflammatory cytokine transcription. *Nat. Commun.* **7**, 1–14 (2016).

349. Qin, W. *et al.* S-glycosylation-based cysteine profiling reveals regulation of glycolysis by itaconate. *Nat. Chem. Biol.* **15**, 983–991 (2019).

350. Nair, S. *et al.* Irg1 expression in myeloid cells prevents immunopathology during M. tuberculosis infection . *J. Exp. Med.* **215**, 1035–1045 (2018).

351. Chaitanya Ganta, V. *et al.* A MicroRNA93-IRF9-IRG1-Itaconic Acid Pathway Modulates M2-like- Macrophage Polarization to Revascularize Ischemic Muscle Running Title: Ganta et al.; miR93 Regulates Macrophage M2-like Polarization. *J. Subj. Terms Angiogenes. Vasc. Biol.* (2017).doi:10.1161/CIRCULATIONAHA.116.025490

352. Ginhoux, F. & Guilliams, M. Tissue-Resident Macrophage Ontogeny and Homeostasis. *Immunity* **44**, 439–449 (2016).

353. Guilliams, M., Thierry, G. R., Bonnardel, J. & Bajenoff, M. Establishment and Maintenance of the Macrophage Niche. *Immunity* **52**, 434–451 (2020).

354. Meiser, J. *et al.* Itaconic acid indicates cellular but not systemic immune system activation. **9**, 32098–32107 (2018).

355. Schiller, H. B. *et al.* The human lung cell atlas: A high-resolution reference map of the human lung in health and disease. *Am. J. Respir. Cell Mol. Biol.* **61**, 31–41 (2019).

356. Mills, E. L. & O'Neill, L. A. Reprogramming mitochondrial metabolism in macrophages as an anti-inflammatory signal. *Eur. J. Immunol.* **46**, 13–21 (2016).

357. Galván-Peña, S. & O'Neill, L. A. J. Metabolic reprograming in macrophage polarization. *Front. Immunol.* **5**, 1–6 (2014).

358. Mills, E. L., Kelly, B. & O'Neill, L. A. J. Mitochondria are the powerhouses of immunity. *Nat. Immunol.* **18**, 488–498 (2017).

359. Saha, S., Shalova, I. N. & Biswas, S. K. Metabolic regulation of macrophage phenotype and function. **280**, 102–111 (2017).

360. El-Chemaly, S. *et al.* Glucose transporter-1 distribution in fibrotic lung disease: Association with [18F]-2-fluoro-2-deoxyglucose-PET scan uptake, inflammation, and neovascularization. *Chest* **143**, 1685–1691 (2013).

361. Patel, A. S. *et al.* Epithelial cell mitochondrial dysfunction and PINK1 are induced by transforming growth factor- beta1 in pulmonary fibrosis. *PLoS One* **10**, 1–14 (2015).

362. Cho, S. J., Moon, J. S., Lee, C. M., Choi, A. M. K. & Stout-Delgado, H. W. Glucose transporter 1-dependent glycolysis is increased during aging-related lung fibrosis, and phloretin inhibits lung fibrosis. *Am. J. Respir. Cell Mol. Biol.* **56**, 521–531 (2017).

363. Verdeguer, F. & Aouadi, M. Macrophage heterogeneity and energy metabolism. *Exp. Cell Res.* **360**, 35–40 (2017).

364. Ryan, D. G. & O'Neill, L. A. J. Krebs cycle rewired for macrophage and dendritic cell effector

functions. *FEBS Lett.* 1–15 (2017).doi:10.1002/1873-3468.12744

365. Ghosez, P. *et al.* Succinate strikes. *Nature* **4**, 5–6 (2014).

366. Sica, A. & Mantovani, A. Plasticity and Polarization. *J. Clin. Invest.* **122**, 787–795 (2012).

367. Bossche, J. Van Den, Neill, L. A. O. & Menon, D. Macrophage Immunometabolism : Where Are We (Going)? *Trends Immunol.* **38**, 395–406 (2017).

368. Al-Khami, A. A. *et al.* Fuelling the mechanisms of asthma: Increased fatty acid oxidation in inflammatory immune cells may represent a novel therapeutic target. *Clin. Exp. Allergy* **47**, 1170–1184 (2017).

369. Riquelme, S. A. *et al.* Pseudomonas aeruginosa Utilizes Host-Derived Itaconate to Redirect Its Metabolism to Promote Biofilm Formation. *Cell Metab.* **0**, 1091–1106 (2020).

370. Tretter, L., Patocs, A. & Chinopoulos, C. Succinate, an intermediate in metabolism, signal transduction, ROS, hypoxia, and tumorigenesis. *Biochim. Biophys. Acta - Bioenerg.* **1857**, 1086–1101 (2016).

371. Macias-Ceja, D. C. *et al.* Succinate receptor mediates intestinal inflammation and fibrosis. *Mucosal Immunol.* **12**, 178–187 (2019).

372. O'Connor, R. S. *et al.* The CPT1a inhibitor, etomoxir induces severe oxidative stress at commonly used concentrations. *Sci. Rep.* **8**, 1–9 (2018).

373. Chakarov, S. *et al.* Two distinct interstitial macrophage populations coexist across tissues in specific subtissular niches. *Science (80-.).* **363**, (2019).

374. Ginhoux, F., Immunology, S. J.-N. R. & 2014, undefined Monocytes and macrophages: developmental pathways and tissue homeostasis. *nature.com* at <https://www.nature.com/articles/nri3671>

375. Byrne, A. J. *et al.* Monocyte-derived macrophages dominate the human airway throughout life. *J. Exp. Med. Submitt.*

376. Joshi, N. *et al.* Single-cell RNA-seq reveals spatially restricted multicellular fibrotic niches during lung fibrosis. *bioRxiv* 569855 (2019).doi:10.1101/569855

377. Butenko, S. *et al.* Transcriptomic Analysis of Monocyte-Derived Non-Phagocytic Macrophages Favors a Role in Limiting Tissue Repair and Fibrosis. *Front. Immunol.* **11**, 1–15 (2020).

378. Zhu, X. *et al.* Frontline Science: Monocytes sequentially rewire metabolism and bioenergetics during an acute inflammatory response. *J. Leukoc. Biol.* **105**, 215–228 (2019).

379. Zhang, S. *et al.* Efferocytosis Fuels Requirements of Fatty Acid Oxidation and the Electron Transport Chain to Polarize Macrophages for Tissue Repair. *Cell Metab.* **29**, 443-456.e5 (2019).

380. Pietrangelo, A. & Ouimet, M. Death Eaters Rely on Metabolic Signaling to Wield Anti-inflammatory Responses. *Cell Metab.* **29**, 234–236 (2019).

381. Amit, I., Winter, D. R. & Jung, S. The role of the local environment and epigenetics in shaping macrophage identity and their effect on tissue homeostasis. *Nat. Immunol.* **17**, 18–25 (2015).

382. Dolan, S. K. & Welch, M. The Glyoxylate Shunt, 60 Years On. *Annu. Rev. Microbiol.* **72**, 309–330 (2018).

383. Wang, H. *et al.* An essential bifunctional enzyme in Mycobacterium tuberculosis for itaconate dissimilation and leucine catabolism. *Proc. Natl. Acad. Sci. U. S. A.* **116**, 15907–15913 (2019).

384. O'Neill, L. A. J. & Artyomov, M. N. Itaconate: the poster child of metabolic reprogramming in macrophage function. *Nat. Rev. Immunol.* **19**, 273–281 (2019).

385. Cordes, T. *et al.* Immunoresponsive gene 1 and itaconate inhibit succinate dehydrogenase to modulate intracellular succinate levels. *J. Biol. Chem.* **291**, 14274–14284 (2016).

386. Ren, K. *et al.* Suppression of IRG-1 Reduces Inflammatory Cell Infiltration and Lung Injury in

Respiratory Syncytial Virus Infection by Reducing. **90**, 7313–7322 (2016).

387. Nair, S. *et al.* Irg1 expression in myeloid cells prevents immunopathology during M. tuberculosis infection. *J. Exp. Med.* **215**, 1035–1045 (2018).

388. ElAzzouny, M. *et al.* Dimethyl itaconate is not metabolized into itaconate intracellularly. *J. Biol. Chem.* jbc.C117.775270 (2017).doi:10.1074/jbc.C117.775270

389. Swain, A. *et al.* Comparative evaluation of itaconate and its derivatives reveals divergent inflammasome and type I interferon regulation in macrophages. *Nat. Metab.* **2**, 594–602 (2020).

390. Lauterbach, M. A. *et al.* Toll-like Receptor Signaling Rewires Macrophage Metabolism and Promotes Histone Acetylation via ATP-Citrate Lyase. *Immunity* **51**, 997-1011.e7 (2019).

391. Ucero, A. C. *et al.* Fra-2–expressing macrophages promote lung fibrosis. *J. Clin. Invest.* **129**, 3293–3309 (2019).

392. Zhou, X. *et al.* Circuit Design Features of a Stable Two-Cell System. *Cell* **172**, 744-757.e17 (2018).

Appendix I: Publications arising from this thesis

Patricia P. Ogger, Gesa J. Albers, Richard J. Hewitt, Brendan J. O'Sullivan, Joseph E. Powell, Emily Calamita, Poonam Ghai, Simone A. Walker, Peter McErlean, Peter Saunders, Shaun Kingston, Philip L. Molyneaux, John M. Halket, Robert Gray, Daniel C. Chambers, Toby M. Maher, Clare M. Lloyd, Adam J. Byrne, 2020. Itaconate controls the severity of pulmonary fibrosis. *Science Immunology*, 5 (52). DOI: 10.1126/sciimmunol.abc1884.

Abstract

Idiopathic pulmonary fibrosis (IPF) is a fatal lung disease in which airway macrophages (AMs) play a key role. Itaconate has emerged as a mediator of macrophage function, but its role during fibrosis is unknown. Here, we reveal that itaconate is an endogenous antifibrotic factor in the lung. Itaconate levels are reduced in bronchoalveolar lavage, and itaconate-synthesizing cis-aconitate decarboxylase expression (*ACOD1*) is reduced in AMs from patients with IPF compared with controls. In the murine bleomycin model of pulmonary fibrosis, *Acod1*$^{-/-}$ mice develop persistent fibrosis, unlike wild-type (WT) littermates. Profibrotic gene expression is increased in *Acod1*$^{-/-}$ tissue-resident AMs compared with WT, and adoptive transfer of WT monocyte-recruited AMs rescued mice from disease phenotype. Culture of lung fibroblasts with itaconate decreased proliferation and wound healing capacity, and inhaled itaconate was protective in mice in vivo. Collectively, these data identify itaconate as critical for controlling the severity of lung fibrosis and targeting this pathway may be a viable therapeutic strategy.

Patricia P. Ogger and Adam J. Byrne, 2020. Macrophage metabolic reprogramming during chronic lung disease. *Mucosal Immunology*. Published online ahead of print on November 12th, 2020. https://doi.org/10.1038/s41385-020-00356-5.

Abstract

Airway macrophages (AMs) play key roles in the maintenance of lung immune tolerance. Tissue tailored highly specialised and strategically positioned, AMs are critical sentinels of lung homoeostasis. In the last decade, there has been a revolution in our understanding of how metabolism underlies key macrophage functions. While these initial observations were made during steady state or using in vitro polarised macrophages, recent studies have indicated that during many chronic lung diseases (CLDs), AMs adapt their metabolic profile to fit their local niche. By generating reactive oxygen species (ROS) for pathogen defence, utilising aerobic glycolysis to rapidly generate cytokines, and employing mitochondrial respiration to fuel inflammatory responses, AMs utilise metabolic reprogramming for host defence, although these changes may also support chronic pathology. This review focuses on how metabolic alterations underlie AM phenotype and function during CLDs. Particular emphasis is given to how our new understanding of AM metabolic plasticity may be exploited to develop AM-focused therapies.

Appendix II: Conference abstracts arising from this thesis

1) Oral presentation at the European Respiratory Society Virtual Congress, September 2020, originally planned for Vienna, Austria

Itaconate drives the resolution of pulmonary fibrosis

Patricia P Ogger[1], Poonam Ghai[1], Richard J Hewitt[1], Philip L Molyneaux[1,2], Toby M Maher[1,2], Clare M Lloyd[1] and Adam J Byrne[1]

[1]Inflammation, Repair & Development Section, National Heart and Lung Institute, Imperial College London SW7 2AZ, UK

[2]NIHR Respiratory Biomedical Research Unit, Royal Brompton Hospital, Sydney Street, London, SW3 6NP, UK

Introduction & Objectives: Airway macrophages (AMs) are implicated in the dysregulated wound healing response in idiopathic pulmonary fibrosis (IPF). The endogenous metabolite itaconate, synthesised by immune-response gene 1 (IRG1), has been shown to influence macrophage function via regulation of succinate dehydrogenase. Here we investigated the role of itaconate in pulmonary fibrosis.

Methods: To assess the expression pattern of *Irg1* in the lung, we analysed gene expression in AMs from IPF patients or controls. To investigate the role of itaconate in the bleomycin model of pulmonary fibrosis we utilised WT and Irg1$^{-/-}$ mice, in addition to therapeutic dosing of exogenous itaconate. To determine the role of secreted itaconate on the stromal compartment in IPF, primary lung fibroblasts were cultured with itaconate *in vitro* and proliferation/wound healing was assessed.

Results: *Irg1* expression was reduced in IPF AMs compared to controls. In the bleomycin model, *Irg1*$^{-/-}$ mice had decreased survival, worsened lung function and increased collagen deposition at the resolution time point (42d post bleomycin). Tissue-resident AMs (Tr-AMs) upregulated the expression of fibrosis-related genes in *Irg1*$^{-/-}$ mice and showed impaired Oxidative Phosphorylation. Inhaled itaconate during the fibrotic phase of the bleomycin model improved lung function and decreased gene expression of type IV collagen and fibronectin. *In vitro* culture of primary human lung fibroblasts with itaconate decreased proliferation and wound healing capacity.

Conclusions: Overall these data indicate that itaconate is essential for the resolution of lung fibrosis and that targeting this pathway may be a viable therapeutic strategy in IPF.

2) Oral presentation at the European Respiratory Society Lung Science Conference, March 2020, Estoril, Portugal

Itaconate drives the resolution of pulmonary fibrosis

Patricia P Ogger[1], Poonam Ghai[1], Richard J Hewitt[1], Philip L Molyneaux[1,2], Toby M Maher[1,2], Clare M Lloyd[1] and Adam J Byrne[1]

[1]Inflammation, Repair & Development Section, National Heart and Lung Institute, Imperial College London SW7 2AZ, UK

[2]NIHR Respiratory Biomedical Research Unit, Royal Brompton Hospital, Sydney Street, London, SW3 6NP, UK

Introduction & Objectives: Airway macrophages (AMs) are implicated in the dysregulated wound healing response in idiopathic pulmonary fibrosis (IPF). The endogenous metabolite itaconate, synthesised by immune-response gene 1 (IRG1), has been shown to influence macrophage function via regulation of succinate dehydrogenase. Here we investigated the role of itaconate in pulmonary fibrosis.

Methods: To assess the expression pattern of *Irg1* in the lung, we analysed gene expression in AMs from IPF patients or controls. To investigate the role of itaconate in the bleomycin model of pulmonary fibrosis we utilised WT and $Irg1^{-/-}$ mice, in addition to therapeutic dosing of exogenous itaconate. To determine the role of secreted itaconate on the stromal compartment in IPF, primary lung fibroblasts were cultured with itaconate *in vitro* and proliferation/wound healing was assessed.

Results: *Irg1* expression was reduced in IPF AMs compared to controls. In the bleomycin model, $Irg1^{-/-}$ mice had decreased survival, worsened lung function and increased collagen deposition at the resolution time point (42d post bleomycin). Tissue-resident AMs (Mo-AMs) upregulated the expression of fibrosis-related genes in $Irg1^{-/-}$ mice and showed impaired Oxidative Phosphorylation. Inhaled itaconate during the fibrotic phase of the bleomycin model improved lung function and decreased gene expression of type IV collagen and fibronectin. *In vitro* culture of primary human lung fibroblasts with itaconate decreased proliferation and wound healing capacity.

Conclusions: Overall these data indicate that itaconate is essential for the resolution of lung fibrosis and that targeting this pathway may be a viable therapeutic strategy in IPF.

→ This presentation was awarded the William McNee Award during the Young Investigator session.

3) Oral presentation at the Inaugural London Respiratory Meeting, January 2020, London, United Kingdom

Itaconate drives the resolution of pulmonary fibrosis

Patricia P Ogger[1], Poonam Ghai[1], Richard J Hewitt[1], Philip L Molyneaux[1,2], Toby M Maher[1,2], Clare M Lloyd[1] and Adam J Byrne[1]

[1]Inflammation, Repair & Development Section, National Heart and Lung Institute, Imperial College London SW7 2AZ, UK

[2]NIHR Respiratory Biomedical Research Unit, Royal Brompton Hospital, Sydney Street, London, SW3 6NP, UK

Introduction & Objectives: Airway macrophages (AMs) are implicated in the dysregulated wound healing response in idiopathic pulmonary fibrosis (IPF). The endogenous metabolite itaconate, synthesised by immune-response gene 1 (IRG1), has been shown to influence macrophage function via regulation of succinate dehydrogenase. Here we investigated the role of itaconate in pulmonary fibrosis.

Methods: To assess the expression pattern of *Irg1* in the lung, we analysed gene expression in AMs from IPF patients or controls. To investigate the role of itaconate in the bleomycin model of pulmonary fibrosis we utilised WT and Irg1$^{-/-}$ mice, in addition to therapeutic dosing of exogenous itaconate. To determine the role of secreted itaconate on the stromal compartment in IPF, primary lung fibroblasts were cultured with itaconate *in vitro* and proliferation/wound healing was assessed.

Results: *Irg1* expression was reduced in IPF AMs compared to controls. In the bleomycin model, *Irg1*$^{-/-}$ mice had decreased survival, worsened lung function and increased collagen deposition at the resolution time point (42d post bleomycin). Tissue-resident AMs (Tr-AMs) upregulated the expression of fibrosis-related genes in *Irg1*$^{-/-}$ mice and showed impaired Oxidative Phosphorylation. Inhaled itaconate during the fibrotic phase of the bleomycin model improved lung function and decreased gene expression of type IV collagen and fibronectin. *In vitro* culture of primary human lung fibroblasts with itaconate decreased proliferation and wound healing capacity.

Conclusions: Overall these data indicate that itaconate is essential for the resolution of lung fibrosis and that targeting this pathway may be a viable therapeutic strategy in IPF.

4) Oral presentation at the British Society for Immunology Congress, December 2019, Liverpool, United Kingdom

Itaconate drives the resolution of pulmonary fibrosis

Patricia P Ogger[1], Poonam Ghai[1], Richard J Hewitt[1], Philip L Molyneaux[1,2], Toby M Maher[1,2], Clare M Lloyd[1] and Adam J Byrne[1]

[1]Inflammation, Repair & Development Section, National Heart and Lung Institute, Imperial College London SW7 2AZ, UK

[2]NIHR Respiratory Biomedical Research Unit, Royal Brompton Hospital, Sydney Street, London, SW3 6NP, UK

Introduction & Objectives: Idiopathic pulmonary fibrosis (IPF) is a devastating disease with limited therapeutic options. Airway macrophages (AMs), key components of airway defence, are implicated in the dysregulated wound healing underlying IPF. Itaconate, an endogenous metabolite with antimicrobial and anti-inflammatory potential is synthesised by immune-response gene 1 (Irg1) and Irg1/itaconate are increased in macrophages upon LPS-stimulation. We hypothesised that AM-derived itaconate contributes to the pathogenesis of pulmonary fibrosis and manipulation of this pathway could ameliorate disease.

Methods: To assess the expression pattern of *Irg1* in healthy/IPF lung, we employed gene expression analysis in AMs from IPF patients or controls. To mechanistically interrogate the role of Irg1 in the bleomycin model of pulmonary fibrosis we utilised WT and $Irg1^{-/-}$ mice, in addition to therapeutic dosing of exogenous itaconate. Finally, to determine the role of secreted itaconate on the stromal compartment in IPF, primary lung fibroblasts were cultured with itaconate in vitro and proliferation/wound healing was assessed.

Results: IPF AMs showed reduced expression of *Irg1* compared to controls. In the bleomycin model, $Irg1^{-/-}$ mice had decreased survival, worsened lung function, and increased collagen deposition at the resolution time point (42d post bleomycin) compared to WT mice. Monocyte-recruited AMs (Mo-AMs) showed higher expression of *Irg1* compared to tissue-resident AMs (Tr-AMs). Tr-AMs significantly upregulated the expression of fibrosis-related genes in $Irg1^{-/-}$ mice compared to WT controls, while the functional phenotype of Mo-AMs remained unchanged. Itaconate treatment during the fibrotic phase of the bleomycin model improved lung function and decreased gene expression of type IV collagen and fibronectin. *In vitro* culture of primary human lung fibroblasts with itaconate decreased proliferation and wound healing capacity.

Conclusions: Overall these data indicate that Irg1-expressing Mo-AMs are essential for the resolution of lung fibrosis and that targeting this pathway may be a viable therapeutic strategy in IPF.

5) Oral presentation at the British Thoracic Society Winter Meeting, December 2019, London, United Kingdom

Itaconate drives the resolution of pulmonary fibrosis

Patricia P Ogger[1], Poonam Ghai[1], Richard J Hewitt[1], Philip L Molyneaux[1,2], Toby M Maher[1,2], Clare M Lloyd[1] and Adam J Byrne[1]

[1]Inflammation, Repair & Development Section, National Heart and Lung Institute, Imperial College London SW7 2AZ, UK

[2]NIHR Respiratory Biomedical Research Unit, Royal Brompton Hospital, Sydney Street, London, SW3 6NP, UK

Introduction & Objectives: Idiopathic pulmonary fibrosis (IPF) is a devastating disease with limited therapeutic options. Airway macrophages (AMs) are key components of airway defence and are implicated in the dysregulated wound healing underlying IPF. Itaconate is an endogenous metabolite with antimicrobial and anti-inflammatory potential. Synthesis of itaconate is catalysed by immune-response gene 1 (Irg1) and Irg1/itaconate are increased in macrophages upon stimulation with LPS[1]. We hypothesised that the expression of Irg1/itaconate in AMs is involved in the pathogenesis/resolution of pulmonary fibrosis and manipulation of this pathway could ameliorate disease.

Methods: To assess the distribution and expression pattern of Irg1 in healthy/IPF lung, we employed gene expression analysis in AMs, bronchial epithelial cells and lung fibroblasts from IPF patients or controls. To mechanistically interrogate the role of Irg1 in the bleomycin model of pulmonary fibrosis we utilised mice expressing, or lacking Irg1, in addition to therapeutic dosing of exogenous itaconate. Finally, to determine the role of secreted itaconate on the stromal compartment in IPF, primary lung fibroblasts were cultured with itaconate in vitro and proliferation/wound healing was assessed.

Results: Irg1 was expressed in AMs, but not epithelial cells or fibroblasts from healthy controls/IPF patients; interestingly, IPF AMs showed reduced expression of *Irg1* compared to controls. In the bleomycin model, $Irg1^{-/-}$ mice had decreased survival, worsened lung function, and increased collagen deposition at the resolution time point (42d post bleomycin) compared to WT mice. Monocyte-recruited AMs (Mo-AMs) showed higher expression of *Irg1* compared to tissue-resident AMs (Tr-AMs). Tr-AMs significantly upregulated the expression of fibrosis-related genes in $Irg1^{-/-}$ compared to WT, while the functional phenotype of monocyte-recruited AMs was not affected by $Irg1^{-/-}$. Treatment with itaconate during the fibrotic phase of the bleomycin model improved lung function and decreased gene expression of type IV collagen and fibronectin. *In vitro* culture of primary human lung fibroblasts with itaconate decreased proliferation and wound healing capacity.

Conclusions: Taken together these data indicate that Irg1-expressing Mo-AMs are essential for the resolution of lung fibrosis and that targeting this pathway may be a viable therapeutic strategy in IPF.

→ *This presentation was awarded the British Association for Lung Research (BALR) Young Investigator Award*

6) Poster presentation at the International Consortium for Lung and Airway Fibrosis (ICLAF), October 2018, Monterey, CA, United States

Airway macrophages in IPF and chronic HP have distinct metabolic alterations

Patricia P Ogger[1], Philip L Molyneaux[1,2], Richard J Hewitt[1], Toby M Maher[1,2], Clare M Lloyd[1] and Adam J Byrne[1]

[1]Inflammation, Repair & Development Section, National Heart and Lung Institute, Imperial College London SW7 2AZ, UK

[2]NIHR Respiratory Biomedical Research Unit, Royal Brompton Hospital, Sydney Street, London, SW3 6NP, UK

Background: Interstitial lung disease (ILD) includes over 300 different conditions, the most common being idiopathic pulmonary fibrosis (IPF) and chronic hypersensitivity pneumonitis (cHP). IPF is a fatal chronic lung disease characterised by excessive accumulation of extracellular matrix in the lung interstitium. Chronic HP, triggered by a hypersensitivity reaction, is more inflammatory but fibrosis can develop in the late stage. Evidence suggests that IPF is partly due to dysregulated wound-healing orchestrated by macrophages. While metabolic reprogramming of macrophages drives inflammation, its contribution to pulmonary fibrosis is unknown. We hypothesise that airway macrophage (AM) metabolic reprogramming underlies pulmonary fibrosis and that manipulation of AM metabolism represents a potential novel therapeutic strategy.

Methods: AM number and phenotype were assessed in interstitial lung disease (ILD) patient bronchoalveolar lavage (BAL) by flow cytometry. Subsequently AMs were enriched based on CD206 expression and metabolic functionality was analysed by targeted GC-MS, extracellular flux analysis (Seahorse) and qPCR of key metabolic enzymes. Metabolic alterations of ILD AMs were integrated with surface marker expression and lung function decline.

Results: IPF AMs had increased gene expression of key enzymes in the first half of the Krebs cycle – *isocitrate dehydrogenase 2 (IDH2), ATP citrate lyase (ACLY)*, *aconitase 2 (ACO2,* mitochondrial), *oxaloglutarate dehydrogenase (OGDH)* and *phosphoenolpyruvate carboxykinase 2 (PCK2)*, while expression of *aconitase 1* (ACO1, cytosolic) and *citrate synthase* (CS) was decreased compared to controls. Extracellular flux analysis showed a trend towards increased oxygen consumption rate (OCR) and higher ATP production in IPF AMs. Chronic HP AMs had increased gene expression of key glycolytic enzymes and first half Krebs cycle enzymes, but a downregulation of second half Krebs cycle genes. Extracellular flux analysis showed high OCR as well as high extracellular acidification rate (ECAR), indicating high spare respiratory capacity and metabolic activity.

Conclusions: Together these data indicate that AMs undergo distinct metabolic alterations during pulmonary fibrosis, which differ across IPF and chronic HP. The differential gene expression of *IDH2* is particularly interesting considering *IDH2* often has a gain-of-function mutation in acute myeloid leukaemia and other types of cancer. Future work aims to further investigate IPF AM *IDH2* mutation status, which might underlie metabolic reprogramming and to analyse how metabolic changes in particularly tissue resident and recruited AM drive pulmonary fibrosis.

7) Poster presentation at the European Respiratory Society Congress, September 2018, Paris, France

Distinct metabolic alterations in airway macrophages during pulmonary fibrosis

Patricia P Ogger[1], Richard J Hewitt[1], Philip L Molyneaux[1,2], Toby M Maher[1,2], Clare M Lloyd[1] and Adam J Byrne[1]

[1]Inflammation, Repair & Development Section, National Heart and Lung Institute, Imperial College London SW7 2AZ, UK

[2]NIHR Respiratory Biomedical Research Unit, Royal Brompton Hospital, Sydney Street, London, SW3 6NP, UK

Background: Idiopathic pulmonary fibrosis (IPF) is a fatal disease with limited treatment options. Evidence suggests that IPF is in part due to dysregulated wound-healing orchestrated by macrophages. While metabolic reprogramming of macrophages drives inflammation, its contribution to IPF is unknown. We hypothesise that airway macrophage (AM) metabolic reprogramming underlies IPF and that manipulation of AM metabolism represents a potential novel therapeutic strategy for IPF.

Methods: To define the role of AM metabolic reprogramming during pulmonary fibrosis we utilised patient bronchoalveolar lavage (BAL) and murine models; AM number and phenotype were assessed by flow cytometry. AMs were sorted from BAL of bleomycin/PBS treated mice and mitochondrial function was assessed by extracellular flux analysis. In IPF AMs and controls we measured expression of key genes involved in the control of glycolysis and OXPHOS, and mitochondrial function.

Results: Upon bleomycin treatment, a newly emerging Siglec-F^{int} macrophage population gradually replaced the Siglec-F^{hi} population, sorted from BAL of bleomycin treated mice, 3 weeks post challenge, and were metabolically reprogrammed with notable changes in OXPHOS. In IPF BAL, AMs were the most abundant immune cell type and multiple genes involved in OXPHOS were upregulated in IPF AMs compared to healthy controls, including *IDH2*, *ACO2* and *OGDH* while *CS* was decreased.

Conclusions: Together these data indicate that during pulmonary fibrosis, AMs undergo metabolic alterations in the OXPHOS pathway. Future work aims to further characterise the metabolic phenotypes of resident and recruited AMs in the lung and assess impact on development of fibrosis.

8) Poster presentation at the European Congress for Immunology, September 2018, Amsterdam, the Netherlands

Metabolic alterations in airway macrophages during pulmonary fibrosis

Patricia P Ogger[1], Philip L Molyneaux[1,2], Richard J Hewitt[1], Toby M Maher[1,2], Clare M Lloyd[1] and Adam J Byrne[1]

[1]Inflammation, Repair & Development Section, National Heart and Lung Institute, Imperial College London SW7 2AZ, UK

[2]NIHR Respiratory Biomedical Research Unit, Royal Brompton Hospital, Sydney Street, London, SW3 6NP, UK

Background: Idiopathic pulmonary fibrosis (IPF) is a fatal disease with limited treatment options. Evidence suggests that IPF is in part due to dysregulated wound-healing orchestrated by macrophages. While metabolic reprogramming of macrophages drives inflammation, its contribution to IPF is unknown. We hypothesise that airway macrophage (AM) metabolic reprogramming underlies IPF and that manipulation of AM metabolism represents a potential novel therapeutic strategy for IPF.

Methods: First we assessed AM number and phenotype in patient bronchoalveolar lavage (BAL) by flow cytometry. Subsequently AMs were enriched and metabolic functionality was analysed by extracellular flux analysis and PCR array of key metabolic enzymes. To investigate the metabolic phenotype of tissue resident and monocyte recruited airway macrophages in pulmonary fibrosis, we utilised the bleomycin mouse model and measured expression of metabolic genes and mitochondrial function in sorted macrophage populations.

Results: IPF AMs show increased expression of *ENO2* and *IDH2*, while *SDHC* gene expression is decreased compared to healthy controls. Upon bleomycin treatment, Siglec-F^{int} monocyte recruited airway macrophages gradually replaced Siglec-F^{hi} tissue resident airway macrophages and show higher gene expression of *HK3* and *IDH2*.

Conclusions: Together these data indicate that during pulmonary fibrosis, AMs undergo metabolic alterations. The differential gene expression of *IDH2* and *SDHC* is particularly interesting considering these are major oncogenes. Future work aims to further characterise the metabolic phenotypes of resident and recruited AMs in the lung and to investigate how alterations in AM metabolic intermediates in IPF may contribute to the disease.

9) Poster presentation at the Translational Immunometabolism Conference, June 2018, Basel, Switzerland

Metabolic alterations in airway macrophages during pulmonary fibrosis

Patricia P Ogger[1], Philip L Molyneaux[1,2], Richard J Hewitt[1], Toby M Maher[1,2], Clare M Lloyd[1] and Adam J Byrne[1]

[1]Inflammation, Repair & Development Section, National Heart and Lung Institute, Imperial College London SW7 2AZ, UK

[2]NIHR Respiratory Biomedical Research Unit, Royal Brompton Hospital, Sydney Street, London, SW3 6NP, UK

Idiopathic pulmonary fibrosis (IPF) is a fatal disease with limited treatment options. Evidence suggests IPF is in part due to dysregulated wound-healing orchestrated by macrophages. While metabolic reprogramming of macrophages drives inflammation, its contribution to IPF is unknown. We hypothesise that airway macrophage (AM) metabolic reprogramming underlies IPF and could be therapeutically targeted. IPF AMs obtained from bronchoalveolar lavage (BAL) showed increased expression of *ENO2* and *IDH2*, while *SDHC* was decreased compared to controls. To further investigate the metabolic phenotype of tissue resident and monocyte recruited AMs in pulmonary fibrosis, we utilised the bleomycin mouse model. Gene expression of *HK3* and *IDH2* was increased in Siglec-F^{int} monocyte recruited AMs, which gradually replace Siglec-F^{hi} tissue resident AMs. These data indicate that changes in alveolar macrophage landscape during pulmonary fibrosis go along with differential metabolic needs of tissue resident and recruited macrophages – which in turn could be targeted specifically in the future.

10) Poster presentation at the European Respiratory Society Lung Science Conference, March 2018, Estoril, Portugal

Distinct metabolic alterations in airway macrophages during pulmonary fibrosis

Patricia P Ogger[1], Toby M Maher[1,2], Clare M Lloyd[1] and Adam J Byrne[1]

[1]Inflammation, Repair & Development Section, National Heart and Lung Institute, Imperial College London SW7 2AZ, UK

[2]NIHR Respiratory Biomedical Research Unit, Royal Brompton Hospital, Sydney Street, London, SW3 6NP, UK

Background: Idiopathic pulmonary fibrosis (IPF) is a fatal disease with limited treatment options. Evidence suggests that IPF is in part due to dysregulated wound-healing orchestrated by macrophages. While metabolic reprogramming of macrophages drives inflammation, its contribution to IPF is unknown. We hypothesise that AM metabolic reprogramming underlies IPF and that manipulation of AM metabolism represents a potential novel therapeutic strategy for IPF.

Methods: To define the role of AM metabolic reprogramming during pulmonary fibrosis we utilised patient bronchoalveolar lavage (BAL) and murine models; AM number and phenotype were assessed by flow cytometry. AMs were sorted from BAL of bleomycin/PBS treated mice and mitochondrial function was assessed by extracellular flux analysis. In IPF AMs and controls we measured expression of key genes involved in the control of glycolysis and OXPHOS, and mitochondrial function.

Results: Upon bleomycin treatment, Siglec-F^{int} monocyte recruited airway macrophages gradually replaced Siglec-F^{hi} tissue resident airway macrophages (Tr-AM). Tr-AMs, sorted from BAL of bleomycin treated mice, 3 weeks post challenge, were metabolically reprogrammed with notable changes in OXPHOS. In IPF BAL, AMs were the most abundant immune cell type and multiple genes involved in OXPHOS were downregulated in IPF AMs compared to healthy controls, including *LDH, SDHD, MDH1* and *PDHB*, while *IDH2* was increased.

Conclusions: Together these data indicate that during pulmonary fibrosis, AMs undergo metabolic alterations in the OXPHOS pathway. Future work aims to further characterise the metabolic phenotypes of resident and recruited AMs in the lung and assess impact on development of fibrosis.

11) Poster presentation at the British Society for Immunology Conference, December 2017, Brighton, United Kingdom

Metabolic alterations of Airway Macrophages during Interstitial Lung Disease

Patricia P Ogger[1], Toby M Maher[1,2], Clare M Lloyd[1] and Adam J Byrne[1]

[1]Inflammation, Repair & Development Section, National Heart and Lung Institute, Imperial College London SW7 2AZ, UK

[2]NIHR Respiratory Biomedical Research Unit, Royal Brompton Hospital, Sydney Street, London, SW3 6NP, UK

Corresponding authors email: p.ogger15@imperial.ac.uk

Background: Interstitial lung disease (ILD) encompasses over 300 different conditions, the most common being idiopathic pulmonary fibrosis (IPF) and chronic hypersensitivity pneumonitis (cHP). IPF is a fatal chronic lung disease characterised by excessive accumulation of extracellular matrix in the lung interstitium. cHP is a complex granulomatous, inflammatory disease affecting both the airways and the lung parenchyma. The role of airway macrophages (AM) in the pathology of both IPF and cHP remains unclear. Recent work has shown that macrophage responses are tightly regulated by metabolic changes, allowing optimal cytokine and effector molecule production. We hypothesise that AM metabolic reprogramming underlies ILD and in particular the pathogenesis of both IPF/cHP.

Methods: We aimed to determine the phenotypic and metabolic characteristics of AMs in ILD. Bronchoalveolar lavage fluid (BALF) from IPF patients (n=31), cHP patients (n=16) and healthy controls (n=7) was analysed by flow cytometry for the enumeration of the major immune cell populations. Sorted AMs were assessed for expression of key genes involved in the control of glycolysis and oxidative phosphorylation enzymes by qPCR.

Results: AMs were the most abundant immune cell population in IPF and showed a distinct metabolic phenotype in comparison to controls. Expression of *LDH, SDHD, MDH1* and *PDHB* were decreased, while *IDH2* was increased in IPF in comparison to healthy AMs. In cHP, AMs were characterised by decreased expression of OXPHOS enzymes and increased glycolysis genes in comparison to both IPF and healthy controls.

Conclusion: Together, these data indicate that during ILD, AMs have profound alterations in the expression of genes controlling glycolysis and TCA cycle, and may suggest that development of therapies, which correct AM-metabolic dysregulation may be a novel therapeutic strategy to treat ILD.